Proceedings

Forecast Engineering:
From Past Design to Future Decision
2017

Contents

Preface

In September 2016, Bauhaus-Universität Weimar, Faculty of Civil engineering startet the EU funded Erasmus+ Strategic Partnership with four partner universities in Portugal, Croatia, Slovenia and Hungary. The aim is to help shape innovative developments in civil engineering in intercultural exchange and to promote the specialist, social and language skills of excellent junior staff.

As part of the program lines »Erasmus +« and »Key Action II: Strategic Partnerships«, the Bauhaus-Universität Weimar is working together with the Universidade de Aveiro (Portugal), the University of Osijek (Croatia), the University of Ljubljana (Slovenia) and the Budapest University of Technology and Economics (Hungary) and put on a strategic footing. At the center of international cooperation is the exchange of technical competencies in the areas of earthquake engineering, steel and bridge construction, mathematical models and structural analysis.

The proceedings at hand are the result from the Bauhaus Summer School Course: Forecast Engineering held at the Bauhaus-Universität Weimar, 2017. It summarizes the results of the conducted project work, provides the abstracts of the contributions by the participants, as well as impressions from the accompanying programme and organized cultural activities.
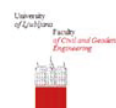
Group Picture of the Summer Course Participants 2017 (Photo: B. Proschak)

Conduction of experiments in part of project No. 4 (Photo: B. Proschak)

Bauhaus Summer School – Forecast Engineering 2017
From past design to future decision

ABRAHAMCZYK Lars, SCHWARZ Jochen

Earthquake Damage Analysis Center, Bauhaus-Universität Weimar, Germany

Targets and objectives

The design of engineering structures takes place today and in the past on the basis of static calculations. The consideration of uncertainties in the model quality becomes more and more important with the development of new construction methods and design requirements. In addition to the traditional forced-based approaches, experiences and observations about the deformation behavior of components and the overall structure under different exposure conditions allow the introduction of novel detection and evaluation criteria.

Bauhaus-Universität Weimar presented special topics of structural engineering to highlight the broad spectrum of civil engineering in the field of modeling and simulation. Participating students were enabled to deal with advanced methods and its practical application. The summer course sought to impart knowledge and to combine research with a practical context, through a challenging and demanding series of lectures, seminars and project work.
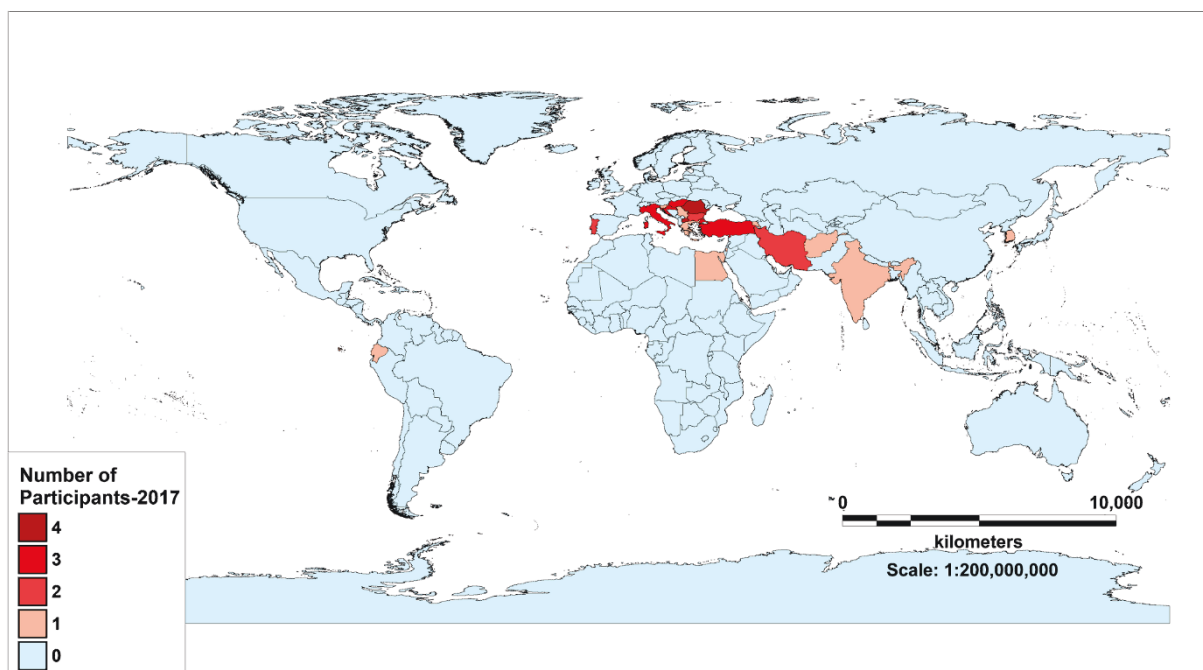
Figure 1. Home countries of the participants attending the Summer School "Forecast Engineering" 2017.

The comprehensive summer school at graduate level introduced selected students to different course topics and six related projects. To enable participants to understand and use the presented concepts in their further professional career a main part of the summer school was devoted to interdisciplinary project work. Discussions and the exchange of ideas with professors, research associates and other participants during and after classes enhanced the personal experience and brought best benefits to all participants. The course was completed by an excursion to the factory of the industry partner Plauen Stahl Technologie and MaxBögl as well as several social/team building activities.

Participants

The summer course is aimed primarily for graduate and postgraduate civil engineering students (the second (M.Sc.) and third cycle (Ph.D.)), from various institutions and countries. It enables the participants to exchain knowledge and train their soft skills (like team working and task sharing), especially during the work in internationally composed project groups. By providing students with advanced, scientifically-based interdisciplinary knowledge, skills and methods, they are trained to react to demanding engineering tasks in the areas of modeling and simulation under specific site, action and loading conditions.

Figure 1 visualize the home countries of the 36 participants from 19 countries and gives an impression upon the internationality of the summer course as well as intercultural exchange of ideas, thinking and life styles.

Course topics

The special character of this course is in the combination of basic disciplines of structural engineering with applied research projects in the areas of steel and reinforced concrete structures, earthquake and wind engineering as well as informatics and linking them to mathematical methods and modern tools of visualization. Its innovative character results from the ambitious engineering tasks and advanced modeling demands. Major course topics were derived from current research fields of the participating institutions at Bauhaus-Universität Weimar and involved European project partners. They were introduced by key lectures in civil engineering and condensed during the project related training of simulation and modeling techniques. The acquired knowledge could be applied to scientific and practically relevant projects within a compact course. Several targets harmonically overlap.

The summer school combines theory and practice on the basis of advanced research and tool development. The modular structure of the programme allows the participants to address current and trendsetting problems and research topics.

Lectures: The necessary theoretical basics, the current state of research (in project targeting fields) as well as special topics are presented by lecturers, leading scientists from the partner institution, and invited guest speakers (cf. Guest lecturers and invited speakers).

Project work: in small groups and intensively supervised. It includes presentation and submission of final results - this (for the participants mostly demanding) part of the course offers the possibility to work in interdisciplinary teams on different projects. The outcome – presented by the herein compiled reports – reaches an impressive level of results and graphical elaboration (cf. Project reports).
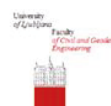
The participants could choose between six offered projects dealing with advanced current engineering research topics:

- Project 1 | Implementation and validation of wireless structural health monitoring systems
- Project 2 | Image analysis for change detection
- Project 3 | Evaluation of existing RC frame structures with URM infill walls
- Project 4 | Numerical analyses on the stability of beam-columns
- Project 5 | Model-updating: theory, algorithms and insights
- Project 6 | Wind-induced vibrations of long-span bridges

Presentation of the participants (workshop character): Participating students were requested to present their work in a special session and to defend their results in front of a broad scientific audience. Therefore each participant had to submit a short abstract together with his/her application. On the basis of these abstracts 15 titles were elected as presentation by the participants, which also shall honor the effort and work of the participant (cf. Papers contributed by the participants).

Excursion: An excursion to just finalized construction sites emphasizes the practical relevance of the course topics and illustrates existing requests for real existing structures. Discussions with professionals provide the opportunity to link theoretical knowledge to practical experience.

Guest lecturers and invited speakers

Nationally and internationally well-known and high-ranked scientist could be welcomed as guest speakers at the engineering summer course at Bauhaus-Universität Weimar in 2017. The current state of research at the project partner's universities as well as lecturers from other disciplines highlighted the future demands on engineers to overcome future requirements on engineered structures.

- Exploring problems in regression analysis |
  Prof. I. Pereira (Universiade de Aveiro, Portugal)

- Dynamic behaviour of stone masonry railway bridges: experimental and numerical approaches |
  Dr. D. Riberio (Polytechnic Institute of Porto, Portugal)

- Inelastic modelling of historic masonry structures for seismic analyses |
  Dr. S. Petrovčić (University of Ljubljana, Slovenia)

- Shear resistance capacity of masonry infilled reinforced concrete frames by members |
  Dr. D. Penava (Josip Juraj Strossmayer University of Osijek, Croatia)

- Construction and application schemes of wind tunnels for model experimentation |
  J.B. Westenberg (Westenberg Engineering, Germany)

- Wind response of modern infrastructure buildings - prediction based on wind tunnel investigations | *Prof. R. Höffer (Ruhr-University Bochum, Germany)*

- Let's rock! Behavior and design of seismic resistant rocking structures |
  Dr. J.A. László (Budapest University of Technology and Economics, Hungary)

- Climate change impact |
  Dr. M. Fink (Friedrich-Schiller-Universität Jena, Germany)

Time schedule

	Monday Aug 21st	**Tuesday** Aug 22nd	**Wednesday** Aug 23rd	**Thursday** Aug 24th	**Friday** Aug 25th	**Sat./Sun.** Aug 26th/27th
09:00 - 10:30	Opening 2017	Prof. I. Pereira (UA, Portugal)	Presentation by participants	Dr. S. Petrovčić (UL, Slovenia)	Prof. R. Höffer (RUB, Germany)	Cultural events and program as part of the Bauhaus Summer School 2017
11:00 - 12:30	Projects 1 & 2	Prof. I. Pereira (UA, Portugal)	Dr. D. Ribeiro (IPP, Portugal)	Dr. D. Penava (GFOS, Croatia)	J.B. Westenberg (Germany)	
	lecture hall C	*lecture hall C*	*lecture hall C*	*lecture hall C*	*lecture hall C*	
	Lunch					
13:30 - 15:00	Projects 3 & 4	Project work	Interdisciplinary experience exchange with specialised courses of Bauhaus Summer School **14:00 - 17:00**	Project work	Project work	
15:30 - 17:00	Projects 5 & 6					
	lecture hall C	*will be announced*			*lecture hall C*	
17:30 - 19:00	Icebreaker party **18:00**		Team building (Sport challenges)		Sightseeing	
	Kasseturm		*Falkenburg*	*will be announced*	*meeting point*	
	Cultural events as part of the Bauhaus Summer School 2017					

	Monday Aug 28th	**Tuesday** Aug 29th	**Wednesday** Aug 30th	**Thursday** Aug 31st	**Friday** Sept 1st	**Sat.** Sept 2nd
09:00 - 10:30	Dr. J.A. László (BME, Hungary)	Dr. M. Fink (Uni Jena, Germany)	Excursion to the companies: Plauen Stahl Technologies and MaxBögl	Project work	Presentation of project works & closure	05:00 - 10:00 Departure
11:00 - 12:30	Presentation by participants	Presentation by participants				
	lecture hall C	*lecture hall C*		*will be announced*	*lecture hall C*	
	Lunch			Lunch		
13:30 - 15:00	Project work	Project work		Preparing of presentation	Preparation of final report	
15:30 - 17:00						
	will be announced			*will be announced*	*will be announced*	
17:30 - 19:00	Barbecue				Farewell party **18:00**	
	M18	*will be announced*			*Mensa*	
	Cultural events as part of the Bauhaus Summer School 2017					

Bauhaus Summer School – Forecast Engineering 2017
Excursion

KAZMI Yasir

NHRE, Bauhaus-Universität Weimar, Germany

As a part of the course "Forecast Engineering" under Bauhaus Summer School, the participants were taken to two major civil engineering companies of Europe, based in Germany, on Wednesday, August 30th. This excursion was led by the course coordinator Dr. Lars Abrahamczyk. The companies visited were based in Plauen and Gera. The first company visited was a steel section manufacturing company named Plauen Stahl Technologie, which is one of the major players in steel welded section manufacturing industry. The next company to visit was Max Bögl, a privately owned company since 1929, which is one of the biggest companies in Europe in terms of its precast concrete member manufacturing industry and is known for its innovative products like thin concrete façade elements. Both companies were welcoming in their approach and understanding of the requirements of the course participants. They explained different part of their respective manufacturing plants and exhibited the different stages of manufacturing process.

The trip started from Weimar early in the morning to reach the first company location around 9 am. This company was founded under name of Firma F. Sachs in Plauen in 1885. During a 30 years period, is gained a major name in the sector. Currently, Plauen Stahl Technologie is one of the most innovative and the biggest steel construction companies in Europe.

This company is producing and assembling huge steel constructions such as steel girders for bridges, steel members for buildings as well as hydraulic structures. It applies state-of-the-art CNC-controlled cutting centres for profile and sheet metal processing, high-performance automatic welding equipment and latest CNC centres for mechanical machining.

The procedure commences with arrival of metal sheets to the store. After checking the quality of the metal sheets by engineers, they are carried to cutting hall by the huge magnetic cranes. In this hall, profiles and metal sheets are cut by modern and automatic systems. In addition, they apply state-of-the-art automated cutting technology.

Figure 1. Preparation for the guided tour *(Photo: Y. Kazmi)*

Figure 2. View to the steel plate arrival portal *(Photo: Y. Kazmi)*

Afterwards, they are transferred to the assembly and welding hall, which is mobilized to the modern and heavy crane with capacity of 160 tons. For welding the massive part of the infrastructures like huge bridge girders, they are greatly benefited from powerful automatic systems and welding machines for hybrid and tandem processes. The next step is the preservation. To protect the steel structures from corrosion they apply a modern painting systems according to the highest environmental protection guidelines. But for long beams, longer than 30 meters, they have to perform it by hand. Once they are transferred to the storage area, they are delivered to construction site by special transports, lorries, and railways. They utilize their own railway connection.

Figure 3. Introduction to company MaxBögl *(Photo: Y. Kazmi)*

The second part of the trip took the participants towards Gera, a city near to Weimar. The Company, Max Bögl, was established in 1929 as a private company which it remains till date. As of now, it is a conglomerate of separate businesses and its field of work covers almost every aspect of the infrastructure industry. Building construction like shopping complex, airports, high rise buildings, infrastructure like roads and bridges, wind turbines and steel girders are few examples of their broad range of expertise. The tour at the facility for precast concrete elements in Gera started after the welcome lunch which was generously provided by the company itself. After a satisfying meal, the participants were lead to a presentation where project manager of the Gera site presented an overview of the company and services it offers. After an informative introduction, participants were led to the actual site where the precast members are prepared in steps.

Figure 4. Precast concrete element production hall *(Photo: Y. Kazmi)*

The tour followed the same path as the manufacturing chain of a member should and hence it was very well connected. The first stage was the preparation of reinforcement for the member which is made manually by skilled workers. The work starts early in the morning at 4 am to let the casting team finish their part before the day ends. After preparation of reinforcement, the casting site is prepared. The hall for this step utilises its 60 m span to cast a series of pre-stressed members in one go. The number of castings depend on the client's requirement. It uses steel casts to prepare the member in which steel reinforcement prepared earlier is placed. Then, it is carefully weighed down by some concrete block to avoid buoyant lifting of the reinforcement during pouring of the concrete. This whole step is performed several times in adjacent halls until sufficient number of members are produced. Along with the process, the manufacturing manager of the plant also explained the cautions to take during process, which not only makes the job more interesting but also a learning experience. The company also spends its resources in research of new products and use of new materials to be a leader in the industry. They displayed some façade elements which are unique in their thickness and span. It was a very informative visit and it was inspiring to see the engineering in action.

The trip back to Weimar was short and comfortable. It was a valuable addition to the summer school program and a wonderful memory for the participants indeed.

Project reports 2017

Distributed damage detection using wireless sensor networks

CRISTIAN Antonio Andrei [a], MATOS Raquel [b], KARIMI Saboor [c], SCUPIN Alexandra [a],
ZHUROVSKI Aleksandar [d]
[a] Technical University of Civil Engineering Bucharest, Romania
[b] University of Aveiro, Portugal
[c] Bauhaus University Weimar, Germany
[d] Institute of Earthquake Engineering and Engineering Seismology, IZIIS-Skopje, Macedonia

Abstract

Given the growing number of ageing buildings and the necessity of damage assessment, the need for reliable structural health monitoring (SHM) strategies is constantly increasing. Wireless sensor networks, compared to conventional cable-based systems, provide a more flexible and cost-efficient approach towards performing damage detection based on embedded algorithms in a decentralized manner. This paper presents the implementation and validation of a wireless SHM system through laboratory experiments on a laboratory test structure. Two different states of the structure have been analyzed by the SHM system, the initial state and the damaged structure. The embedded algorithms in the sensor nodes measure acceleration response data and convert the raw data into the frequency domain using fast Fourier transforms (FFT). Natural frequencies have been identified by the wireless SHM system and changes of the test structure have been identified. Finally, conclusions are drawn with respect to the system dynamics and the performance of the proposed SHM system.

This research has been conducted at Bauhaus-University Weimar, Germany, during the Forecast Engineering Course from Bauhaus Summer School 2017.

Introduction

Structural Health Monitoring (SHM) systems with embedded computing capabilities serve to diagnose the condition of a structure at any time during its life cycle (Balageas, et al., 2010). Since knowledge on the structural condition are essential to ensure the safety of a structure, visual inspection methods can be combined with sensor technology to provide reliable damage detection (Wenzel, 2008). Wireless sensor nodes may perform monitoring tasks autonomously, such as collecting, processing, and analyzing sensor dat. The data collected by permanently SHM systems enables a rapid assessment of a structure's overall integrity and a timely repair of damage detected (Lynch et al., 2004). In addition, wireless SHM systems offer a flexible and cost-effective approach (Zimmerman et al., 2008; Zoubek, et al., 2015; Lei, et al., 2010).

Embedded computing is an integral aspect of wireless SHM systems, and it is used to perform monitoring tasks directly on the sensor nodes (Zoubek, et al., 2015). Many research approaches have been presented in this area, as described below. A SHM system with embedded computing capabilities was introduced by Lynch et al. (2004), who have solved damage detection with embedded algorithms based on auto-regression with exogenous inputs (ARX). Since then, research interest in wireless structural health monitoring has increased. Zimmerman et al. (2008) have presented a SHM system with embedded system identification algorithms. In order to estimate cable forces in cable stayed bridges, Cho, et al. (2008) have presented a wireless tension force estimation system. Lei, et al. (2010) have also presented a study of two embedded engineering algorithms, fast Fourier transform (FFT) and peak-picking (PP), as implemented on a wireless sensor node and applied to the laboratory test structure. Subsequently, Smarsly and Law (2013) have proposed a SHM system with embedded software to detect and analyze potential anomalies on-demand, based on a migration-based approach. Also, Dragos and Smarsly (2015) have proposed an embedded computing approach to perform on-

board condition assessment of structures based on system identification and structural dynamics. Embedding artificial intelligence techniques into wireless sensor nodes is another example of applying sophisticated embedded algorithms to SHM (Smarsly and Law, 2014). Zoubek, et al. (2015) have applied a SHM system for automated, decentralized modal analysis that allows identification of natural frequencies of structures. The system is based on embedded fast Fourier transforms and aims to measure and process acceleration data directly on the sensor nodes. Automated damage detection is implemented into the sensor nodes. The sensor nodes record acceleration response data and transform the data into the frequency domain using Frequency Domain Decomposition (FDD) by applying the FFT algorithm.

This paper presents a wireless SHM system with embedded algorithms to improve the damage assessment process based on the identification of natural frequencies of monitored structures. The embedded algorithms are based on an FFT algorithm, where the acquisition of the data and the conversion into the frequency domain is processed on the sensor nodes. The proposed SHM system is applied to a four-story shear frame structure under two different conditions, at initial stage and at a state with introduced damage. The natural frequencies and mode shapes resulting from the two validation tests are finally compared and the results are discussed. In the first section of the paper, general concepts of wireless structural health monitoring are provided. Then, the embedded algorithms of the wireless SHM system are briefly introduced. Next, a description of the validation tests is provided. Finally, the conclusions are drawn and future studies in this field are suggested.

Design and implementation of a wireless structural health monitoring system

The aim of this study is to investigate the performance of the embedded algorithms implemented for decentralized damage detection. The wireless SHM system consists of wireless sensor nodes, a server, and a base station, which connects wireless sensor nodes and server.

As it is illustrated in the **Figure 1**, during SHM system operation, each component carries out various SHM tasks. The procedure commences with initial model parameter after that the sensor nodes are responsible for collecting the acceleration response data, applying the fast Fourier transform and the application of a peak picking algorithm for calculating the fundamental frequency and the Fourier magnitude of the acceleration response data of the model structure. Finally, the processed data is transmitted through the base station to the server.
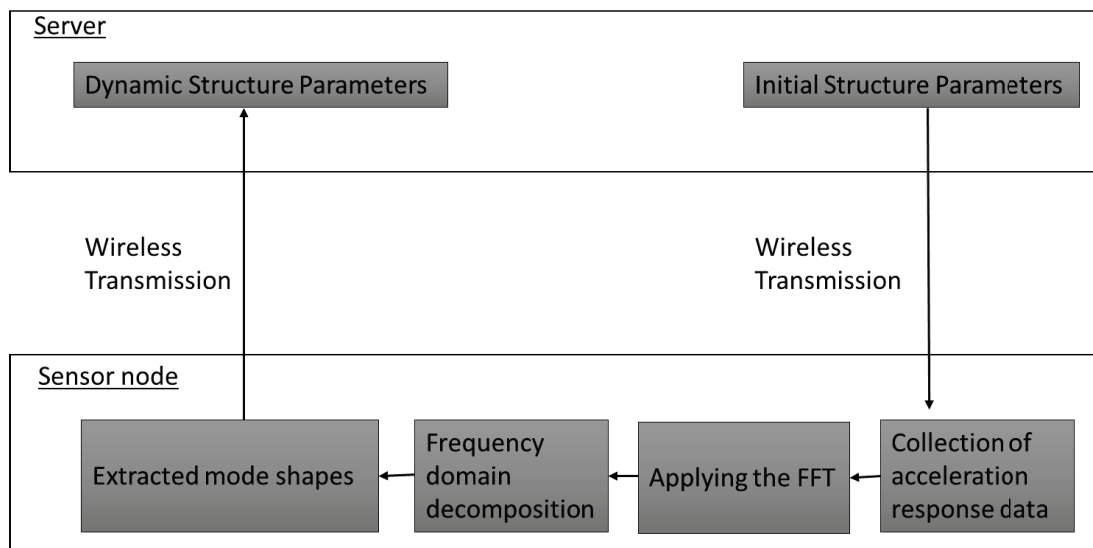
Figure 1. Brief description of the wireless SHM system.

Identification of natural frequencies using fast Fourier transform

The proposed wireless SHM system handles data processing and modal identification. Basically, the sensor data recorded is transformed into the frequency domain directly on the sensor nodes before being transmitted wirelessly to the server. The fast Fourier transform method is used to transform the data from time domain into the frequency domain. The following subsection gives an overview of the mathematical background of the FFT.

Mathematical background

According to theory of structural dynamics, structural response can be represented by the superposition of the responses in its "vibration (natural) modes" i.e. a sum of harmonic functions with different frequencies and oscillation amplitudes. In experimental structural dynamics, the objective is to identify the natural frequencies of vibration modes using digital signal processing techniques such as the Fourier transform. Practically, the Fourier transform is a representation of the time signal recorded (i.e., the response of the structure) into a plot of the amplitudes versus frequencies (i.e., representation of the recorded signal into frequency domain), the so-called frequency spectrum. The recorded peaks in the frequency spectrum are then denoted as natural frequencies of the structure. The Fourier transform of a continuous time signal $f(t)$ is defined as:

$$F(\omega) = \int f(t) \cdot e^{2\pi i \omega t} dt \tag{1}$$

Eq. (1) cannot be used for analysis of the measured data because the time signal that is recorded is not continuous but discrete. That is why the discrete Fourier transform (DFT) is used, and each Fourier amplitude in the frequency spectrum is obtained from eq. (2):

$$F_k = \sum_{n=0}^{N-1} f_n \cdot e^{-2\pi i k \frac{n}{N}} \qquad k \in [0, N) \qquad N \in Z \qquad \omega = \frac{k}{N} \tag{2}$$

where f_n is the discrete function of $f(t)$. N is the length of the discrete time series. The Fourier amplitude F_k is a complex number. The frequency of each sinusoid is described as k cycles per N samples. It is noted that the DFT algorithm needs N^2 calculations because the calculations produces N outputs of F_k and each output is obtained as a sum of N terms. Having in mind the computational effort required to process these transformations, Cooley and Tukey (1965) have proposed the fast Fourier transform in an attempt to reduce the number of to $N \cdot logN$ alculations. The FFT divides the DFT of size N into smaller DFTs of sizes N_1 and N_2 (calculations having the rule $N=N_1 \cdot N_2$) leading to fewer calculations. In what is most common application algorithm of FFT, is the Cooley-Tukey version, a radix-2 decimation-in-time FFT is done so that the DFT of size N is divided into two DFTs (even part and odd part) of size $N/2$ with each recursive stage as shown in equation 3 and 4:

$$F_k = \sum_{n=0}^{N/2-1} f_n \cdot e^{-2\pi i k \cdot \frac{n}{N}} + \sum_{n=0}^{N/2-1} f_{n+1} \cdot e^{-2\pi i k \cdot \frac{n+1}{N}} = \sum_{n=0}^{N/2-1} f_n \cdot e^{-2\pi i k \cdot \frac{n}{N}} + e^{-\frac{2\pi i k}{N}} \cdot \sum_{n=0}^{N/2-1} f_{n+1} \cdot e^{-2\pi i k \cdot \frac{n}{N}} \tag{3}$$

From the identity $e^{2\pi i n} = 1$ ($n \in Z$):

$$F_{N+k} = \sum_{n=0}^{N-1} f_n \cdot e^{-2\pi i (N+k) \cdot \frac{n}{N}} = \sum_{n=0}^{N-1} f_n \cdot e^{-2\pi i k \cdot \frac{n}{N}} \cdot e^{-2\pi i n} = \sum_{n=0}^{N-1} f_n \cdot e^{-2\pi i k \cdot \frac{n}{N}} \tag{4}$$

Validation tests

The objective of the experimental test is to validate the capability of the embedded algorithm to detect damage of the laboratory test structure by performing a FFT and monitoring the changes in frequencies.

Experimental setup

The performance of the wireless SHM system proposed is validated on the laboratory test structure, a four-story shear frame. As shown in Figure 2, each story is made from rectangular aluminum plates, 300 mm x 200 mm, fixed to four aluminum columns of 20 mm x 2 mm. The plates are connected to the columns using screws, representing a fully fixed connection. The columns are connected at the base to a solid wooden block ensuring a fixed connection.

The SHM system hardware are Oracle SunSPOT (Small Programmable Object Technology) wireless sensor nodes (Oracle, 2010). The sensor nodes feature a 400 MHz ARM microprocessor with an embedded Java Squawk Virtual Machine, 512 kB RAM and 4 MB flash memory. The wireless communication is achieved via an IEEE 802.15.4 radio transceiver using the ZigBee protocol. The SunSPOT is equipped with a 3D digital accelerometer, a temperature sensor and a light sensor. The accelerometer samples at 125 Hz, with selectable measurement ranges of ±2 g, ±6 g or ±8 g at a resolution of 8 bit.

Description of the tests

In order to test the embedded algorithm, two tests have been performed. In the first test, the shear frame is excited by a deflection at the top story. The sensor nodes start collecting accelerations after the threshold of 0.5 g is exceeded at all stories. For the second test, damage is simulated by weakening the connection between the aluminum plates and the columns. The location of the induced damage is shown in Figure 4.

The validation of the algorithm is based on the comparison between the two states of the laboratory test structure. In, the second (damaged) stage, the structure is more flexible due to the damage; hence this must be observed on the Fourier spectrum calculated by the wireless SHM system.

Figure 2. Experimental setup with the laboratory test structure instrumented with the wireless SHM system.
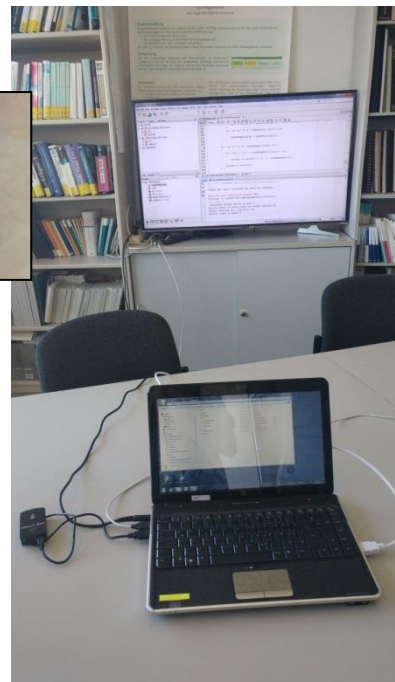
Figure 3. The base station connected to the computer.

Figure 4. The damaged test structure and the location of the damage.

A clear difference can be observed between the frequency spectra obtained from the two tests. For the first eigen mode, the initial frequency was of 1.574 Hz and decreased for the damaged structure to 1.150 Hz. This migration of the peaks from the frequency spectra shows the difference between the initial state of the structure and the damaged state of the structure. This difference can also be identified by extracting the mode shapes.
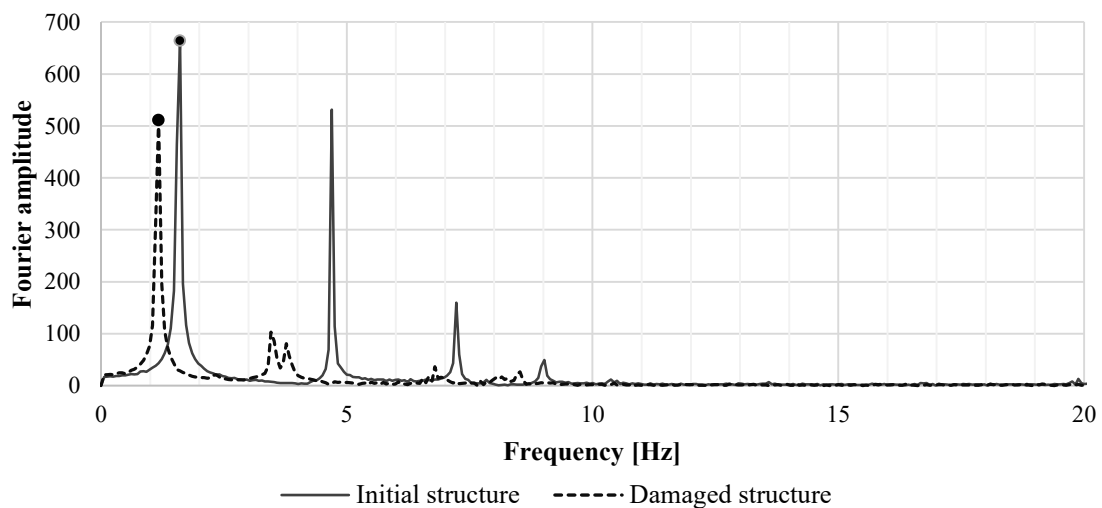
Figure 5: Comparison between the Fourier Spectra for the two stages of the structure.

Table 1. Comparison between the eigen frequencies.

Mode of vibration	Eigen frequencies [Hz]		Decrease in frequency [%]
	Initial structure	Damaged structure	
1st	1.574	1.150	26.92%
2nd	4.602	3.391	26.32%
3rd	5.268	4.844	8.05%
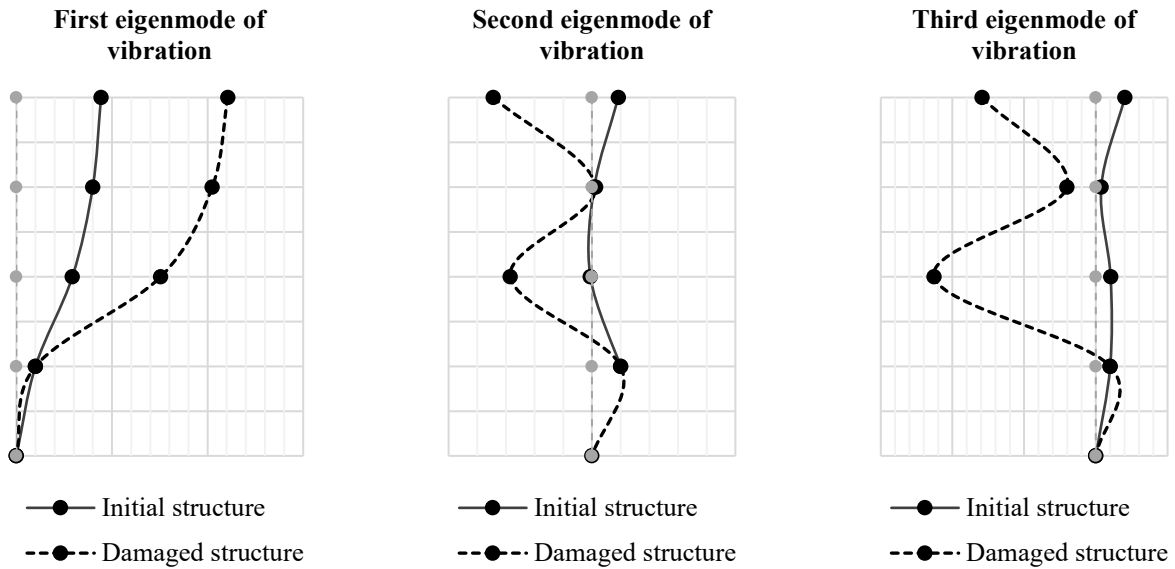
Figure 6: Change in the mode shapes of the structure.

a)

b)
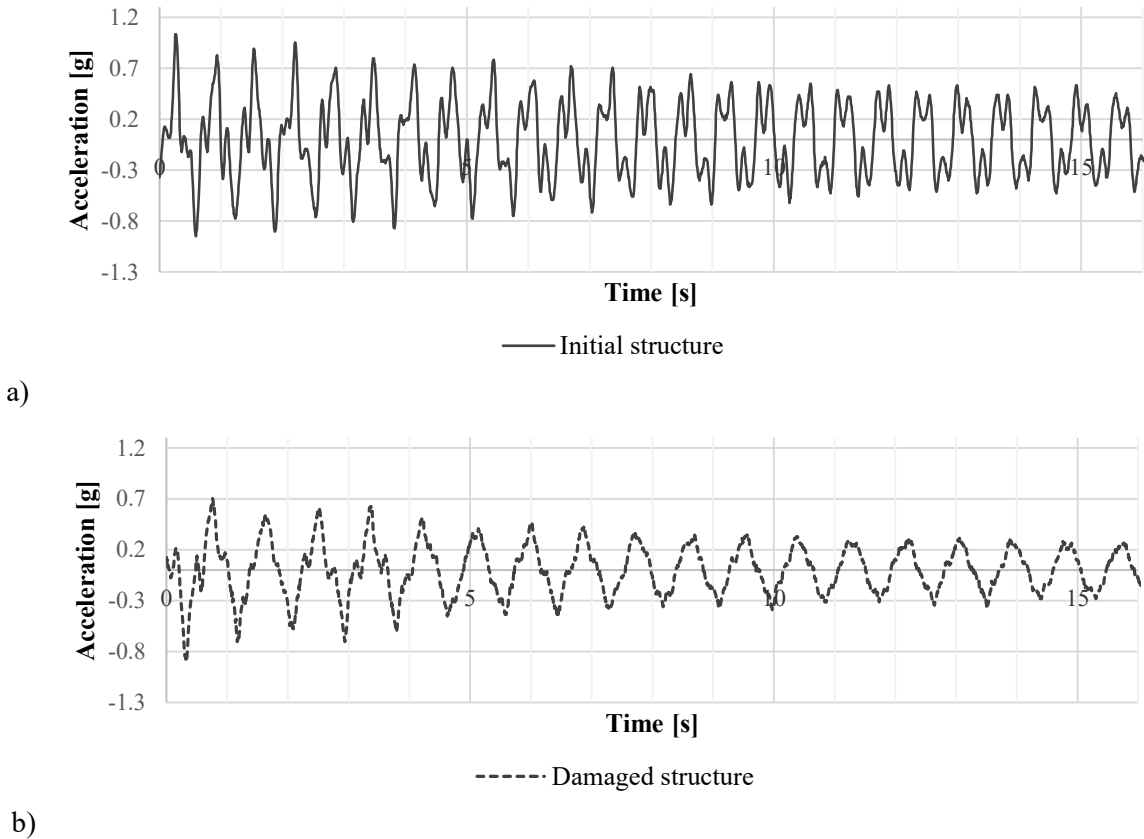
Figure 7: Measured top floor acceleration in the two cases: a) and b).

Summary and conclusions

The paper has shown the application of an automated, decentralized wireless structural health monitoring (SHM) system for the identification of damage through analysis of natural frequencies and mode shapes. The validation of the wireless SHM system proposed was done using a laboratory test structure, a four-story shear frame structure. Using embedded algorithms, the sensor nodes have started recording acceleration response from the structure once the pre-defined threshold of 0.5 g had

been exceeded. After the application of the fast Fourier transformation and peak picking algorithms on the data recorded, the eigen frequencies and the corresponding modes of vibration have been obtained. By analyzing both, the initial state and the damaged state of the structure, the eigen frequencies obtained have been used to identify changes in the dynamic properties. It has been observed a decrease in stiffness, due to the loosening the screws (1st and 3rd floor). Further research can be performed in this field, to implement wireless SHM systems for detecting and quantifying potential damage. For future research, the current SHM system, due to its modular nature, can be transformed into an active control system by adding actuators, in order to reduce the reaction of the structure and to prevent possible damage.

Acknowledgments

References

Balageas, D., Fritzen, C.P., Guemes, A. (2010): *Structural Health Monitoring* – Published by John Wiley & Sons.

Cho, S., Yun, C. B., Lynch, J.P., Zimmerman, A., Spencer Jr., B. and Nagayama T. (2008): Smart wireless sensor technology for structural health monitoring. *Steel Structures* **8** (4): 267-275.

Dragos, K. & Smarsly, K. (2015): Embedding numerical models into wireless sensor nodes for structural health monitoring. In: *Proc. of the 10th International Workshop on Structural Health Monitoring*; Stanford, CA, USA, September, 01, 2015.

Dragos, K. (2016): An embedded physics-based modeling approach for wireless structural health monitoring systems. *28th Forum Bauinformatik 2016*. Leibniz Universitat Hannover, September, 13-21, 2016.

Jahr, K., Schlich, R., Dragos, K., and Smarsly K. (2015): Decentralized autonomous fault detection in wireless structural health monitoring systems using structural response data. *20th International Conference on the Application of Computer Science and Mathematics in Architecture and Civil Engineering*, Weimar, Germany, July, 20-22, 2015.

Lei, Y., Shen, W.A.,Song, Y. and Wang, Y. (2010): Intelligent wireless sensors with application to the identification of structural modal parameters and steel cable forces: from the lab to the field. *Advances in Engineering Software* 2010: 1-10.

Lynch, J.P., Sundararajan, A., Law, K., H., Sohn and Farrar, C.R (2004): Design of a wireless active sensing unit for a structural health monitoring. *In Proc of SPIE's 11th Annual International Symposium on Smart Structures and Materials;* San Diego, CA, USA, March, 03, 2004.

Smarsly, K., and Law, K.H. (2013): A migration-based approach towards resource-efficient wireless structural health monitoring. *Advanced Engineering Informatics* **27** (4): 625-635.

Smarsly, K., and Law, K.H. (2014): Decentralized Fault Detection and Isolation in Wireless Structural Health Monitoring Systems using Analytical Redundancy. *Advances in Engineering Software* **73** (2014): 1-10.

Wenzel, H. (2008): *Health Monitoring of Bridges* – Published by John Wiley & Sons.

Zimmerman, A., Shiraishi, M., Schwartz, A. and Lynch, J.P. (2008): Automated modal parameter estimation by parallel processing within wireless monitoring systems. *ASCE Journal of Infrastructure Systems* (1): 102-113.

Zoubek, B., Manojlovski, F., Zhelyazkov, A., Naeimi, N., Nishino, H., Abdollahi, H. (2015): A wireless structural health monitoring for automated decentralized modal analysis. *Forecast Engineering: From Past Design to Future Decision,* in Bauhaus Summer School, Weimar, German, August, 17-28, 2015.

Cooley J W & Tukey J W (1965): An algorithm for the machine calculation of complex Fourier series. *Math. Comput.* **19**:297-301, 1965.

Object-based analysis of satellite images for building change detection after an earthquake: The case study of L'Aquila

KERSTEN Jens[a], HADIDIAN Nooshin M.[a], HWIRANG Kang[b], KARAGIANNI Aikaterini[c], KAZMI Yasir[a], MANOJLOVSKI Filip[d]

[a] *Bauhaus-Universität Weimar*
[b] *Chung-ang University Seoul*
[c] *Aristotle University of Thessaloniki*
[d] *Institute of Earthquake Engineering and Engineering Seismology Skopje*

Abstract

Earthquake is one of the most catastrophic natural disasters that can affect large areas, which include a variety of structures (buildings, dams, tunnels, road network, slopes, etc.). The changes that an earthquake may cause to urban areas are among the interests of a civil engineer having a direct relation to the risk of exposure of these areas and the extent of the damages. According to World's Seismic Hazard Maps (*Giardini, & colleagues et al., 2003*), risk is the potential that exposure to the hazard will lead to a negative consequence such as loss of life or economic value. Detecting the areas that are affected, may be the first analysis step especially when earthquake events destroy cities and populated areas which are not easily accessible in time to assess the situation. Remote sensing as well as digital image processing and analysis, may be a powerful tool to detect changes that caused by an earthquake. This study presents post-earthquake change detection applying object-based satellite image analysis to locate damaged buildings in the city of L'Aquila, capital of the Province of L'Aquila in Italy after an earthquake event which happened on April 6, 2009. Two high-resolution QuickBird satellite images covering the city of L'Aquila were used, acquired before and after the earthquake. The software that was used to implement object-based image analysis (OBIA) for change detection was QGIS software, a free and open Source Geographic Information System that provides data viewing, editing, analysis, and mapping capabilities. The Mean shift segmentation and the supervised non-parametric support vector machine (SVM) were applied to segment and classify a subset of the images in order to detect the changes in the roof shape of buildings after the event. Evaluation and comparison with other related approaches demonstrate the value and high accuracy of the selected change detection method.

Introduction

After an earthquake, assessment of the health of the affected buildings is of concern to a civil engineer. In order to choose methods of rehabilitation for buildings damaged, one must have knowledge about where and how many buildings have been damaged. This must be done quickly, in order to save lives. Detecting the areas that are affected may be the first step to further analysis. Remote sensing and digital image analysis may be a powerful tool to detect changes that have occurred after an earthquake (*Ramachandra & Kumaret al., 2004*). Interpretation and processing of high-resolution satellite images before and after the event could provide valuable information regarding the position and the extent of the changes as well as the severity of the damages. A variety of temporal images and spatial resolutions could be used to detect and monitor the changes in the terrain (*Rogan & Chen et al., 2004*).

Especially for change detection studies in urban areas caused by earthquakes, land cover classification of pre and post satellite imagery can be performed to delineate the changes. To detect land use and land cover, several techniques have been developed. The resolution of satellite images is the main factor that should be considered to choose and apply the appropriate technique for better results. Among the techniques that have been developed are the traditional pixel-based techniques and the recently developed object or segment based approaches (object-based image analysis-OBIA).

In pixel-based image analysis, the multispectral data are used to perform the classification and each pixel is used as the numerical basis for categorization (spectral pattern). In this approach, the maximum likelihood classifier is considered to provide the best results since it takes into consideration the shape, size, and orientation of a cluster (collection of similar objects in group). Based on mean value of the class and the variance-covariance matrix, an unknown pixel is assigned to the most likely class. The classification method assumes that the training samples are normally distributed (*Gholoobi et al., 2010*).

The basic elements of an object-oriented approach are image segments. Segmentation subdivides an image into homogeneous multi-pixel regions based on several user-defined parameters. It is used to produce image object primitives as the first step for further classification and other processing procedures (*Castillejo-González et al., 2009*). The segments can be linked to a hierarchical network, where they are attributed with a high-dimensional feature space (*Gholoobi et al., 2010*).

According to (*Blaschke et al., 2010*), OBIA builds on older segmentation, edge-detection, feature extraction and classification concepts that have been used in remote sensing image analysis the past years. Implementation of OBIA is wider in the past few years as its applications have been extended in various fields, especially for land use/land cover classification, forest mapping, agricultural studies etc. (*Adam et al., 2016*).

As a further step, integration of remote sensing and Geospatial Information System (GIS) can be used in conventional image analysis (pixel-based algorithm) as well as in object-based image analysis (Adam et al., 2016). In the latter case implementing GIS tool may be effective because in this approach objects are the basic units (*Gholoobi et al., 2010*).

In this study, an object-based approach is applied in order to detect the changes (affected and damaged buildings) after the L'Aquila earthquake in central Italy in 2009. Two QuickBird satellite images with a spatial resolution of 60 cm are analyzed. The first image was obtained before the event (2006) and the second immediately after the event (2009). Both images cover the same area. Due to the high spatial resolution of the images, a segment-based approach was considered more effective in order to classify the pre and post scenes and detect changes by analyzing the color and texture information of the segments. As a first step, a mean-shift segmentation is utilized in order to group similar pixels (so-called super-pixels). To classify the changes, support vector machine (SVM) was used, leading to an easier grouping of several spectral classes and subsequently to faster change detection. The utilized multi-date direct comparison (MDC) of images enables a direct classification of changes and therefore requires less manual interaction than the typical post classification comparison, where the individual classification of the pre and post scene is necessary.
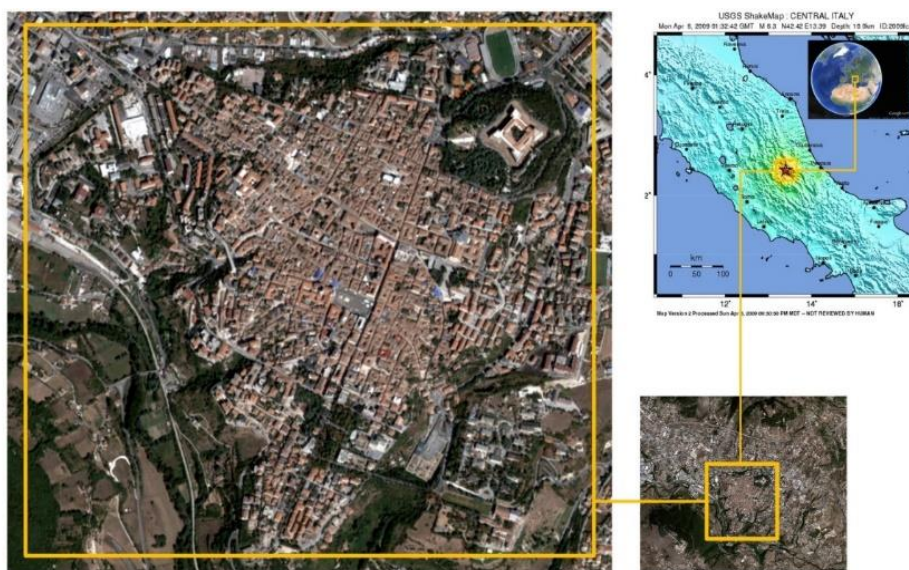
Figure 1. Case study area: the city of L'Aquila in Italy (11 September 2011) and a map of the ground motion intensity during the earthquake (*Contreras et al., 2017*).

Figure 2. Input QuickBird scene before the earthquake (*DigitalGlobe, 2006*).

Study area and satellite data

Study area concerns the city of L'Aquila, capital of the Province of L'Aquila in Italy, with a population of approximately 72.800. On 6 April 2009, an earthquake of a 6.3 magnitude struck the city. The epicenter was located 3.4 km to the southwest of the city at a depth of 10 km. The historic center suffered serious damages (material damage and loss of lives) with 308 fatalities and over 100.000 damaged buildings (*Contreras et al., 2017*). The cost of the damages of the buildings/infrastructure was estimated to be 16 billion Euros (*UNIFI, 2010*). Figure 1 presents the location of the city and a map of ground motion intensity during the earthquake.

Two QuickBird scenes covering the city of L'Aquila acquired on September 4, 2006, and April 8, 2009, respectively, were used in this study (*DigitalGlobe, 2006 & DigitalGlobe, 2009*). The spatial resolution of pan-sharpened scenes is 0.6 m, they consist of four spectral bands (R = red, G = green, B = blue and NIR = near infrared) and they cover an area of 25 km². The input pre-disaster QuickBird scene is presented in Figure 2, while the subsets of the two images that were used for change detection after the earthquake are presented in Figure 3 for pre-scene (*September 4, 2006*) and post-scene (*April 8, 2009*) respectively.

The software that was used to implement OBIA for change detection was QGIS software, a cross-platform and open-source desktop GIS application that provides data viewing, editing, analysis and mapping capabilities (QGIS, 2017). The specific software supports several raster formats, giving the ability of georeferencing and furthermore allows the users to create maps with multiple layers using different map projections (Treglia, 2015).

Change detection in images

In remote sensing (RS) applications, changes are considered as surface component alterations with varying rates. Land-cover (LC) and land-use (LU) change information is important because of its practical uses in various applications, including deforestation, damage assessment, disasters monitoring, urban expansion, planning, and land management. Hence, change detection methods play a central role in the resource management procedure during and after a crisis.

Singh (1989) defined change detection (CD) as "the process of identifying differences in the state of an object or phenomenon by observing it at different times". CD methods use multi-temporal datasets (for example images) to qualitatively analyse the temporal effects of phenomena and quantify the changes.

Pre-scene (September 4, 2006)   Post-scene (April 8, 2009)

Figure 3. Subsets of the two QuickBird scenes that were used for change detection, covering a part of the city of L'Aquila (pre-scene: left image and post-scene: right image) (*DigitalGlobe, 2006 & 2009*).

CD methods for images, scale from simple ones (e.g. the difference image) to more complex methods. In (*Habib et al., 2007*) over a hundred change detection methods are analysed. Here, six main categories of change detection methods were identified: statistical, analytical, learning based, multi-scale, and morphological and segmentation/object-based approaches. Figure 4 presents the popularity of each approach based on a population of 105 different change detection method.

The analysis demonstrates that 24 % of all analysed methods are using image segmentation. Especially in case of high spatial image resolutions (e.g. 50 cm per pixel), OBIA is known to provide potentially better results than traditional pixel-based methods.

Only 9 % of the investigated methods were based on learning. In this paper, the combination of image segmentation and learning based methods is evaluated. The motivation for this is to combine the strength of OBIA with the robustness of tailored classifiers learned from training data.
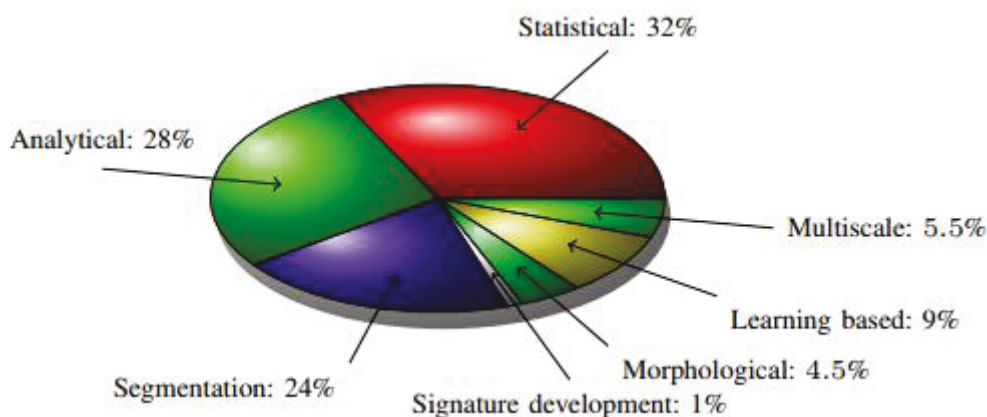
Figure 4. Change detection methodologies (*Habib et al., 2007*).

Proposed CD Workflow

In this study, a segment-based CD workflow is proposed. It consists of the following main steps: Pre-processing, mean-shift image segmentation, CD using SVM and accuracy assessment. Since a MDC approach for CD is used, the first two steps are applied on both pre-scene and post-scene individually. Then, the two scenes are stacked to one multi-band image and a SVM model is trained in order to directly classify each image segment into the classes changed or unchanged. The complete workflow (Figure 5) is described in the following.

Pre-processing

Pre-processing of satellite sensor images prior to actual change detection is essential. Some of the main goals are the establishment of a more direct linkage between the data and biophysical phenomena, the removal of data acquisition errors and image noise, and the masking of contaminated (e.g. clouds) and/or irrelevant (e.g. Water bodies when looking at changes in vegetation) scene fragments. (*P. Coppin et.al -2004*). The pre-processing of multi-date sensor imagery, when absolute comparisons between different dates or periods are to be carried out, is much more demanding than in the single-date case.
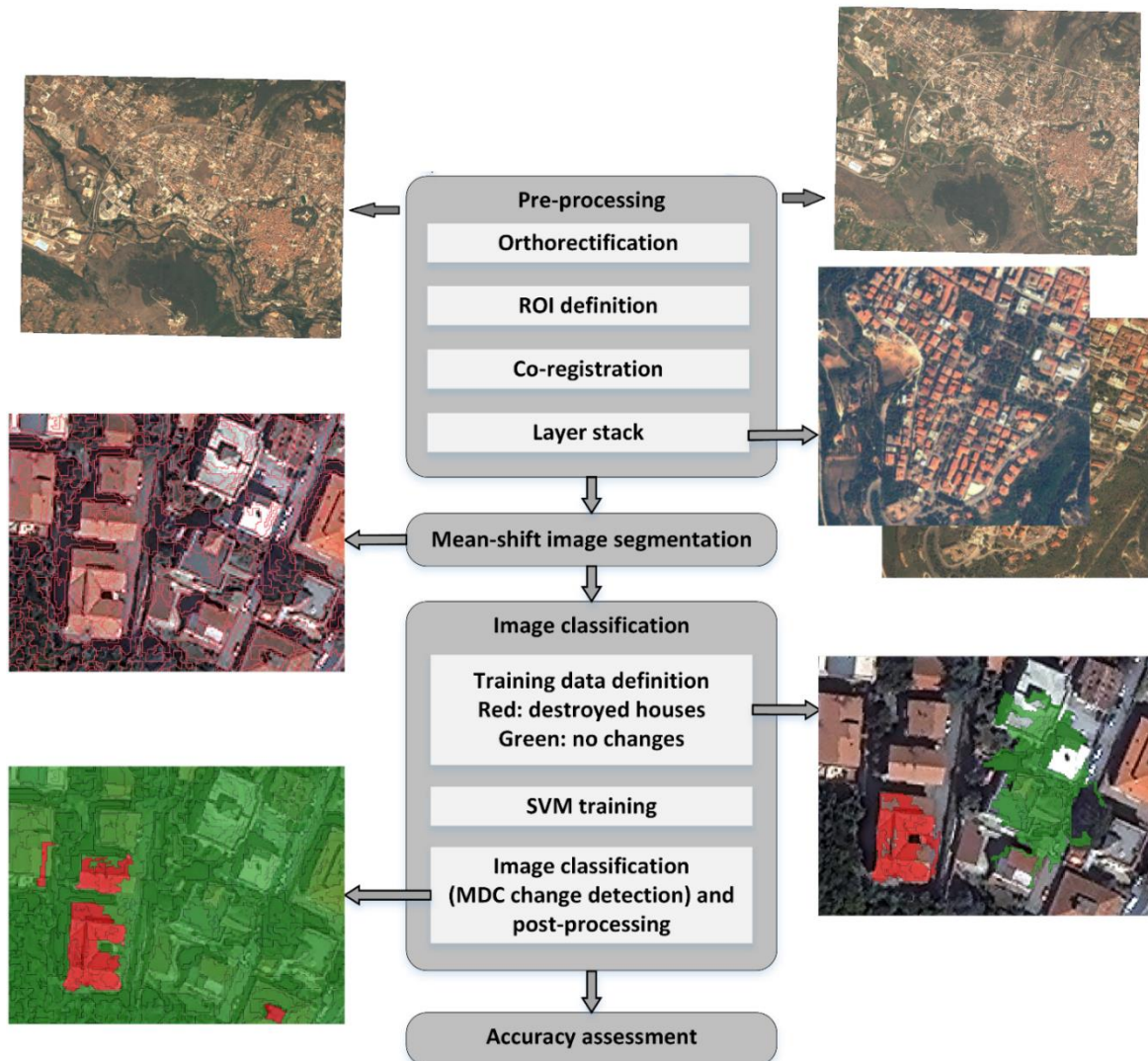
Figure 5. Change detection workflow.

It commonly comprises a series of sequential operations, including (but not necessarily in this order) calibration to radiance or at-satellite reflectance, atmospheric correction or normalization, image registration, geometric correction, mosaicking, sub-setting and masking (e.g. for clouds, water, irrelevant features). Often these procedures are accompanied by a data transformation to vegetation indices that are known to exhibit a strong positive eco system monitoring. The principal advantages of vegetation indices over single-band radiometric responses are their ability to reduce considerably the data volume for processing and analysis, and their inherent capability to provide information not available in any single band. However, no single vegetation index can be expected to summarize totally the information in multidimensional spectral data space. (*Wallace & Campbell at al., 1989*) aptly stated that adequate indices can be found for different purposes and that indices derived for one analysis may be inappropriate in another context.

The topographical variations of the earth's surface, as well as the tilt of the satellite sensor, affect the position on which objects are mapped in satellite images. The more topographically diverse the landscape, the more distortion inherent to the image.

As image distortions are an inevitable source of errors especially in CD, they must be removed or reduced as much as possible. Ortho-rectification (See Figure 6) is a process of removing perspective distortions for each image pixel individually (*GIS dictionary, 2015*).

For each differential rectified destination pixel (4) on the discrete grid in Figure 6, the corresponding elevation data point (1) of the terrain is projected into the image plane (3) using the exterior orientation of the sensor (2). The colour values of the new pixel in (4) are interpolated from the sub-pixel position in (3) using the neighbouring colour values (resampling). In this study, the ASTER global digital elevation model (GDEM) V2 available at (*ASTER, 2015*) with a ground sampling distance of 30 m was used.

To reduce the computational loads and the complexity of CD for this study, a region of interest (ROI) is defined in the ortho-rectified images (See Figure 7). All further processing steps are applied on these sub-images.

Whereas pixel displacements due to sensor orientation and topography are removed by the ortho-rectification step, it is still possible that the two scenes do not exhibit perfect overlay due to inaccuracies of the provided satellite metadata and the used terrain model. Therefore, a further image-to-image- or co-registration is required, which geometrically transforms one of the images to have a perfect overlay with the second one. Similar to the ortho-rectification, this step has a crucial value since the CD results depend on the registration quality. A four-parameter 2D-Helmert transform is used for this step, where at least two corresponding points must be identified manually in the two scenes to estimate the transformation parameters (two translations, one rotation and a scale factor). The best matching accuracy can be achieved by providing a higher number of corresponding points uniformly covering the entire image area.
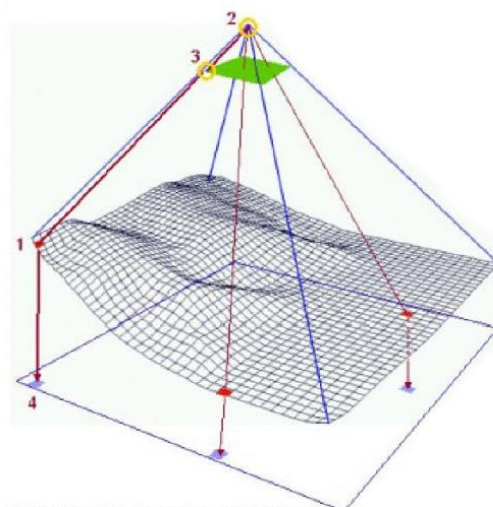
Figure 6. Ortho-rectification process.
(https://www.satimagingcorp.com/services/orthorectification)

Figure 7. Defined ROI (pre-scene).

Since no detailed information regarding the objects on top of the earth's surface, for example, buildings, are incorporated into the ortho-rectification step, the rooftops and other objects usually still are displaced in the images according to the sensor pose and the height of the object. Hence, it is crucial to use corresponding points located on the ground for the registration. A Helmert transformation in QGIS software can be applied easily with the 'Georeferencer' plugin.

To enable comparisons and analysis on pixel-level, the spatially transformed image is finally resampled with respect to the reference image using the nearest neighbour interpolation. After this step, both scenes have the same spatial resolution and pixel positions.

Mean-shift image segmentation

Image segmentation is an integral part of the Object-Based Image Analysis methodology (*Benz et al., 2004*). Here, the digital image is no longer considered as a grid of pixels, but as a group of primitives and homogeneous regions called primitive image objects. The object-oriented representation provides to the classification process information that could not be derived from single pixels such as context and shape information. These are very important factors for photo-interpretation and image understanding (*Lillesand & Kiefer et al., 1987, Sonka et al., 1998, Biederman et al., 1985*). Objects can be more intelligent than pixels, in a sense of knowing their "neighbours" and the spatial or spectral relations with and among them. (*Tzotsos et al., 2008*).

Subdividing an image into non-overlapping segments can generally be done by grouping spatially adjacent pixels. By assigning different labels on groups of pixels, they are categorized into sets (segments) which helps to utilize their characteristics for further analyses. Hence, image segmentation can be seen as the first step in image understanding, since it aims at finding boundaries of semantic objects or object parts.

In this paper, the non-parametric mean-shift algorithm is used. A pixel of a colour image (with three channels (red (R), green (G), blue (B)) can be mapped to a point in a corresponding 3D-feature space. Mapping all pixels of an image into this space, we are interested in identifying the local maxima of this density. The mean-shift algorithm starts at every pixel location in the feature space and iteratively

computes the centroid of the local neighbourhood around the current position. A local maximum is found when the centroid does not move anymore while iterating. All spatially adjacent starting pixels (feature space points) which converge to the same centroid will be part of the same image segment. A preliminary edge-aware smoothing helps to reduce the number of local maxima and therefore bigger segments can be obtained.

The mean-shift algorithm is valuable in many aspects. It is general, application-independent, and robust against outliers and model-free, i.e., no assumptions regarding the shape (spherical, elliptical, etc.) of data clusters and the number of clusters have not to be introduced. Furthermore, it uses just a single parameter, which defines the radius for the centroid computation (window size) in the feature space domain. However, selecting this parameter may not be trivial since it directly affects the size and number of output segments. It must be noted that this method also does not scale well with respect to the number of feature space dimensions.

Image classification

SVM is a supervised non-parametric statistical learning technique, therefore there is no assumption made on the underlying data distribution. In its original formulation (*Vapnik et al., 1979*) the method is presented with a set of labelled data instances and the SVM training algorithm aims to find a hyperplane that separates the dataset into a discrete predefined number of classes in a fashion consistent with the training examples.

SVMs use non-linear functions to separate classes in the feature-space domain therefore provide a theoretically superior machine learning methodology with great results in the classification of high-dimensional datasets and have been found competitive with the best machine learning algorithms. In the past, SVMs were tested and evaluated only as pixel-based image classifiers with very good results (*Huang et al., 2002, Brown et al., 2000, Foody & Mathur et al., 2004, Gualtieri & Cromp et al., 1999, Melgani & Bruzzone et al., 2004*).
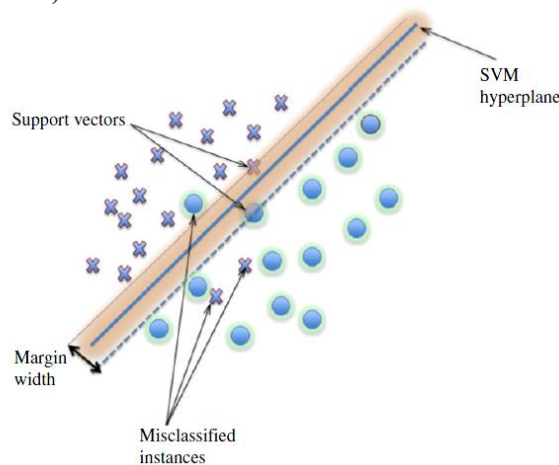
Figure 8. Linear support vector machine example (*Burges et al., 1998*).
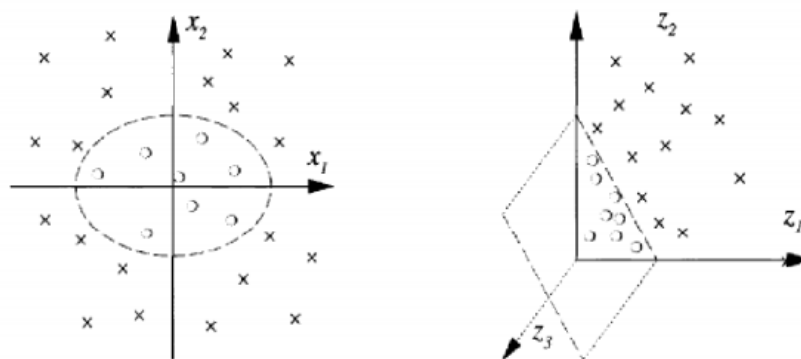
Figure 9. Kernel function map for nonlinear SVM (*Goumehei et al., 2010*).

In its simplest form, SVMs are linear binary classifiers that assign a given test sample a class from one of the two possible labels. (See Figure 8). The example of nonlinear classification can be described by using kernel functions. (See Figure 9)

To find hyperplane that enables the separation of two classes, the dimensionality of the feature space could be increased (Figure 9, right). Instead of explicitly map the feature space to higher dimensions, a non-linear function is applied to the data points. This so-called kernel trick leads to non-linear surfaces in the original feature space.

The achieved results after using mean shift approach and SVM classifier in MDC method is the layer where the value of pixel denotes its class membership, which is defined here as changed and Unchanged.

Accuracy Assessment

Similar to the manual labeling done in the SVM training step, an additional set of test segments must be defined for this task. To get reliable assessment results, these regions should not be used in the training procedure. Furthermore, the percentage of tested segments for each class should be like the number of segments actually representing this class in the image. This helps to avoid overfitting behavior of the trained classifier.

Based on the known class membership of the test segments as well as the predicted class label from the CD analysis, a square 2 x 2 confusion matrix can be obtained. Usually, the rows of this matrix represent the true test instances, whereas the columns are related to the predicted changes using the SVM. A perfect classifier would result in a diagonal confusion matrix. The more incorrect predictions which observed, the more the larger off-diagonal elements can be observed. The overall accuracy (OA) can be derived by counting all correctly classified CD test segments and dividing this sum by the total number of all test segments. In order to derive more detailed class-related information, the user's and producer's accuracy can be computed for each class. The producer's accuracy (PA) refers to the probability that a certain land cover of an area on the ground is classified as such, while the user's accuracy (UA) refers to the probability that a segment labeled as a certain land cover in the map is really this class. The obtained overall accuracy of the results obtained in this study is **98.72 %**, which shows a significant improvement compared to the results obtained in similar previous studies. Table 1 presents data from previous studies (*Cerovecki et al., 2015*) and (*Kersten et al., 2016*), along with the results from this paper.

The results from 2015 were obtained with pixel-based methods. In 2016, an object-based post-classification comparison (PCC) using SVMs was conducted. Since the results of PCC depend on the accuracy of the classification of the pre- and the post-scene, the direct classification of changes using the MDC approach was done in this study. Compared to the PCC results, the obtained producers' accuracy of the class changed is significantly lower.

Table 1. Accuracy assessment results for the proposed MDC approach (2017) compared to the pixel-based results (*Cerovecki et al., 2015 & Kersten et al., 2016*) using PCC and MDC.

Accuracy	Class	2015 (PCC)	2015 (MDC)	2016 (PCC)	2017 (MDC)
OA [%]	All	94.20	96.57	98.35	**98.72**
PA [%]	Changed	61.54	63.96	76.22	**62.06**
	Unchanged	97.24	99.60	100.00	**99.87**
UA [%]	Changed	67.53	93.77	100.00	**93.83**
	Unchanged	96.44	96.74	98.26	**98.82**

Discussion

The aim of this paper is to demonstrate the use of SVM for CD by detecting changes that represent damaged and collapsed buildings. In the pre-processing step, an accurate orthorectification and image co-registration is done. Since man-made objects are not captured in DEMs used for orthorectification, the sensor configuration, acquisition time and season should be nearly identical to ensure the same displacements of high buildings as well as similar shadow arrangements. This was ensured for the used images. The pre-processed images were stacked together for the subsequent MDC analysis.

The Mean shift segmentation was applied to the stacked images. The quality of segmentation directly affects the detection results. In case of very large image segments large areas are covered and therefore several thematic objects are likely to be covered in a single segment. This under-segmentation disables to distinguish between different objects represented by a single segment. In turn, a so-called over-segmentation is given when each thematic object is represented by many small image segments. The difficult task in segmentation is to find a suitable set of parameters which provides a good segmentation in which the segment borders correspond to the borders of the thematic objects of interest. With respect to the applied mean-shift segmentation, a window size of **x** was found to be suitable.

SVMs implemented in QGIS are user-friendly and easy to use. The non-parametric approach allows defining arbitrary thematic classes without considering their spectral distribution in the feature space domain. SVM training was done based on a manually selected and labelled subset of building image segments. Detecting damaged and destroyed houses with MDC can be done by defining the two thematic classes changed and unchanged. Then, this SVM is used for the analysis of the whole image, i.e., all image segments. Figure 10 represents example changes classified by the trained SVM, where red color represents the destroyed buildings.

The quality of output of SVM classifier is affected in higher percentages by the temporal changes in the structure which may be due to e.g., construction activities or reasons other than the earthquake itself. The impact of this ambiguity increases as the difference between the acquisition times of two images becomes bigger. This may produce false positives and therefore an overestimation of damages to the buildings. However, the results in Table 1 demonstrate that the completeness of detected changes is high. Although the detected changes may overestimate the number of damaged buildings, they can point out the areas with the highest potential for damage. Thus, the time taken to make decisions regarding disaster management, after an initial assessment of the event, is reduced (see Figure 11).

Pre-scene (September 4, 2006)   *Post scene (April 8, 2009)*

Figure 10. Detection of changes in the roof of buildings after applying SVM (*DigitalGlobe, 2006 & 2009*).

Figure 11. Post-earthquake damaged buildings, Norcia region, Italy.
(http://www.blueseis.com/single-post/2016/12/06/Norcia)

Conclusion and outlook

In this study, an object-based CD workflow using non-parametric machine learning methods for segmentation and classification is proposed and evaluated in the context of detecting destroyed buildings in VHR (very high resolution) satellite images. An object-based approach is chosen as it is computationally economical and with better results for processing when compared to traditional pixel-based methods for the analysis of VHR satellite imagery.

The proposed workflow fails in some cases where spectral ambiguities could not be resolved. Hence, the incorporation of additional features, like texture and shape parameters, as well as the incorporation of contextual information, for example, the expected position of shadows from buildings, is strongly recommended for future works. In general, the result of the CD accuracy assessment indicates that the segment-based approach produces better results than pixel-based approaches for the used dataset. The applied MDC approach turned out to be less accurate than the object-based PCC approach in this study. One reason for this might be the more complex task of defining suitable training segments based on a stack of two images from different points in time. However, with the faster MDC approach the changes can be classified directly, whereas the images have to be classified individually in advance of a CD in PCC.

Overall, it can be concluded that CD based on machine learning methods requires some experience in selecting the training data and requires less domain knowledge than traditional supervised classification approaches. The proposed workflow has shown to be effective for the areas with a greater probability of experiencing change. While it can be challenging to identify such changes in very large satellite images manually, using SVM can reduce this effort and serve as a useful tool in decision making.

References

Adam, H. E., Csaplovics, E., Elhaja, M. E. (2016): A comparison of pixel-based and object-based approaches for land use land cover classification in semi-arid areas, Sudan. *8th ISM International Conference and Exhibition on Remote Sensing & GIS (IGRSM 2016)-IOP Conf. Series: Earth and Environmental Science*, **37**, pp. 1-10.

Blaschke, T. (2010): Object-based image analysis for remote sensing. *ISPRS Journal of Photogrammetry and Remote Sensing*, **65**, pp. 2-16.

Castillejo-Gonzáleza, I.L., López-Granados, F., García-Ferrer, A., Pena-Barragán, J.M., Jurado-Expósitob, M., Ordena, M.S. (2009): Object- and pixel-based analysis for mapping crops and their agro-environmental associated measures using QuickBird imagery. *Computers and Electronics in Agriculture*, **68**, pp. 207–215.

Contreras, D., Blaschke T., Hodgson, M.E. (2017): Lack of spatial resilience in a recovery process: Case L'Aquila, Italy. *Technological Forecasting & Social Change*, **121**, pp. 76–88.

DigitalGlobe (2006): QuickBird scene 054594261010_01_P001, Level S2AS, DigitalGlobe, Longmont, Colorado, 09/04/2006.

DigitalGlobe (2009): QuickBird scene 054594261020_01_P001, Level S2AS, DigitalGlobe, Longmont, Colorado, 04/08/2009.

Dong, L., Shan, J. (2013): A comprehensive review of earthquake-induced building damage detection with remote sensing techniques. *ISPRS Journal of Photogrammetry and Remote Sensing*, **84**, pp. 85–99.

Gholoobi, M., Tayyebi, A., Taleyi, M., Tayyebi, A.H. (2010): Comparing pixel-based and object-based approaches in land use classification in mountainous areas. *International Archives of the Photogrammetry, Remote Sensing, and Spatial Information Science*, **38** (8), pp. 789-794.

QGIS (2017): http://www.qgis.org/en/site/, Last accessed October 18, 2017.

Ramachandra, T., Kumar, U. (2004): Geographic Resources Decision Support System for Land Use, Land Cover Dynamics Analysis. *Proceedings of the FOSS/GRASS Users Conference*, Bangkok, Thailand.

Rogan, J., Chen, D. (2004): Remote Sensing Technology for Mapping and Monitoring Land-Cover and Land-Use Change. *Progress in Planning*, **61** (4), pp. 301-325.

Tarek, H., Jocelyn, C., Jordi, I., Gregoire, M. (2007): Abrupt change detection on multitemporal remote sensing images: a statistical overview of methodologies applied to real cases, *IEEE- 1-4244-1212-9/07/2007*.

Jim, T., Joe, J., Ahsan, K., Kevin, B. (2009): Efficacy of Damage Detection Measures from Satellite Images. *American conference on wind engineering, San Juan, Puerto Rico.*

Giorgos, M., Jungho, I., Caesar, O. (2010): Support vector machines in remote sensing: A review, *ISPRS Journal of Photogrammetry and Remote Sensing.*

Burges, C.J.C. (1998): A tutorial on support vector machines for pattern recognition. Data Mining and Knowledge Discovery 2 (2), 121–167.

Coppin, P., Jonckheere, I., Nackaerts, K., Muys, B. (2004): Digital change detection methods in ecosystem monitoring: A review, *INT. J. REMOTE SENSING, VOL. 25, No. 9, 1565–1596.*

Tzotsos, A., Argialas, D.P (2008): Support Vector Machine Classification for Object-based Image Analysis. https://www.researchgate.net/publication/225929583- DOI: 10.1007/978-3-540-77058-9_36.

Goumehei, E. (2010): Contextual image classification with support vector machine-University of Twente-Faculty of GEO-information science-ITC

Habib, T., Chanussot, J., Inglada, J., Mercier, G. (2007): Abrupt change detection on multitemporal remote sensing images: a statistical overview of methodologies applied on real cases. *IEEE International Geoscience and Remote Sensing Symposium*, Barcelona, 2593-2596.

Treglia, M.L. (2015): An Introduction to GIS using QGIS (v. 2.6.1). https://mltconsecol.github.io/QGIS-Tutorial/QGIS-Tutorial/OldTutorials/Treglia_QGIS_Tutorial_2_6.pdf, Last accessed October 18, 2017. Burges, C.J.C., 1998. A tutorial on support vector machines for pattern recognition. Data Mining and Knowledge Discovery 2 (2), 121–167.

UNIFI 2010: Integrated health, social and economic impacts of extreme events: evidence, methods, and tools - *MICRODIS*. Annex 2 - Proposal Part B, p. 19.

Thapa, R.B., Murayama, Y. (2009): Urban Mapping, Accuracy, & Image Classification: A Comparison of Multiple Approaches in Tsukuba City, Japan. *Applied Geography*, **29** (1): 135-144.

Evaluation of existing RC frame structures with URM infill walls

ARCINIEGA Daniel[a], BARSOUM Nancy[b], BULJETA Anita[c], CORREIA LOPES Gonçalo[d],
ALICI Firat Soner[e], GRUBESA Tomislav[f], KAATSIZ Kaan[g], POPOSKA Angela[h]
[a] *Private Consultant Office Ing. Patricio Ramos, Quito, Ecuador*
[b] *Department of Civil Engineering, Birzeit University, Birzeit, Palestine*
[c] *Faculty of Civil Engineering, Josip Juraj Strossmayer University of Osijek, Croatia*
[d] *Department of Civil Engineering, University of Aveiro, Aveiro, Portugal*
[e] *Department of Civil Engineering, Middle East Technical University, Ankara, Turkey*
[f] *Faculty of Civil Engineering, Josip Juraj Strossmayer University of Osijek, Croatia*
[g] *Department of Civil Engineering, Middle East Technical University, Ankara, Turkey*
[h] *Institute of Earthquake Engineering and Engineering Seismology, S.s Cyril and Methodius,*
   University of Skopje, Macedonia

AL-HANOUN Hisham M.[i], ABRAHAMCZYK Lars[i], PENAVA Davorin[f]
[i] *Earthquake Damage Analysis Center, Bauhaus Universität Weimar, Germany*

Abstract

An investigation regarding the modelling of unreinforced masonry walls (URM) and their contribution to the lateral load resisting performance of structures is inspected in this study. The objective of the study includes performing a comprehensive examination of the existing macro models for modelling of URM infill walls. It is later accompanied with a detailed assessment of the effects of openings in the URM walls to the seismic performance. Finally, an existing RC frame building with URM infill walls is evaluated in order to further investigate the effect of the infill walls on the seismic performance. The infill walls are included in the analytical model by implementing well-known single diagonal strut approach. Comparisons between seismic responses of the bare frame analytical model and the model with the URM walls included are performed. A significant change in the damage distribution throughout the building is observed when URM infill walls are included to the analytical model.

Introduction

URM infill walls are commonly used within the RC frame structural systems around the world. If the infills are properly distributed throughout the structure and properly considered in the design, then they usually have a beneficial effect on the seismic response of the structure since they help in resisting the lateral loads by providing extra strength to the structure. To predict the behaviour of such URM infill walls the selection of the strut model is necessary. Since there are several equations for the width and for the hysteresis curves a parametric study should be made and then validated with experimental investigation.

Modelling of masonry infill walls without openings

Description

Having masonry infill walls in reinforced concrete structures can alter the behavior of the structure tremendously, especially under lateral loading. With that being said, infill walls should definitely be considered in the model. Moreover, this requires selecting an appropriate frame model that would be able to capture the actual behavior. Masonry infill walls can be modelled using both macro- and micro-modelling, however, the selected frame was analytically modelled using macro-modelling, and

considering a single strut approach. This is because experimental and conceptual observations of the first attempts to model the response of the composite infilled-frame structures have indicated that a diagonal strut with appropriate geometrical and mechanical characteristics, as shown in Figure 1, could possibly provide a solution to the problem (Panagiotis *et al.*, 2012).
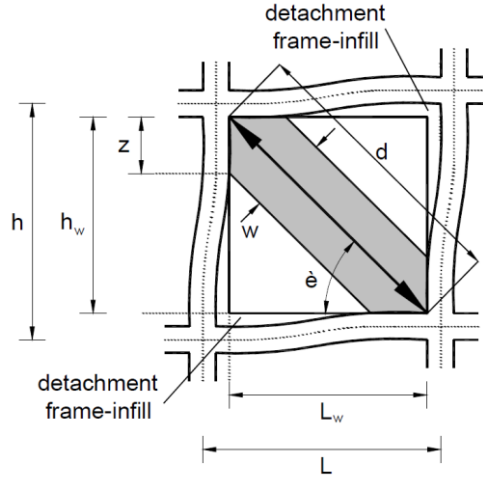
Figure 1. Masonry infill frame sub-assemblage (*Panagiotis et al., 2012*).

Equivalent Strut width

Few previous studies provide different approaches to define the equivalent width of the proposed strut. Based on the conclusions of a sensitivity study of strut width conducted in the investigation of Abrahamczyk *et al.*, the following five equations of Liaw & Kwan, Paulay & Priestley, Bertoldi, Hendry, and Cavaleri & Papia, showed comparable results as demonstrated in Figure 2.

- Liaw & Kwan (1984)

$$w = \left(\frac{0.95\, sin(2\theta)}{2\sqrt{\lambda_1 H\prime}}\right) d \qquad (1)$$

- Paulay & Priestley (1992)

$$w = \frac{d}{4} \qquad (2)$$

- Bertoldi (1993)

$$w = \left(\frac{1.3}{\lambda_1 H\prime} - 0.178\right) d; \; if \; \lambda_1 < 3.14 \qquad (3)$$

$$w = \left(\frac{0.707}{\lambda_1 H\prime} + 0.01\right) d; \; if \; 3.14 < \lambda_1 < 7.85$$

$$w = \left(\frac{0.47}{\lambda_1 H\prime} + 0.04\right) d; \; if \; \lambda_1 > 7.85$$

- Hendry (1998)

$$w = 0.5\sqrt{\alpha_1 + \alpha_2}; \; where: \qquad (4)$$

$$\alpha_1 = \frac{\pi}{2}\left(\frac{E_1 I_1 H}{2\, E_2\, t\, sin(2\theta)}\right)^{\frac{1}{4}} \qquad \alpha_2 = \frac{\pi}{2}\left(\frac{E_1 I_{11} H}{2\, E_2\, t\, sin(2\theta)}\right)^{\frac{1}{4}}$$

- Cavaleri & Papia (2003)

$$w = \frac{d\, k\, c}{z\, \lambda^\beta}; \; where: \qquad (5)$$

$$k = 1 + (18\lambda + 200)\,\varepsilon \quad \varepsilon = \frac{F}{2A_1 E_1}$$

$$c = 0.249 - 0.0116\gamma + 0.567\gamma^2 \qquad z = 1 + 0.25\left\{\left(\frac{L}{H\prime}\right) - 1\right\}$$

$$\lambda = \frac{E_2 t\, H\prime}{E_1 A_1}\left(\frac{H\prime^2}{L^2} + \frac{A_1 L}{4A_{11} H\prime}\right) \qquad \beta = 0.146 + 0.0073\gamma + 0.126\gamma^2$$
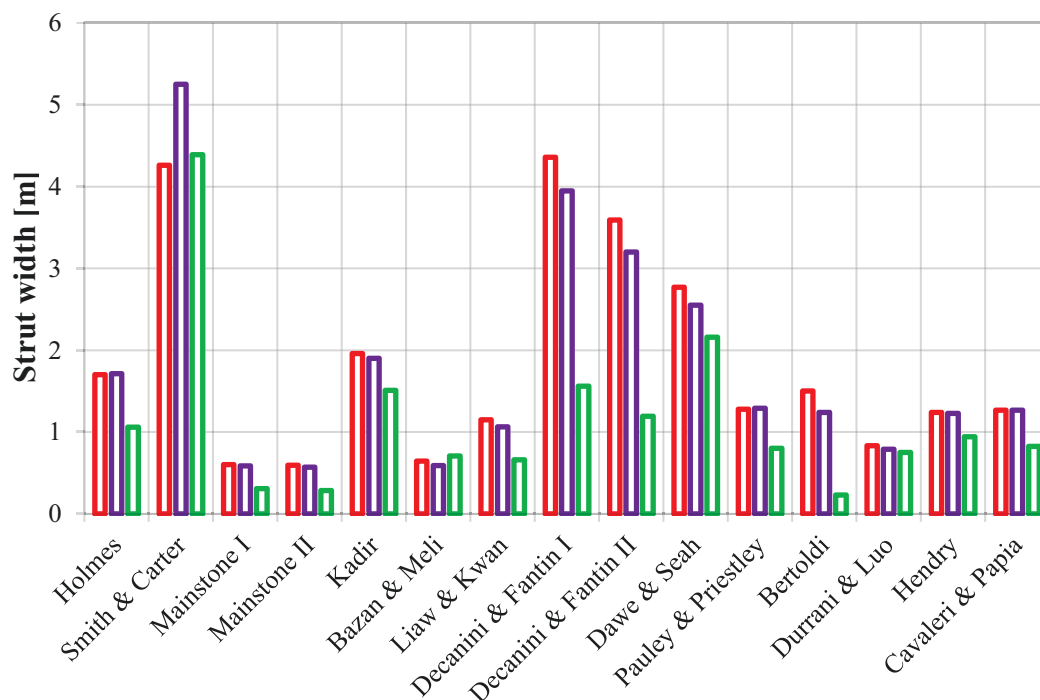
Figure 2. Comparison of strut width for different length of infill walls from different empirical equations
(*Abrahamczyk et al., 2016*).

Regarding the project at hand, only the aforementioned approaches were considered in investigating the appropriate equivalent strut width as explained earlier. Furthermore, the comparative study of the different expressions performed by Abdelkareem *et al.* showed that the Paulay & Priestley equation is the most suitable choice for calculating the diagonal equivalent strut width due to its simplicity. In fact, it was observed that this equation gives an approximate average value among those studied in this work.

In order to simplify the selected equations some parameters were kept constant. In Table 1 are the variables and constants for the different strut- width equations.

Figure 3. shows equivalent strut width proposed by different researchers according to different aspect ratios. Cavaleri & Papia formula gives the most conservative results. Therefore it gives the biggest strut stiffness, while aspect ratio have small influence on Hendry´s formula. Liaw & Kwan and Paulay & Priestley formulae gives the best results according to average line. Paulay & Priestley formula depends only on strut length so it is simple to use.

Table 1. Constants and variables for strut width equations.

Constants		Variables	
Beams' cross-section	w = 0.2 m; h = 0.5 m	Pillars' cross-section	w; h
Pillars' height	H' = 2.875 m; H = 2.625 m	Span length	L'; L
Infill thickness	t = 0.2 m	Aspect ratio	d; θ
Material properties	E = 2100000 kN/m^2 v = 0.15 G = 913043.5 kN/m^2 fc = 303 kN/m^2		
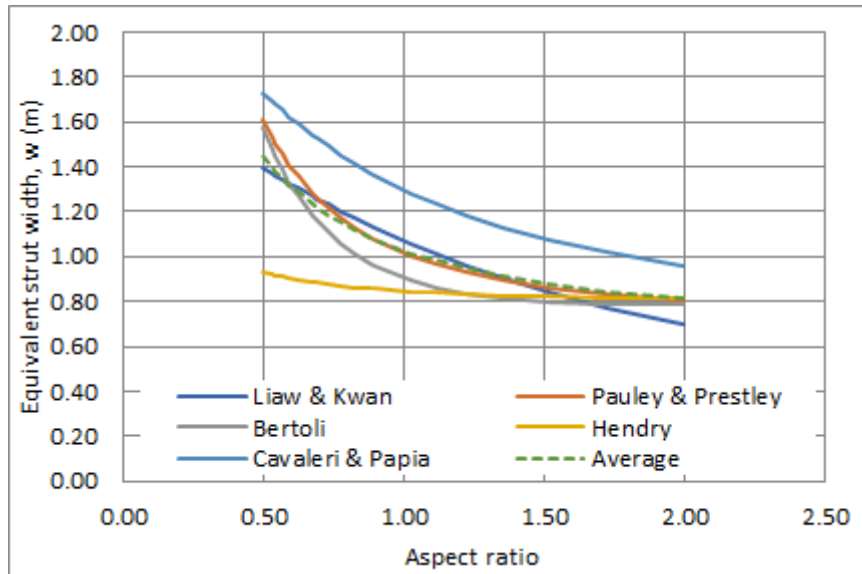
Figure 3. Comparison of the curves for the strut width equations (obtained for the pillar cross section 25x70 cm^2).

Modelling of masonry infill walls with openings

Equations for the reduction factor

The reduction factor for the equivalent strut width (w) in relation to the opening percentage can be obtained by one of the following approaches:

- Panagiotis *et al.* (2012) $\lambda = 1 - 2\alpha_w^{0.54} + \alpha_w^{1.14}$; where: (6)

- Raghavendra *et al.* (2014) $D_{rf} = 3.58(O_{ar})^2 - 3.56(O_{ar}) + 1$ (7)

where, α_w and O_{ar} are the opening area ratio.

It should be noted that these expressions have been developed only for centered windows and that they do not take into consideration the number and aspect ratio of the openings.

Classification of the openings

The classification of the equivalent strut for each infilled frame depending on the opening ratios was made as follows:

-         Ao/Ai ≤ 7.5% → small opening → no reduction of w

-   7.5% < Ao/Ai ≤ 15% → medium opening → reduction of w

-    15% < Ao/Ai ≤ 35% → large opening → reduction of w

-        Ao/Ai > 35% → extra large opening → w=0 (bare frame)

From Figure 4 it is observed that Raghavendra *et al.* gives high decreasing of stiffness after reaching Fy, than Panagiotis *et al.* approach for small and medium openings. For large openings difference between them is small, so they give almost the same results in that case. Maximum base force is almost the same, difference is that in Raghavendra *et al.* approach maximum force is at smaller displacement, than in Panagiotis *et al.* approach. Both of the approaches provide bigger displacements of maximum base force by increasing area of openings.
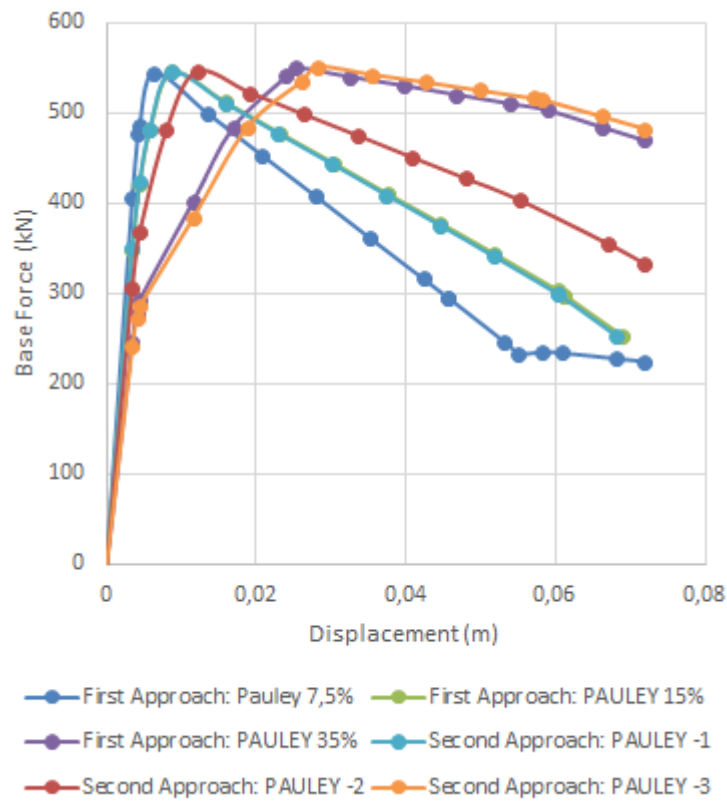
Figure 4. Comparison of the results for different width reduction approaches for different area of openings (frame 50x50-540).

Selection of the constitutive laws for strut hinges

Two approaches have been selected for the constitutive law (*Asteris et al., 2011*), whose correspondent hysteresis curves are illustrated in Figure 5:

- Žarnic

- Panagiotakos & Fardis
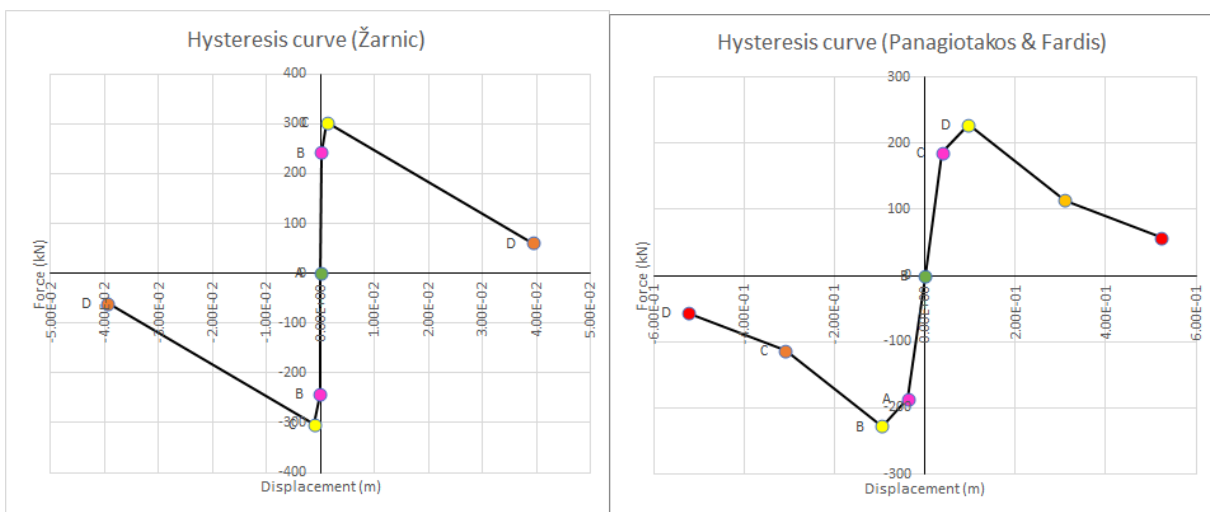
Figure 5. Comparison of the hysteresis curves from the two different approaches selected.
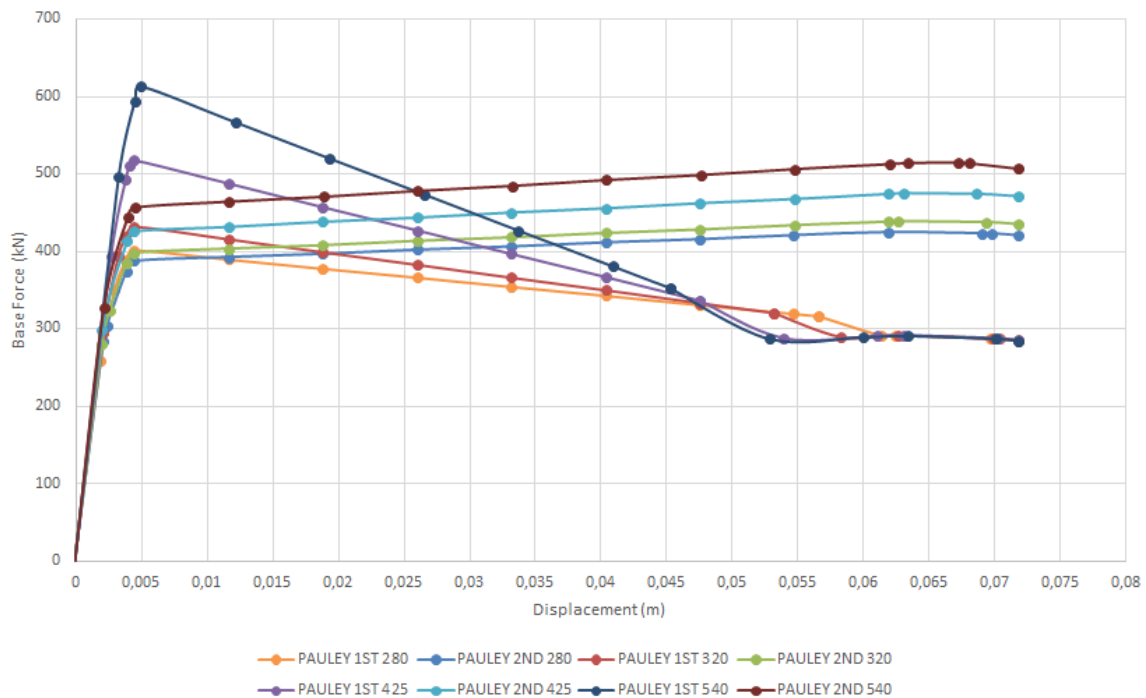
Figure 6. Comparison of the results for different approaches for constitutive law (frame 25x70-Pauley).

From Figure 6 it is observed that Žarnic approach show decreasing of stiffness after reaching F_y. For different aspect ratios Žarnic approach gives tendency of meeting in one point, probably after bearing capacity of infill wall is lost.

Panagiotakos & Fardis approach gives increasing stiffness after reaching F_y. Different aspect ratios have parallel increasing of stiffness. Ductility of strut in this approach is bigger than in Žarnic approach.

Case study: Evaluation of an existing RC frame structure

General Description

The implementation of URM infill wall to the analytical model was conducted with an existing RC frame building. This structure was built in 1996, and is located in Hatay which is a high seismic area located in Turkey. The building is a 5-storey RC frame structure consisting of one basement floor surrounded by a continuous shear wall, four floors with a typical plan and one roof floor. The plan and general view of the structure are given in Figure 7. Concrete and steel strength characteristics are 16 MPa and 420 MPa, respectively. The loads acting on the system are composed of the self-weight of the members and the slabs ($t_{slab} = 120mm$), and a uniform live load of 2.0 kN/m². In addition to these loads, the loads from both the exterior and interior infill walls are also taken into consideration in terms of uniformly applied line loads in the model.

The analytical model of the 5-storey frame building was generated using SAP2000 (v19) software program. Inelastic behaviour of the structural members is represented by defining plastic hinges in the ends of beams and columns where PP-M2-M3 and M3 hinge types are employed for columns and beams, respectively. The plastic hinge analogy and their application to the analysis software is illustrated in Figure 8. Slabs at each storey were also defined on the analytical model by utilizing shell element. Rigid diaphragms are assigned to each storey level, and P-Δ effects are not taken into account in the model.

(a)

(b)

Figure 7. (a) General view of the existing RC structure, (b) Typical floor plan for the upper stories. (*Abrahamczyk, 2014*).
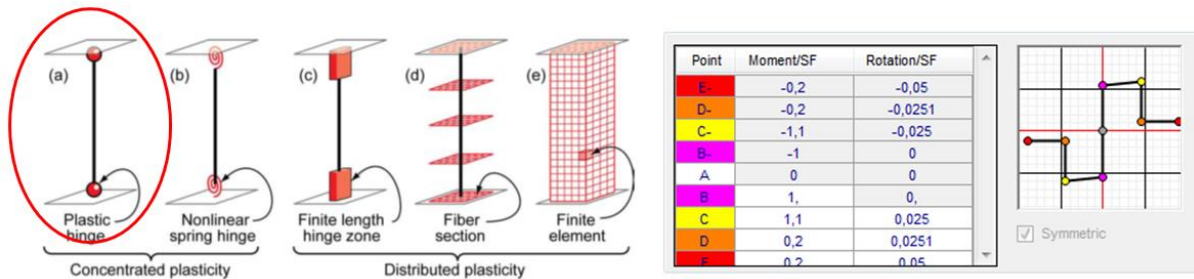
Figure 8. Schematic visualization of the concentrated plasticity hinges and their moment curvature relationship definition to the analysis software (*Reinhorn et al., 2010; SAP2000*).

Modeling of the URM Infill Walled Structure

After investigating possible ways to include the effect of URM infills on the inelastic response of the structure, it was decided to employ the single diagonal strut members in the analytical model. These members are generated such that their widths vary according to their spans and their opening ratios. After structural plans are investigated, each infill wall was classified according to its structural properties and the effective widths have been calculated. An excerpt from the tables containing infill wall information can be seen in Table 2. Infill walls, classified from small opening to large opening, were included in the model. However; their respective widths were reduced with respect to their opening ratios.

Table 2. Calculations for the strut elements.

| Label | Storey # | Column Dimesions | | | | Opening | | | | | Infill | | | | Ratio | Opening Type | d (m) | w_o' (m) |
		L_{in1}	L_{out1}	L_{in2}	L_{out2}	$L_{opening,w}$ (m)	$H_{opening,w}$ (m)	$L_{opening,d}$ (m)	$H_{opening,d}$ (m)	A_{infill} (m²)	L (m)	H (m)	t	A_0 (m²)	(A_{infill}/A_0)			
D5-E5	1.storey	0,60	0,25			0,00	1,50	0,90	2,10	1,89	3,23	2,30	0,10	7,43	0,25	large	4,35	0,32
D5-E5	2., 3.storey	0,60	0,25			0,00	1,50	0,90	2,10	1,89	3,23	2,30	0,10	7,43	0,25	large	4,35	0,32
D5-E5	4. storey	0,60	0,25			0,00	1,50	0,90	2,10	1,89	3,23	2,30	0,10	7,43	0,25	large	4,35	0,32
D11-E11	4. storey	0,60	0,25			0,00	1,50	0,90	2,10	1,89	3,23	2,30	0,10	7,43	0,25	large	4,35	0,32
C9-C7	1.storey	0,25	0,80	0,25	0,80	0,00	1,50	0,00	2,10	0,00	1,80	2,30	0,20	4,14	0,00	small	3,27	0,82
C7-C9	2., 3.storey	0,25	0,80	0,25	0,80	0,00	1,50	0,00	2,10	0,00	1,80	2,30	0,20	4,14	0,00	small	3,27	0,82
C7-C9	4. storey	0,25	0,60	0,25	0,60	0,00	1,50	0,00	2,10	0,00	1,80	2,30	0,20	4,14	0,00	small	3,27	0,82
C'6-C'5	Roof	0,25	1,25			0,60	0,60	0,00	2,10	0,36	2,10	2,30	0,20	4,83	0,07	small	3,38	0,85
C'9-C'10	Roof	0,25	1,25			0,60	0,60	0,00	2,10	0,36	2,10	2,30	0,20	4,83	0,07	small	3,38	0,85

After the infill walls are added to the model, constitutive relationships regarding their axial load-deformation behaviours are also calculated. In order to fulfill the requirements for all URM walls, they have been grouped according to their characteristics and 19 different force-deformation curves are determined and implemented in the model as axial plastic hinges. These axial force-deformation curves are given in Figure 9. It should also be noted here that these struts do not have any tensile strength defined to them as they are not expected to perform under tensile forces.

The general view of the analytical model with the single diagonal strut elements is given in Figure 10. It should be noted that basement storey has surrounding shear walls that have been modeled as shell elements which are not displayed in Figure 10. Modal analyses for both bare frame and URM infill walled structure has been performed and first three fundamental vibration modes of both structures in each direction are given in Table 3. As it can be deduced from the results given in Table 3, both structures are torsionally flexible since their first mode is in torsion. Moreover, it can also be noticed that the inclusion of the diagonal struts to the analytical model results in an increase in stiffness; hence reduction of the period in all principal directions.
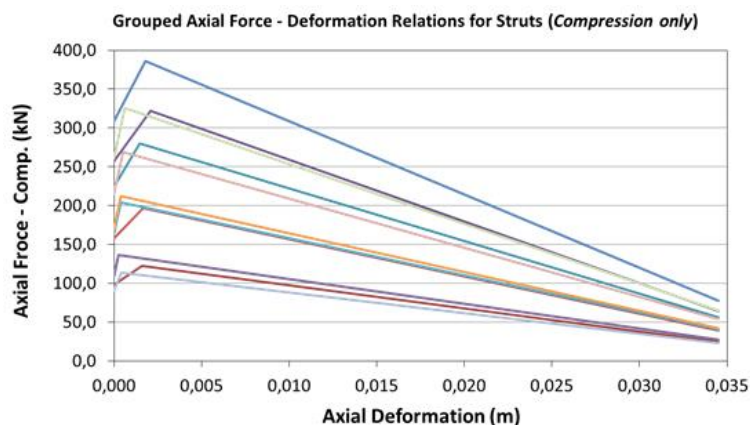
Figure 9. Grouped axial force-deformation curves of the struts (compression only).

Table 3. Comparison of the dynamic properties between the bare frame model and the model with URM infill walls.

Fundamental Periods (s)			
System	**T1 (θ)**	**T1 (Y)**	**T1 (X)**
Bare Frame	0.61	0.57	0.47
URM Frame	0.47	0.41	0.33
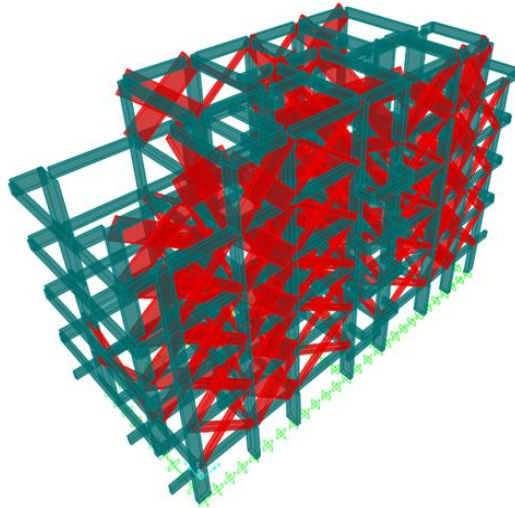
Figure 10. General layout of the analytical model after implementing the corresponding single diagonal struts.

Evaluation of the Inelastic Response

In order to assess the influence of the URM walls on the inelastic response of the structure, incremental pushover analysis has been performed on both bare frame and URM infill walled frame model. Simple triangular load distribution is applied to the center of each diaphragm. Systems are pushed up to a monitored displacement of 38cm in both directions, which is approximately 2.5% of the height of the structure.

The obtained capacity curves at the end of the pushover analyses are presented in Figure 11 for X direction (strong) and Y direction (weak) of both structures, respectively. It can easily be observed in both figures that inclusion of the URM infill walls to the analytical models results in an increase at the global stiffness as observed in the change of fundamental periods. This is also accompanied by the strength increase in the URM infill walled system, as well.

Another important comparison that could be made by inspection of the obtained response is the damage distribution in both structures. The plastic hinge distribution at collapse prevention damage state of the exterior frame of both infill walled and the bare frame structure models are shown in Figure 12. Upon inspecting the Figure, it can be seen that there is significant amount of plastic hinging at the column ends of the bare frame structure. While this results in a column mechanism for this system; URM infill walled structure display no plastic hinging at columns. Rather, a high amount of plasticity is concentrated in compression struts of the infill walls. In addition to this there is some plastic hinging present at the beams, as well. In addition to this, all the tensions struts in the model is beyond elastic behaviour as there is no tensile resistance in these struts.
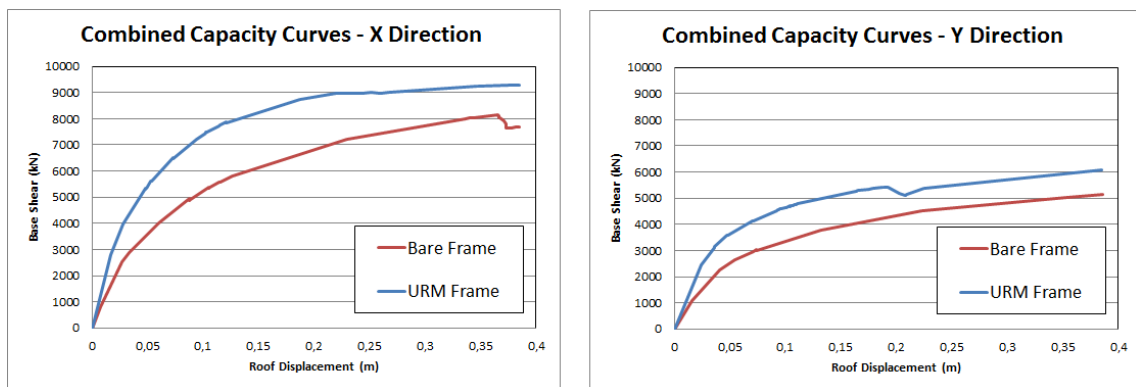
Figure 11. Comparison of the capacity curves in x-direction of the bare frame model and the model with URM infill walls in both orthogonal directions.
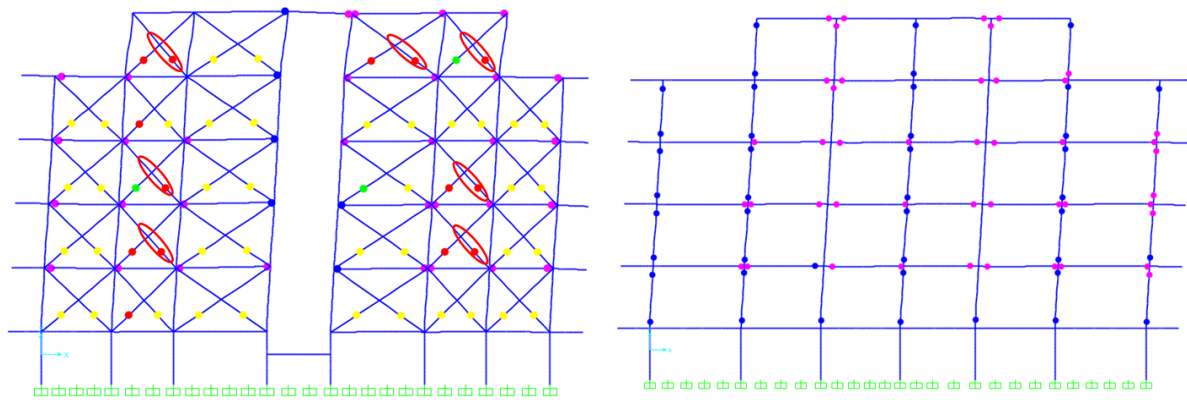
Figure 12. Difference between the damage distribution in x-direction from the bare frame model and the model with URM infill walls at the collapse prevention performance limit where the colour dots indicate the formation of plastic hinges.

Conclusions

Deciding on the adequate equivalent strut of an infill wall is generally based on empirical equations that compute the width of the proposed strut. Different conclusions were conducted for the two cases of the fully infilled walls and the infill walls with openings. On the one hand, for the single strut models without the openings, the capacity curves for the different equations are similar, however introducing a different constitutive law enabled us to conclude that the length of the strut is an important parameter, as it decreases the capacity under larger displacements. On the other hand, for a single strut model with openings, the capacity curves for the different equations are not similar and when comparing the capacity curves with the two constitutive laws we have different behaviour in the curve that brings into conclusion that the reduction factor also change the behaviour of the structure.

The results obtained from the case study suggest that including the URM infill wall to the analytical model of a structure increase the lateral load resisting capacity with decreasing expected damage on members, especially on columns. The effect of the infill walls on the lateral load capacity and response of the structural system also depends on the layout of the infills on the plan of the building, and the type of the infills based on the opening ratios. Consequently, it can be said that inclusion of URM infills completely change of the damage distribution throughout the building, and considering URM infills in performance evaluation of a building can give more accurate response and capacity.

References

Abrahamczyk, L. (2014): Kenngrößen zur Prognose des Verhaltens von Geschossbauwerken in Erdbebengebieten und Kriterien für den Ertüchtigungsbedarf. *Dissertation*. Schriftenreihe des Instituts für Konstruktiven Ingenieurbau der Bauhaus-Universität Weimar, Band **24**, VDG Weimar.

Abrahamczyk L., Schwarz J., Shetty N. (2016): Quality assessment of equivalent strut models for RC frames with URM walls. *Structural Analysis of Historical Constructions*. Taylor & Francis Group, London, pp. 1268-1275.

Abrahamczyk L., Schott C., Schwarz J., Swain T.M. (2004): Vulnerability of RC frame structures in Turkish earthquake regions (Part 2): Modelling and analysis. *13th World Conference on Earthquake Engineering, 1–6 August 2004*. Vancouver, Canada, Paper no. 220.

Abdelkareem K.H., Abdel Sayed F.K., Ahmed M.H., AL-Mekhlafy N. (2013): Equivalent strut width for modeling RC infilled frames. *Journal of Engineering Sciences.* Assiut University, Faculty of Engineering, Vol. 41, No. 3, pp. 851-866.

Akhaveissy A.H. (2012): Finite element nonlinear analysis of high-rise unreinforced masonry building. *Latin American Journal of Solids and Structures,* 9: 547–567.

Asteris P.G., Giannopoulos I.P., Chrysostomou Ch.Z. (2012). Modeling of Infilled Frames With Openings. *The Open Construction and Building Technology Journal.* No. 6, (Suppl 1-M6), pp. 81-91.

Asteris P.G., Kakaletsis D.J., Chrysodtomou C.Z., Smyrou E. (2011): Failure of infilled frames. *Electronic Journal of Structural Engineering*, No. 11(1): pp. 11-20.

Crisafulli F.J., Carr A.J., Park R. (2000): Analytical modelling of infilled frame structures – A general review. *Bulletin of the New Zealand Society for Earthquake Engineering,* 33(1): 30–45.

Haldar P., Singh Y., Paul D.K. (2013): Identification of seismic failure modes of URM infilled RC frame buildings. *Engineering Failure Analysis,* 33: 97–118.

Holmes M. (1961): Steel frames with brickwork and concrete infilling. *Proceedings of the Institution of Civil Engineers,* 19(4): 473–478.

Kadir M.R.A. (1974): The structural behavior of masonry infill panels in framed structures. *PhD Thesis,* University of Edinburgh.

Murty C.V.R., Jain S.K. (2000): Beneficial influence of masonry infill walls on seismic performance of RC frame buildings. *12th World Conference on Earthquake Engineering.*

Paulay T., Priestley M.J.N. (1992): Seismic design of reinforced concrete and masonry buildings. John Wiley & Sons, Inc. New York.

Pinho R., Elnashai A.S. (2000): Dynamic collapse testing of a full – scale four story RC frame. *ISET Journal of Earthquake Technology*, Paper No. 406, 37(4): 143–163.

Pinto A., Varum H., Molina J. (2002): Experimental assessment and retrofit of full scale models of existing RC frames. *In: Proceedings of the 12th European Conference on Earthquake Engineering*. Elsevier Science Ltd, London.

Polyakov S.V. (1960): On the interaction between masonry filler walls and enclosing frame when loading in the plane of the wall. *Translation in earthquake engineering, Earthquake Engineering Research Institute (EERI)*, 36–42.

Prasad R., Rahman S.S., Chandradhara G.P. (2014): Equivalent diagonal strut for infilled frames with openings using finite element method. *IOSR Journal of Mechanical and Civil Engineering (IOSR-JMCE)*, 24–29.

Pujol S., Benavent-Climent A., Rodriguez M.E., Smith-Pardo J.P. (2008): Masonry infill walls: An effective alternative for seismic strengthening of low rise reinforced concrete building structures. *The 14th World Conference on Earthquake Engineering, 12-17 October 2008*. Beijing, China.

Raghavendra P.M.D., Ur Rahman S.S., Chandradhara G.P. (2014): Equivalent diagonal strut for infilled frames with openings using finite element method. *IOSR Journal of Mechanical and Civil Engineering*, pp. 24–29.

Reinhorn A., Deierlein G., and Willford M. (2010): Nonlinear Structural Analysis for Seismic Design- A Guide for Practicing Engineers.

Samoila D.M. (2012): Analytical modelling of masonry infills. *Acta Technica Napocensis: Civil Engineering & Architecture,* 55(2): 127–136.

Schwarz J., Abrahamczyk L., Leipold M., Wenk T. (2014): Vulnerability assessment and damage description for RC frame structures following the EMS-98 principles. *Bulletin of Earthquake Engineering,* 13(4): 1141–1159.

Smith B.S. (1962): Lateral stiffness of infilled frames. *Journal of Structural Division,* 88(6): 183–199.

Skafida S., Koutas L., Bousias S.N. (2014). Analytical modelling of masonry infilled RC frames and verification with experimental data. *Hindawi Publishing Corporation, Journal of Structures, Article ID 216549,* 1–17.

Uva G., Raffaele D., Porco F., Fiore A. (2012): On the role of equivalent strut models in the seismic assessment of infilled RC buildings. *Engineering Structures,* 42: 83–94.

Numerical Analyses on the Stability of Beam-Columns

COBZARU Stefan [a], IBRAHIM Mohamed [b], JAKAB Dominiq [c], KARABULUT Burak [d], VELA Silvia [e]
[a] *Technical University of Civil Engineering of Bucharest*
[b] *Ain Shams University*
[c] *Politehnica University of Timisoara*
[d] *KU Leuven*
[e] *University of Genoa*

Abstract

Stability of beam-columns is of paramount importance since vulnerability to instability problems is most of the time the governing design criterion for steel structural systems. The comparison between Eurocodes (EN 1993-1-1 2006) and German DIN standards (DIN 18800-1 2008) for evaluating the lateral torsional behaviour of beam elements has been a controversial discussion over the last decades. Especially, calculation of critical moment value (M_{cr}) differs remarkably between Non-Contradictory Complementary Contribution (NCCI) documents referring to recent editions of Eurocodes and former applications in German practice (Bureau and Galea 2005, DIN 18800-2 2008). In order to bring enlightenment to this topic, a comparative analytical study has been performed. As a part of this contribution, an experimental test has also been designed to investigate the different failure modes associated with the beam elements as a result of bending about strong and weak axes. The experimental part has been furthermore extended with numerical analyses performed by ANSYS finite element (FE) solver (ANSYS Inc. 16.2 2015). Moreover, a parametric study investigating the influencing parameters such as geometric properties of the cross-sections, length of the beam element, load application point and so forth was conducted.

Introduction

A necessary condition that structures must satisfy in order to meet the performance requirements is equilibrium. Equilibrium is defined as "stable" when the system returns to its initial state after a small perturbation. Equilibrium is defined as "unstable", when the system cannot return into its initial condition after a perturbation and cannot reach another equilibrium configuration. It is defined as indifferent when the system finds a new equilibrium condition after a perturbation.

Instability of structural members must be taken into account for the design of structural members, especially when dealing with steel structures. Instability reduces the capacity of the steel structures by hindering the plastification of the cross sections.

Problems associated with instability may be either global or local. Global instability occurs when the entire element is involved, while local instability occurs within the parts of cross sections, involving their most slender parts. Local instability is taken into account by the classification of cross sections, yet the topic is not relevant to this paper, which deals only with global instability problems. When considering a steel beam in compression, two types of global instability may occur:

- Flexural buckling (FB)
- Lateral torsional buckling (LTB)

From an analytical point of view, FB problems are solved by Euler´s theory which shapes the basis for the coded approach. Current codes report a more comprehensive approach that accounts also of the material imperfections, residual stresses and geometric imperfections by defining an equivalent imperfection factor.

Lateral-torsional buckling may occur in the case of beams or lattice girders. It can either be prevented by performing checks using suitable coded relations, or by introducing some bracings whose purpose is to reduce the distance on which the phenomenon may occur. Another way to address this instability problem is of course to pick up cross-sections which are not susceptible to LTB such as circular or hollow sections.

The relationship given in Eurocode 3 Part 1-1 (EN 1993-1-1 2006) for lateral-torsional buckling resistance is:

$$M_{b,Rd} = \chi_{LT} W_y \frac{f_y}{\gamma_{M1}} \qquad (1)$$

where:

χ_{LT} – the reduction factor for lateral torsional buckling;

W_y – the appropriate section modulus:

- $W_y = W_{pl,y}$ for Class 1 or 2 cross-sections;
- $W_y = W_{el,y}$ for Class 3 cross-sections;
- $W_y = W_{eff,y}$ for Class 4 cross-sections;

f_y – the yielding limit;

γ_{M1} – the partial safety factor for resistance of members to instability assessed by the member checks ($\gamma_{M1}=1.1$ in the German National Annex).

χ_{LT} is computed from the appropriate buckling curve, based on the non-dimensional slenderness:

$$\bar{\lambda} = \sqrt{\frac{W_y f_y}{M_{cr}}} \qquad (2)$$

where:

M_{cr} is the elastic critical moment for lateral-torsional buckling, whose expression is not given in Eurocode 3 Part: 1-1. Under these circumstances, it can be calculated according to recognized sources such as publications, or software programs. Some examples of such sources are the following ones:

- the previous editions of Eurocode 3 Part: 1-1 (EN 1993-1-1 2006);
- published mechanics books (Timoshenko and Gere 1961);
- NCCI – Elastic critical moment for lateral torsional buckling (Bureau and Galea 2005);
- LTBEAM software developed at Centre Technique Industriel de la Construction Metalique (CTICM) which is accessible free of charge: www.cticm.com.

The relation recommended by Bureau and Galea 2005 is:

$$M_{cr} = C_1 \frac{\pi^2 E I_z}{(k_z L)^2} \left[\sqrt{\left(\frac{k_z}{k_w}\right)^2 \left(\frac{I_w}{I_z}\right) + \frac{(k_z L)^2 G I_t}{\pi^2 E I_z} + \left(C_2 z_g\right)^2} - C_2 z_g \right] \qquad (3)$$

where:

E – modulus of elasticity (Young's modulus);

G – shear modulus;

I_z – moment of inertia with respect to the weak axis;

I_T – torsional constant of the section;

I_w – warping constant of the section;

L – the beam length between two points having lateral restraints (considered 6 m);

k_z – the effective length factor that refers to the end rotation about the z-z axis;

k_w – the effective length factor that refers to the end warping;

z_g – the distance between the point of load application and the shear center (considered equal to half of the height of the C.S);

C_1, C_2 – coefficients depending on the loading and end restraint conditions.
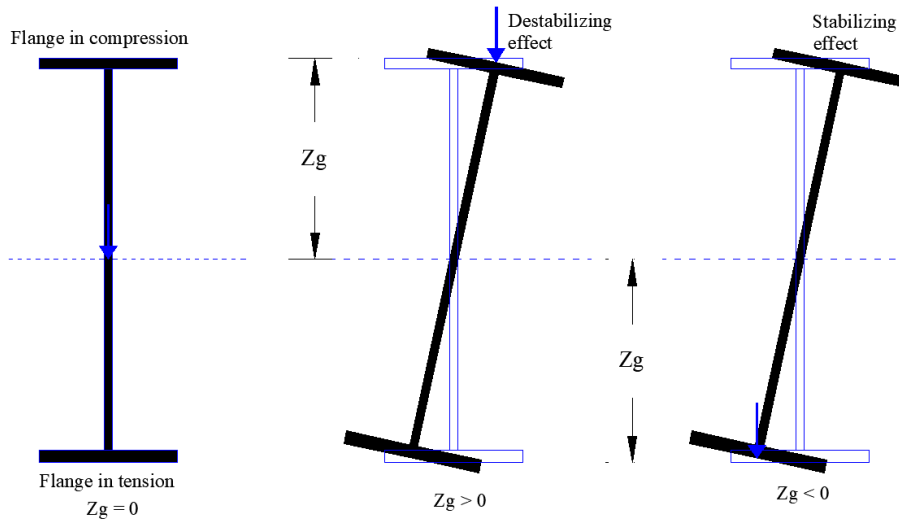
Figure 1. Influence of the position of the loading point.

It is important to note that the value to the critical moment is influenced by the position of the loading point. The load can either has a stabilizing or a destabilizing effect (Fig. 1).

The used method for computing χ_{LT}, is the modified general approach, which is specific for rolled sections or equivalent welded sections. A correction is introduced, to take into account the bending moment diagram along the bar. On this line, a modified reduction factor is calculated as follows:

$$\chi_{LT,mod} = \frac{\chi_{LT}}{f} \quad \text{but} \quad \chi_{LT} \leq 1.0 \qquad (4)$$

The correction factor k_c is given as a function of moment distribution (Fig. 2).
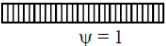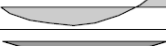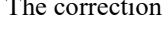
In DIN 18800-2 2008, the elastic critical moment may be defined in a different manner (Kindmann and Kraus 2011):

$$M_{cr,y} = \frac{k}{L}\sqrt{EI_z GI_T} \qquad (5)$$

where:

k is a lateral-torsional buckling parameter which depends on the torsional stiffness parameter:

$$\frac{EI_W}{L^2 GI_T} = \frac{1}{\varepsilon_T^2} \qquad (6)$$

Moment distribution	k_c
$\psi = 1$	1,0
$-1 \leq \psi \leq 1$	$\dfrac{1}{1,33 - 0,33\psi}$
	0,94
	0,90
	0,91
	0,86
	0,77
	0,82

Figure 2. The correction factor k_c (EN 1993-1-1).

Experimental study

In order to investigate the actual experimental behaviour for lateral torsional buckling, a 1.5 m long cantilever beam made of an IPE 140 profile has been submitted to gravity point loading at the tip. The experimental setup has been performed such that it is fully restrained for both translational and rotational degrees of freedoms at one end, whereas it has been set free at the other end where the tip load is located (Fig. 3a). The load is applied through a pendulum (1 m long) which is acting at the tip of the beam. The mechanism is hinged so that lateral behaviour can be imposed to the system. The displacements have been measured via five displacement transducers (LVDT's) one placed at the bottom flange in the loading direction and four located in the out of plane direction (Fig. 3b). The load has been recorded through a load cell located underneath the pendulum. In the latest provisions of EN 1993-1-1, it is clearly stated that lateral torsional behaviour can be neglected in case the beam is submitted to bending about the weak axis. So as to observe that statement as well as to calibrate the numerical study based on flexural behaviour, a complementary experimental setup made of the same cross section as the previous experiment has been built up letting the specimen bend about the weak axis. The loading pace has been arranged such that the force applies in a static manner as shown in Fig. 4 (0.1 cm/min for strong-axis bending and 0.35 cm/min for weak-axis bending). Both of the experimental setups are depicted in Fig. 5. The results of the experiments are shown in Fig. 6.

| (a) | (b) |
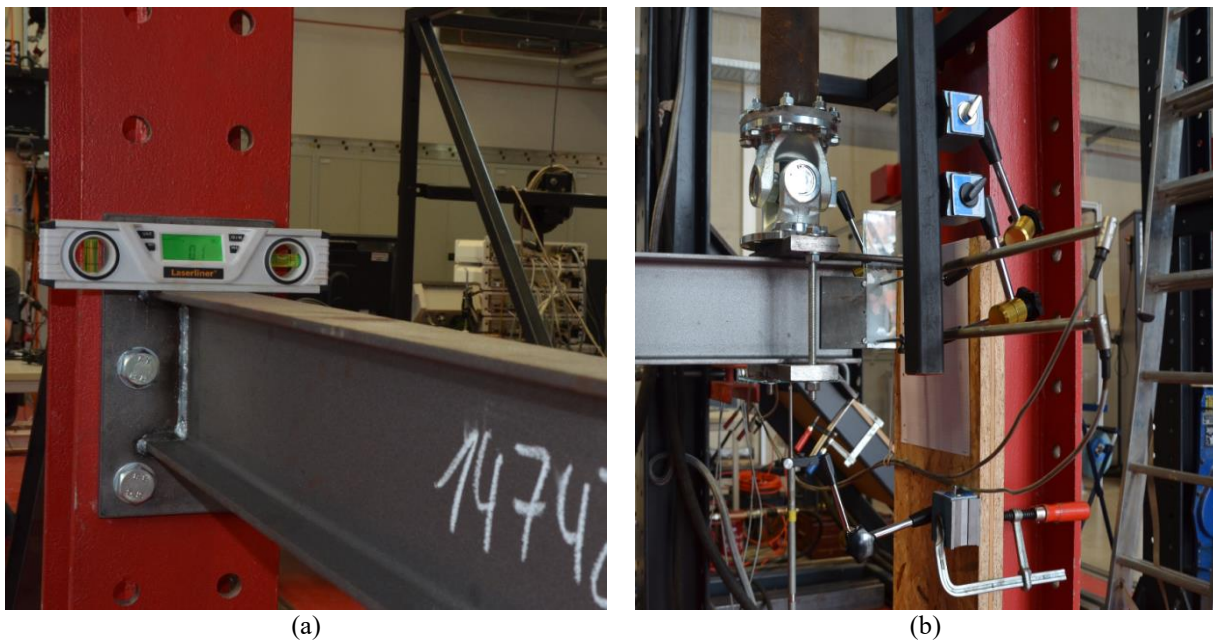
Figure 3. IPE 140 beams: (a) support conditions; (b) test instrumentation.

| (a) | (b) |
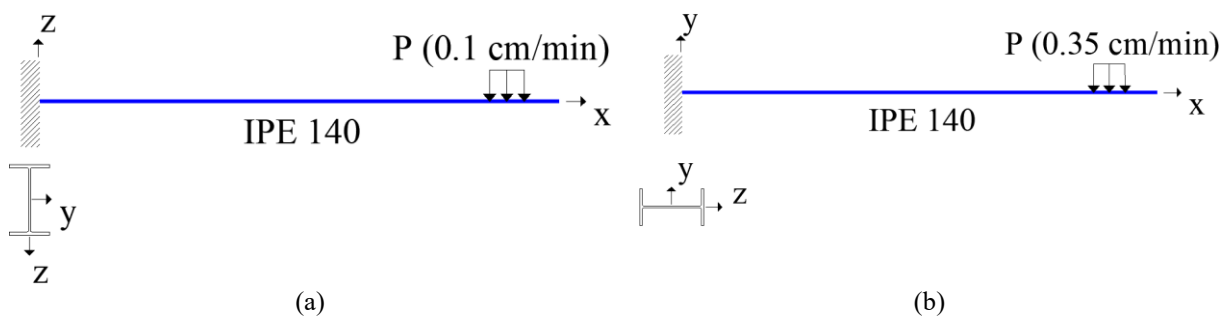
Figure 4. Schematic view of IPE 140 beams: (a) strong axis orientation; (b) weak axis orientation.

(a)   (b)
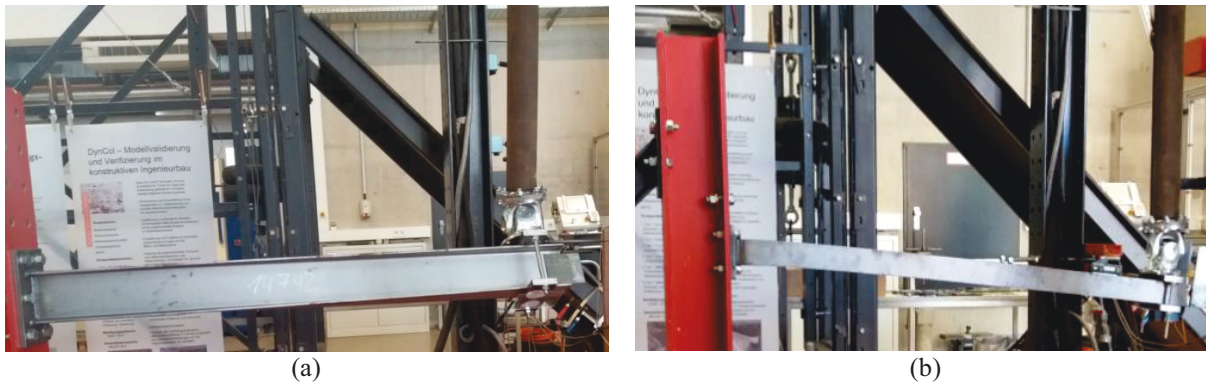
Figure 5. Tests on IPE 140 beams: (a) bending about strong axis (LTB); (b) bending about weak axis (flexure).
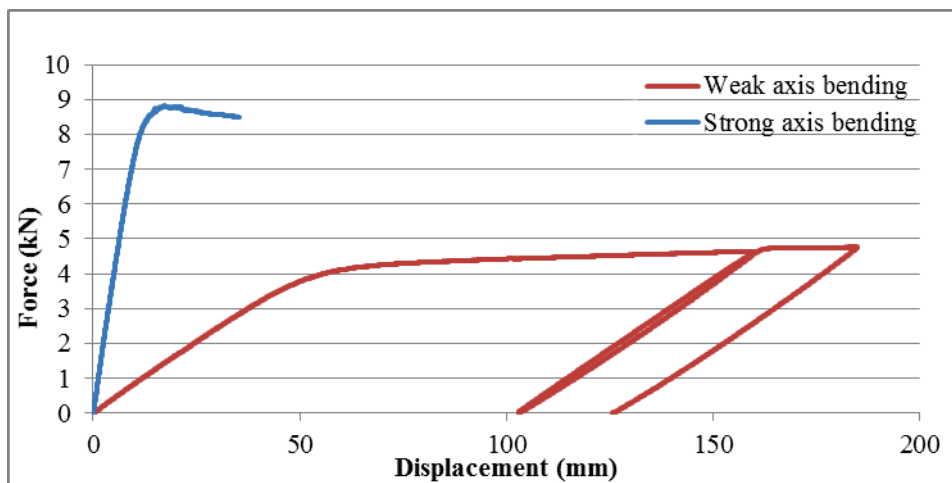
Figure 6. Force-displacement relationship.

When the results of the experiments are evaluated, it is worth mentioning that greater load bearing is achieved when the beam is oriented towards the strong axis which dictates lateral torsional behaviour and the failure mode is observed to be loss of strength. However, the configuration which allows bending around weak axis yields a significant ductility with a gradual increase in deformations without dramatic drop in the resisted loads. That behaviour is identified by pure flexure, whereas failure mode is characterized by large deflections.

Analytical and numerical study

A linear buckling analysis (LBA) was performed in order to determine the critical buckling load multiplier for the case of lateral torsional buckling. Consequently, the elastic critical moment was computed considering the force lever arm. For LBA (i.e. first order theory), an idealized model was considered, without any imperfections and the material having a perfectly elastic behaviour. The second type of analysis performed was the geometrically and materially nonlinear analysis with imperfections (GMNIA) which is a structural analysis method designed to verify the strength capacity of a structure. In terms of results obtained, GMNIA provides the force-displacement curve for the model analysed. Currently, GMNIA is considered to be the most sophisticated and prospectively the most accurate method of numerical buckling strength verification techniques.

FE model description

Using ANSYS finite element analysis commercial software, four 3D finite element models were created using shell elements to simulate the experimental setup. The models account material non-linearity by characterizing the material as elastic-perfectly plastic behaviour with a modulus of elasticity of E = 210 GPa and yield strength of f_y = 235 MPa. The models also account for geometric non- linearity by considering the large deformations during analysis, which is an analysis feature supported by ANSYS FE software. To simulate the pendulum post used in the test, a rotational spring with the same length as the pendulum was used to apply the load at the same point as per the experiment (Fig. 7).

| (a) | (b) |
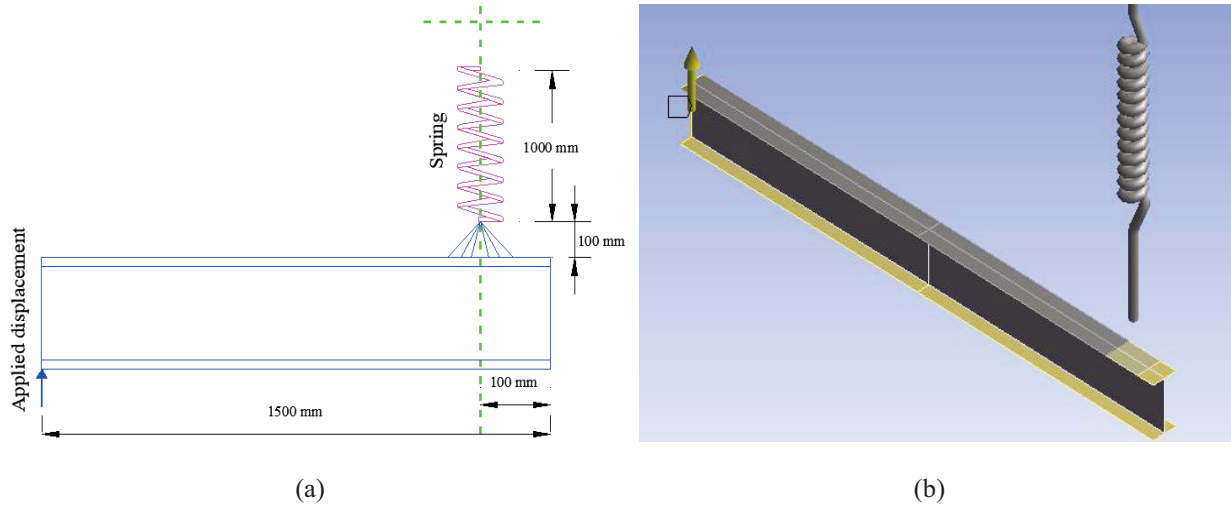
Figure 7. Schematic diagram of the FEA model: (a) geometric details; (b) ANSYS model.

A remote displacement was applied at the fixed end of the cantilever to simulate the fixation and the displacement control procedure used in the test. The spring elastic force was monitored to determine the capacity of the specimen.

Regarding the imperfections, the Eurocode 3 Part: 1-1 imposed a value of L/400 (3.75mm) to be used as a bow imperfection. Another value of L/200 (7.50mm), according to DIN 18800-2, was introduced for comparison. Eurocode is not clear about how to apply this imperfection to a cantilever beam; therefore two sets of imperfections were used as in Fig. 8.

| (a) | (b) |
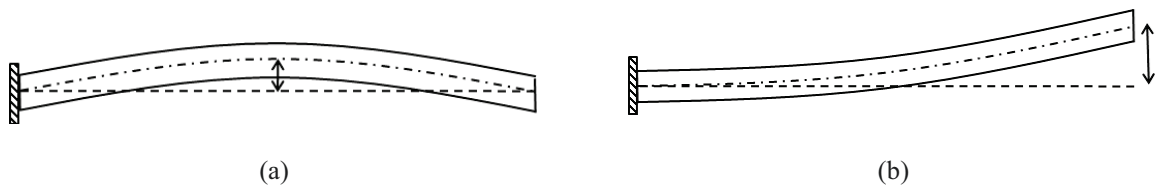
Figure 8. Bow imperfections: (a) full wave; (b) half wave.

FEA results of the strong axis loading

All finite element models have shown a clear lateral torsional buckling failure mode. The ratios between computed failure load and experimentally measured failure load have been summarized in Table 1.

Table 1. Summary of FEA model results

Imperfection	Failure Load (kN)	FEA/Experiment Ratio
L/400 full wave	8.649	0.982
L/400 half wave	8.658	0.983
L/200 full wave	7.977	0.905
L/200 half wave	8.422	0.956

The failure load for both models (the full wave and half wave modes respectively) are in a good correlation with the experimentally obtained values. Deformed shapes for each imperfection mode are presented in Fig. 9 and Fig. 10.

In order to properly validate the experiment, two ANSYS models were created using solids: the first one considering the full-wave bow imperfection and the second one including a half-wave bow imperfection. It may be observed that the value of bow imperfection, according to Eurocode 3 Part 1-1 and DIN 18800-2, has no major influence on the final Force-Displacement curve (Fig. 11).

The curves in Fig. 11 show that numerical models are somehow stiffer than the real experiment, due to the fact that, in reality, the process is influenced by many factors which are not considered in the ANSYS model such as actual stiffness of the hinges. Furthermore, the comparison can also be drawn between the experimental results and the numerical results considering the shell element models (Fig. 12). It can be seen that the distribution of the bow imperfection has only a small difference on the Force-Displacement curve.
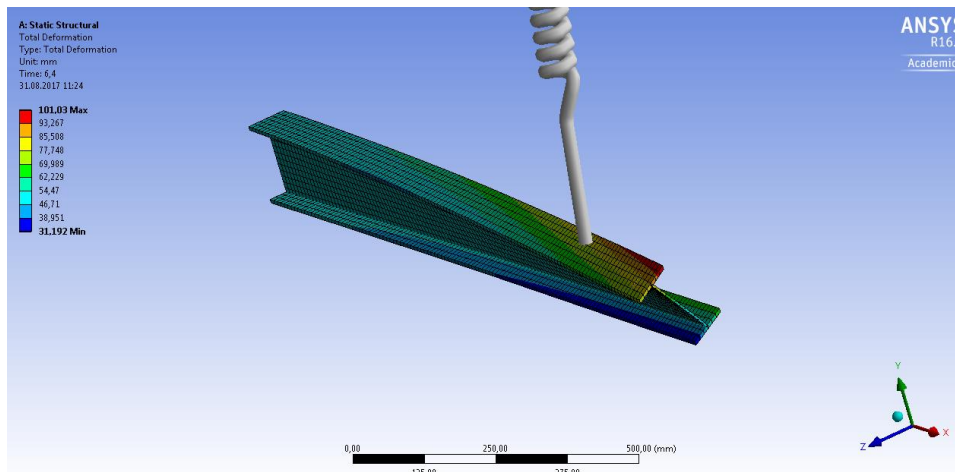
Figure 9. Deformed shape for full wave bow imperfection (L/400).
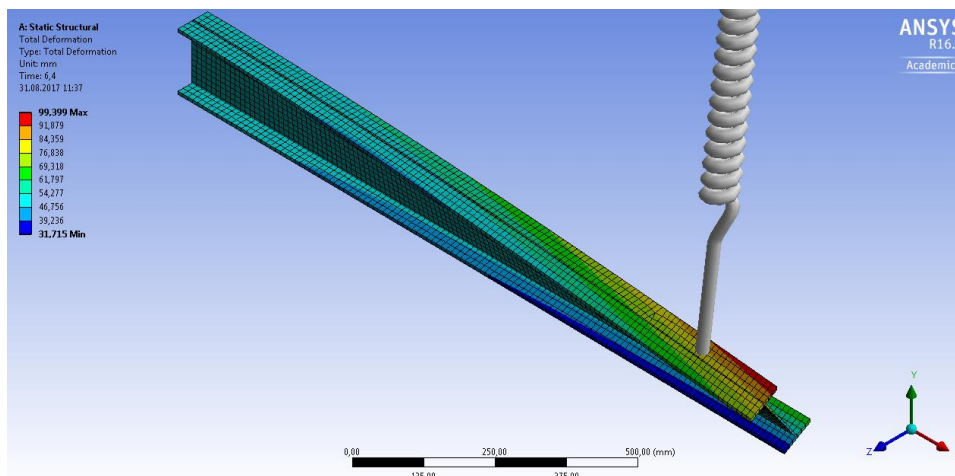
Figure 10. Deformed shape for half wave bow imperfection (L/400).
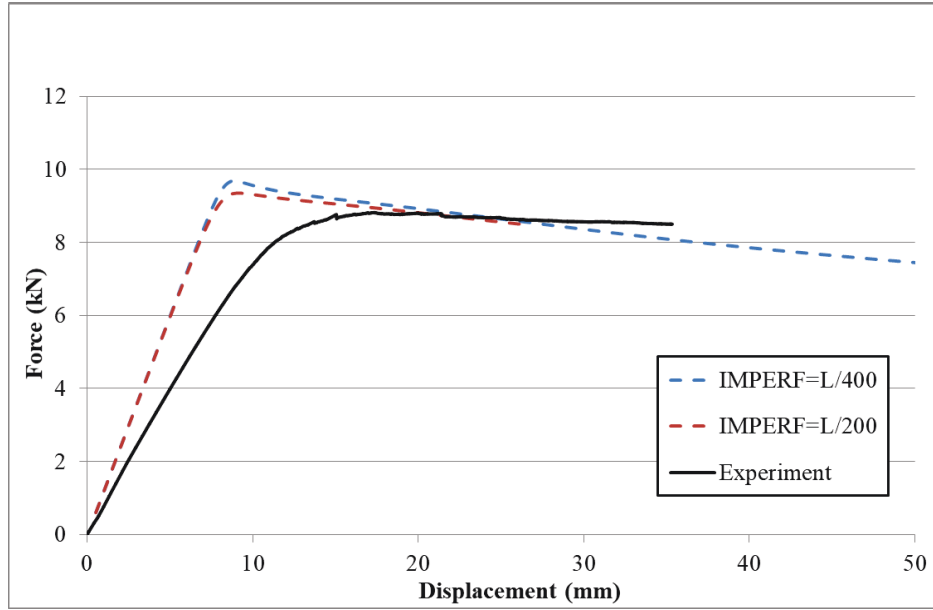
Figure 11. Force-Displacement curves for the experiment and two solid element models.

As far as the elastic critical moment is concerned, the shell element models slightly underestimate the capacity, when compared to the solid models.

Comparison between analytical and numerical procedures

For some of the most commonly used hot-rolled profiles, such as IPE, HEA and HEB sections, an analytical study was performed in terms of length (between 1.4 m and 4 m) and elastic critical moment M_{cr}. This was performed considering several approaches: NCCI – Elastic critical moment for lateral torsional buckling (Bureau and Galea 2005), relationship proposed in DIN 18800-2 2008, elastic buckling analysis performed in ANSYS FE solver (considering both shell and solid elements) and FE-STAB software (which uses the beam theory). Fig. 13 presents the outcome of the study just for three usual cross-sections. Nevertheless, the graphs for the other cross-sections lead to the same conclusions. The comparative study has been recapped in Fig. 13.
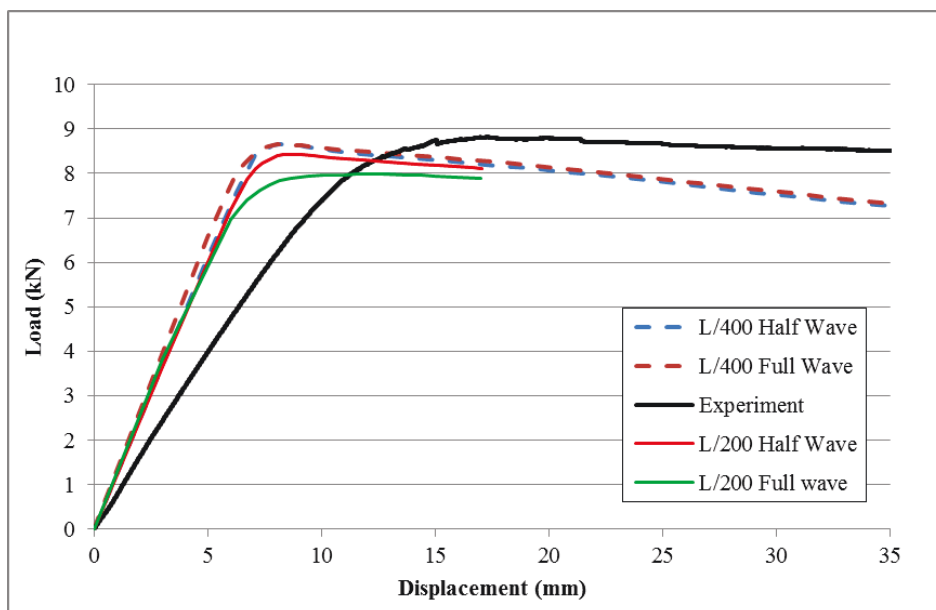
Figure 12. Load-Displacement curves for the experiment and four shell element models.
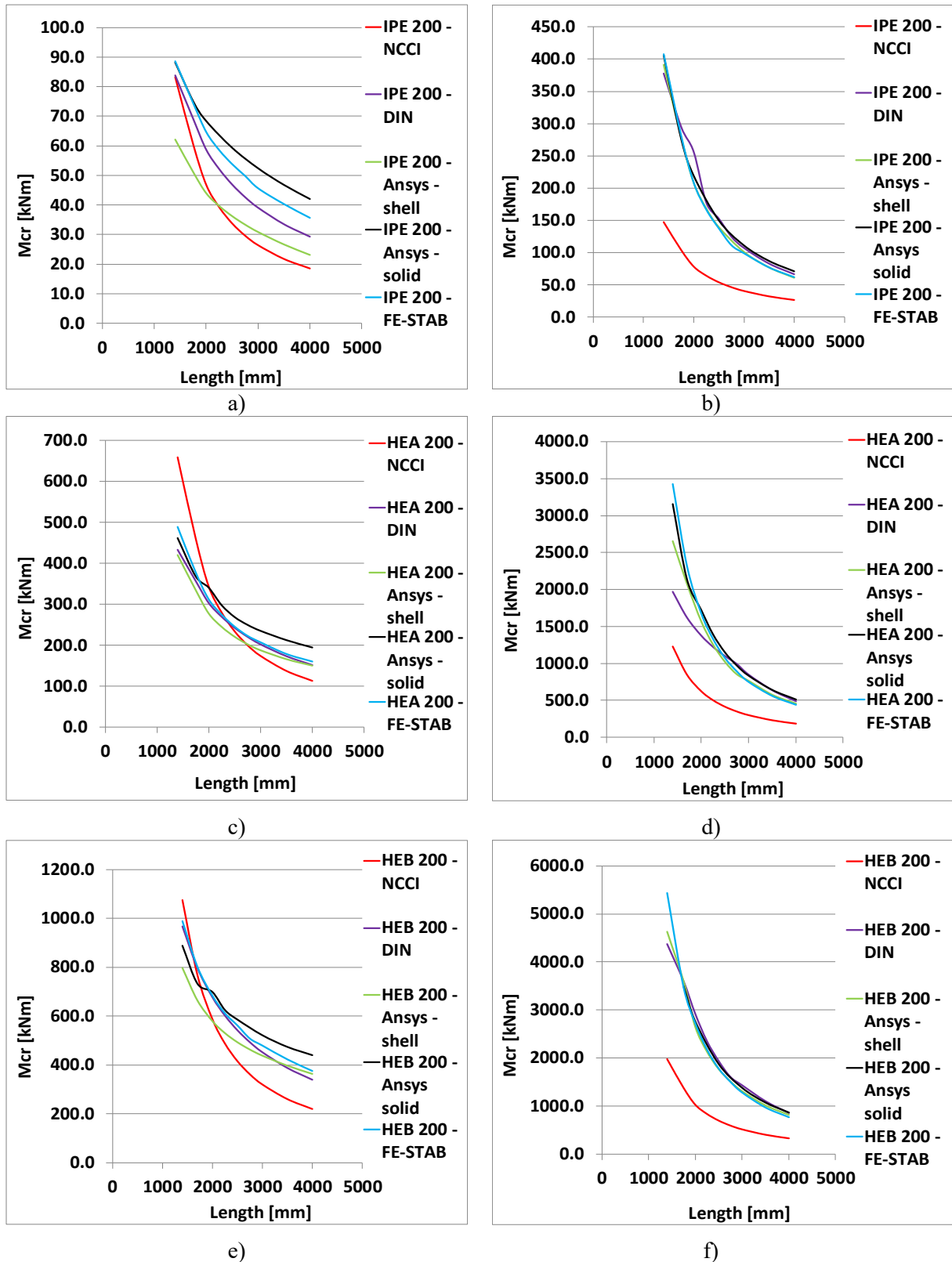
Figure 13. Results for different hot-rolled cross-sections in terms of span vs. elastic critical moment: (a) IPE, (c) HEA; (e) HEB with force at the top flange, (b) IPE; (d) HEA; (f) HEB with force at the bottom flange.

Validation of flexural experiment

In case of the strong axis bending (first experiment), the behaviour of the cantilever beam was governed by instability phenomenon (lateral-torsion buckling). On the contrary, failure occurred due to large deflections when the same element was loaded about the weak axis (pure flexural behaviour). In the first experiment, the cantilever remained only in the elastic domain, so the yielding strength was not a parameter that could influence the output. However in the second case, the yielding stress could be reached before instability problems. Therefore, a comparison between f_y of different steel grades and the actual behaviour could be drawn in order to observe the influence of different steel grades (Fig. 14).
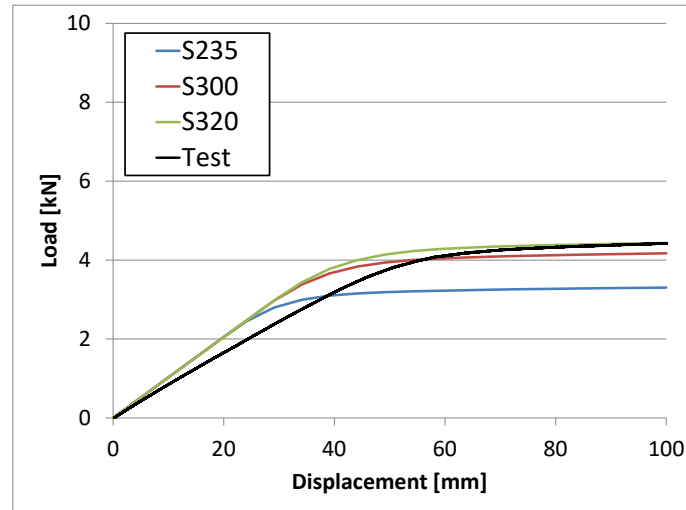
Figure 14. Experiment validation of the second beam considering the influence of the steel grade.

The bow imperfections do not have a major influence on the behaviour, which is therefore the main reason for the yielding strength becoming the governing parameter.
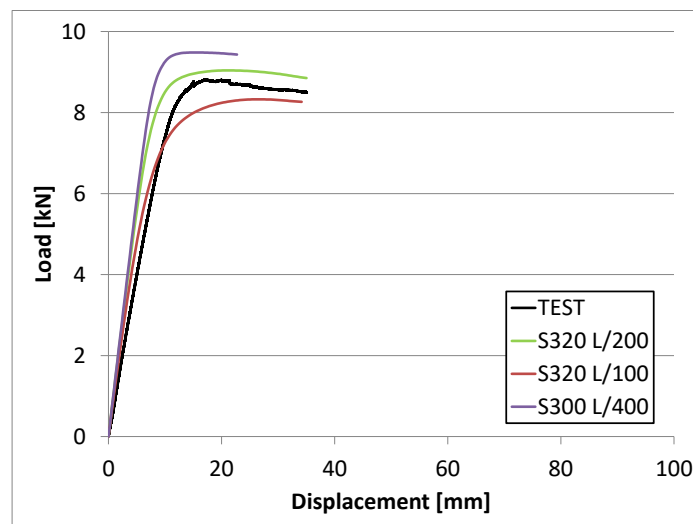
Figure 15. Experiment validation of the first specimen considering the influence of the imperfections.

Conclusions

Taking the outlined steps regarding the analyses into account, the following conclusions can be drawn:

- LBA using shell elements are not as compatible as solid elements to evaluate the flexural torsional buckling of cantilevers (due to the influence of flange-to-web chamfers)

- The procedure provided by NCCI – underestimates the buckling load (especially for the load on the bottom flange)

- The most reliable evaluation for lateral torsional behaviour can be done following the procedures according to DIN 18800-2, the software using beam theory (FE-STAB software) and numerical analyses using solid elements (ANSYS FE solver)

- GMNIA analysis could precisely predict the behaviour of the structure if appropriate calibrated and validated models are used

- The proposed FEA models can replicate the experimental test results accurately. Yet, additional material tests are recommended to clearly determine the mechanical properties. It is furthermore suggested to perform imperfection measurements

- Both modes of imperfections could be used to predict the cantilever beam capacity reasonably well

- The computed failure load decreases with the increase of imperfection magnitude (for stability induced failure)

Acknowledgements

References

ANSYS Inc. Version 16.2. (2015). Canonsburg, Pennsylvania, USA.

Bureau A., Galea Y. (2005). *Elastic critical moment for lateral torsional buckling.* Non-Contradictory Complementary Contribution (NCCI).

DIN 18800-1. (2008). Stahlbauten – *Teil 1: Bemessung und Konstruktion (Steel structures - Part 1: Design and construction).*

DIN 18800-2. (2008). Stahlbauten – *Teil 2: Stabilitätsfälle – Knicken von Stäben und Stabwerken (Steel structures - Part 2: Stability - Buckling of bars and skeletal structures).*

European Committee for Standardization (2006). *Eurocode 3: Design of steel structures – Part 1-1: General rules and rules for buildings*. CEN.

Kindmann R., Kraus M. (2011). *Steel structures – Design using FEM*. Wiley Online Library. DOI: 10.1002/9783433600771.

Kindmann R. (2014). *FE-STAB: Tragfähigkeit und Stabilität von Stäben bei zweiachsiger Biegung mit Normalkraft und Wölbkrafttorsion*. Ruhr-Universität Bochum.

LTBEAM Version 1.0.11. (2002). Centre Technique Industriel de la Construction Metalique (CTICM) and European Coal and Steel Community (ECSC).

Timoshenko S.P., Gere J.M. (1968). *Theory of elastic stability, 2nd edition*. McGraw-Hill.

Model-updating: Theory, Algorithms and Insights

ILLÉS Zsombor [a], PANTUSHEVA Mariya [b], RAYCHEVA Lora [b]
[a] Budapest University of Technology and Economics (BME)
[b] University of Architecture, Civil Engineering and Geodesy, Sofia (UACEG)

Abstract

We, engineers often rely on measured experimental data in order to calibrate numerical structural models and proceed with different numerical analysis of the investigated structure. Often, the problem of matching the experimental and numerical results in terms of structural displacements turns out to be misleading. Reason for this is the existence of correlation between the structural parameters, describing the overall structural performance and thus resulting in a non-unique solution. In order to approach the true solution some specific methods shall be applied.

As a part of the Bauhaus Summer School Forecast engineering course 2017, the authors of this paper have studied different Model-updating techniques. First of all, we have examined the equation of motion as free damped vibrations of a single degree of freedom (SDOF) system. Its analytical solution has been known for hundreds of years. But studied more closely, it is revealed that the main parameters are highly correlated. This results in lack of unique analytical solution of the problem which leaves us with an ill-posed problem.

The elaborated project considers two ways for solving the problem of the equation of motion - deterministic and stochastic. The main steps of these procedures are described in the current paper. Approaching the problem deterministically, we use Nelder-mead method and in order to overcome the non-uniqueness of the solution Tikhonov regularization is applied. As for the stochastical approach, we use the maximum likelihood and minimum error. In order to draw the whole probability distribution of the solution (the posterior), the probabilistic Bayesian updating and the Metropolis-Hastings algorithm are used. Methods for further optimization of the solution are also examined.

Introduction

Direct vs. Inverse Problems

Problems in general can be classified as direct problems or inverse problems. When causes lead to effects the problem is posed as a direct (forward) one and if the relation is reversed, then it is an inverse problem. The differentiation between direct and inverse problems is presented in Figure 1.
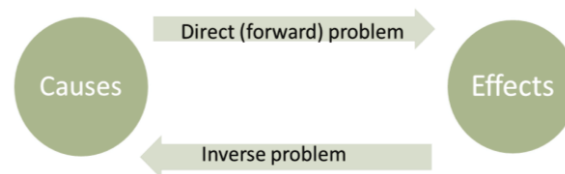
Figure 1. Direct vs. Inverse Problems.

An example of inverse problem is the analytical solution of the equation of motion - the algorithm starts with some prior information of the effects and after that an estimation of the uncertain parameters is made.

Most phenomena in mathematics, astronomy, physics, geodesy, remote sensing, machine learning, etc. are dependent on parameters that cannot be unequivocally identified. This fact makes solving inverse problems an important issue in every scientific field. In most cases the inverse problems are also ill-posed.

Well-posed vs. Ill-posed Problems

Any faced problem needs to be resolved. Prior to that, however, it is necessary to be clarified the essence of the problem. In order to search for the most suitable way to find a fitting solution, the problem should be identified either as well-posed or as an ill-posed one. Hadamard, 1902 suggests the following three criteria for well-posed problems:

- Existence: a solution to the problem exists;
- Uniqueness: there is maximum one solution to the problem;
- Stability: the solution depends continuously on the data.

If all or any of those criteria are not fulfilled the problem could be classified as an ill-posed one.

Equation of Motion. Definition of the Problem.

In order to be solved, ill-posed problems often need to be narrowed down by bringing up new assumptions or by reformulating the problem. This process is also referred to as regularization.

As a simple example let us consider the free vibration of a damped single degree of freedom (SDOF) system. It consists of a single concentrated mass, a spring and a damper each described accordingly by the parameters: mass (m), stiffness (k) and damping (c). The motion of the mass is allowed only along the spring elongation direction and may be expressed by the equation of a damped harmonic wave (1):

$$m\frac{d^2y}{dt^2} + c\frac{dy}{dt} + ky = 0 \tag{1}$$

where:

- the first argument presents the acceleration force, consistent of the multiplication of the vibrating mass (m) and the acceleration (d^2y/dt^2),
- the second argument is the damping force, that acts to dissipate energy by opposing motion, provided that dy/dt is the velocity and c is a positive constant describing the damping;
- the third component represents the spring force (also acting in direction opposite of the displacement), described by the stiffness (k) of the spring and the displacement of the mass (y).
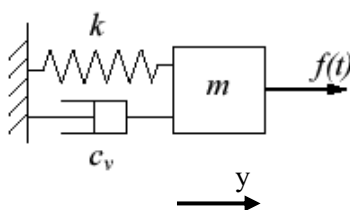
Figure 2. Damped SDOF System.

Approaches for Solving the Ill-Posed Problem

The problem of defining the law of motion for this system could be approached using one of the following:

- Analytical Solution or
- Numerical Solution.

Each of them uses different methods. The analytical solution usually requires integration of the equation and the numerical one uses deterministic or stochastic methods for approaching the results. Both methods for solving the ill-posed problem of the equation of motion are presented in detail in the current report, supported by an example, elaborated in MATLAB.
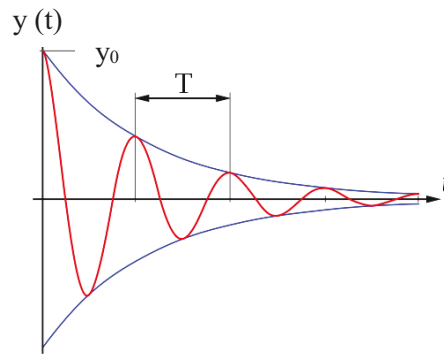
Figure 3. Damped SDOF System.

Analytical Solution

The analytical solution presents the solution of the differential equation for the damped harmonic wave in the following manner expressed by Figure 3 and Equation (2):

$$y(t) = y_0.e^{-\delta}.\sin(\omega t + \varphi_0) \tag{2}$$

where:

$$\delta = \frac{c}{m} \tag{3} \qquad\qquad \omega = \sqrt{\frac{k}{m} - \frac{c^2}{4m^2}} \tag{4}$$

The initial conditions are:

y_0 - initial amplitude;

φ_0 - initial phase of wave = 0.

In this particular case there is no driving force acting on the mass, the system vibrates under the initial displacement y_0 and the response is damped free. But taking into consideration only the initial conditions cannot lead to a unique solution regarding the unknown parameters m, c and k.

If we take a closer look into equations (3) and (4) it is visible that the parameters δ and ω are dependent on the relations k/m and c/m, and not on the three parameters independently. This means that changing the values for m, c and k gives the same results for the parameters δ and ω, each of them being a solution of the equation of motion. This phenomenon is illustrated by expression (5).

$$\frac{k}{m} = \frac{0.001}{0.002} = \frac{1}{2} = \frac{2}{4} = \frac{8000}{16000} \tag{5}$$

The non-uniqueness of the solution violates the second law of Hadamard and means that determining the characteristics m, c and k of a damped SDOF, given only the initial conditions is y_0 and φ_0 is an ill-posed problem.

Numerical Solution

Structural engineers and researchers often face difficulties with ill-posed problems. They usually rely on experimental data in order to calibrate numerical structural models and proceed with different numerical analysis of the investigated structure. Unfortunately, there is still the problem with the non-uniqueness of the solution and although the performance of the model matches the one obtained by experiments, the structural parameters turn out to be different. In order to obtain a reliable numerical model, the first step is the definition of the nature of the problem. The second step for using the numerical approach efficiently is to fulfil the requirements, presented in Figure 4.

The reliable forecast of the response of a structure requires:

| Reliable measurement data U^{meas} | Data from numerical model U^{model} (para) | Efficient parameter identification algorithm (Least Square) |
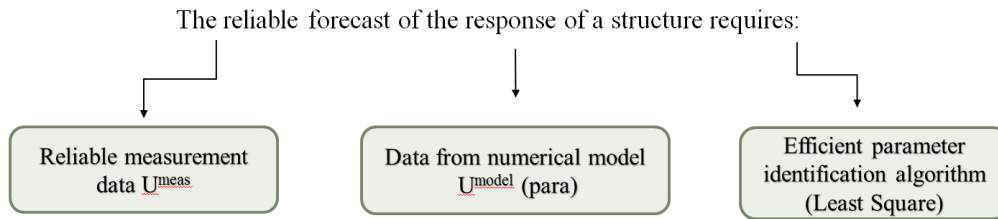
Figure 4. Numerical Solution Requirements.

The connection between the reliable measurements and the data from the numerical model could be described by the following expression:

$$U^{meas} = U^{model} + \varepsilon \tag{6}$$

And the error, which is the residual between measured data and the model, is expressed by equation 7.

$$\varepsilon = \left\| U^{meas} - U^{model}(para) \right\|_2 = \sum \left(U^{meas} - U^{model}(para) \right)^2 \tag{7}$$

The following paragraphs represent brief theoretical insight and implementation of two numerical approaches for solving ill-posed problems – deterministic and stochastic and some methods for regularization.

The presented examples are carried out by the authors of this paper as a part of their involvement in the project: "Model-updating: Theory, Algorithms and Insights", part of the Bauhaus Summer School 2017 Forecast Engineering course.

Deterministic Solution

Parameter Estimation

Parameter estimation (or data fitting) is a technique used for calibrating models by using sample data to estimate the unknown parameters describing the relative process.

Tikhonov Regularization

A deterministic solution can be provided in case all parameters that define the problem are identified in a manner that gives a unique solution. Parameter estimation or data fitting is an important issue in solving inverse problems. Let us say that there is a physical phenomenon described by a certain model. Assuming that a certain number of experiments are carried out and the observed quantities are measured, it would be found that due to measurement errors (called noise) those quantities would not be an exact match with the ones derived from the model. Therefore, the parameters should be sought in a manner so that the model fits the data from the experiments.

In solving such problems, the Tikhonov regularization could be used. It is a commonly applied technique for deterministic solution.

Let us consider the problem and the method of Tikhonov regularization, presented for clarity schematically in Figure 5.
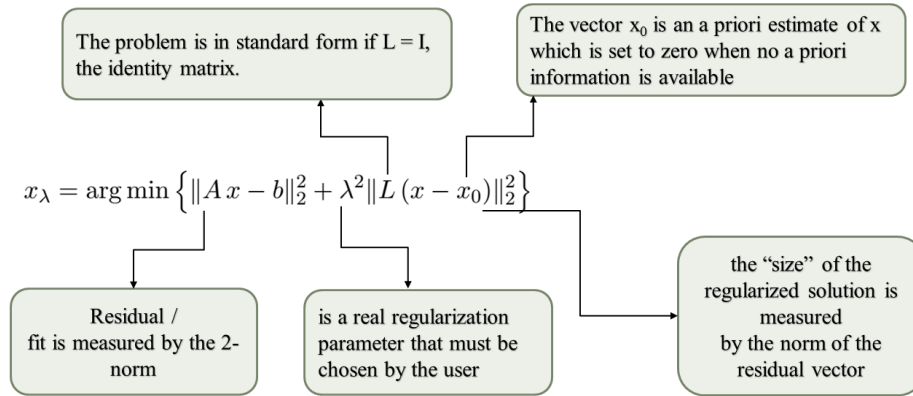
Figure 5. Tikhonov Regularization.
(Note: Definitions by *Hansen, 1999*)

A suitable way to solve the equation presented in figure 5 numerically is to treat it as a least square problem.

$$x_\lambda = \arg\min \left\| \begin{pmatrix} A \\ \lambda L \end{pmatrix} x - \begin{pmatrix} b \\ \lambda L x_0 \end{pmatrix} \right\|_2 \tag{8}$$

The residual represents the difference between an observed value and the fitted value provided by the model. The goal is to obtain a minimized sum of squared residuals, that would lead to the best fit in the least-squares. This method is suitable for approximate solution of overdetermined systems, but should be avoided if there are substantial uncertainties regarding the independent variable (*Hansen, 1999*).

The least square problems (residuals are linear) have a closed-form solution. Whereas the nonlinear least squares problems require an iterative approximation to a linear problem in order to be solved.

The importance of determination of the parameter of regularization λ is illustrated by Figure 6.
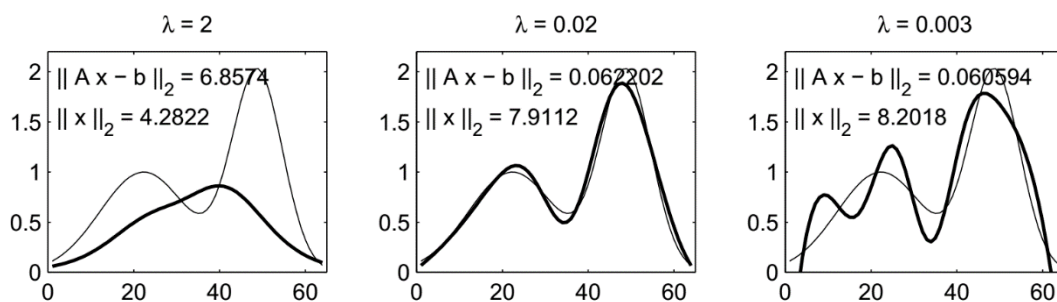
Figure 6. The exact solution (thin lines) and Tikhonov regularized solutions x, (thick lines) for three values of λ, corresponding to oversmoothing, appropriate smoothing, and under-smoothing (*Hansen, 1999*).

The balance in choosing this parameter is essential. Too much regularization leads to overestimated residual and too few regularization leads to a solution dominated by the contribution of errors. In both cases the solution does not fit properly the initial data.

The L-curve

The norms of the regularized solution and the residual are plotted vs. each other in a log-log plot form the L-curve presented in Figure 7.

The L-curve is a suitable graphic tool for determining the optimum value of the regularization parameter λ^2 that is represented by the area at the corner of the curve.
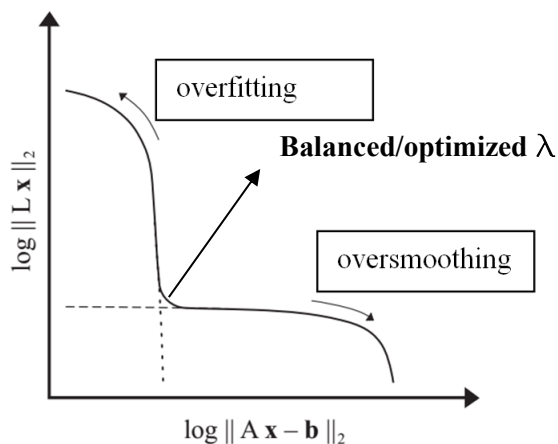
Figure 7. L – curve method.

Implementation of the Algorithms

The following paragraphs present the implementation of the deterministic approach and Tikhonov regularization for solving ill-posed problem of the equation of motion.

We received five set of measurements, u_{meas0}-u_{meas09}, the noise of the measurement was gradually decreased from u_{meas09} to u_{meas0}. Our calculations proved that the data set with less noise provided a better solution.

We had a prior knowledge of the solution [4.5 0.65 4.0] (stiffness, damping, mass). So first we ran our script only providing an input parameter for stiffness and mass as they are not dependent on each other. We used three pairs of values [2.5 0.3]; [4.0 0.45]; [10.0 0.8]. The idea was to see how convergence of the Nelder-mead method is affected by the starting value. Nelder-mead is a gradient free method implemented in MATLAB's *fminsearch* function.

On Figure 9 and 10 the results are presented of two different data sets u_{meas0} and u_{meas09}. In both cases we applied the same script with the same initial guess.

From Table 1 it is clear that if we use a measurement, which is affected by noise (measured data shown on Figure 10) the error will increase although the solution found by *fminsearch* function of MATLAB will be similar to the previous one.
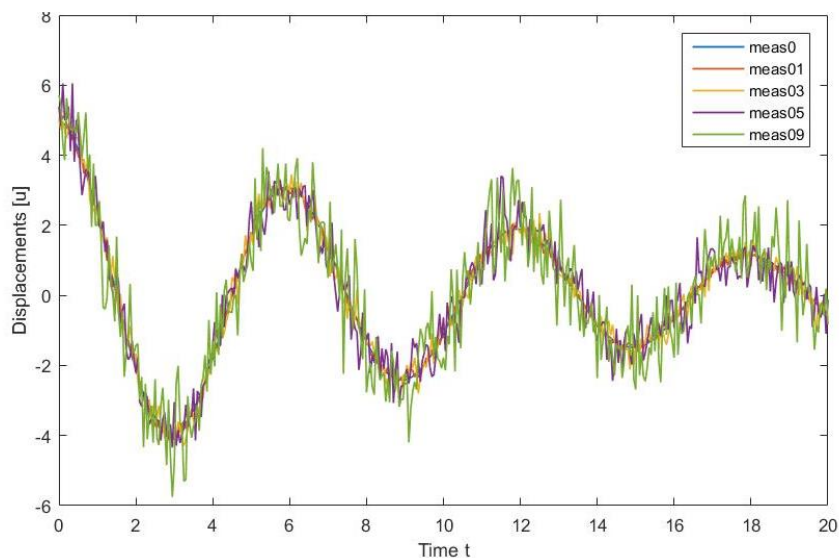
Figure 8. Harmonic oscillation (five set of measurements).
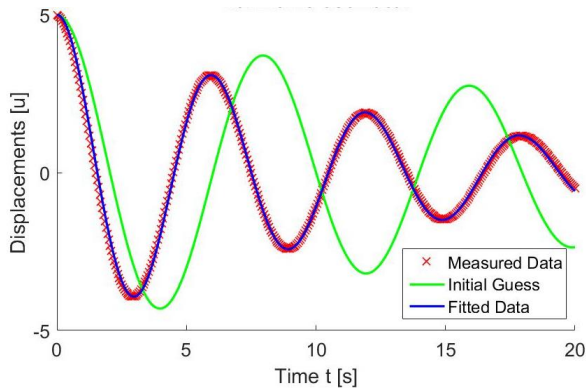
Figure 9. Harmonic oscillation u_{meas0}.
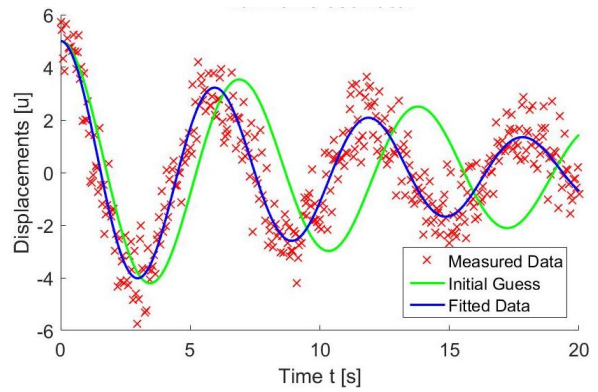
Figure 10. Harmonic oscillation u_{meas09}.

Table 1. Stiffness, damping and error on different set of measurements.

[2.5 0.3] u_{meas0}		[2.5 0.3] u_{meas09}	
k	4.4891	k	4.4967
c	0.6477	c	0.5884
fval (error)	1.9034	fval (error)	17.0316

To display that the problem is ill-posed, see the difference between the input of two and three parameters. The calculations were carried out on the same set of measurements umeas0, the one without noise. First, we defined stiffness and damping at later calculations mass was added to the input parameters as well.

From the solutions a conclusion can be drawn that if we only fix stiffness (k) and damping (c) we receive an answer much closer to the original one no matter how far our initial guess is. However, if we have an initial guess for all three parameters, the method might converge until some point, but it could be a local minimum and not the global one. The proportion of parameters k and c in both cases are equal.

In the analytic solution of the equation of motion there are three parameters - stiffness (k), damping (c) and mass (m) each of them are plotted against one another. For all three pairs, contour line and surface plots were created. First of all, the k-c contour line (Figure 13) and c-m surface plot (Figure 14) are presented. In both cases the plots show a unique solution of the problem.
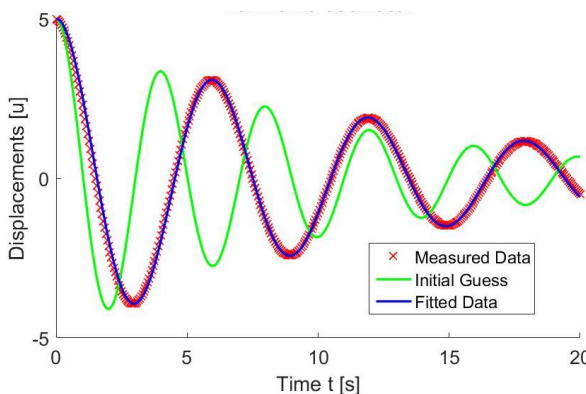
Figure 11. Harmonic oscillation u_{meas0}, [k,c].
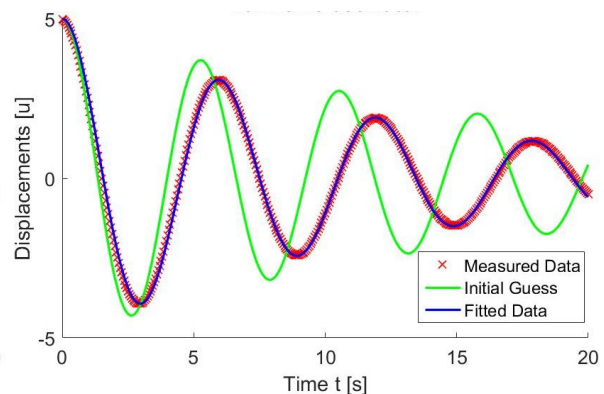
Figure 12. Harmonic oscillation u_{meas0}, [k,c,m].

Table 2. Stiffness, damping and mass error on different set of measurements.

[10.0 0.8] u_{meas0}		k/c	[10.0 0.8 7.0] u_{meas0}		k/c
k	4.4891	6.9308	k	6.7466	6.9310
c	0.6477		c	0.9734	
m	-		m	6.0116	
fval (error)	1.9034		fval (error)	1.9034	
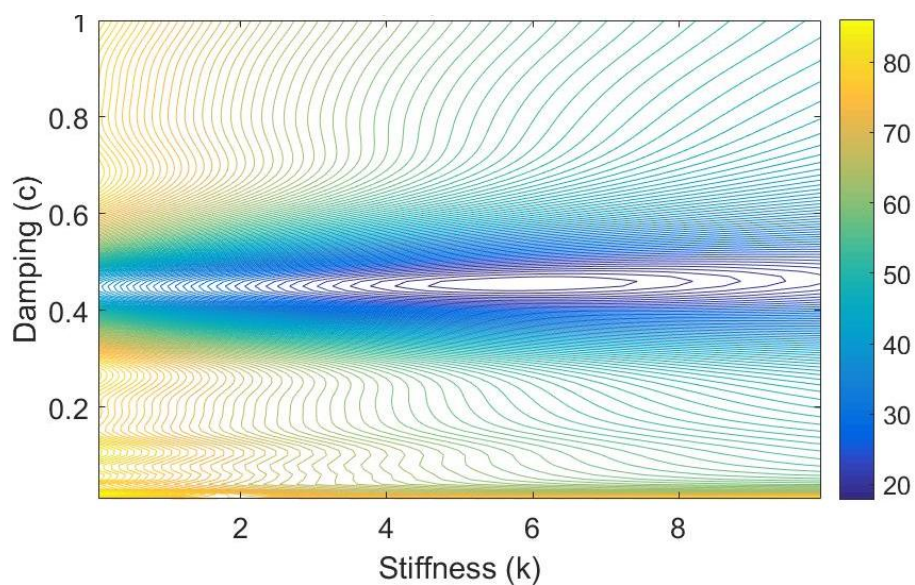
Figure 13. Contour lines of (k-c) Harmonic oscillation (m=4,0).
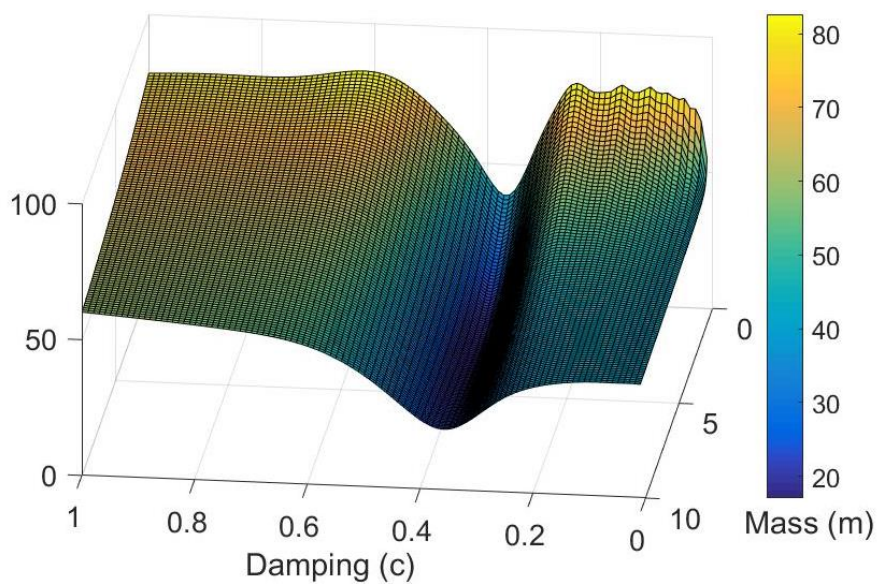
Figure 14. Surface plot of (c-m) Harmonic oscillation (k=4,0).

However, when stiffness and mass are plotted both the contour (Figure 15) and the surface plot (Figure 16) show the non-uniqueness of solutions.
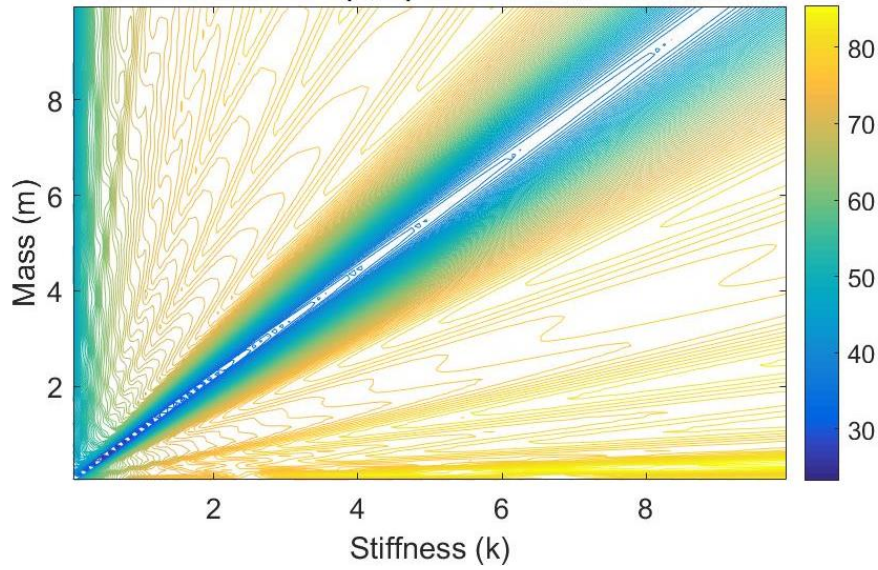
Figure 15. Contour lines of (k-m) Harmonic oscillation (c=0,5).
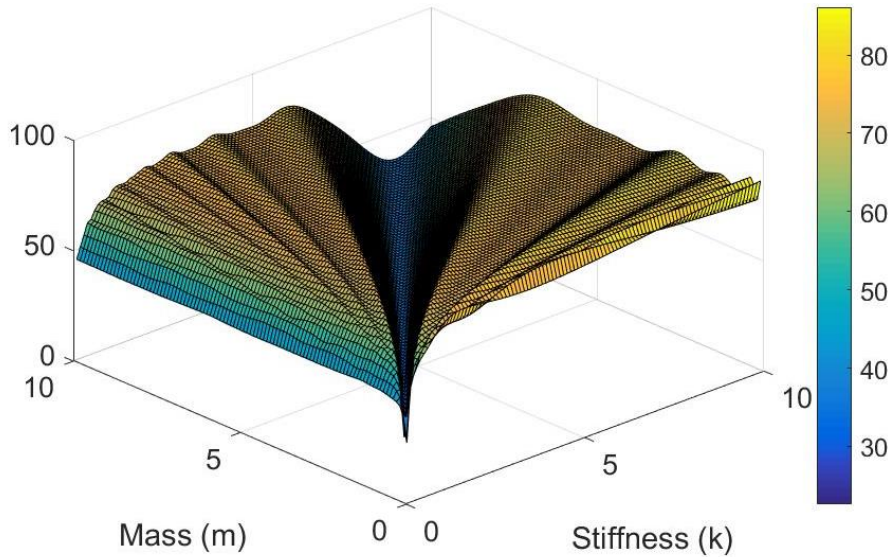
Figure 16. Surface plot of (k-m) Harmonic oscillation (c=0,5).

To overcome the non-uniqueness of the solution we used Tikhonov regularization. We implemented a regularisation factor B. The same plots are shown with the regularization factor of B=0.5. The contour lines have less local minimums, the surface plot of (k-m) became smoother (Figure 18). Table 3. shows the effect of B value. If the regularisation factor is too high, we receive our x0 prior as a solution. The error in all five cases are quite high, it is due to the use of data set, as we used the one with the most noise, u_{meas09}.
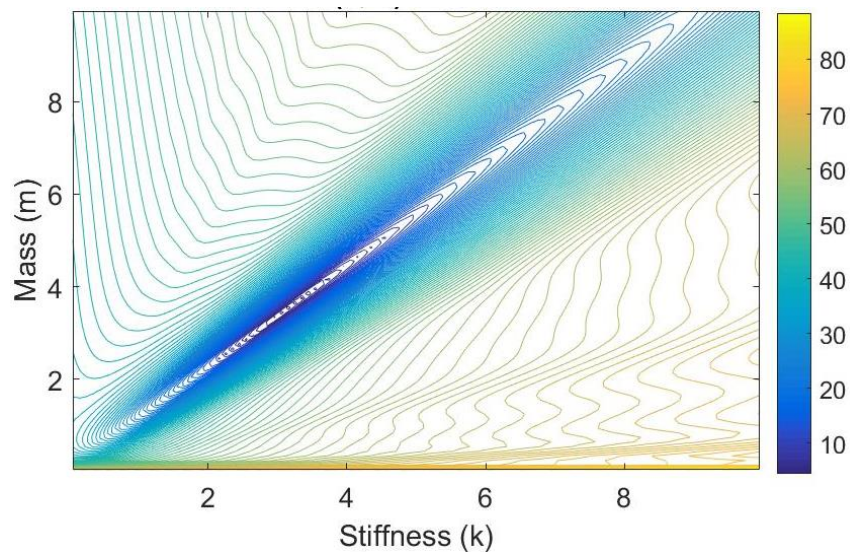
Figure 17. Contour lines of (k-m) Harmonic oscillation (c=0.5, B=0.5).
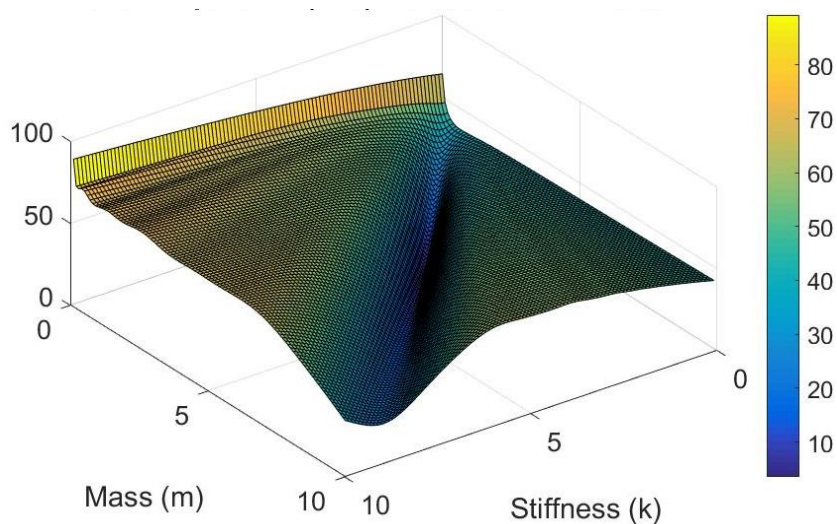
Figure 18. Surface plot of (k-m) Harmonic oscillation (c=0.5, B=0.5).

Table 3. Effect of B, Tikhonov regularization factor on the solution.

B	0.1	0.5	5.0	25.0	50.0
0	[3.0 0.35 4.0]	[3.0 0.35 4.0]	[3.0 0.35 4.0]	[3.0 0.35 4.0]	[3.0 0.35 4.0]
x0 prior	[3.5 0.3 4.0]	[3.5 0.3 4.0]	[3.5 0.3 4.0]	[3.5 0.3 4.0]	[3.5 0.3 4.0]
k	4.6318	4.6309	4.6215	4.5623	3.00
c	0.6059	0.6049	0.5961	0.5921	0.30
m	4.1210	4.1237	4.1530	4.3034	6.00
fval (error)	17.2824	18.2848	29.49	77.6179	67.2466

Stochastic Solution

Another approach for dealing with ill-posed problems is through stochastic methods for determination of the closest to the real solution. In comparison to the deterministic approach, the stochastic one includes the uncertainty in the parameters which requires some probabilistic evaluation of the distribution of the parameters of interest. Concerning this matter all the parameters and observations must be expressed by their statistical distribution. Usually the normal Gaussian distribution is used (*normpdf* function used in MATLAB). This is also the case in the current project. For information about other standard probability distributions the reader is kindly referred to Gelman et al. 2013.

Maximizing the Likelihood (ML)

First approach for solving the problem in stochastic way is to maximize the likelihood for a parameter to be one of the closest to real solution with least residual. This might be associated with the least square solution concerning the deterministic approach. The solution is the maximum considered probability as a mean value of the multivariate normal distribution (Figure 19).

General expression of the ill-posed problem that is investigated in the current project is given by eq. (9):

$$d = G(m) + \varepsilon, \tag{9}$$

where:

$d = \{d_1, d_2, \ldots, d_k\}^T$ is the set of observations or measures; the values of this vector are independent;

$m = \{m_1, m_2, \ldots, m_k\}^T$ is the vector of model parameters;

k is the number of parameters in the model;

ε is the noise of measurements;

$G(m)$ are the model observations in relation with the parameters;
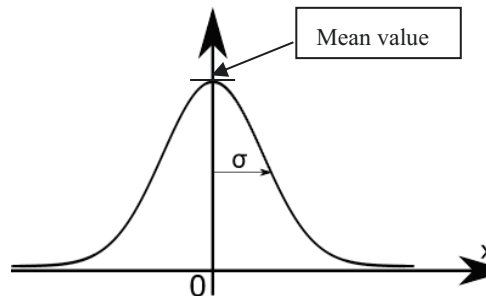
Figure 19. Normal Gaussian distribution.

Considering that the observed data (d_i) are normally distributed, the normal distribution of the likelihood is given by eq. (10):

$$L(m \mid d) = \frac{1}{\prod_{i=1}^{k} \sigma_i \left(\sqrt{2\pi}\right)^k} e^{-\sum_{i=1}^{k} \frac{(G(m_i)-d_i)^2}{2\sigma_i^2}} \tag{10}$$

Also considering that the components of each observation d are uncorrelated, the likelihood is expressed by eq. (11):

$$L(m \mid d) = \frac{1}{2\pi^{\frac{1}{2}} \sqrt{|C|}} e^{-\frac{1}{2}(G(m)-d)^T (C)^{-1}(G(m)-d)} \tag{11}$$

Eq. (11) represents the probability density function of the *k*-dimensional multivariate normal distribution (*mvnpdf* function used in MATLAB) and can be regarded as a generalization of the univariate normal to *k* variables. This is a distribution for random vectors of correlated variables, each element of which has a univariate normal distribution.

The multivariate normal distribution is parameterized with a mean vector (the mean of the parameters) and a covariance matrix **C** of the observations *d* (eq. (12)). These are analogous to the mean value and the standard deviation σ of a univariate normal distribution.

$$C = \begin{pmatrix} C_{11} & & & \\ & C_{22} & 0 & \\ 0 & & .... & \\ & & & C_{nn} \end{pmatrix}_{nxn} \tag{12}$$

The diagonal elements of the covariance matrix **C**, $C_{ii}=(\sigma_i)^2$ are the covariance of each component. It is evident that the solution is quite sensitive to the selection of the standard deviation σ.

In order to evaluate the mean value of the parameters, the maximum of likelihood multivariate distribution must be assessed. After some transformation of expression (10) and presenting it in log format, equation (13) is defined:

$$\min \ log \ L = \min\left(-\frac{1}{2}\frac{(G-d_i)^2}{\sigma_i^2} \right) \tag{13}$$

The resultant eq. (13) defines a concave function. In order to assess the maximum of likelihood, the minimum of the lognorm likelihood must be evaluated. The right side of eq. (13) gives a negative constant multiplied by the weighted least square using a pre-defined standard deviation of the normal distribution of each parameter. The condition for evaluating the maximum likelihood and the minimum error, respectively, can be expressed by eq. (14):

$$\max \frac{(G-d_i)^2}{\sigma_i^2} = \min(error) , \tag{14}$$

This approach does not solve the problem with the non-uniqueness of the solution. It gives the mean value but does not take into account the possibility that the resultant value may be just a local solution. In order to give concern to the nature of the ill-posed problem some methods for regularization of the solution are proposed and presented in the following points.

Bayesian updating

In order to draw the whole distribution of the posterior the Bayesian updating was used. Bayesian approach is based on Bayes' rule (eq. (15)) that describes the probability of an event, based on prior knowledge of conditions related to the event. This is the so-called 'prior', expressed as a normal distribution in this report. The results are also evaluated in means of a probability distribution ('posterior').

$$P(A \mid B) = \frac{P(B \mid A)P(A)}{P(B)} , \tag{15}$$

where:

P(A|B) is a conditional probability of event A when event B has happened with the assumption that *P(B)* $\neq 0$;

Expressed in terms of the ill-posed problem that is investigated, eq. (15) is presented as eq. (16):

$$q(m \mid d) = \frac{\left(f(d \mid m) p(m)\right)}{\left(p(d)\right)}, \tag{16}$$

where:

$p(m)$ is the prior;

$p(d)$ is the evidence;

$f(d|m)$ is the likelihood;

$q(d|m)$ is the posterior;

Accepting that the evidence $p(d)$ are constant, they may be presented by a constant c (eq. (17)). After the subsequent transformation of eq. (16), eq. (18) is derived:

$$c = \int f(d \mid m) p(m) dm \tag{17}$$

$$q(m \mid d) \propto \left(f(d \mid m) p(m)\right), \tag{18}$$

In other words, eq. (18) defines the posterior as a multiplication of the likelihood and the prior distribution. The result is expressed as multivariate distribution.

Having an inverse problem, we should expect that the stochastic solution would be an iterative process. It includes definition of the mean value of the posterior distribution for each of the parameters that gives the resultant vector. After evaluation of the error, the posterior vector may be taken as a prior and the whole Bayesian regularization process may be repeated until achievement of the most optimized solution.

More information regarding the Bayesian approach to inverse problems, the reader may find in Gelman et al. 2013 and Idier 1999.

Some additional methods for optimization of the solution are suggested in order to approach the real solution. One possible approach is integration of the posterior but it is much time-consuming. In this regard, the Monte Carlo Markov Chains (MCMC) method is used.

Sampling from the posterior. Monte Carlo Markov Chains (MCMC) method

This method for optimization is a random method. It includes sampling from the posterior and accepting and rejecting samples with respect to the comparison of probability. In order to apply the MCMC method, the Metropolis-Hastings (M-H) Algorithm is used. Figure 20 and Figure 21 illustrate the main principles of the algorithm.

The Metropolis-Hastings (M-H) Algorithm relies on rejection or acceptance of samples that are compared with a prime point from the posterior. If the possibility of the candidate point is higher than the possibility of the prime point, the candidate is accepted. Otherwise, taking into account the fact that the posterior may not be a smooth function, rejection of the point is considered conservative.
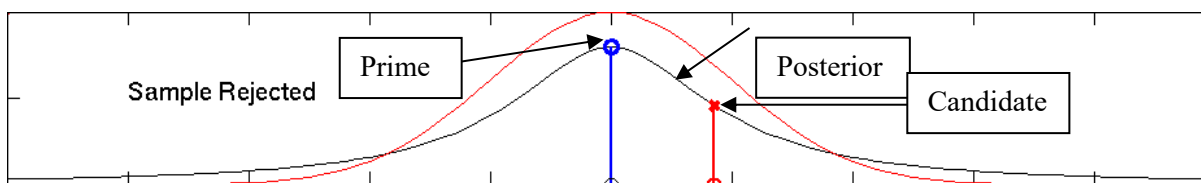
Figure 20. Metropolis-Hastings (M-H) Algorithm.
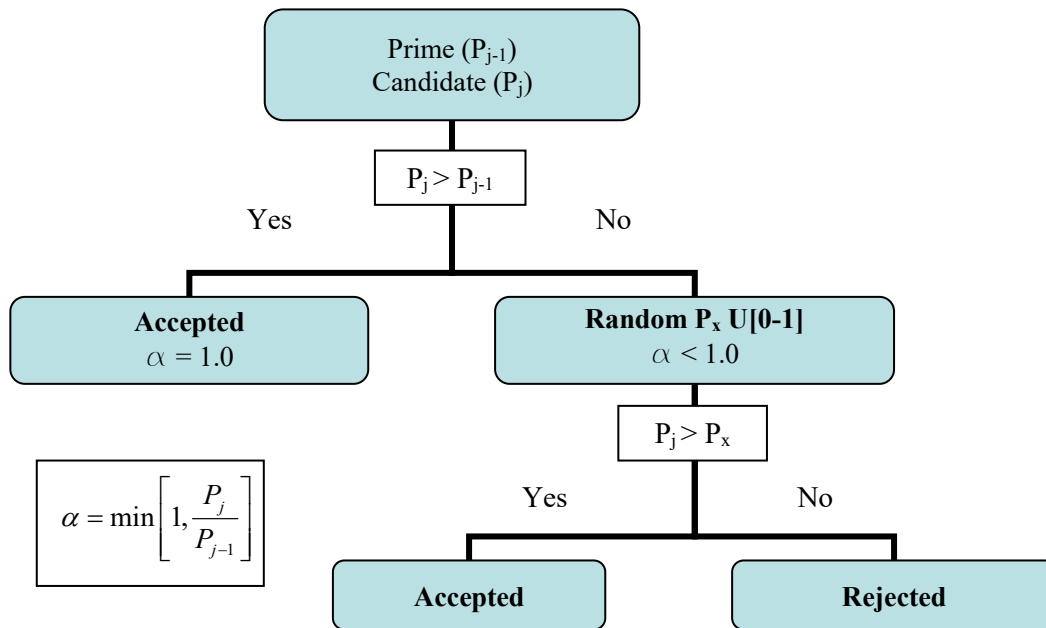
Figure 21 Acceptance and rejection of samples by Metropolis-Hastings (M-H) Algorithm.

In order to achieve convergence of the solution when $P_j < P_{j-1}$, the random process is activated. It consists of random selection of a sample from the posterior with probability (P_x), comparison with the probability of the candidate (P_j) and acceptance/rejection of the candidate. For more information, refer to Green et al. 2015.

Implementation of the stochastic method

Building the Prior

The given ill-posed problem is treated by means of stochastic methods and regularization. The prior information is presented as normal distribution of each of the parameters (k, c, m) of the examined equation of motion. Figure 22 illustrates the priors' distribution.
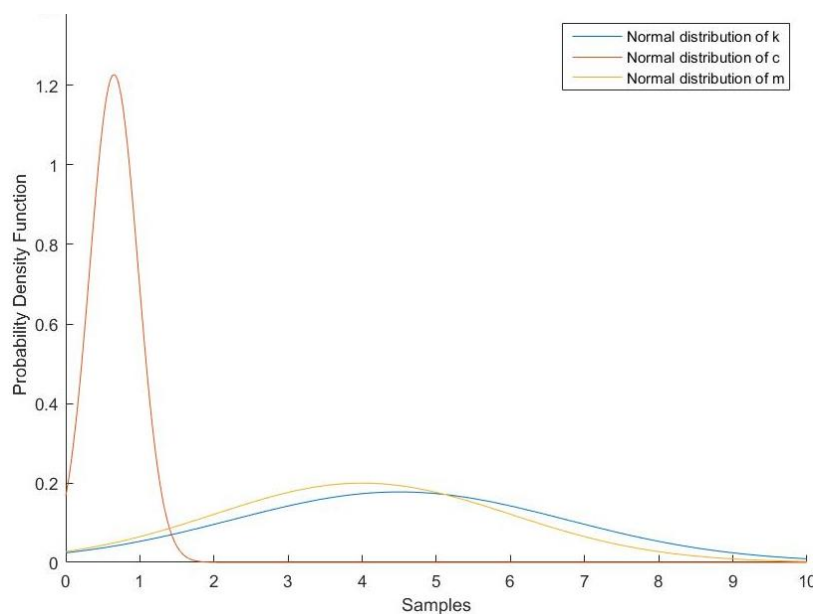
Figure 22 Priors' probability normal distribution (k, c, m).

Maximizing the Likelihood

The report treats only the first iteration of the stochastic solution in detail. It takes into account 8000 samples. After performing the Bayesian regularization, the plot of the maximized likelihood and the values of each of the parameters for the whole set of samples is illustrated in Figure 23.
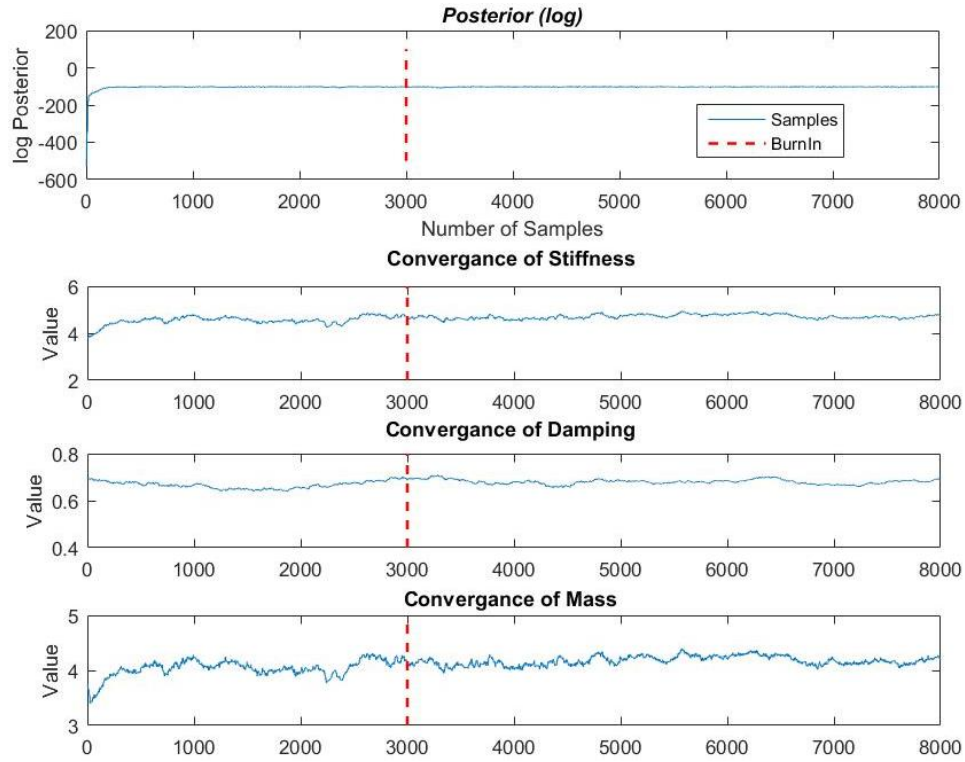
Figure 23 Plot of the posterior and parameters (Definition of Burn-In optimization).

It may be observed from Figure 23, that after a specific limit the posterior and the parameters fluctuate around a relatively constant value. This is the so-called "Burn-In" value. In this specific project, at the first iteration, the defined Burn-In is 3000. This is an optimization approach by which from the posterior are excluded the samples with high probability. The final solution from the first iteration is taken as a vector of the mean values of the samples after the Burn-In process.
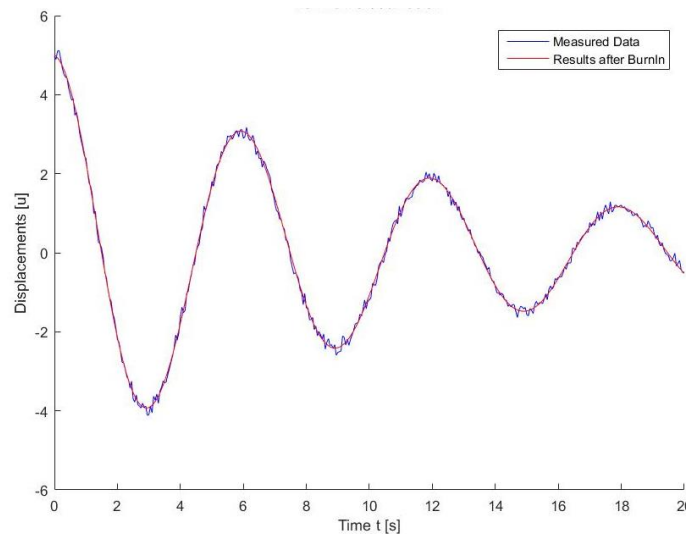
Figure 24 Harmonic function of measured data and results after Burn-In optimization.

Table 4. Comparison of the true solution and Bayesian solution after Burn-In optimization.

	k	c	m
Bayesian 1st iteration	4.71	0.68	4.18
Real solution	4.50	0.65	4.00
Difference, %	**4.47**	**4.47**	**4.31**

Burn-In optimization

Figure 24 illustrates the comparison between the harmonic function of the measured data with relatively high noise and the harmonic function with the mean values of parameters after Burn-In. The good match between the two functions is visible. Furthermore, the numerical difference between the real solution and the Bayesian solution with Burn-In is given in Table 4.

It is evident from Table 4 that the adopted Bayesian updating and Burn-In optimization leads to very low errors between the real and numerical solution with difference lower than 5% even at the first iteration of the solution. Undoubtedly, the precision of the numerical solution and the number of iterations needed is related to the precision of the prior information.

If a matrix plot of the samples after the Bayesian update and Burn-In is performed, one can notice that the scatter plot of mass related to stiffness converges to a line. So these two parameters are highly correlated, which proves the non-uniqueness of the solution. The relation between k and m was previously remarked when the ill-posed problem of the equation of motion was formulated. The scatter plot of k in relation to c indicates less of correlation between these parameters.

The same conclusions can be made from the resultant correlation coefficient matrix. Correlation coefficient between m and k is close to 1,0, indicating high correlation between these parameters. The observed linear relation between the parameters proves that the problem is inverse, ill-posed with non-unique solution.
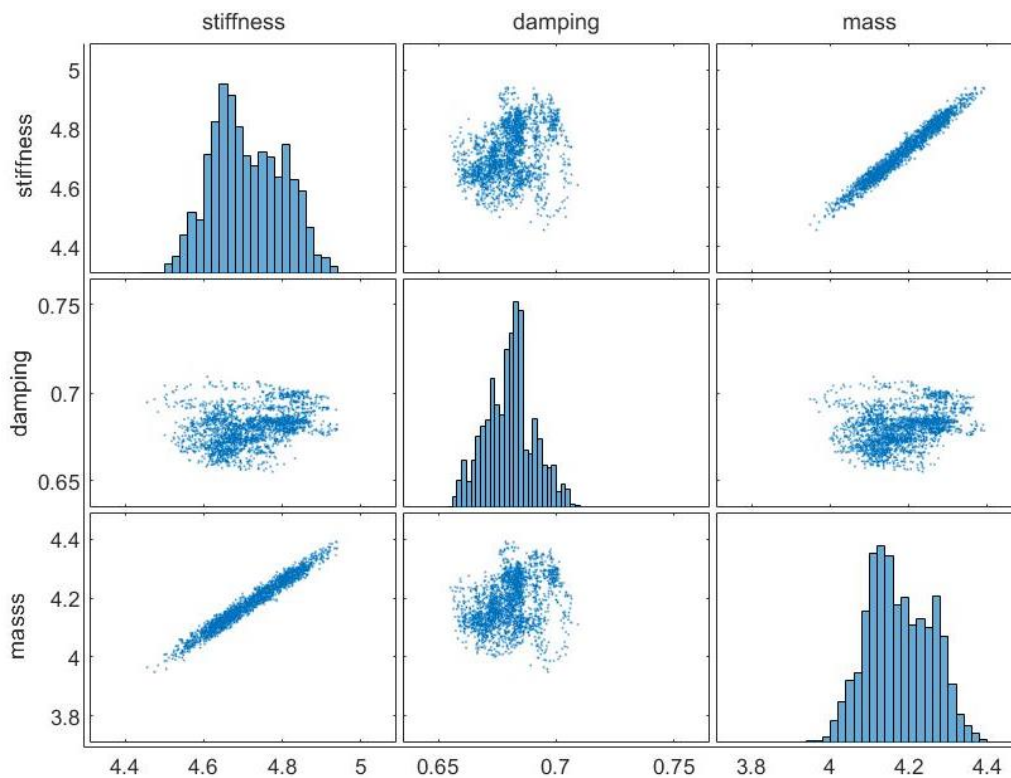
Figure 25 Matrix plot of samples after Burn-In optimization.

Table 5. Correlation coefficient matrix.

	k	c	m
k	1.000	0.261	**0.983**
c	0.261	1.000	0.237
m	**0.983**	0.237	1.000

a) Stiffness, k

b) Damping, c
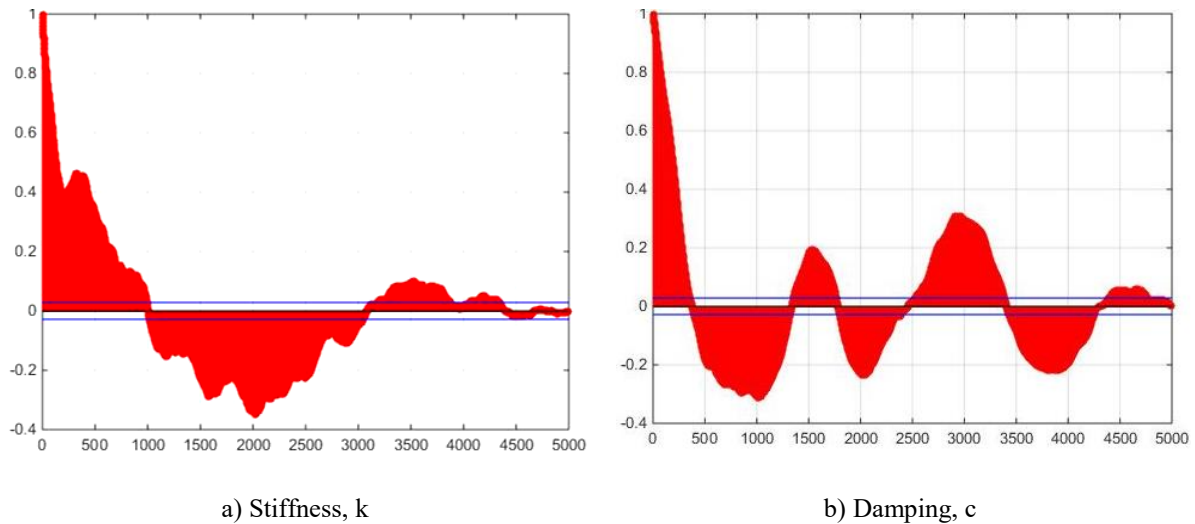
Figure 26 Autocorrelation of parameters.

Autocorrelation

Another approach for optimizing the solution is the evaluation of the autocorrelation of the resultant parameters. Figure 26 illustrates the autocorrelation for the parameters stiffness (k) and damping (c) after the Bayesian updating. The autocorrelation represents a plot of the ratio between the resultant value of the parameter for the first sample and the value of the parameter for each sample from the selected set of samples.

In order to reduce the autocorrelation of the parameters and thus approach the unique solution, another sort of optimization may be applied by making samples from the autocorrelation plots. For other iterative methods for optimization the reader is referred to Kelley et al. 1999.

Conclusion

Major concern of ill-posed problems is the lack of unique solution due to high relation between some of the parameters. The elaborated project 5 of the Forecast Engineering course, Bauhaus Summer School 2017 treated the equation of motion and defined it as an ill-posed problem with high correlation between some of the parameters. In order to cope with the problem an inverse approach must be applied. The solution requires some prior information that is taken as initial guess. By deterministic and/or stochastic approaches it is regularized, leading to smoother resultant function and reduction of the non-uniqueness of the solution. Some advantages of the stochastic solution over the deterministic one are denoted – the inclusion of the uncertainty in parameters and the expression of results as multivariate distributions. The applied regularization methods for ill-posed problems find vast application in calibration of numerical models (model updating) to experimental observations and thus increase the credibility of numerical investigations. Furthermore, those methods can be used basically in any science filed for parameter identification, model selection and averaging.

Acknowledgements

The authors of this paper would like to express their gratitude to Muyiwa Alalade, Feras Alkam, PhD students of the Bauhaus-University of Weimar and Prof. Dr. Tom Lahmer. Without their guidance, help and support the authors would not have gotten an insight of the essence of this contemporary problem, the approaches for its solution and their numerical implementation.

Furthermore, the authors would also like to acknowledge with much appreciation the crucial role of the Bauhaus Summer School staff and especially to Dr.-Ing. Lars Abrahamczyk for the warm hospitality, the provision of advanced projects and lectures on crucial scientific problems in the field of engineering and last but not least, the precise organization that made our stay in Weimar fruitful and pleasant.

References

Alalade M., Nguyen-Tuan L., Wuttke F., Lahmer T. (2018): Damage identification in gravity dams using dynamic coupled hydro-mechanical XFEM, *International Journal of Mechanics and Materials in Design*, Vol. 14(1): pp 157-175.

Alalade M., Kafle B., Wuttke F., Lahmer T. (2016): Inverse analysis of cyclic constitutive models for unsaturated soil under consideration of oscillating functions, *in E3S Web of Conferences*, vol. 9, EDP Sciences, p. 08012.

Aster R., Borchers B., Thurber C. (2005): Parameter estimation and inverse problems, *Elsevier, second edition*

Brownjohn J. (2005): Single degree of freedom (SDOF) systems, University of Plymouth.

Ching J., Chen Y.-C. (2007): Transitional markov chain monte carlo method for bayesian model updating, model class selection, and model averaging, *Journal of engineering mechanics*, 133, pp. 816–832.

Gelman A., Carlin J., Stern H., Rubin D. (2014): Bayesian data analysis, vol. 2, *Chapman & Hall/CRC Boca Raton*, FL, USA, third edition ed.

Green P., Worden K. (2015): Bayesian and markov chain monte carlo methods for identifying nonlinear systems in the presence of uncertainty, *Phil. Trans. R. Soc. A, 373*, p. 20140405.

Hadamard J. (1902): Sur les problèmes aux dérivées partielles et leur signification physique. Princeton University Bulletin. pp. 49–52.

Hansen Per C. (1999): The L-curve and its use in the numerical treatment of inverse problems. *IMM, Department of Mathematical Modelling, Technical University of Denmark*.

Idier J. (1999): Bayesian approach to inverse problems, John Wiley & Sons, 2013 Kelley, Carl T.: Iterative methods for optimization. *SIAM*.

Kelley Carl T. (1999): Iterative methods for optimization. *SIAM*

Mathworks Inc.: Matlab 2012b., Natick, USA.

Tarantola A. (2005): Inverse problem theory and methods for model parameter estima-tion. *SIAM*.
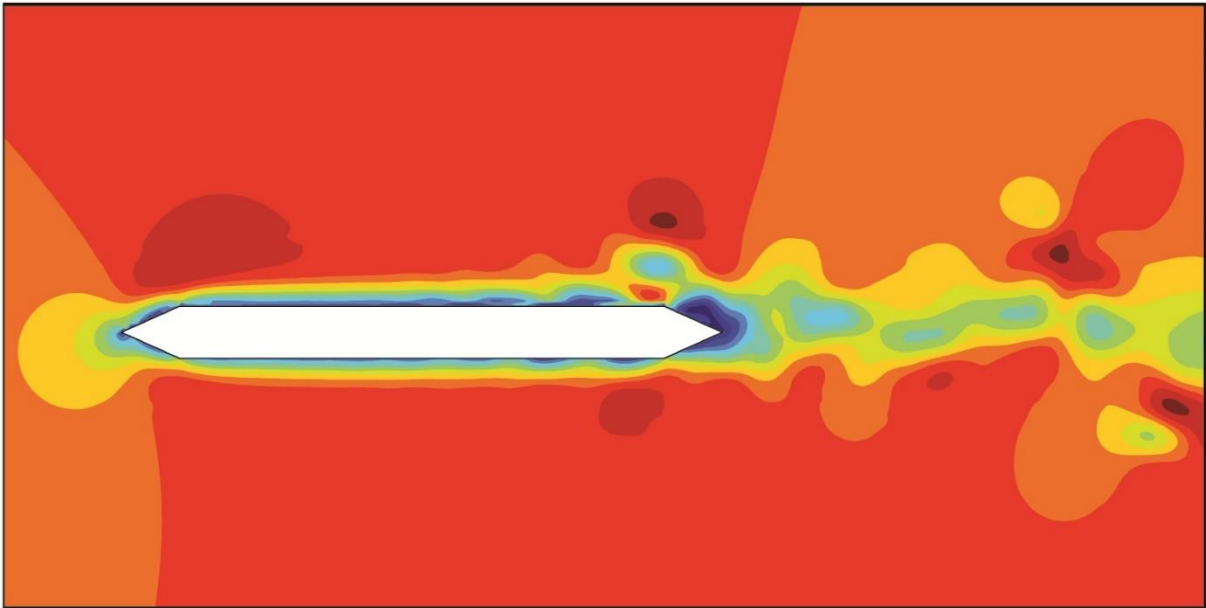
Wind-induced vibrations of long-span bridges

MORGENTHAL Guido

Chair of Modelling and Simulation of Structures, Bauhaus-Universität Weimar, Germany

The project deals with the structural modelling and dynamic analysis of long-span cable-supported bridges under wind excitation. In three sub-groups the participants of the project are trained within the:

- Numerical modelling techniques for long-span cable-supported bridges;
- Simulation of dynamic structural behaviour;
- Models for Predicting Wind-induced Vibrations of Long-span Bridges;
- Numerical (CFD) analysis of bridge aerodynamics and dynamic response to wind;
- Optimising aerodynamic performance.

In the course the participants first looked at methods of modelling the structural behaviour of such bridges, specifically cable-stayed and suspension bridges, in commercial Finite Element software. The specific focus was on determining the dynamic properties, like natural frequencies and corresponding mode shapes. In the next step, various phenomena of dynamic wind excitation were introduced. These include turbulence-induced buffeting, vortex-induced vibrations and instabilities like flutter. A Computational Fluid Dynamics (CFD) software was introduced and applied to determine the aerodynamic properties of bridge decks. These results were used to assess the wind excitation phenomena using various analytical and numerical methods. Also fully coupled numerical fluid-structure interaction analyses were performed.

Wind-induced vibrations of long-span bridges: Buffeting Response of a Cable-stayed Bridge in Construction Stage

RONCALLO Luca[a], PETRESKI Borjan[b], PETER Zsolt[c]
[a] *Faculty of Civil Engineering, University of Genoa, Genoa, Italy*
[b] *Institute of Earthquake Engineering and Engineering Seismology, University of Ss. Cyril and Methodius, Skopje, Macedonia*
[c] *Department of Structural Engineering, Budapest University of Technology and Economics, Hungary*

Abstract

The following report deals with the wind-induced vibrations on a cable stayed bridge due to inflow turbulence. The study has been carried out considering the bridge under construction. The analyses were conducted using a Computational Fluid Dynamics (CFD) tool VXflow for a static and moving deck, in order to evaluate the aerodynamic coefficients and the maximum displacements due to induced vibrations.

Introduction to Buffeting Phenomenon

Buffeting includes the vibrations produced in a structure as a result of the velocity fluctuations, generally associated with a turbulent regime. Due to the roughness of the terrain a turbulence is induced indeed. Said turbulence is represented by fluctuations in three space directions, u,v and w, longitudinal, transversal and vertical respectively, as a function of the average wind velocity in the main direction U. Those fluctuations are described by turbulent intensity I_u, I_v and I_w, which are defined as the ratio between the standard deviation value (per each component) and the mean wind velocity U.

The buffeting analysis consists of applying a wind turbulent profile on the bridge model and studying its dynamic response. Due to the nature of the actions it is compulsory to carry out a three-dimensional analysis in order to obtain sufficiently approximate result, even if the bridge can be considered as a line-like structure. Since the 3D Computational Fluid Dynamics (CFD) analysis is computationally burdensome, a Pseudo-3D analysis was carried out. In fact it is also possible to make a two-dimensional treatment taking various representative cross sections simultaneously, introducing also the use of correlation functions in the global model.

The structural response regarding buffeting is characterised by its generally irregular and relatively lower oscillation amplitude time history. It is then requested a serviceability limit state and fatigue checking, especially if the oscillations due to buffeting effects are frequent.

Reference object

The reference object is a modified version of the Mersey Gateway Bridge, depicted in Fig. 1. The bridge is a cable-stayed bridge with total length of 2130 m and a main span length of 1000 m. Geometric details of the bridge are depicted in Fig. 2. Cross section carries 3 lanes of traffic in each direction; its total width is 33m with height of 4.8 m Fig. 3.

Figure 1. Reference Bridge (www.google.com).
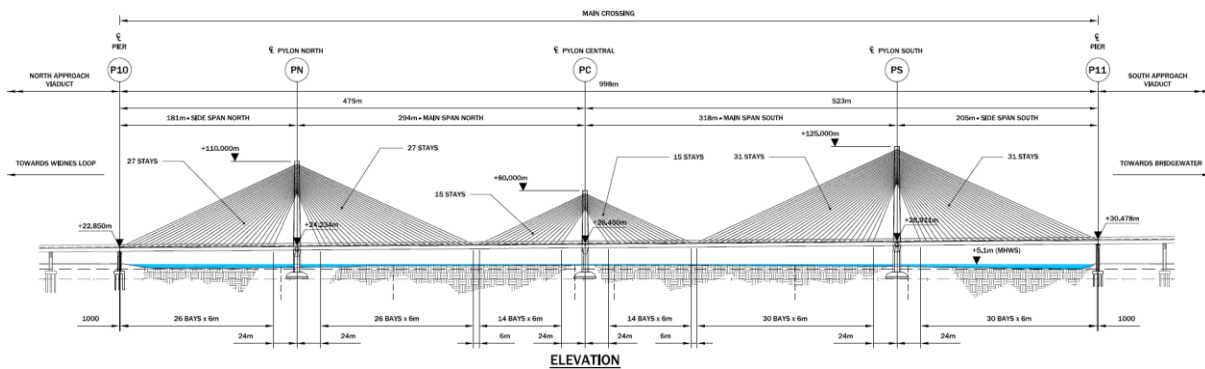
Figure 2. Elevation view of the bridge (Morgenthal, 2017).
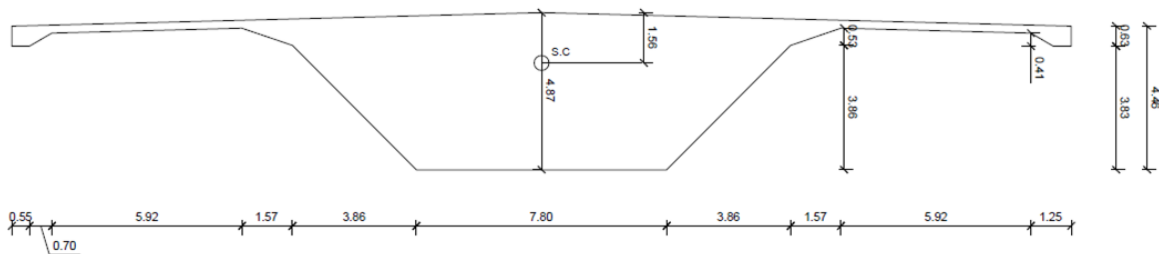
Figure 3. Deck dross-section (dimensions: m).

Due to its complicity bridge was analysed as a whole structure using commercial code SOFiSTiK (Fig. 4). In this report only middle span at the stage of construction was considered. Model was provided in the project description and it was used to conduct modal analysis in order to determine frequencies associated with excitation of middle section. All the dynamic properties of the bridge were given by the program. Since the bridge was analysed in the maximum cantilever stage, only the modes which involve west crossing are considered. Some of them are represented below (Figs. 5, 6 and 7).
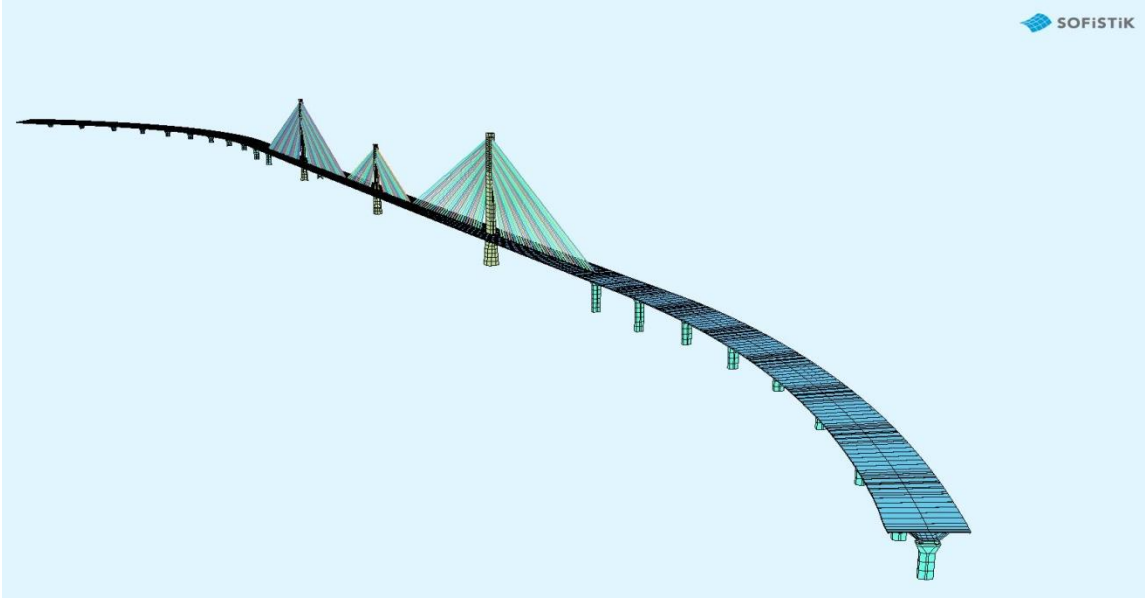
Figure 4. Finite element model of the bridge.
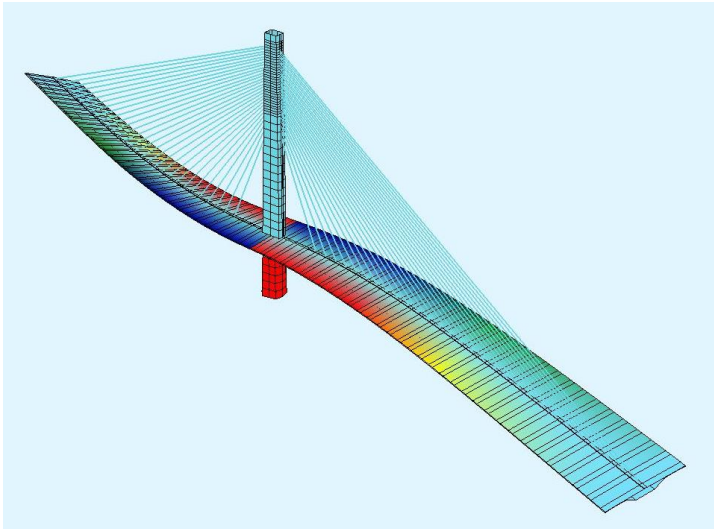
Figure 5. First lateral mode (f = 0.303 Hz).
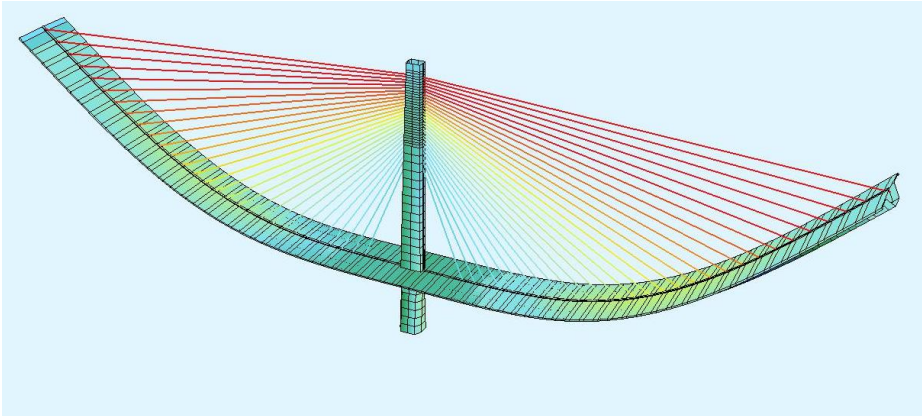
Figure 6. First vertical mode (f = 0.444 Hz).
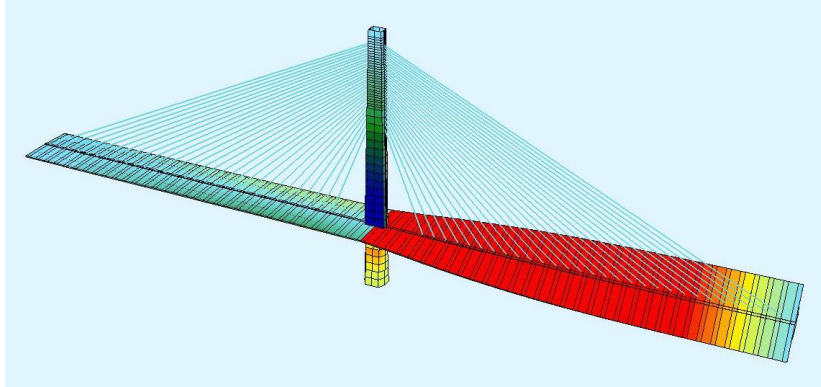
Figure 7. First torsional mode (f = 0.913 Hz).

Numerical Simulations

The CFD simulations were conducted using VXflow which is fundamentally based on Vortex Particle Method (Morgenthal G. 2002). Due to limited time and resources only two simulations were made.

First of them will be referred to as "Static". This simulation was used to obtain time averaged values of lift, drag and moment coefficients C_L, C_D and C_M, which, for different incident angle, can be used to find the buffeting forces on structure. In order to carry on the simulation the structure was fixed.

Second simulation will be referred to as "Dynamic". It was conducted in "Pseudo-3D" using eight parallel two-dimensional cases calculated simultaneously. In order to evaluate the maximum displacement of the tip of the deck, the cross section was allowed to move under wind actions.

Incoming wind fluctuations

In order to carry on the simulations the oncoming wind has to be modelled. To do so it is necessary to know to mean wind velocity U and the turbulence intensity for each of the three component of fluctuations u, v and w. For the static analysis the mean wind velocity U was defined as 20 m/s with no turbulence and Reynold's number of 10^5, in order to evaluate the aerodynamic coefficients in steady flow. For the dynamic analysis U was defined as 55 m, with isotropic turbulence of 10%. Turbulent fluctuations are the superposition of eddies in periodic motion. The Power Spectral Density (PSD) describes the energy content of single eddies. Mechanical and thermal convections produce low frequency kinetic energy associated with large eddies. In the inertial subrange there is neither production nor dissipation of energy but an energy transfer from larger to smaller eddies. In the high frequency range small eddies dissipate viscous energy. The sequence of these phenomena is called energy cascade. The Von Karman PSD is showed in Fig. 8.
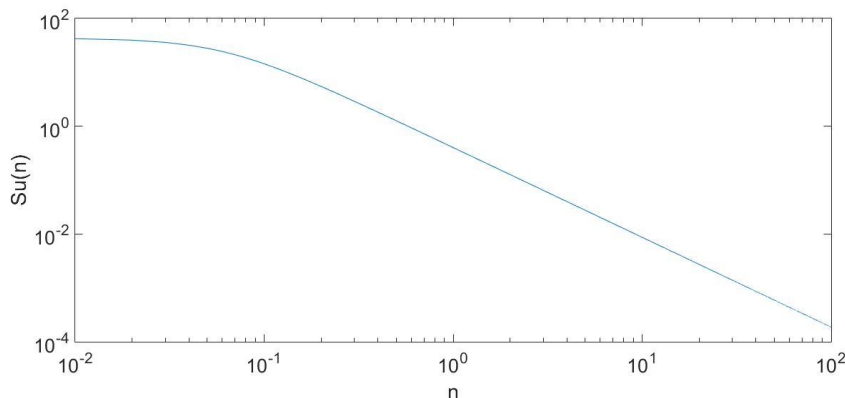
Figure 8. Von Karman PSD for oncoming turbulence.

Results

Static simulation

Static calculation results were used to obtain drag, lift and moment coefficients C_L, C_D and C_M.

The aerodynamic coefficients have been calculated for different angles of attack of the wind, with a maximum value of 6° and a minimum value of -6°. In Fig. 9 are showed the time history calculation of C_L, C_D and C_M for angle of attack zero.
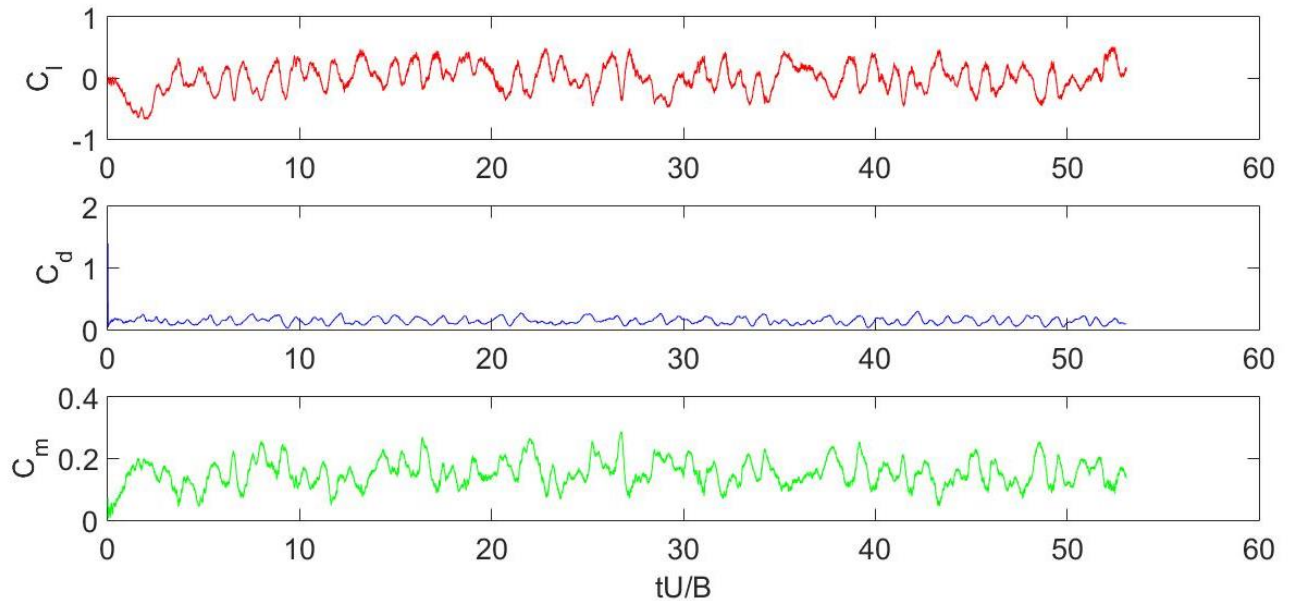
Figure 9. Aerodynamic coefficients time history for angle of attack zero.

All the static coefficients are referred to the total length of the cross section, which is B=33m.

$$\begin{cases} C_D = F_D/(0.5 \cdot \rho \cdot U^2 \cdot B) \\ C_L = F_L/(0.5 \cdot \rho \cdot U^2 \cdot B) \\ C_M = F_M/(0.5 \cdot \rho \cdot U^2 \cdot B^2) \end{cases} \tag{4}$$

The average values of the aerodynamic coefficients calculated for angle of attack zero are:

- C_L = 0.028;

- C_D = 0.14;

- C_M = 0.16;

Where F_D, F_L and F_M are total forces acting on section, U is oncoming wind speed.
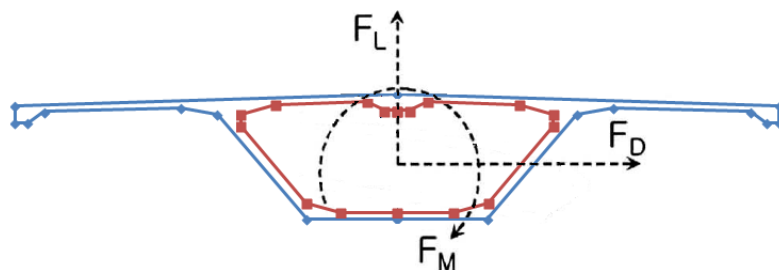
Figure 10. Aerodynamic forces induced by wind on the cross section.
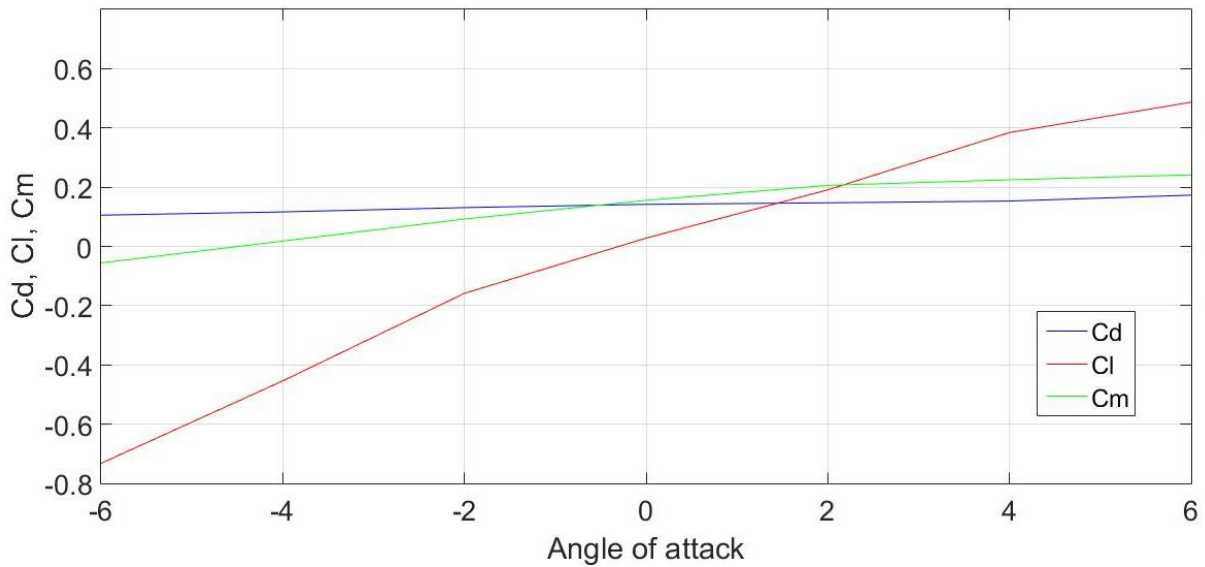
Figure 11. Aerodynamic coefficients for different angle of attack.
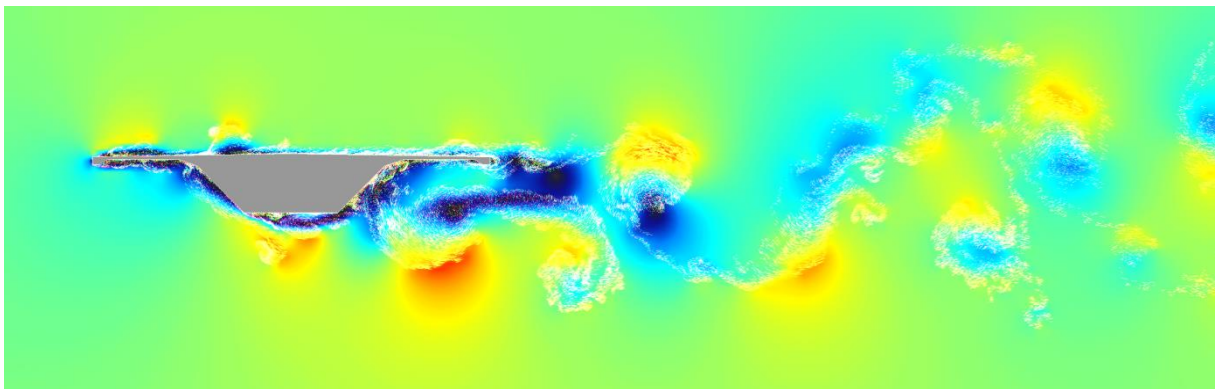
Figure 12. Instantaneous flow field.

As pointed out previously, the aerodynamic coefficients were calculated also for different angle of attack besides zero. Various angles were considered and their values are shown in Fig. 11. In Fig.12 instantaneous snap-shot is depicted of the velocity field for laminar inflow past the bridge deck.

The colour blue represents the low velocity, while the red colour indicates high velocity. The vortices created by the deck are clearly visible. As result of the pressure around the body, forces are acting on the bridge deck. The integral of the pressure distribution yields in static forces, acting on the body due to wind-structure interaction. A snap-shot of the instantaneous pressure field is shown in Fig. 13. The blue vectors represent a positive pressure, while the red vectors represent the suction.
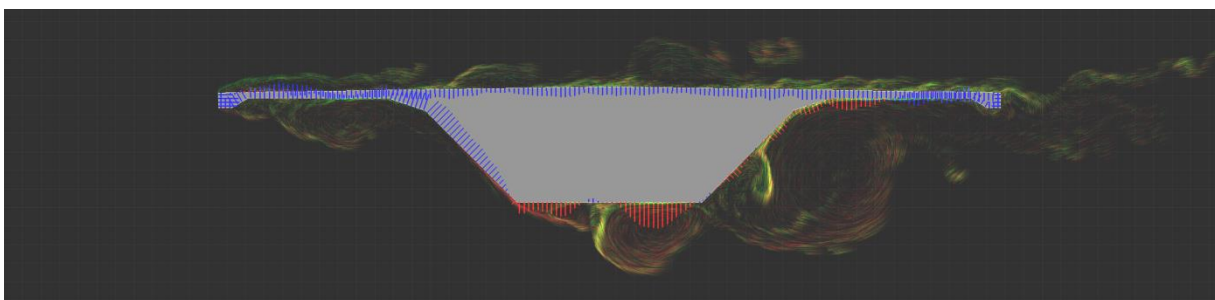
Figure 13. Instantaneous pressure distribution around the bridge deck.

Dynamic simulation

Pseudo-3D dynamic simulations were carried out by using eight 2D slices, in order to determine the maximum displacements associated with modal excitations of the tip of the deck. To do so, 600 seconds of turbulent inflow were generated. The correlated turbulent wind field was modelled for each section with U = 55m/s and an isotropic turbulence intensity of 10%. A total of fifteen modes were used in the Pseudo-3D analysis. The time-histories of the displacements are shown in Figs. 14-16.
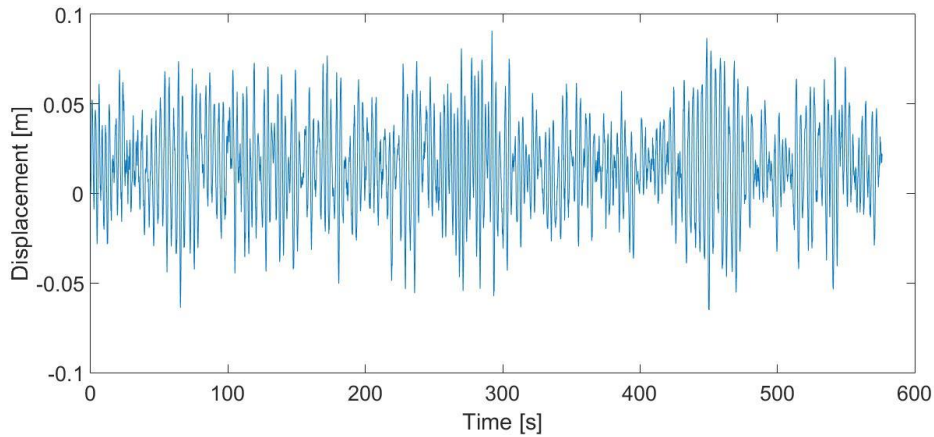
Figure 14. Lateral displacement at the tip of the cantilever.
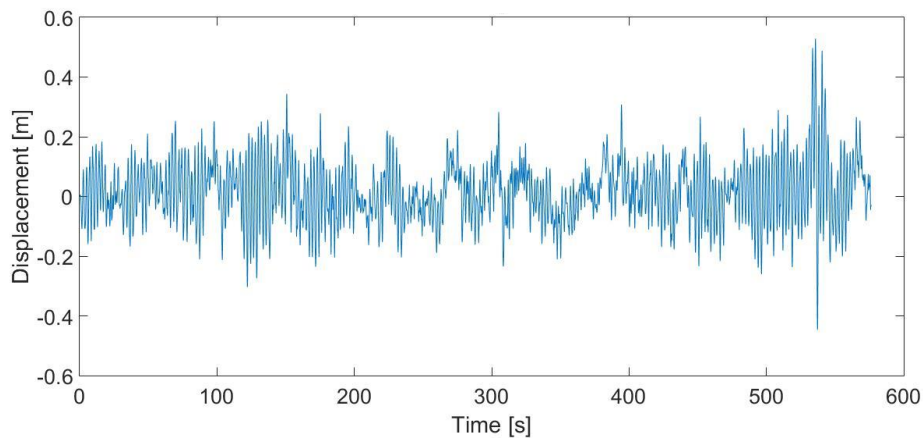
Figure 15. Vertical displacement at the tip of the cantilever.
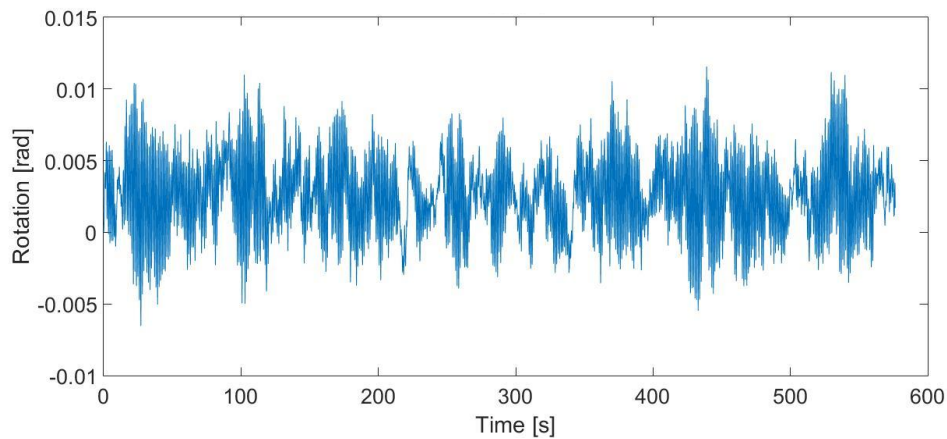
Figure 16. Rotation at the tip of the cantilever.

Table 1. Mean, RMS and maximum value for displacement and rotation.

	Lateral [m]	Vertical [m]	Rotation
Mean	0.0153	0.0144	0.0026
RMS	0.0298	0.1023	0.0037
Max	0.0908	0.5284	0.0116

The mean, Root-Mean-Square (RMS) and the maximum absolute displacement for each direction were computed and are given in Tab. 1.

The PSD of the lateral, vertical and torsional displacements are given in Figs. 17, 18 and 19. The contribution of the higher modes is clearly indicated by the peaks, for each direction of oscillation.
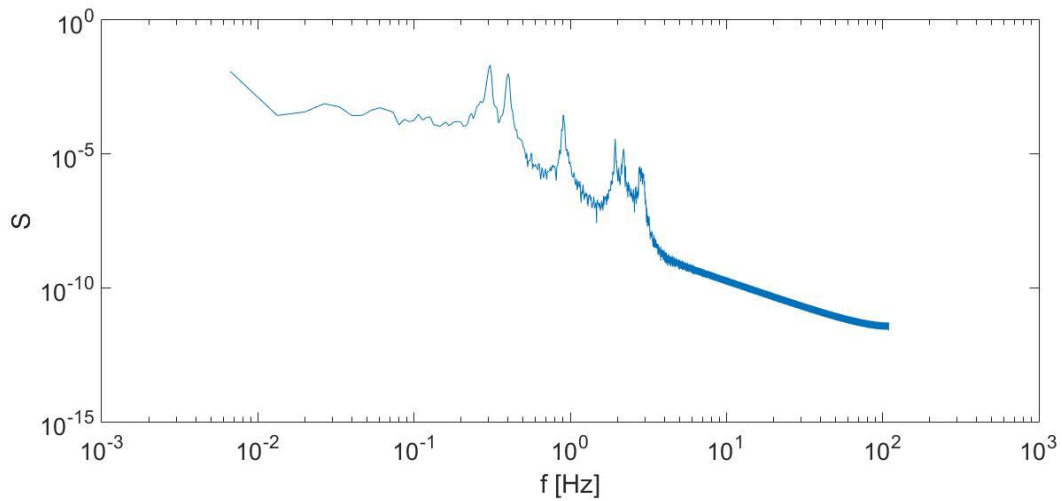
Figure 17. PSD of the lateral displacement at the tip of the cantilever.
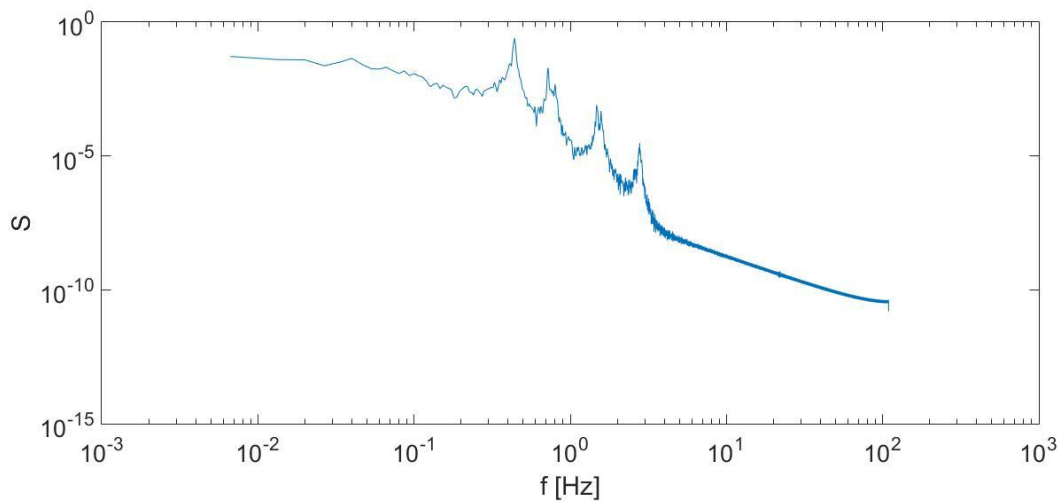
Figure 18. PSD of the vertical displacement at the tip of the cantilever.
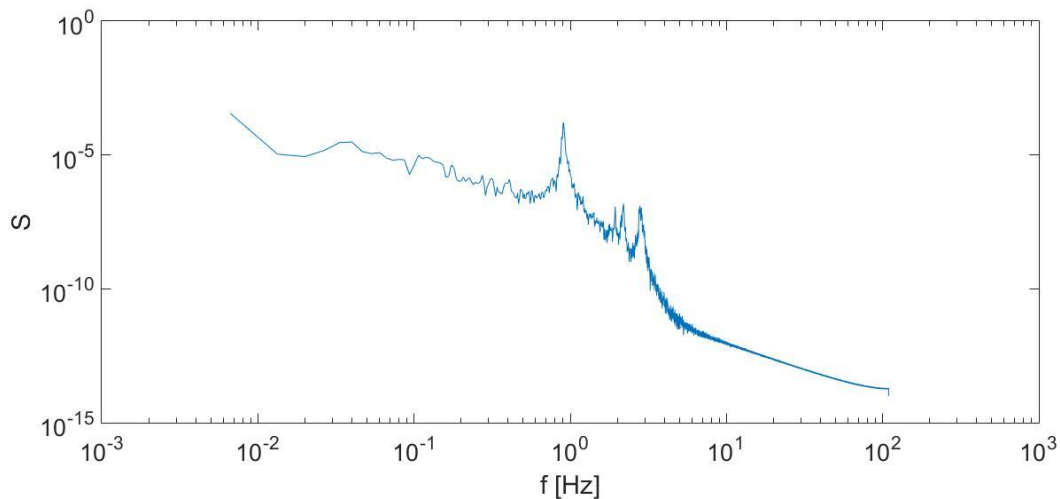
Figure 19. PSD of the rotation at the tip of the cantilever.

Conclusions

From the static analysis it can be seen how the aerodynamic coefficients vary by changing the angle of attack. In particular the lift coefficient has a slope of around 5.

The dynamic analysis showed that the maximum value of vertical displacement that can be reached is more than half a meter. This means that during the construction stages the bridge is subjected to a wind load that has to be taken into account during the design. Also, these vibrations could lead to some serviceability problems related to the workers. The spectrum shows that the first natural frequencies in each direction have the main contribution to the response; however, higher modes should be considered as well since their contribution is not negligible.

References

You-Lin X. (2014): *Wind Effects on Cable-Supported Bridges*, First Edition, John Wiley & Sons.

MGB (2014): *Mersey Gateway Bridge – Wind Tunnel Testing Interpretive Report.* Flint & Neill Ltd.

Strømmen E.N (2010): *Theory of Bridge Aerodynamics,* Springer.

Morgenthal G. (2002)*: Aerodynamic Analysis of Structures Using High-resolution Vortex Particle Methods, PhD thesis, University of Cambridge.*

Simiu E. and Scanlan R.H. (1996): *Wind Effects on Structures*, Third edition, John Wiley & Sons.

Morgenthal G. (2017): *PROJECT 6: WIND-INDUCED VIBRATIONS OF LONG-SPAN BRIDGES*, Bauhaus Summer School 2017, course material.

SOFiSTiK A.G. (2014): SOFiSTiK analysis programs version 2014, Oberschleißheim: SOFiSTiK AG.

Morgenthal G. (2013): VX Flow Primer v.0995. Bauhaus-University Weimar, Weimar.

Solari G., Piccardo G. (2000): Probabilistic 3-D turbulence modeling for gust buffeting of structures, *Probabilistic Engineering Mechanics* **16** (2001) 73–86

Wind-induced vibrations of long-span bridges: Flutter stability analysis of Lillebaelt suspension bridge in Denmark

TADIĆ Ivana [a], BULIĆ Nenad [b], SHAHNAZARYAN, Davit [c]
[a] University of Belgrade, Serbia
[b] University of Ljubljana, Slovenia
[c] Istituto Universitario di Studi Superiori di Pavia, Italy

Abstract

Flutter is a dynamic instability of an elastic structure characterized by the combination of more than two structural vibration modes. Flutter occurs as a result of interactions between aerodynamics, stiffness, and inertial forces on the structure. In this study we analyzed the flutter stability of the Lillebaelt Bridge.

Modelling and simulation of the reference bridge cross-section is performed using CFD tool VXflow (Morgenthal, G., 2002) to compute force coefficients. As a final goal, fully coupled and forced vibration simulations are performed to determine and to compare the critical wind speed, at which the flutter phenomena occurs.

Introduction

Aerodynamic stability is one of the most important issues in wind resistance design for long-span bridges. Nowadays, with rapid increase of the bridge span the impact of wind loads needs serious attention because of the failure not necessarily being at the maximum wind speed. There are four main categories of wind effects on bridge decks: flutter, buffeting, vortex excited vibration, and galloping. The flutter is one of the main parameters in design of long-span bridges because it can lead to total failure of the structure.

Flutter is a dynamic instability of an elastic structure caused by the motion-induced or self-induced force and may lead to excessive vibrational amplitudes. The classical flutter case consists of two vibration modes, vertical displacement mode, or heave, and torsional rotation mode, or pitch, and the coupling between these two represents critical problem in long-spans. The vibration frequency associated with the instability is between the natural frequencies of the respective coupled modes, known as flutter frequency.

Experimental and analytical procedures can be used to define critical wind speed. The standard procedure for experimental testing methods and investigation of aerodynamic stability are wind tunnels with scaled model as a prototype structure. The goal is to predict the lowest critical wind velocity that induces the flutter instability. Analytical methods are derived based on frequency and time domain (Sukamta, 2017).

Reference structure

The study case is the Lillebaelt suspension bridge, located in Denmark. It has a total length of 1080 m, with a central span of 600 m and two lateral spans of 240 m each. The ultrathin design of this bridge yields significant susceptibility to wind-induced vibrations. In this study, sophisticated analysis methods are applied to determine critical wind velocities of flutter.
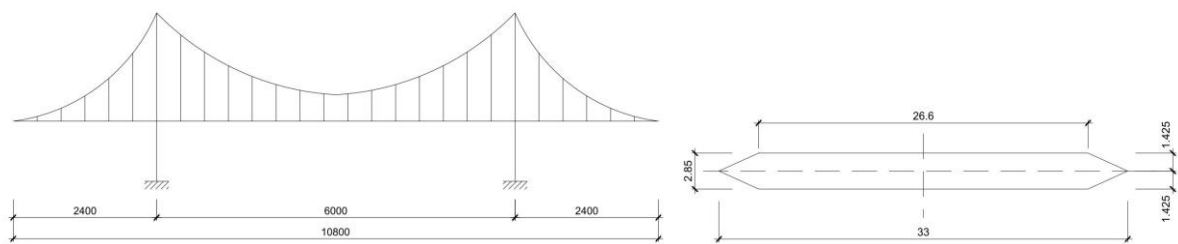
Figure 1. (left) Scheme of the bridge elevation and (right) its section geometry.

Depending on the type of cross section of the bridge, different types of flutter phenomenon may occur. For this cross section the coupled flutter is governing. The dimensions and geometry of the cross section are presented in Fig, 1. The fences on the bridge are not taken into account in analysis. Section is defined as a 2D model, and either only one or multiple structure slices of section are considered.

Structural characteristics

Dynamic characteristics of the bridge are calculated by means of SOFiSTiK (Fig. 2, the QR code can be scanned via a smartphone, with any QR code scanner app, to an external URL with the animation GIF). The frequency ratio of fundamental vertical and torsional mode is a good estimator for flutter forecast. The ratio for the bridge is 3.2, which being larger than three, indicates that the critical wind speed for flutter occurrence will be high.
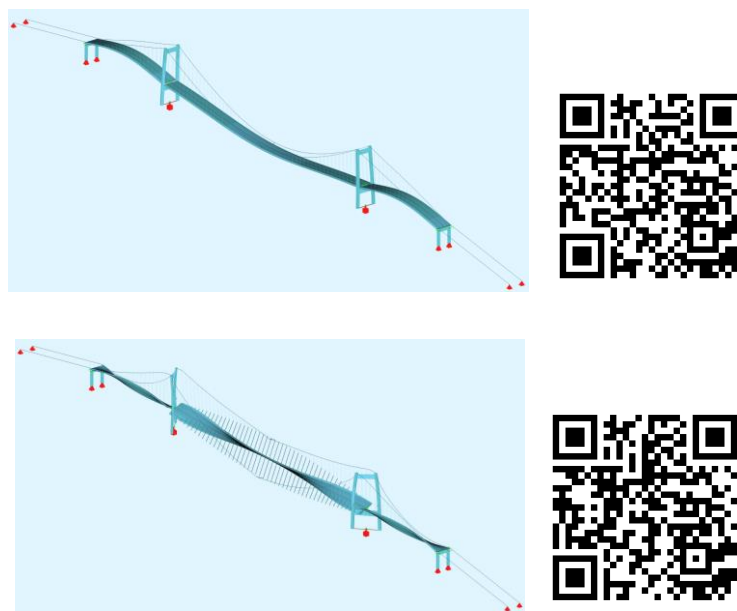
Figure 2. Fundamental mode shapes**:** (top) 1st vertical mode shape and (bottom) 1st torsional mode shape.

Table 1. Dynamic characteristic of Lillebaelt Bridge (Ostenfeld, 1970).

	Frequency	Equivalent mass
1st vertical mode	0.156 [Hz]	11667 [kg/m]
1st torsional mode	0.500 [Hz]	1017778 [kgm^2/m]

Static wind coefficients

The modelling and simulation of the reference cross-section is done using computational fluid dynamics (CFD tool) and VXflow (Morgenthal, G., 2002) at steady flow. First, the influence of wind is observed as a static loading for fixed wind speed of 50 m/s, by studying the static wind coefficients. These coefficients are defined through aerodynamic forces that result from the integration of pressures exerted by the wind around the section contour.

$$C_D = \frac{F_D}{\frac{1}{2}\rho U_\infty^2 D}$$

$$C_L = \frac{F_L}{\frac{1}{2}\rho U_\infty^2 B} \tag{1}$$

$$C_M = \frac{F_M}{\frac{1}{2}\rho U_\infty^2 B^2}$$

Aerodynamic forces F_D, F_L and F_M are named as drag, lift and moment force, because of the occurrence they describe. The coefficient values are given for different angles of attack of wind in order to observe which of three wind-induced forces gives the dominant resistance for specific angle of attack (Fig. 3).

After analyzing the static simulation, two different numerical approaches were used to determine critical wind speed. Forced vibration simulations were performed to compute aerodynamic derivatives for an analytical model, in order to calculate the critical wind speed based on eigenvalue analysis. Another approach was to observe wind-structure interaction performing fully coupled simulation for different wind speeds. In addition, Pseudo-3D model is used to include the influence of higher modes on the critical flutter speed.
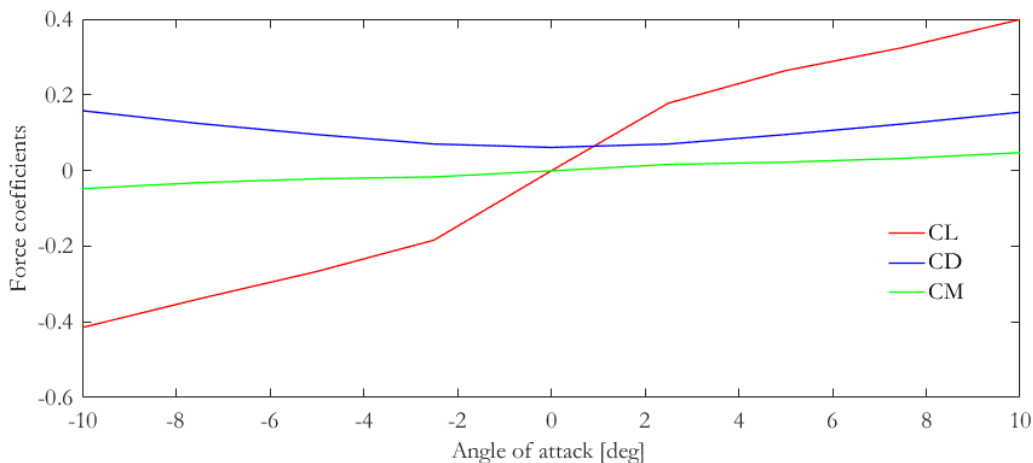
Figure 3. Force coefficients of the bridge deck.

Semi-analytical flutter analysis

As a next step, analytical analysis is carried out according to several methods. Forced vibrations method is incorporated by using the Scanlan's theory (Simiu and Scanlan, 1996). It assumes that the self-excited

lift (F_L) and moment (F_M) for a bluff body may be treated as linear in displacement h and rotation a and their first- and second-order derivatives. The method involves the application of the forced vibrations with defined period and amplitude to determine the flutter derivatives, which are frequency dependent coefficients describing the motion-induced forces. To determine the derivatives, uncoupled response of the deck in vertical and torsional modes should be simulated. Fig. 4 illustrates the uncoupled simulations of the bridge deck under vertical (heave) and torsional (pitch) modes. In the figure, one QR code is presented for each of the modes.

As a result, aerodynamic derivatives are obtained (Fig. 5). After computing the Scanlan's derivatives and solving the eigenvalue problem, we obtained a critical wind velocity of 95 m/s.
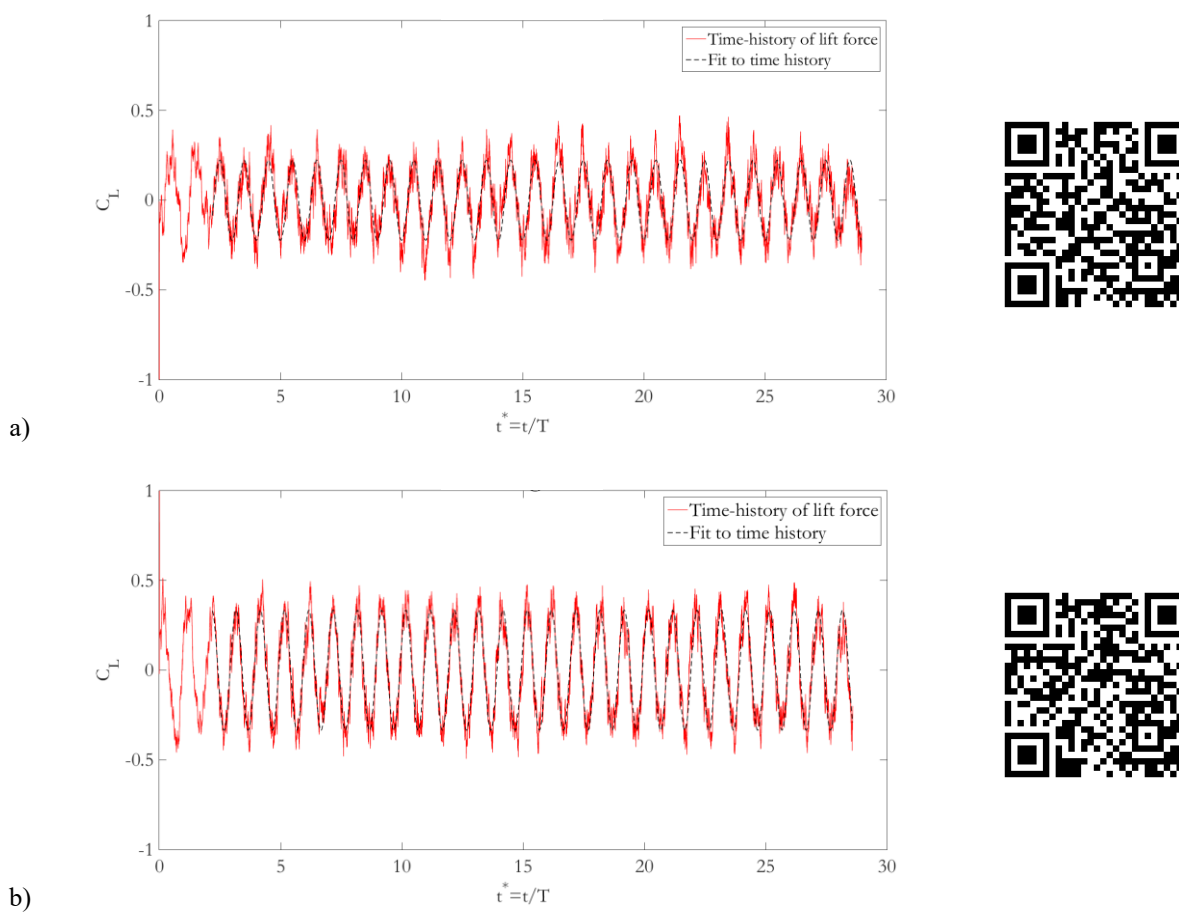
Figure 4. Lift force time histories and corresponding least-squares fit for (a) heave and (b) pitch uncoupled simulations.
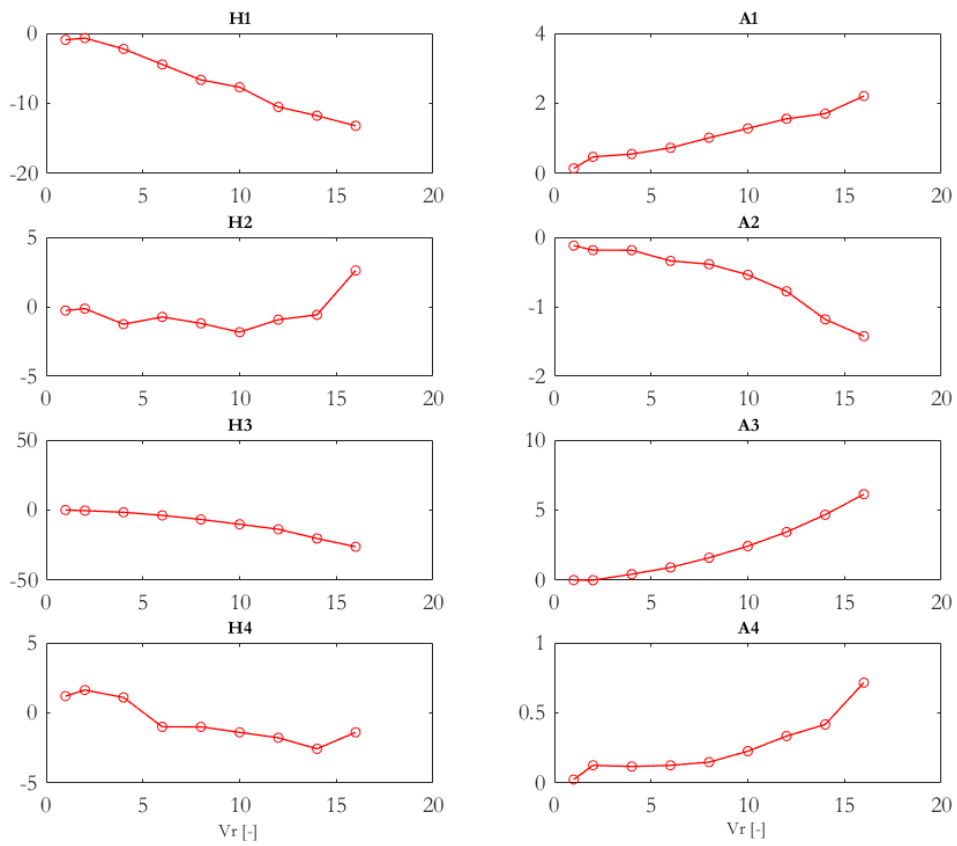
Figure 5. Flutter derivatives of simplified Lillebaelt deck section from CFD forced vibration simulations.

At certain wind speed, if the real eigenvalue becomes positive (Fig. 6), then this wind speed is considered as the critical wind velocity.
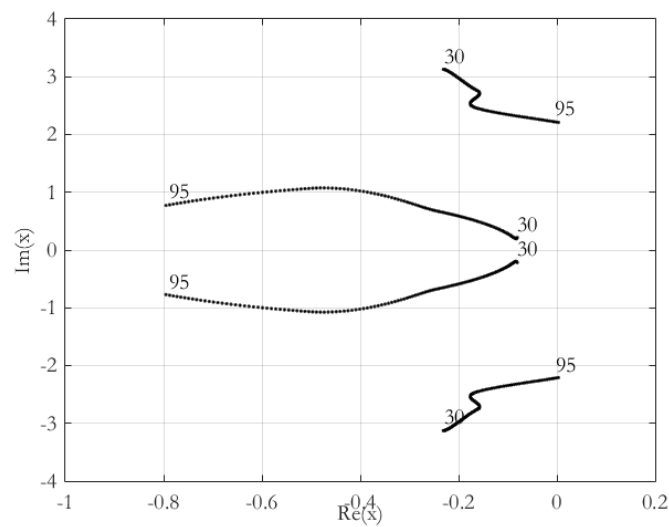
Figure 6. Eigenvalues corresponding to 1.0% damping ratio at various wind speeds using Lillebaelt structural properties and aerodynamic derivatives from CFD simulations.
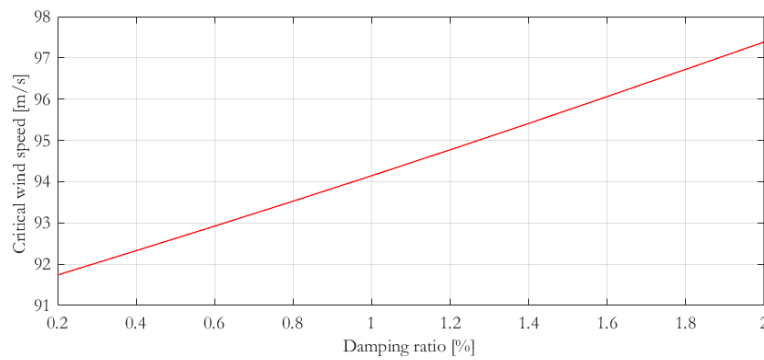
Figure 7. Damping effect on critical wind speed prediction.

By increasing a damping ratio higher critical wind speeds can be achieved. For the chosen damping ratios, the relation seems linear (Fig. 7), but it is not necessarily true as for higher damping ratios the wind velocity tends to increase more intensely.

2D Fully-coupled CFD analysis

The flutter phenomenon is analyzed by simulating the fluid-structure interaction problem. Dynamic analysis is performed for a fully coupled CFD in the VXflow software (Morgenthal, G., 2002). The bridge deck under wind velocities of 91 to 96 m/s was simulated. In Fig. 8, torsional displacements are presented comparatively for wind velocities of 91 and 95 m/s. One can observe that at around 60 seconds the displacement difference starts increasing extensively for the wind velocity of 95 m/s, while the response of the deck oscillates around zero for the wind velocity of 91 m/s. At around 100 seconds, the response in torsion stabilizes for the wind velocity of 95 m/s, namely limit cycle oscillations are happening.
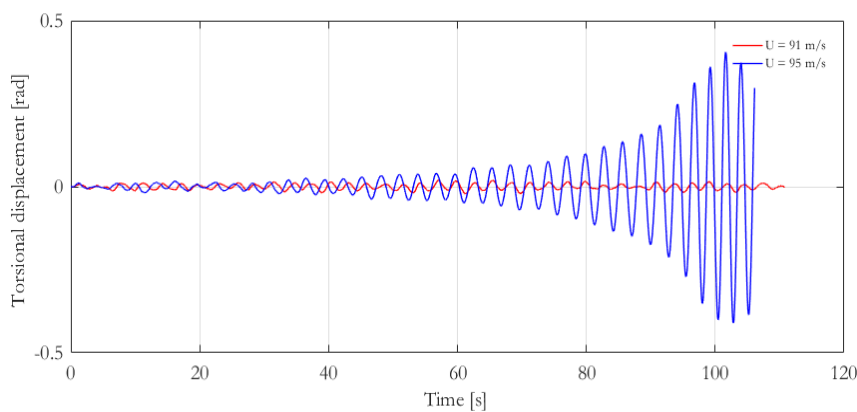
Figure 8. Coupled displacement response for lead and trail edges from CFD simulations at 95 m/s wind speed.

Pseudo-3D Fully-coupled CFD analysis

Previous dynamic and static analysis were performed using one single slice with 1 m reference length, and the critical wind speed was determined to be 95 m/s. In order to investigate critical wind speed of the whole bridge deck including higher number mode-shapes, Pseudo-3D analysis should be conducted, in which the structure is coupled in a 3D manner with flow in 2D planes. Due to computational and time limits, the analysis is performed for previously defined critical wind speed to observe the behavior of whole bridge deck. For each slice, different mode shape characteristics were defined using SOFiSTiK software (Fig. 9).
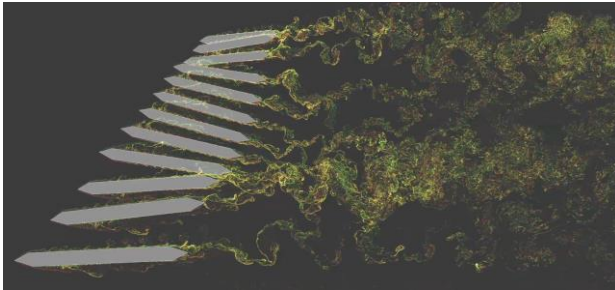
Figure 9. Instantaneous frame from a CFD simulation showing divergent response of the multi-slice model.

Conclusions

Modelling and simulation of chosen cross section of Lillebaelt Bridge was carried out. Fundamental vertical (0.156 Hz) and torsional (0.500 Hz) modes were computed using a structural model created with SOFiSTiK. Then static analysis was performed in order to define force coefficients for different angle of attack and to observe the influence of wind on drag, lift and rotation of the section. With the increase of angle of attack of wind lift resistance of the section increases, while against rotation remains close to constant, and the resistance against drag is the lowest at 0 degree of angle of attack of wind. Dynamic analysis is performed to obtain critical wind speed using two different approaches: combination of the aerodynamic derivatives and eigenvalue analysis, and a CFD numerical model for different wind speeds in order to observe at which wind speed the flutter phenomenon occurs. The same critical wind speed of 95 m/s was obtained from both dynamic analyses. This displays very good accuracy of numerical models and the reliability of both dynamic simulations for providing the proper results. Similar to dynamic analysis, a wind speed of 95 m/s was estimated through analytical expressions, which is an indicator of very good comparison between analytical and numerical approaches (Tab. 2).

Table 2. Comparison of critical wind speed.

Model	U_{cr} (m/s)
2D Semi analytical model	95
2D CFD model	95
Pseudo-3D CFD model	95

References

Ge Y., Tanaka H. (2000): Aerodynamic flutter analysis of cable-supported bridges by multi-mode and full-mode approaches. *Journal of Wind Engineering and Industrial Aerodynamics*, **86** (2-3): 123-153.

Morgenthal G. (2002): *Aerodynamic Analysis of Structures Using High-resolution Vortex Particle Methods*. Ph.D. Thesis, University of Cambridge, Cambridge

Ostenfeld C., Frandsen A.G., Jessen J.J., and Hass G. (1970): Motorway bridge across Lillebaelt, publication XI: Model tests for the superstructure of the suspension bridge. Report

Simiu E., Scanlan R.H. (1996): *Wind effects on structures: Fundamentals and Applications to Design (Third edition)*. Jon Wiley & Sons.

Sukamta, Guntorojati I., Fariduzzaman (2017): Flutter analysis of cable stayed bridge. *Procedia Engineering*, **171** ;1173-1177.

Wind-induced vibrations of long-span bridges: Vortex-induced Vibration Analysis of Alconetar Bridge in Construction Stage

KARSHENASS Arash[a], NEMETH Gabor[b], PEJAKUSIC Davor[c]
[a] Middle East Technical University, Turkey
[b] Budapest University of Technology and Economics, Hungary
[c] University of Josip Juraj Strossmayer Osijek, Croatia

Abstract

As the spans of bridges get larger, they become more sensitive to wind-induced oscillations. When wind passes through bridge, vortices are generated due to separation of boundary layer and as a result dynamic loads appear. Vortex-induced vibrations (VIV) restrict the design of structure strength, rigidity and stability of bridges. Therefore, it is of importance to study the impact of VIV on bridges and the response of structure to this dynamical load.

The present paper focuses on the study of the VIV on the Alconetar Viaduct Bridge in Spain, in order to find the critical wind speed at which the amplitude of produced vibration reaches to maximum due to vortex shedding. Critical wind speeds and maximum amplitudes at these conditions are investigated for four different cross-sections of the bridge spans in order to find the improved shape of spans.

Introduction

Vortices are circular patterns in the air flow that exist due to interaction of air with a body which is the aim of current study. When air flow passes body, a very thin layer of air is created over the surface, called boundary layer and it becomes thicker as it moves downstream. However at a point, boundary layer gets separated from the surface and this is a point at which the slop of velocity profile becomes zero at the surface of the body (White 1974). Just downstream of separation points, vortices begin to appear, due to the lack of any flow inlet from upstream. Interaction of vortices with the body is followed by unbalanced pressure distribution over the face of structure and is followed by movement of the body. Resultant forces along and perpendicular to the streamline are called drag and lift forces respectively. Due to elastic behavior of the structure material and damping effect of both structure and air, oscillations begin to occur.

Reference object

Alconetar Viaduct (Fig. 1) is a freeway, deck-arch Bridge which is constructed 2006 over the Tagus River to connect Canaveral and Caceres cities in western Spain. Arch is made of steel with span of about 220 meters (structurae.net). After installing the arch, vortex-induced vibrations become significant and there is the need to control them. So, here four different cross-sections of the arch are investigated to obtain the wind velocity, at which the structure is put into resonance. Investigated cross-sections are demonstrated in Fig. 2 while natural frequency, damping and mass are considered the same for all of them as 0.7 Hz, 0.03 kg/s and 1130 kg/m respectively (Sánchez Corriols 2015).

Figure 1. Alconetar Viaduct Bridge (Sánchez Corriols 2015).
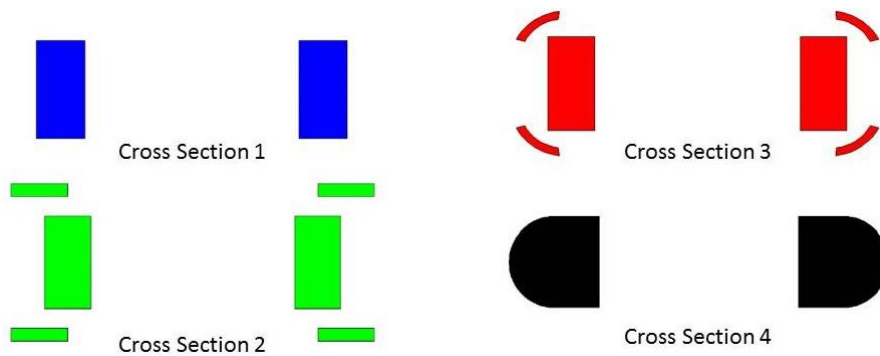
Figure 2. Investigated cross-sections.

Static Analysis

Static analysis is done based on an assumption that the body is fixed in space. In this way, the frequency of generated vortices can be obtained from the fluctuation of the lift force and is directly proportional to the mean velocity of upstream air. Making this ratio non-dimensional, the Strouhal number can be defined as

$$St = \frac{f_v D}{U},$$ (1)

where D is the characteristic length of the geometry.

Each geometry has its specific Strouhal number, so it is possible to find out the frequency of generated vortices for any upstream flow velocity if St is known as a priori. To find it, static flow analyses for four geometries are done separately using VXflow (Morgenthal 2002). The Strouhal number was determined by performing the Fast Fourier Transform (FFT) of the lift coefficient and the results are listed in Tab. 1. Fig. 3 demonstrates the lift coefficient in frequency domain for case 1. Finally, it is possible to find the frequency of generated vortices for any inlet flow velocity. When this frequency meets the natural frequency of the body, resonance occurs. In other words, we can find the required flow velocity to have vortices with frequency equal to natural frequency, Eq. (2).

$$St = \frac{f_n D}{U_{cr}} \rightarrow U_{cr} = \frac{f_n D}{St}$$ (2)
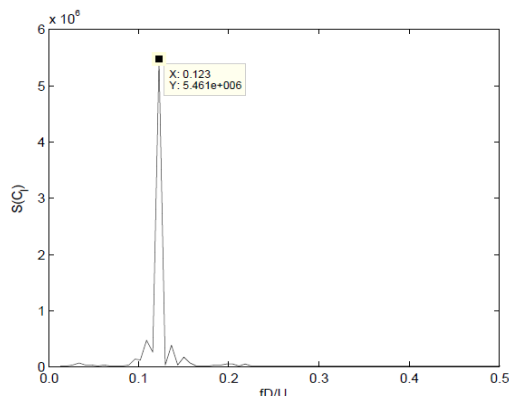
Figure 3. Lift Coefficient of cross-section 1 in frequency domain

Dynamic Analysis

In dynamic analysis, which also is done in VXflow, exerted force from flow is coupled with the equation of motion of the body to obtaining interactions of body and flow on each other. Once the aerodynamic forces have been analyzed, the system response is evaluated by the equation of motion, Eq. (3) (Simiu and Scanlan 1996).

$$M\ddot{x} + C\dot{x} + Kx = F(t) \qquad (3)$$

Obtained critical velocities from static analysis are associated with fixed body and are used as an estimation to find the actual critical values of wind speed in dynamic analysis. However, due to the motion of body in a dynamic system, frequencies of generated vortices are slightly different from those in fixed body. Consequently, for each of geometries dynamic analyses are done for about 10 to 13 different wind velocities near the critical wind speed, obtained from the static analyses. Fig. 4 demonstrates the maximum displacements of geometries at different wind velocities. Additionally, in Tab. 1, the critical wind speed based on the Strouhal number and dynamic analyses are given. Critical wind speeds are clearly visible in all cases as the peaks of the curves where amplitude of oscillation has the maximum value. Based on the dynamic analysis, cross-sections 2 and 4 appear to be the most optimal from oscillation point of view.
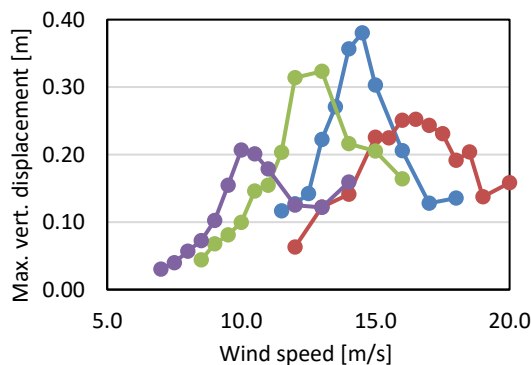
Figure 4. Maximum vertical displacements for cross sections 1 (blue), 2 (red), 3 (green) and 4 (purple).

Table 1. Strouhal number and critical wind speeds.

	Width of cross-section (m)	Strouhal number	Critical wind speed from static analysis (m/s)	Critical wind speed from dynamic analysis (m/s)
Cross-section 1	2.4	0.1230	13.7	14.5
Cross-section 2	4.0	0.1656	16.9	16.5
Cross-section 3	3.5	0.2002	12.4	13.0
Cross-section 4	2.4	0.1917	8.8	10.0
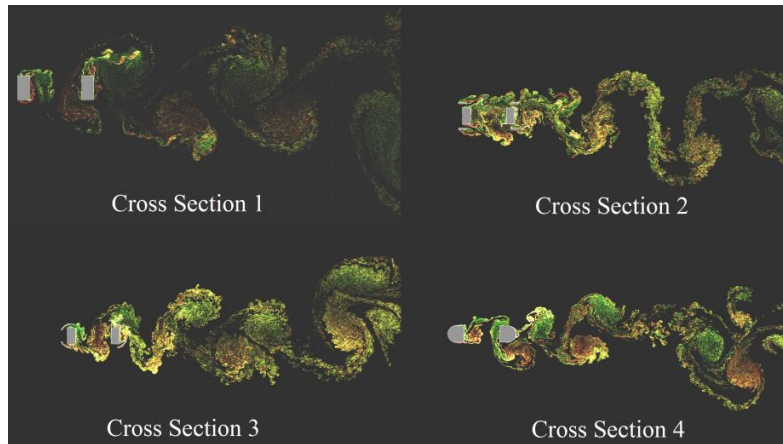
Figure 5. Dynamic analysis at critical wind speeds.

Cross-section 2 vibrates with larger amplitudes, but lock-in happens less frequently as the critical wind speed is higher. Although cross-section 4 has minor displacements during resonance, it vibrates more frequently with maximum amplitudes. Comparing two figures, characteristics of average values are the same as the maximum values; this confirms the conclusions drawn so far. Cross-section 1 is the original design and also has the maximum displacement. Fig. 5 depicts a snapshot of the four cross-sections, oscillating at the critical wind velocities.

The other important thing to note is that VIV is not a diverging phenomenon. The reason behind this behavior is the change of frequency of vortices due to the motion of body, meaning that after an initial transient period, frequency of vortices become different than natural frequency which they had had at the beginning. Consequently, a balance appears between the amplitude of vibration and frequency of vortices that limits the continuous growth of amplitude of vibration.

Conclusion

Since vortex shedding is only a problem during the construction for this particular case-study, cross-section 4 could be utilized as there is limited period of time for fatigue impacts. But, refining the initial cross-section into case 4 is the most difficult. However, cross-section 2 can be obtained by adding only a few plates into initial geometry, while the displacements from the dynamic analysis are not particularly larger than the ones obtained for cross-section 4. So, considering both technical and economic aspects of the project, cross-section 2 would be the optimal choice.

Cross-section 3 performed poorly compared to the other alternatives. The reason for the results is that the flaps do not lead the wind in the correct direction as the arcs extended to the front of the original cross-section. If we use flaps in more horizontal shape than current circular form, better results could be achieved.

References

Morgenthal G. (2002): *Aerodynamic Analysis of Structures Using High-resolution Vortex Particle Methods*. Ph.D. Thesis, University of Cambridge, Cambridge.

Sánchez Corriols A. (2015): *Vortex-induced vibrations on bridges: the interaction mechanism in complex sections and a new proposed semi-empirical*. Ph.D. Thesis, Technical University of Madrid, Madrid.

Simiu E., & Scanlan R. H. (1996): *Wind effects on structures: Fundamentals and application to design*. John Willey & Sons Inc.

White F.M. (1974). Viscous flow. *Mc Graw Hill*

Papers contributed by the participants

Fatigue Behaviour of Duplex Welded Bridge Details

KARABULUT Burak
Katholieke Universiteit Leuven, Netherlands

LOMBAERT Geert
Katholieke Universiteit Leuven, Netherlands

DEBRUYNE Dimitri
Katholieke Universiteit Leuven, Netherlands

ROSSI Barbara
Katholieke Universiteit Leuven, Netherlands

Abstract

Stainless steel, as Chromium-Nickel (Cr-Ni) alloys, has recently gained increased interest for construction owing to the combination of excellent corrosion resistance and mechanical strength. In particular, duplex grades, with a balanced austenite ferrite microstructure, show greater proof strength and ductility than that of standard austenitic stainless steel groups which were often used in bridges in corrosive environments over the last decades (Baddoo and Kosmac 2010). The interest for stainless steel for bridges also increased due to the good fatigue resistance of duplex welded components (Zilli et al. 2008). The EN 1.4162 and 1.4062 duplex grades are characterized by a lower Nickel and Molybdenum content which makes them price-stable, but more prone to pitting corrosion at the same time. In mildly corrosive environments, they can be a good alternative to protected carbon steel (qua maintenance) or austenitic grades (qua initial price). Additionally, it has been proven recently that those grades have corrosion resistance which is comparable to the austenitic stainless steels EN 1.4307 and EN 1.4404 grades (Iversen 2006).

This research project seeks to bring enlightenment to this topic via two main tasks: (1) Through experimental investigations: the tests will comprise the determination of the cyclic stress-strain hysteretic curves of the base material and the welded zone as well as the development of Wöhler curves for selected welded details. Constant amplitude cyclic tension tests will be performed. The tested details will then be submitted to post-weld treatments and the improvement of the fatigue resistance will be assessed. This is the only way to assess the fatigue resistance of duplex welded structural details. The Wöhler curves, both with and without post-weld treatments, will be compared with the current carbon steel design rules and further recommendations will be made for the inclusion of the beneficial effect of post-weld treatment; (2) Through numerical studies based on the former experimental investigations: finite element models, initially developed to reproduce the experiments, will then be used to generate a series of parametric studies further nourishing the previous experimental investigation. The hot spot stress, already measured experimentally, will also be assessed numerically.

This contribution is focussed on one objective which is to calculate the possible weight reduction in an existing carbon steel girder bridge, when lean duplex welded components are used. The benefit from the greater mechanical properties of the latter are considered according to the latest published design rules for stainless steel (EN 1993-1-4 2006, DMSSS 4th edition 2017). The fatigue design is made using the hot spot stress method (Hobbacher 2015) combined with finite element (FE) models to assess the local stress distribution, considering selected relevant details along the girder.

State of the art

General positioning of the problem

New materials are employed in complex structures such as offshore structures and wind turbines subjected to diverse static and dynamic loads. This leads to many challenges in terms of design of safer, optimized and lighter, more economical and more sustainable structures. To be more efficient and use fewer resources, the design rules should reflect the real behaviour of materials and structures as closely as possible. Recent years have witnessed increasing interest in the use of stainless steel in a variety of contemporary architecture owing to its attractive aesthetic appeal, excellent mechanical properties, favourable corrosion resistance and low maintenance costs. Depending on the microstructure, four families of grades exist: martensitic, ferritic, austenitic and austenitic-ferritic (duplex) grades. Duplex types, presenting a microstructure made of austenite and ferrite, share the properties of both families, and are mechanically stronger (Fig. 1).
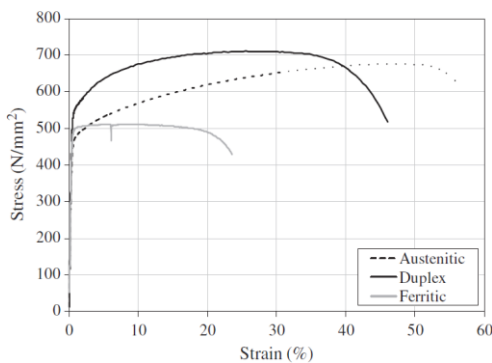
Figure 1. Stress-strain curves for austenitic, ferritic and duplex stainless steel.

Figure 2. Two examples of bridges using duplex EN 1.4162. Left: Sant Fruitos Bridge; Right: Likholefossen Bridge.

The lean duplex stainless steel (also known as grades EN 1.4162 and EN 1.4062 included in the latest revisions of Eurocode 3 Part 1-4) is characterized by a lower level of Nickel and a higher level of Nitrogen, which results in significant reduction in cost compared to other austenitic and standard duplex grades, yet having better mechanical properties and comparable corrosion robustness to austenitic grades EN 1.4307 and EN 1.4404 (Merello et al. 2003, Iversen 2006, Olsson and Snis 2007, Wei et al. 2008). The ferritic/austenitic structure is sustained by providing Nitrogen and Manganese as an offset for lowered Nickel content, which somehow maintains the balanced microstructure providing more economic solutions (Berezovskaya et al. 2008). These lean duplex grades are furthermore characterized by good weldability and can be welded by the same processes used for other grades, with restrictions in arc energy less tight than for conventional duplex due to the low alloy and high Nitrogen content. It explains why lean duplex is more and more used in welded structures as a good alternative to carbon steel equivalents (Fig. 2).

Although several established structural design codes for stainless steel exist (such as Eurocode 3 Part 1-4), studies have highlighted undue conservatism in some of their provisions, leading to unsound use of the materials in structures. Structures exposed to loading cycles are prone to fatigue, the effect of which is a paramount design aspect. The verification hereof is a relatively recent requirement in design codes. The effects on structures have been studied since the 1960s and a fatigue check was first implemented in the ECCS recommendations for steel bridges (Nussbaumer et al. 2011). Today, the Eurocode 3 Part 1-9 (EN 1993-1-9 2005) provides the design rules applicable to all grades of structural steels, stainless steels and unprotected weathering steels if these materials comply with the toughness requirements of Eurocode 3 Part 1-10 (EN 1993-1-10 2005). Additional literature review reveals few but relevant information about the fracture toughness and the fatigue behaviour of stainless steels, in which, overall, mostly austenitic grades were studied. No such research was yet performed for lean duplex, although both grades are currently used in structures exposed to cyclic

loads. Moreover, the fatigue strength curves and the categorization of structural details present in Eurocode 3 Part 1-9 are mainly based on tests carried out on carbon steel details with a nominal yield stress between 235 and 400 MPa. However, numerous studies have shown that higher strength materials (such as duplex) have better fatigue properties. It is presently not possible to fully exploit this property because the design is based on structural details, regardless of the performance of the base materials. In addition, assessing the fatigue life of a structure does not only require accurate data on the materials involved but also on the environmental conditions (as in offshore structures), the presence of corrosion (stainless steel is called "stain-less" because it stains less than carbon steel, not because it is immune to corrosion), and the details of the fabrication. As an example, it is essential to consider thermal or mechanical post weld treatments (PWT) (such as weld geometry improvement or residual stress methods), providing enhanced fatigue resistance by eliminating or reducing the tensile residual stress in the welds, in the assessment of fatigue. This is illustrated by table 8.2 of Eurocode 3 Part 1-9 where the fatigue resistance is given for welded built-up sections as well as in the literature which abundantly reports the beneficial effects of PWT on the fatigue resistance in high strength steel welded details. In recent years, the application of lean duplex has progressed, the effective utilisation of which is however often limited by the fatigue strength of critical welded details. To allow lean duplex to manifest its high material resistance, the use of PWT is promising. Nevertheless, the current scientific knowledge is still scarce and, besides, PWT for improvement of fatigue strength other than stress relief are today not covered in Eurocode 3 Part 1-9.

Material level

Together with the Welding Engineering Centre, a characterization of the welds' quality was made in a parallel research using digital x-ray images to investigate inadequate penetration, mismatch, cracks or inclusions. A parametric analysis was carried out to study the influence of the welding parameters, such as the number of pass, speed or heat input, leading to the development of certified welding procedures for gas metal arc welding (GMAW) for 10 mm and 25 mm butt and filet welds made of EN 1.4162 and 1.4062 grades. The microstructure of the base material (BM) and the microstructural changes near the welds (heat affected zone (HAZ) and fusion zone (FZ)) were also characterized (see Fig. 3) using optical micrograph. The ferrite-austenite composition balance confirmed the quality of the produced welds. Additionally, tension, compression and cyclic tests have been performed on 10 mm and 25 mm lean duplex dog-bone coupons, revealing the material behaviour along the rolling direction (RD), transverse direction (TD) and at 45° directions. The Ramberg-Osgood's as well as Swift's material law parameters were assessed. They characterize the anisotropy and hardening behaviour. Reversed tension-compression cyclic tests were used to investigate the Bauschinger effect. The hardness and Charpy impact toughness were also reported.

| (a) | (b) | (c) |
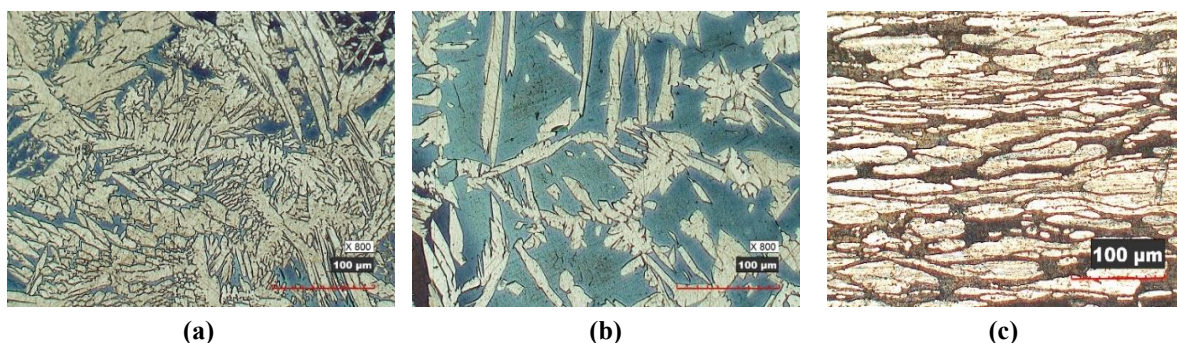
Figure 3. Magnified view of the weld microstructure of the 10-mm-thick plate: (a) FZ and (b) HAZ, blue: ferrite, white: austenite; (c) BM, brown: ferrite, white: austenite (along RD).

Literature review on the fatigue behaviour of stainless steel welded details

Concerning the cyclic behaviour of stainless steel in general, a few experimental tests have been carried out in the past (Chudnovskii 1968, Taran et al. 2002, Nebel and Eifler 2003, Lahti et al. 2000) to obtain the cyclic stress-strain hysteretic curves, which show quite different material characteristic compared to the static behaviour. Some experimental investigations were also achieved on the cyclic fatigue behaviour of stainless steel welds at the microstructure level and, to some extent, on austenitic lap joints, ferritic fillet welds and duplex spot-welded details (Jang et al. 2010, Nordberg 2005, Linder et al. 1998), showing that the fatigue crack growth is dependent upon both the microstructure and the presence of residual stress. Advanced non-destructive methods (Kudryavtsev et al. 2004, Kudryavtsev and Kleiman 2007, Fitzpatrick et al. 2005) have also been involved in the measurement of residual stresses. Numerical simulations of the temperature field and residual stress in welds with coupled thermal-structural analyses (Deng and Murakawa 2006, Yaghi et al. 2006, Cho and Lee 2016) have also been performed to understand the cause of fatigue failure in welds, and various theories on fatigue analysis of welded joints have been developed to predict the fatigue strength (Fricke 2003, Zhang et al. 2015). Numerous experimental investigations (Cheng et al. 2003, Zhang et al. 2015, Wang et al. 2009) were made on the influence of different types of PWT on carbon steel welds providing information on the residual stress modification and the improved fatigue strength, mostly translated into the flattering of the S-N curve at high number of cycles, but very few on stainless steel. Recently, one study on duplex (EN 1.4462) welds with short time PWT (Young et al. 2007) showed that the relieved residual stress plays a more important role than the microstructure in improving the fatigue strength. High frequency mechanical impact (HFMI) treatment as a residual stress relief approach has been studied in RFCS project "FATWELDHSS" yielding positive results with improved fatigue life for high strength steel (HSS) welded components (Vanrostenberghe et al. 2015). HFMI treatment has also been investigated by (Kuhlmann and Breunig 2017) resulting in improved fatigue strength for HSS due to enhancement of residual stress state, particularly for transverse stiffeners and longitudinal fillet welds. Those findings regarding HFMI are promising for lean duplex grades EN 1.4162 and EN 1.4062, since maintenance of balanced microstructure of those grades is crucial which restricts the PWT possibilities to the mechanical ones only, eliminating heat treatment options. In (Lakshminarayanan and Balasubramanian 2012) advanced welding methods (friction stir welding) applied on ferritic grades are studied. At the structural member level, two former RFCS projects "BRIDGEPLEX" and "SAFSS" (Zilli et al. 2008 and Baddoo et al. 2013) aimed at verifying the technical feasibility of welded bridge using duplex EN 1.4462 and provided tests results for a few joints (Hechler et al. 2007) while (Di Sarno et al. 2003, Di Sarno et al. 2006, Nip et al. 2010) concerned the estimation of the structural performance of stainless steel frames and braces under seismic actions mainly focusing on the influence of hysteretic material behaviour on the member cyclic behaviour. The over-conservatism of Eurocodes for fatigue verification has been highlighted extensively in the RFCS project "BRIDGEPLEX" (Zilli et al. 2008) resulting in economic justification of duplex replacing ordinary carbon steel components owing to the greater mechanical strength and fatigue life of the former. Possibilities of weight reduction in steel bridges by using higher strength steel grades have also been investigated in the RFCS project "OPTIBRI" stressing out the higher fatigue life associated with the latter (Pedro et al. 2017, Baptista et al. 2017).

When it comes to the fatigue assessment of welded joints, different techniques exist such as the nominal stress approach, the effective notch stress method, fracture mechanics and structural hot spot stress method via experimental or numerical investigations. The hot spot stress method to assess the fatigue strength of welded details is continuously used as a straightforward approach due to the exclusion of stress inducers of the weld itself. The method is referenced in the fatigue-based design books and International Institute of Welding (IIW) guidelines (Nussbaumer et al. 2011, Hobbacher 2015). The calculation of the hot spot stress is based on linear or quadratic extrapolation of the stresses at the reference points adjacent to the weld toe where the hot spot is most of the time located, which is the location where fatigue crack initiation is expected (Fricke 2002, Fricke et al. 2002, Niemi and Marquis 2002). As emphasized in the research of Aygül et al. 2012, fatigue design of steel bridges which is most of the time carried out using the nominal stress approach is no longer applicable in cases

where complex geometry with stress-raising effects exists, in which cases the hot spot stress design approaches are needed (e.g. for orthotropic bridge decks). Researches on fatigue life evaluation using hot spot stress method revealed that appropriate modeling techniques play a crucial role on the stress estimations, among other parameters, the element type, the mesh size and mesh type are of prime importance (Aygül et al. 2012, Liu et al. 2014, Lee et al. 2010, Park and Kim 2014). Besides, many findings in the literature point out lower fatigue life based on hot spot stress computation than the one obtained through experimental measurements. Since the hot spot stress computation (e.g. via finite element models) purely exclude the imperfections that have so-called adverse effects on the fatigue resistance (such as the residual stresses), the last statement appears rather illogical.

It can be concluded that the research on duplex welded details submitted to dynamic loading is today scarce. It is either concentrating on austenitic grades, spot welding methods or focussing on the microstructure level. But there exist substantial differences (between high-strength lean duplex and carbon steel) to motivate a specific treatment of the fatigue resistance of duplex, for a safer and more economical use of this material in engineering structures.

General scope of the thesis project

The applicability of lean duplex welded joints in structures submitted to variable loading such as bridges, offshore structures, trucks sub-structures or wind towers necessitates to investigate the proneness of welded details to fatigue. To build a systematic understanding of all the phenomena ruling this research domain is a long and tedious task. Within this project, we will seek to bring enlightenment to this topic via experiments and numerical studies.

The first goal of this research project is to contribute to an increased knowledge of the fatigue behaviour of as-welded lean duplex details via a comprehensive experimental campaign with detailed analyses of the results. Tests under constant amplitude pulsating tension will be conducted on the base material followed by a series of welding jobs on one selection of details, which will be undertaken in the Welding Engineering Centre located on Campus De Nayer (TC Mechanical Engineering). The weld quality and residual stress will be measured and put into perspective to the subsequent comprehensive fatigue testing campaign of these as-welded details.

Eurocode 3 Part 1-9 requires at least 10 to 12 tests to achieve a relevant fatigue curve. On the one hand the tests will sometimes require a relatively high force (up to 100 kN) and, to tackle the slope of the Wöhler curve, a high number of cycles is required on the other hand, therefore leading to time consuming tests. The very high cycle fatigue (above 10^7) is of less interest than the behavior around 2×10^6 cycles for engineering applications but it is our desire to also investigate this aspect, especially to bring enlightenment to the endurance limit of lean duplex. It is hence highly important to devote enough time to this experimental campaign. The experimental findings will be compared to the Eurocode 3 Part 1-9 detail categories. This stage of the project also includes the utilisation of digital image correlation (DIC) method during the tests which provides a detailed information about the entire field of deformation history of the specimens, rendering accurate and precise measurement of the structural stresses during the experiments (Sutton et al. 2009).

The second goal of this research is based on the finite element method. The numerical evaluation of hot spot stress will be done for all the details. Step-by-step FE analyses will be achieved, from simple to complex models. Simple models only consider shell-elements and elastic behaviour disregarding the welds' geometry, geometric discontinuities (misalignment), mechanical imperfections and residual stresses; whereas complex models consider solid-element with the measured material properties within the welding zones (BM, HAZ and FZ) including the welds' geometry, misalignment and the residual stresses. Therefore, a comparison between the experimental results and computed ones will lead to conclusions on the influencing parameters.

In conclusion, including the complexity within the numerical models to assess the structural hot spot stress will enable to illustrate the influence of the imperfections on the fatigue resistance.

The deliverables of the study are: to enrich the literature regarding the use of welded bridge details made of lean duplex grades; to amend the current Eurocodes rules with respect to fatigue of stainless steel (e.g. proposing new detail categories); to improve the general hot spot stress method.

Selection of details

Several researches studying critical fatigue details in bridges based on investigations upon real damage cases exist (Haghani et al. 2012, Al-Emrani and Kliger 2009, Lukic et al. 2017 - ongoing). Fig. 4 gives an overview of the most-pronounced fatigue-prone details in steel bridges. It goes without saying that fatigue is most of the time the designing criterion for a continuous (open or closed) girder (orthotropic deck) due to the presence of several of those critical welded details. Moreover, considering the possible reduction of the cross-sectional areas (plate thicknesses) as a result of an effective utilization of the high mechanical strength of duplex grades, the proneness to fatigue increases. An initial design of a bridge with its main girders made of EN 1.4162 grade was compared to the corresponding designs made of S355 and S690. This will be elaborated hereafter, drawing attention on the possible weight reduction.
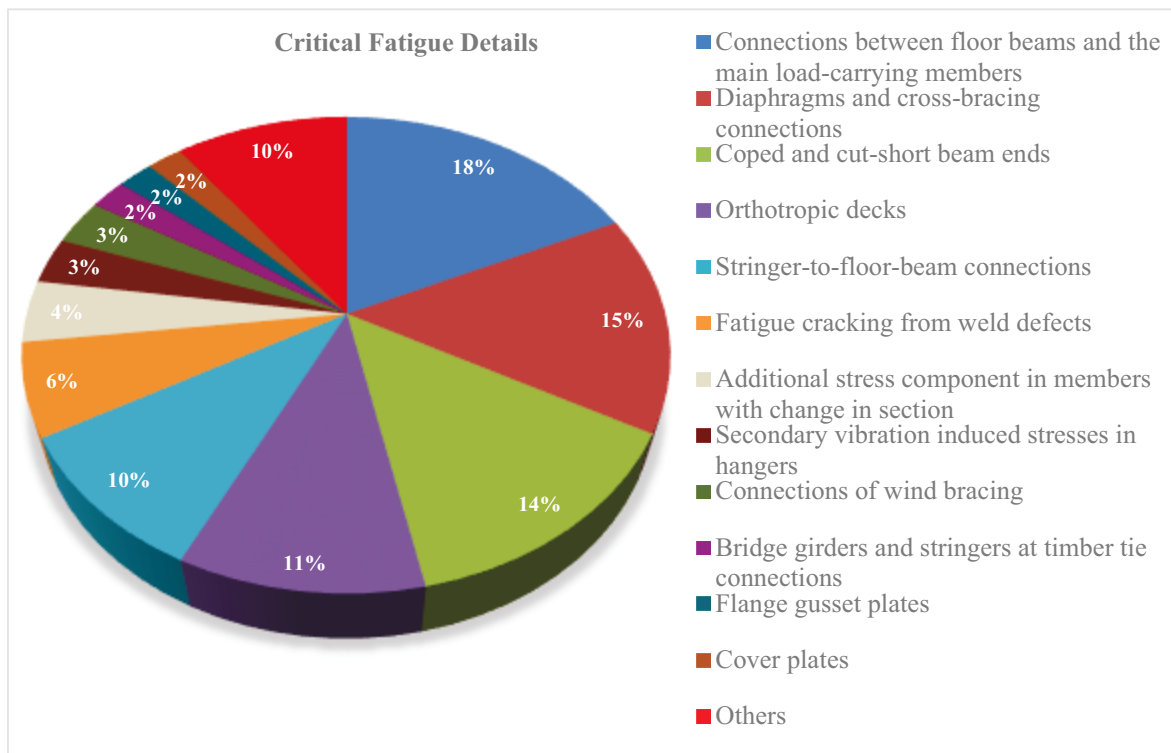
Figure 4. Hierarchy of fatigue-prone details (*Haghani et al., 2012*).

A preliminary selection of 8 critical welded bridge details was made based on the references and on Eurocode 3 Part 2 (EN 1993-2 2006). A schematic representation of these selected details, with respect to the fatigue detail categories of Eurocode 3 Part 1-9 is given in Fig. 5 and the details are presented as follows:

(a) Bearing plate attached to the bottom flange of the longitudinal main bridge girder with the welds all around submitted to tension (detail also-called "NEOPRENE");

(b) Longitudinal weld attachment between the web and flanges;

(c) Transversal stiffeners with welds longitudinal or transverse to the loading direction (unavoidable detail due to susceptibility to shear buckling phenomena);

(d) Cope holes on the main bridge girders;

(e) Tapered flanges inducing additional stress concentration;

(f) Full penetration butt joints of the flanges.
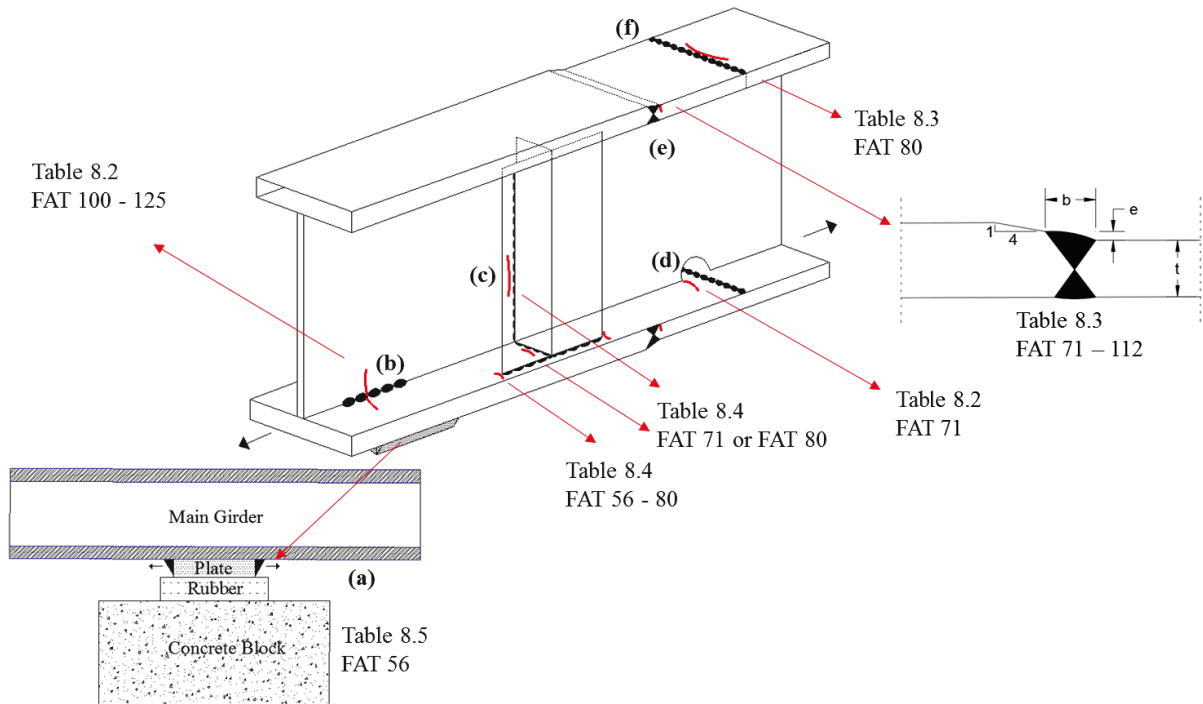
Figure 5. Scheme of the selected critical details.

Case study

The case study presented herein is performed in two steps. Firstly, we consider the main girders of an existing bridge and design them using EN 1.4162, replacing the designs already done by a civil engineering design corporation named "GRID International" for carbon steel, both for S355 and S690.

The hot spot stress of the welded details included in the main girders is evaluated using FE models. Thus, secondly, our intention is to compare the theoretical findings following the Eurocode 3 Part 1-9 to those of the finite element models and hot-spot stress method.

Bridge made of EN 1.4162 duplex grades versus S355 and S690

The objective of this phase is to calculate the possible weight reduction when lean duplex welded components are used. The benefits from the greater mechanical properties of the material are considered according to the latest published design rules for stainless steel (EN 1993-1-4 2006, DMSSS 4th edition 2017). The design has been performed for the 80 meters long inner span of the bridge (Fig. 6), considering the sections located at the supports and at mid-span (Fig. 7). The verifications at Ultimate Limit State (ULS) have been done for the cross-section bending resistance, lateral torsional buckling (LTB) and shear buckling. Serviceability Limit State (SLS) checks whereas, have been performed for the deflection at mid-span.
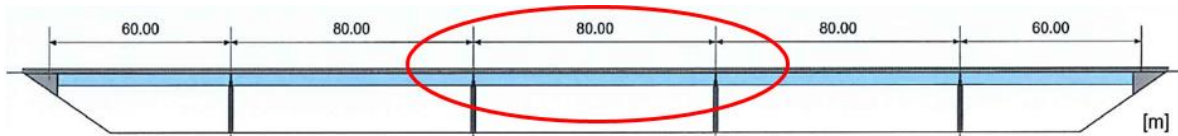
Figure 6. Inner span of the bridge considered for the design of the main girders (*Pedro et al., 2017*).
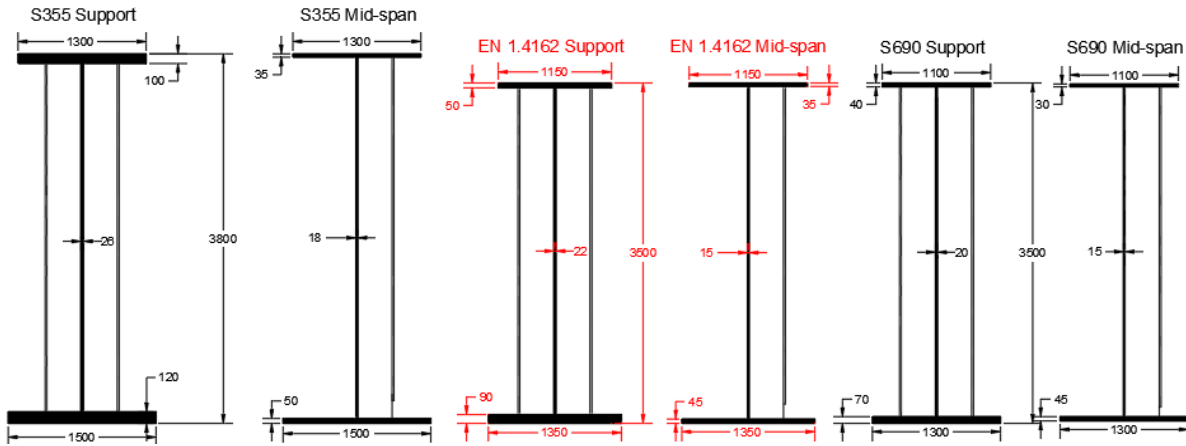
Figure 7. Preliminary design of the main girders made of EN 1.4162 versus S355 and S690.

The following table presents the weight reduction when compared to the solution using carbon steel S355, and weight increase in comparison with carbon steel S690 (Table 1).

Table 1. Comparison of weight for EN 1.4162 vs. S355 and S690.

Obtained values	S355 (kg/m)	S690 (kg/m)	EN 1.4162 (kg/m)	Weight reduction (vs. S355)	Weight increase (vs. S690)
Main girders - support	3164.2	1592	1985.422	-37.25%	+24.71%
Main girders - mid-span	1470.9	1121.6	1195.555	-18.72%	+6.59%

As can be seen from the table, design of the main girders utilizing EN 1.4162 provides a great chance to reduce the weight of the overall structure considerably compared to S355. It is furthermore possible to deduce that the geometry for both S690 and EN 1.4162 are analogous. It is important to mention that the design for EN 1.4162 is not optimized completely; therefore the likelihood to reduce the cross-sectional areas further still exists (ongoing study).

Hot spot stress method versus EN 1993-1-9

This phase of the case study focuses on the comparison between codified predictions and hot spot stress method. Theoretical values of the stress distribution at SLS are calculated based on fatigue load model 3 (FLM3) according to Eurocode 1 Part 2 (EN 1991-2 2003) and Eurocode 3 Part 2. The fatigue design is made using the hot-spot stress method based on finite element models to assess the local stress distribution, considering eight critical details along the girder. For the chosen case study, longitudinal welds, transversal stiffeners and tapered flanges (three details: (b), (c) and (e) of Fig. 5 considering the welds parallel and perpendicular to the load) have been studied. Expanding the study to the rest of the details will be done in the future. The theoretical values for the equivalent constant amplitude stress range have been calculated at the SLS following Eurocode 3 Part 1-9, and compared to the hot spot stress findings obtained from FE analyses. Similarly, the fatigue resistance acquired from detail categories has been compared to the one obtained from the hot spot stress method, using a reference detail. The evaluation is implemented depending on the type of hot spots: type "a" hot spots refer to the weld toe on the plate surface; whereas type "b" hot spots refer to the weld toe at the plate

edge. Surface stress extrapolation is to be carried out through the reduced integration method in which the extrapolation points have been picked up following the IIW guidelines, depending on the mesh size. Fine meshes have been assigned for each reference detail and the stress extrapolation has been implemented using the following equations for type "a" and type "b" hot spots respectively:

$$\sigma_{hs} = 1.67 * \sigma_{0.4t} - 0.67 * \sigma_{1.0t} \tag{1}$$

$$\sigma_{hs} = 3 * \sigma_{4mm} - 3 * \sigma_{8mm} + \sigma_{12mm} \tag{2}$$

The fatigue resistance is calculated using a reference detail which represents the actual detail as closely as possible. As suggested by the IIW guidelines for fatigue resistance evaluation, using the hot spot stress method, the actual detail and the reference detail should be equivalent in terms of meshing and element types. Firstly, the type of stress should be identified which is the nominal stress as in the detail categories. Afterwards, the reference detail and the assessed detail are submitted to equivalent loading, based on the nominal stress described previously. The fatigue resistance of the considered detail, corresponding to 2 million cycles, is a proportion between structural stresses calculated for the reference detail (in consistency with the assigned FAT category) and the assessed details:

$$FAT_{assess} = \frac{\sigma_{hs,ref}}{\sigma_{hs,assess}} FAT_{ref} \tag{3}$$

In cases where shell elements are used, Hobbacher 2008 and Niemi et al. 2006 recommend to use 8-noded quadratic elements, arranged in the mid-plane of the plates that should be modelled. Yet, the study showed that the difference between the numerical results for 8-noded elements and 4-noded elements does not exceed 1 percent, therefore 4-noded elements have been used. The quad element shape with medial axis algorithm has been selected minimizing the mesh transition. Element size has been based on curvature control not exceeding the maximum deviation factor for the aspect ratio which is 0.1; similarly, minimum size control has been based on fraction of global size which is set to 0.1 (same for solid elements). 4-noded shell elements have also been suggested by Lee et al. 2000, especially for analysing thicker plates. If the geometry is modelled using shell elements, the welds are disregarded, as long as the results are not influenced by local bending phenomena. The load could be applied either as a uniformly distributed load on one end of the beam or as a point load acting at a reference point on that end (preferably centroid to avoid additional bending). The reference point is kinematic coupled with the edges of the region of interest. Both possibilities lead to identical hotspot stress values. As a material model, elastic behaviour is considered in consistency with IIW guidelines for hot spot stress evaluation. This assumption conforms to the current stress state in which hot spot stress is calculated, referring to SLS which is far below the yield limit. As the boundary conditions, "Encastre" type restraints are defined on fixed end of the beam, whereas all the translational and rotational degrees of freedoms are fixed except for the loading direction on the free edge of the beam.

(a)   **(b)**
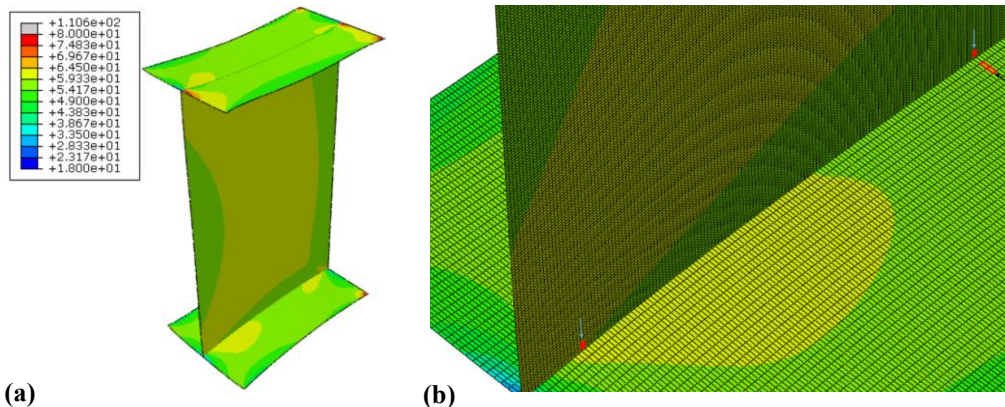
Figure 8. ABAQUS model of longitudinal welds for design of S355: (a) principal in-plane stress distribution along the beam; (b) closer view at the stress extrapolation points.

Table 2. Theoretical values vs. hot spot stress method findings for fatigue verification of longitudinal welds.

Design	$\Delta\sigma_E\,\gamma_{Mf}\,\gamma_{Ff}$ [MPa] (EC3 1-9)	Hotspot stress [MPa] (FEM)	FAT resistance [MPa] (EC3 1-9)	FAT resistance [MPa] (FEM)
S355	57.4	61.5	80	85.1
S690	77.8	82.2	80	85.3
EN 1.4162	48.9	50.1	80	95

Detail (b): Longitudinal welds

In FEM of the present model, no mesh refinement is supplied since the exact location of hot spots was not known. The principal in-plane stress distribution together with part where the surface stress extrapolation occurs are depicted in Fig. 8. The comparison between the hot spot stress method and the theoretical values for that detail can be seen in Table 2.

The detail category based on Eurocode 3 Part 1-9 and on the hot spot stress method are also provided in Table 2, showing good agreement between the codified values and the calculated ones.

Detail (c): Transversal stiffeners

For the detail of transversal stiffeners, finer meshes are used close to the region of hotspots whereas coarser meshes are used elsewhere, reducing the computational time without significant influence on the results. The connection between the stiffeners and the flanges has been defined as tie constraints based on a master-slave surface relationship provided in ABAQUS FE solver. Linear extrapolation has been chosen over quadratic extrapolation since the stress variation close to the hot spots is small. The extrapolation points together with the stress distribution are given in Fig. 9.

The theoretical values are compared to the hot spot stress for the transversal stiffeners in Table 3, as well as the fatigue detail categories.

(a)   **(b)**
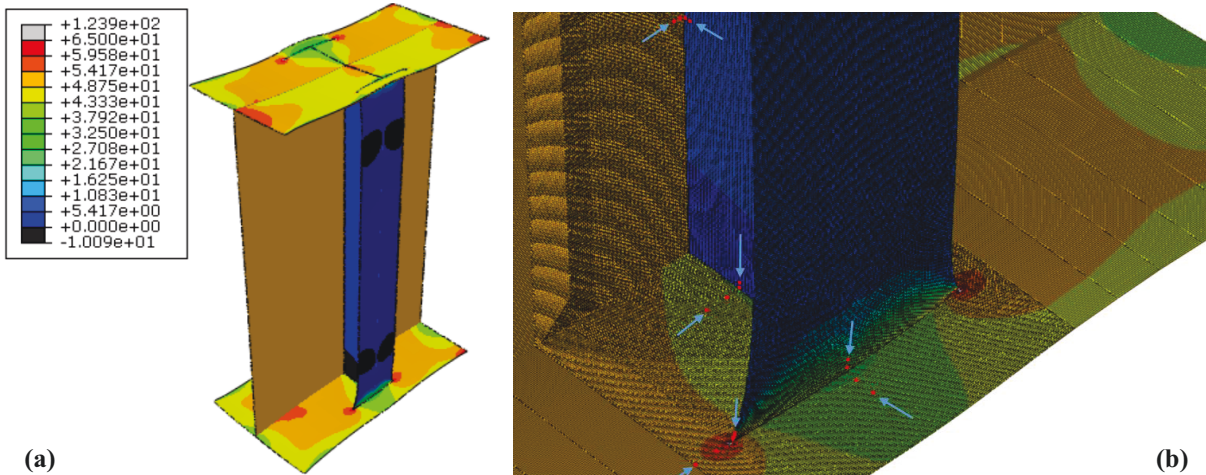
Figure 9. ABAQUS model of transversal stiffeners for design of S690: (a) principal in-plane stress distribution along the beam; (b) closer view at the stress extrapolation points.

Table 3. Theoretical values vs. hot spot stress method findings for fatigue verification of transversal stiffeners.

Design	$\Delta\sigma_E\,\gamma_{Mf}\,\gamma_{Ff}$ [MPa] (EC3 1-9)	Hotspot stress [MPa] (FEM)	FAT resistance [MPa] (EC3 1-9)	FAT resistance [MPa] (FEM)
S355	25.5	26.7	80	98
S690	50	56.4	56	92
EN 1.4162	42.1	45.8	56	91.6

Table 4. Theoretical values vs. hot spot stress method findings for fatigue verification of tapered flanges (S355).

Design	$\Delta\sigma_E \, \gamma_{Mf} \, \gamma_{Ff}$ [MPa] (EC3 1-9)		Hotspot stress [MPa] (FEM)		FAT resistance [MPa] (EC3 1-9)		FAT resistance [MPa] (FEM)	
Section	Support	Mid-span	Support	Mid-span	Support	Mid-span	Support	Mid-span
S355 Top flange	23	14	26.4	18.5	73	84	72	63
S355 Bottom flange	26	57	30.6	68.9	71	78	70	68.6
S690 Top flange	36	7	38	5.19	87	87	78	112
S690 Bottom flange	50	78	50	84.9	75	80	83	76
EN 1.4162 Top flange	25.9	10.3	29	13.9	84	84	100	112
EN 1.4162 Bottom flange	42.1	48.9	45.6	58.1	73	80	76.7	94

The values of the stresses based on the equivalent constant amplitude stress range at SLS and the hot spot stress obtained via FEM are in good agreement. However, fatigue resistance estimations diverge quite a lot from each other. The fatigue resistances estimated by the hotspot stress method tend to be larger than those found using the Eurocode 3 Part 1-9 FAT categories, especially for S690 and EN 1.4162 grades.

Detail (d): Tapered flanges

Due to the local stress concentration effects arising from geometric detail of the tapered flanges, the detail has been modeled using solid elements. Recommendations given by IIW guidelines point out that the use of 20-noded isoparametric elements is appropriate when solid elements are employed.
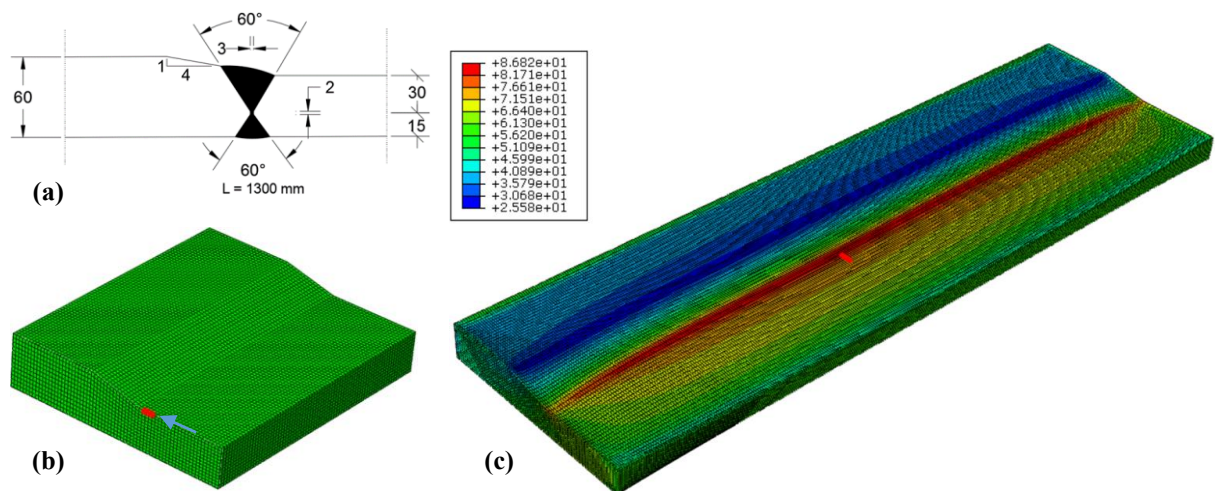
Figure 10. ABAQUS model of tapered flanges: (a) geometry for design of S690 - mid-span; (b) closer view at the stress extrapolation points; (c) normal stress distribution along the tapered flange.

Again, 8-noded solid elements have been preferred over 20-noded elements since the difference between the results did not exceed 1 percent. The hex element shape with advancing front algorithm has been chosen using mapped meshing where appropriate. The finite element model together with the extrapolation points for the bottom flange at the mid-span are depicted in Fig. 10. The theoretical findings based on stresses at SLS and detail categories in Eurocode 3 Part 1-9 are compared to the hot spot stress evaluations, and the results are recapped in Table 4.

Conclusion

This research paper is an introductory document to my long-term PhD project (November 2016 – November 2020) which aims to systematically evaluate the fatigue resistance of lean duplex welded details for engineering applications. The paper briefly summarizes the state of the art mainly focusing on stainless steel as a material, duplex grades and their applications, fatigue resistance of welded components made of this grade, welding practices, and structural hot spot stress method for fatigue verification. A selection of critical welded bridge details has been done based on references and actual stainless steel applications. Based on this selection, two calculations have been carried out. The first one is inspired by RFCS project "OPTIBRI" (Pedro et al. 2017, Baptista et al. 2017), focusing on the design of the main girders of a bridge, the option made of EN 1.4162 grades is designed and compared to carbon steel designs (S355 and S690). The initial conclusions about the preliminary design are promising, especially illustrating a high possibility to reduce the cross-sectional areas compared to the S355 option. It is worth noting that the design has not been optimized yet, hence comparison with S690 design is not reasonable for the moment. Nonetheless, our preliminary calculations for EN 1.4162 lead to similar cross-sectional areas as for the S690 bridge. The second evaluation is based on the hot spot stress method. The theoretical values which are derived based on stresses at SLS and detail categories in Eurocode 3 Part 1-9 are compared to the hot spot stresses, based on FEM. Since the geometry of the cross-sections has a direct influence on the fatigue verification based on hot spot stress method, more time will be allocated to the design optimization as a future work, accordingly the study will be expanded to the rest of the details, made of EN 1.4162.

The first conclusion that we can draw is the conservatism of the Eurocode to assess the fatigue resistance of the high strength steel option. This has already been highlighted several times in different research. For instance, in Zilli et al. 2008 (Bridgeplex), the experimental fatigue resistance of duplex components corresponding to 2 million cycles is 124 % greater than the one estimated by Eurocode 3 Part 1-9. In addition, it is important to remember that the fatigue life estimated by the hot spot stress method is inclined to be smaller than the experimental measurements (Rong et al. 2014). This issue can be primarily explained by the 'residual stress' phenomenon which is a well-known parameter having a paramount impact on the fatigue resistance of welded joints, depending on its direction (tension or compression), distribution and most importantly magnitude (Barsoum and Gustafsson 2009, Barsoum et al 2009). At first sight, it seems that the detrimental effect of the residual stresses is not so high. However, it is only possible to draw such a conclusion after nourishing the analytical study with a significant amount of experimental work which indeed shapes the future of this particular research.

References

Al-Emrani M., Kliger R. (2009): Fatigue prone details in steel bridges. In: *Nordic Steel Construction Conference,* Malmö, Sweden, 8 pp.

Aygül M., Al-Emrani M., Urushadze S. (2012): Modelling and fatigue life assessment of orthotropic bridge deck details using FEM. *International Journal of Fatigue* **40**: 129–142. doi:10.1016/j.ijfatigue.2011.12.015.

Baddoo N. R., Kosmac, A. (2010): Sustainable duplex stainless steel bridges. In: *8ᵗʰ Duplex Stainless Steels Conference*; Ascot, UK. 12 pp. Steel Construction Institute (SCI).

Baddoo N., Faivre L., Rossi B., Manninen T., Serrano V.M., Taljia A., Torkar M., Real E., Gedge G. (2013): *Structural Applications of Ferritic Stainless Steels (SAFSS)*. Research Fund for Coal & Steel (RFCS).

Barsoum Z., Gustafsson M. (2009): Fatigue of high strength steel joints welded with low temperature transformation consumables. *Engineering Failure Analysis* **16**: 2186–2194.

Barsoum Z., Barsoum I. (2009): Residual stress effects on fatigue life of welded structures using LEFM. *Engineering Failure Analysis* **16**: 449–467.

Berezovskaya V, Kostina M, Blinov E, Bannykh I, Bobrova V, Mel'Nik V. (2008): Corrosion properties of austenitic Cr-Mn-Ni-N steels with various manganese concentrations. *Russian Metallurgy (Metally)* **2008** (1): 29-33.

Cheng X., Fisher J.W., Prask H.J. (2003): Residual stress modification by post-weld treatment and its beneficial effect on fatigue strength of welded structures. *International Journal of Fatigue* **25** (9): 1259-1269.

Cho J., Lee C.H. (2016): FE analysis of residual stress relaxation in a girth-welded duplex stainless steel pipe under cyclic loading. *International Journal of Fatigue* **82** (3): 462-473.

Chudnovskii A.D. (1968): The low-cycle fracture strength of austenitic steel. *Metal Science and Heat Treatment* **10** (7): 501-504.

Deng D., Murakawa H. (2006): Numerical simulation of temperature field and residual stress in multi-pass welds in stainless steel pipe and comparison with experimental measurements. *Computational Materials Science* **37** (3): 269-277.

Di Sarno L., Elnashai A.S., Nethercot D.A. (2003): Seismic performance assessment of stainless steel frames. *Journal of Constructional Steel Research* **59** (10): 1289-1319.

Di Sarno L., Elnashai A.S., Nethercot D.A. (2006): Seismic retrofitting of framed structures with stainless steel. *Journal of Constructional Steel Research* **62** (1): 93-104.

Euro Inox and the Steel Construction Institute (2017): *Design Manual for structural stainless steel (DMSSS), fourth edition*. Steel Construction Institute (SCI).

European Committee for Standardization (2003): *Eurocode 1: Actions on structures - Part 2: Traffic loads on bridges*. CEN.

European Committee for Standardization (2005): *Eurocode 3: Design of steel structures - Part 1-9: Fatigue*. CEN.

European Committee for Standardization (2005): *Eurocode 3: Design of steel structures - Part 1-10: Material toughness and through-thickness properties*. CEN.

European Committee for Standardization (2006): *Eurocode 3: Design of steel structures – part 1-4: General rules - Supplementary rules for stainless steels*. CEN.

European Committee for Standardization (2006): *Eurocode 3: Design of steel structures – Part 2: Steel bridges*. CEN.

Fitzpatrick M.E., Fry A.T., Holdway P., Kandil F.A., Shackleton J., Suominen L. (2005): *Determination of residual stresses by X-ray diffraction – Issue 2*. National Physical Laboratory.

Fricke W., Cui W., Kierkegaard H., Kihl D., Koval M., Mikkola T. (2002): Comparative fatigue strength assessment of a structural detail in a containership using various approaches of classification societies. *Marine Structures* **15**: 1–13.

Fricke W. (2002): Evaluation of hot spot stresses in complex welded structures. In: *Proceedings of the IIW fatigue seminar, commission XIII, international institute of welding;* Tokyo, Japan, 12 pp.

Fricke W. (2003): Fatigue analysis of welded joints: state of development. *Marine Structures* **16** (3): 185-200.

Haghani R., Al-Emrani M., Heshmati M. (2012): Fatigue-prone details in steel bridges. *Buildings* **2**: 456–476. doi:10.3390/buildings2040456

Hechler O., Feldmann M., Rauert T., Maquoi R., Zilli G., Maiorana E. (2007): Fatigue of welded details made of duplex stainless steel. In: *Duplex 2007 International Conference & Expo,* Grado, Italy.

Hobbacher A. (2015): *Recommendations for fatigue design of welded joints and components*. International Institute of Welding (IIW Collection). doi:10.1007/978-3-319-23757-2.

Iversen A.K. (2006): Stainless steels in bipolar plates--Surface resistive properties of corrosion resistant steel grades during current loads. *Corrosion Science* **48** (5): 1036-1058.

Jang C., Cho P.Y., Kim M., Oh S.J., Yang J.S. (2010): Effects of microstructure and residual stress on fatigue crack growth of stainless steel narrow gap welds. *Materials & Design* **31** (4): 1862-1870.

Kudryavtsev Y., Kleiman J., Gushcha O., Smilenko V., Brodovy V. (2004): Ultrasonic technique and device for residual stress measurement. In: *X International Congress and Exposition on Experimental and Applied Mechanics,* Costa Mesa, California, USA.

Kudryavtsev Y, Kleiman J. (2007): Fatigue of welded elements: residual stresses and improvement treatments. *Welding in the World-London* 2007; **51**(1):255.

Kuhlmann U., Breunig S. (2017): Categorization of fatigue details in view of post-weld treatments. In: *OptiBri workshop on design guidelines for optimal use of HSS in bridges*; Stuttgart, Germany.

Lahti K.E., Hanninen H., Niemi E. (2000): Nominal stress range fatigue of stainless steel fillet welds — the effect of weld size. *Journal of Constructional Steel Research* **54**: 161-172.

Lakshminarayanan A.K., Balasubramanian V. (2012): Assessment of fatigue life and crack growth resistance of friction stir welded AISI 409M ferritic stainless steel joints. *Materials Science and Engineering* **539**: 143-153.

Lee J., Seo J., Kim M., Shin S., Han M., Park J. (2010): Comparison of hot spot stress evaluation methods for welded structures. *International Journal of Naval Architecture and Ocean Engineering* **2010** (2): 200–210. doi:10.3744/JNAOE.2010.2.4.200.

Linder J., Melander A., Larsson L., Bergengren Y. (1998): Fatigue design of spot welded austenitic and duplex stainless steels. *Fatigue & Fracture of Engineering Materials & Structures* **21** (6): 673–686.

Liu R., Liu Y., Ji B., Wang M., Tian Y. (2014): Hot spot stress analysis on rib-deck welded joint in orthotropic steel decks. *Journal of Constructional Steel Research* **97**: 1–9. doi:10.1016/j.jcsr.2014.01.012.

Merello R., Botana F.J., Botella J., Matres M.V., Marcos M. (2003): Influence of chemical composition on the pitting corrosion resistance of non-standard low-Ni high-Mn-N duplex stainless steels. *Corrosion Science* **45** (5): 909-921.

Nebel T., Eifler D. (2003): Cyclic deformation behaviour of austenitic steels at ambient and elevated temperatures. *Sadhana* **28** (1-2): 187-208.

Niemi E., Marquis G. (2002): Introduction to the structural stress approach to fatigue analysis of plate structures. In: *Proceedings of the IIW fatigue seminar, Tokyo Institute of Technology;* Tokyo, Japan, 18 pp.

Niemi E., Fricke W., Maddox S.J. (2006): *Fatigue analysis of welded components: designer's guide to the structural hot spot stress approach*. The international institute of welding (IIW Doc.), IIW-1430-00, Boca Raton, Fla: CRC Press.

Nip K.H., Gardner L., Elghazouli A.Y. (2010): Cyclic testing and numerical modelling of carbon steel and stainless steel tubular bracing members. *Engineering Structures* **32** (2): 424-441.

Nordberg H. (2005): *Fatigue properties of stainless steel lap joints. Spot welded, adhesive bonded, weldbonded, laser welded and clinched joints of stainless steel sheets-a review of their fatigue properties*. SAE International. doi:10.4271/2005-01-1324

Nussbaumer A., Borges L., Davaine L. (2011): *Fatigue design of steel and composite structures*. ECCS – European Convention for Constructional Steelwork, ISBN (ECCS): 978-92-9147-101-0.

Olsson J, Snis M. (2007): Duplex -- A new generation of stainless steels for desalination plants. *Desalination* **205** (1-3): pp.104-113.

Park J.Y., Kim H. (2014): Fatigue life assessment for a composite box girder bridge. *International Journal of Steel Structures* **14**: 843–853. doi:10.1007/s13296-014-1215-x.

Reis A., Pedro J.O., Baptista C., Virtuoso F., Vieria C. (2017): Challenges and benefits of high strength steel (HSS) in highway bridges. In: *OptiBri workshop on design guidelines for optimal use of HSS in bridges;* Stuttgart, Germany.

Reis A., Pedro J.O., Baptista C., Virtuoso F., Vieria C. (2017): Improved bridge design by use of high strength steel (HSS) with OPTIBRI developments. In: OptiBri *workshop on design guidelines for optimal use of HSS in bridges*; Stuttgart, Germany.

Sutton M.A., Orteu J.J., Schreier H. (2009): Image correlation for shape, motion and deformation measurements: basic concepts, theory and applications. Springer Science & Business Media, New York, NY 10013, USA.

Taran Y.V., Daymond M.R., Eifler D., Nebel T., Schreiber J. (2002): *Study of mechanical features for low cycle fatigue samples of metastable austenitic steel AISI 321 by neutron stress analysis under applied load.* Communication of the Joint Institute for Nuclear Research, E14-2002-161.

Vanrostenberghe S, Clarin M, Shin Y, Droesbeke B, Mee V, Doré M, Marquis G, Parantainen J, Kannengiesser T, Barsoum Z. (2015): *Improving the fatigue life of high strength steel welded structures by post weld treatments and specific filler material (FATWELDHSS)*. Research Fund for Coal & Steel (RFCS).

Wang T., Wang D., Huo L., Zhang Y. (2009): Discussion on fatigue design of welded joints enhanced by ultrasonic peening treatment (UPT). *International Journal of Fatigue* **31** (4): 644-650.

Wei Z., Laizhu J., Jincheng H., Hongmei S. (2008): Study of mechanical and corrosion properties of a Fe-21.4Cr-6Mn-1.5Ni-0.24N-0.6Mo duplex stainless steel. *Materials Science and Engineering* **497** (1-2): 501-504.

Yaghi A., Hyde T.H., Becker A.A., Sun W., Williams J.A. (2006): Residual stress simulation in thin and thick-walled stainless steel pipe welds including pipe diameter effects. *International Journal of Pressure Vessels and Piping* **83** (11): 864-874.

Young M.C., Tsay L.W., Shin C.S., Chan S.L.I. (2007): The effect of short time post-weld heat treatment on the fatigue crack growth of 2205 duplex stainless steel welds. *International Journal of Fatigue* **29** (12): 2155-2162.

Zhang Q.H., Cui C., Bu Y.Z., Liu Y.M., Ye H.W. (2015): Fatigue tests and fatigue assessment approaches for rib-to-diaphragm in steel orthotropic decks. *Journal of Constructional Steel Research* **114**: 110-118.

Zhang H., Wang D., Xia L., Lei Z., Li Y. (2015): Effects of ultrasonic impact treatment on pre-fatigue loaded high-strength steel welded joints. *International Journal of Fatigue* **80**: 278-287.

Zilli G., Maiorana E., Peultier J., Fanica A., Hechler O., Rauert T. (2008): *Application of duplex stainless steel for welded bridge construction (BRIDGEPLEX)*. Research Fund for Coal & Steel (RFCS).

Seismic Design of Steel and Composite Lateral Resisting Systems

SHAHNAZARYAN Davit
University School for Advanced Studies Pavia (IUSS)

SILVA Antonio
University School for Advanced Studies Pavia (IUSS)

ODABAŞI Ömer
University School for Advanced Studies Pavia (IUSS)

GARCIA DE QUEVEDO Pablo
University School for Advanced Studies Pavia (IUSS)

Abstract

The purpose of the project is the seismic design of steel and composite lateral resisting systems, based on the European design guidelines detailed in EN1998-1 (EC8-1) [CEN, 2004]. Number of design scenarios, pertaining different combinations of lateral resisting and gravity resisting systems, are considered. Design is carried out for moment resisting (MRFs) and concentrically braced, namely X-braced and single diagonal, frames (CBFs). The influence of the analysis methods, second-order effects is analyzed. Steel (HEB) is compared to composite (CFST) columns. Whilst also the requirements of EC8-1 are implemented, to account for the inaccurate approach of the code for the calculation of the overstrength factor, Ω, of the dissipative elements, the suggested approach by Elghazouli [2009] is followed. Seismic design is carried out in conjunction with Part 1-1 of Eurocode 3 or EC3-1-1 [CEN, 2005]. Initial structural designs, based on gravity loads for Ultimate Limit State (ULS), are also conducted.

Seismic design of multiple sub-scenarios is considered, with different levels of behaviour factor, q. Third behaviour factor level is adopted, based on the Improved Force-Based Design (IFBD) methodology proposed by Villani *et al.* [2009]. Capacity design beam-to-column joint requirement of the code is taken into account in the design of the frames. All frames are designed based on the modal response spectrum analysis method (MRSM), with a selected few designed with the equivalent lateral force method (ELFM). The most competitive scenarios are pointed out with synoptic tables. Pushoover and non linear time history (NLTH) is carried out to assess the performance of the systems under design level earthquake demands. Results obtained are evaluated by comparing the pushover response with design levels of base shear and overstrength.

The results of a total of 24 design configurations, pushover and NLTH analysis, are synthesized to investigate the way in which the requirements of the code provisions affect the seismic behaviour of the frames. Notable differences are observed between MRF and CBF systems. The similarities and differences as well as drawbacks of the provisions are thoroughly discussed.

Building specification

The building under consideration is part of a 6-storey hotel complex. The seismic action was assumed to be defined as: Spectrum Type 1, Soil Type C, Importance Class II and a_{gR} of 4.0m/s^2 (see Figure 1). Only the seismic design of the transverse lateral resisting system was considered. Regarding the structural loads, the values specified in Table 1 were adopted. It was assumed that whilst for the typical floors the permanent load came from both a 120mm concrete slab and an additional 2.0kN/m^2 for floor finishing and partitions/glazing, for the roof only the former was assumed. Furthermore, different imposed loads were assumed for the common areas/ground floors/access/corridors and for the bedrooms/roof. A number of design scenarios, pertaining different combinations of lateral resisting and gravity resisting systems (seismic frames, or SFs, and gravity frames, or GFs, respectively), were considered, as summarized in Figure 2.

What differentiates the scenarios is the fact that the total seismic mass per floor should be divided by the number of seismic frames. Gravity frames reduce the gravity load of the seismic frames, due to lower areas of influence in the latter. To check for stability though, which in EC8-1 is accounted for with the θ parameter, the gravity load of the gravity frames should be included in that of the seismic frames. Thus, the considered design scenarios were: V3 - SFs at 8m, intermediate GFs; V4 - SFs at 8m, no intermediate GFs; V5 - SFs at 4m, no intermediate GFs; V6 - SFs at 16m, intermediate GF. The seismic masses of the structure, as well as the ones associated with each seismic frame for each scenario, are summarized in Table 2. A combination of permanent and 30% of imposed loads was adopted for the calculation of the seismic masses.
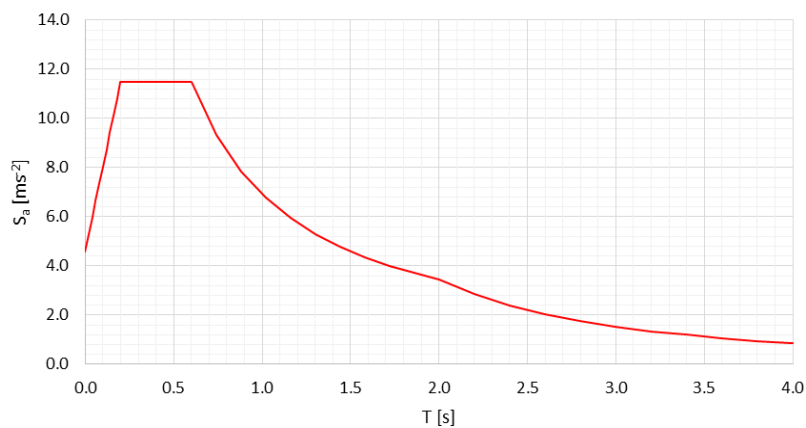
Figure 1. Elastic response spectrum.

Table 1. Structural distributed loads.

Load type		p$_1$ [kN/m^2]	p$_2$ [kN/m^2]	p$_3$ [kN/m^2]
g$_k$	Roof	3.0	3.0	3.0
	Floor	5.0	5.0	5.0
q$_k$	Roof	2..0	2..0	2..0
	Floor	2.0	4.0	2.0
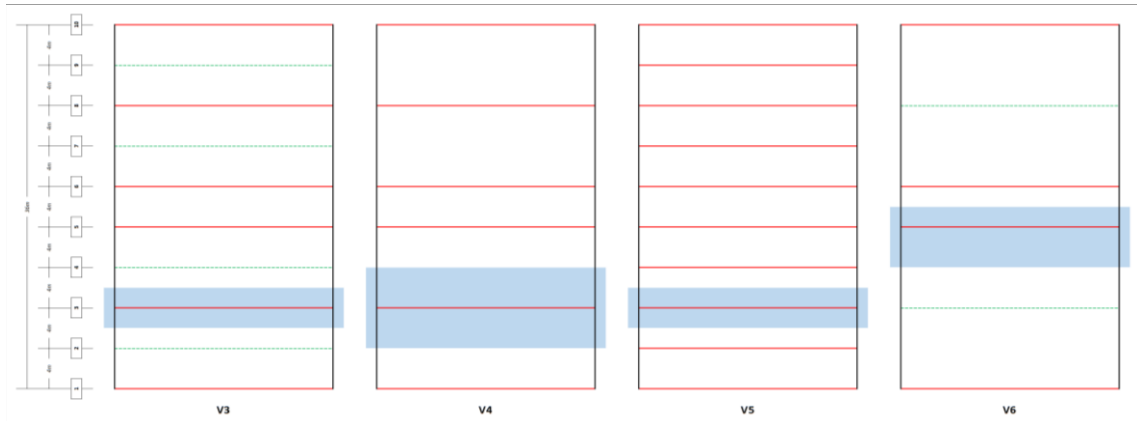
Figure 2. Plan view of the design scenarios.

Table 2. Seismic masses for each design scenario.

Scenario	Total mass [t]	Mass per seismic frame [t]	Mass in roof (per seismic frame) [t]	Mass in floors (per seismic frame) [t]
V3		392	44	70
V4	2352			
V5		235	26	42
V6		588	66	104

Table 3. Gravity point loads for each design scenario.

Scenario	Load type	F_A [kN]	F_B [kN]	F_C [kN]
V3	$G_{k,roof}$	18	33	36
	$G_{k,floor}$	30	55	60
	$Q_{k,roof}$	12	22	24
	$Q_{k,floor}$			36
V4	$G_{k,roof}$	36	66	72
	$G_{k,floor}$	60	110	120
	$Q_{k,roof}$	24	44	48
	$Q_{k,floor}$			72
V5	$G_{k,roof}$	18	33	36
	$G_{k,floor}$	30	55	60
	$Q_{k,roof}$	12	22	24
	$Q_{k,floor}$			36
V6	$G_{k,roof}$	27	50	54
	$G_{k,floor}$	45	83	90
	$Q_{k,roof}$	18	33	36
	$Q_{k,floor}$			54

Regarding the gravity loads on the seismic frames, they were assumed to be transmitted to the main beams by secondary beams in the longitudinal direction. In each of the 8.5m transversal spans, two longitudinal beams at a distance of 3m of the columns were considered to exist. In the central 3m span, the gravity loads were assumed to be transmitted directly to the columns. Table 3 summarizes these concentrated loads, without applying any seismic combination coefficient.

Design of moment resisting systems
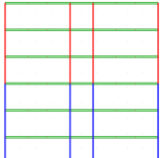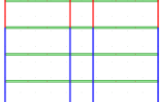
One of the lateral resisting systems considered in this assignment pertains moment-resisting frames. To design these systems, the requirements of EC8-1 were implemented, whilst also accounting for the inaccurate approach of the code for the calculation of the overstrength factor, Ω, of the dissipative elements. The suggested approach by Elghazouli [2009] was followed. Seismic designs were carried out in conjunction with Part 1-1 of Eurocode 3 or EC3-1-1 [CEN, 2005]. Initial structural designs based on gravity loads for Ultimate Limit State (ULS) were also conducted. European S355 steel I-shaped IPE and H-shaped HEB sections were adopted for the beams and columns, respectively. Frames were designed with an elastic analysis using Autodesk Robot Structural Analysis Professional 2018 [Autodesk, Inc., 2018], assuming rigid beam-column connections and a fully fixed base. For both gravity and seismic design, beams and columns were assumed to be laterally restrained, hence no design checks of member stability were carried out.

Gravity design

For the design of the frames for gravity loads at ULS, a factoring of 1.35 and 1.50 of the permanent and imposed loads, respectively, was employed. Beams were designed against flexural demand versus strength, with a single beam section throughout the frame; columns were designed against buckling under compression and combination of axial load and bending moment. Additional serviceability checks were carried out, by limiting beam deflections to L/250, using a characteristic combination of permanent and imposed load. Two groups of column sections were adopted, namely for the lower and upper three storeys. Rather than designing specifically for the scenarios shown in Figure 2, three levels of longitudinal influence widths were considered, namely 4m (V3 and V5), 6m (V6) and 8m (V4). These design solutions were also used for the gravity frames, depending on their own longitudinal influence width (4m and 8m for V3 and V6, respectively). Table 4 summarizes the multiple gravity design solutions obtained.

As one may infer from the summary above, and as expected, member sizes tend to increase with the influence width. In reality, whilst force-related checks governed the sizes of the columns, beam sizes were governed by the serviceability requirement imposed (L/250).

Table 4. Gravity ULS design solutions.

| Longitudinal influence width [m] | Member groups overview | Beams | Columns | | Weight [t] |
			Upper group	Lower group	
4.0		IPE330	HE180B	HE220B	11
6.0		IPE460	HE200B	HE240B	12
8.0		IPE400	HE240B	HE280B	16
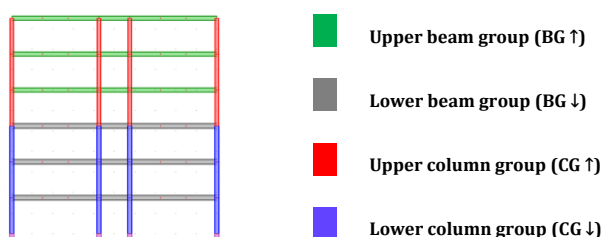
Figure 3. Beam and column groups for seismic design.

Seismic design

Regarding the seismic design of scenarios V3 to V6, multiple sub-scenarios were considered, namely with different levels of the behaviour factor, q. Values of 4 and 6.5, related with DCM and DCH ductility classes of EC8-1, respectively, were adopted. Steel sections of dissipative elements were selected according to the cross-sectional class requirements of the code. A third behaviour factor level was adopted, based on the Improved Force-Based Design (IFBD) methodology proposed by Villani *et al.* [2009]. As before, two groups of column sections were adopted, namely for the lower and upper three storeys, the same as for the beam section groups, as shown in Figure 3.

The capacity design beam-to-column joint requirement of the code (i.e. weak beam-strong column) was taken into account in the design of all frames Moreover, the damage limitation performance requirement was considered by limiting the interstorey drift to 0.75% of the interstorey height. Seismic design of the lateral resisting systems was performed by taking into account second-order effects, limiting the maximum value of the interstorey drift sensitivity coefficient to 0.2, applying the seismic force increase suggested by the code if between 0.1 and 0.2. All frames were designed based on the modal response spectrum analysis method (MRSM), with a selected few designed with the equivalent lateral force method (ELFM).

Steel MRFs

One of the first tasks undertaken in this assignment pertains the seismic design of steel MRF solutions, using the modal response spectrum analysis method (MRSM). Firstly, scenario V3 was adopted, without having defined other alternatives at this stage. For q of 4, it was found that the design was being governed by the serviceability requirement ($d_r v/h \leq 0.75\%$), whilst force-related checks were not a problem. Since this requirement is independent of the behaviour factor adopted, the same design solution was obtained for a higher behaviour factor of 6.5. Obviously, given the dependency of θ with relation to q, the values of θ would increase, and hence the seismic forces might need to be amplified to account for second-order effects. Given that the seismic forces would decrease do to a lower q, and slightly increase due to θ (which is also related with q), the seismic forces obtained in the design combination for non-dissipative elements would be the same. The same, however, does not occur for the combination for dissipative elements, in which Ω is not used. Hence, the use of a higher behaviour factor lowers the forces in the dissipative combination. Given that serviceability related checks are very important in this scenario, the dissipative elements end up being overdesigned just to ensure a sufficient level of lateral stiffness in the frame. Hence, even with low behaviour factors, force related checks end up being guaranteed without needing to resort to different sections. As one may infer, given the lack of sensitivity of the design solution with the behaviour factor adopted, the use of IFBD to estimate the most appropriate q factor ends up being irrelevant. However, it does bring about some important evidence of, at least, what would be the lower bound value this parameter could be taken as, effectively ensuring that the structure is not overdesigned. This, of course, is very important in other scenarios in which guaranteeing a maximum value of θ of 0.2 (or even 0.1) is governing the design.

Table 5. Comparison of seismic design solutions for V3 to V6 steel MRFs.

	V3			V4			V5			V6		
q	2.0[*]	4	6.5	2.1[*]	4	6.5	1.7[*]	4	6.5	2.2[*]	4	6.5
BG ↑	IPE450						IPE400			IPE500		
BG ↓	IPE500						IPE450			IPE550		
CG ↑	HE400B						HE320B			HE450B		
CG ↓	HE450B						HE360B			HE500B		
T_1 [s]	1.00						0.97			1.05		
M [t]	24						20			27		
%M_{GRAV}	215%			151%			180%			216%		
W [kN]	3846						2308			5769		
V_{el} [kN]	2197						1371			3152		
V_{el}/W	57%						59%			55%		
V_d [kN]	1098	549	338	1046	549	338	807	343	211	1433	788	485
{d_rv/h}$_{MAX}$	0.72%						0.69%			0.75%		
θ_{MAX}	0.057	0.114	0.185	0.060	0.114	0.185	0.038	0.089	0.144	0.058	0.105	0.171
Ω	1.00	1.78	2.66	1.04	1.75	2.62	1.03	2.42	3.36	1.01	1.64	2.46
M_{GLOB} [t]	187			143			199			139		
{M_{GLOB}} $_{NORM}$	1.3			1.0			1.4			1.0		

[*] Obtained using IFBD

Since θ is proportional to q, IFBD can prove to be quite a useful approach to counteract the somewhat inaccurate formulation of this parameter in the code.

Given the brief discussion shown above, the design solutions can be summarized as shown in Table 5. In the table, a number of parameters are provided, namely the: i) members adopted for the upper and lower beam and column groups; ii) fundamental period, T_1; iii) total steel weight of the beams and columns of the design solution, M; iv) percentage of M in relation to the respective design solution for gravity design (Table 4), %M_{GRAV}; v) total seismic mass, W, of the frame (Table 2), vi) elastic seismic base shear, V_{el}; vii) ratio of seismic base shear to seismic mass, V_{el}/W; viii) design seismic base shear, V_d, obtained by the quotient of V_{el} and q; ix) maximum value of d_rv/h obtained for the design solution; x) maximum value of θ obtained for the design solution; xi) value of overstrength, Ω, obtained for the design solution; xi) global amount of steel of the design solution (SFs and GFs); xii) normalized global amount of steel.

Looking specifically to scenario V3, analysis of the results shown in the table shows what was discussed in previous paragraphs, namely that the same design solution was obtained regardless of the behaviour factor used. The effect of q can, though, be clearly seen when analysing both θ_{MAX} and Ω. For the former, there is linear dependency to the q factor, being that the lower q suggests that the structure would not be susceptible to second-order effects, and hence these could be ignored, whilst the higher q suggest that the frame would be highly susceptible to the same effects. In this case, the code even suggests to factor the seismic forces by $1/(1-\theta)$, which roughly translates to a 23% increase. This, of course, is clearly inaccurate: the susceptibility of the structure to second-order effects should be independent, in this case, of the behaviour factor adopted in the design, since both the design intensity level and the (design solution of the) structure are the same for different values of q. Regarding Ω, it is clear that the optimal design would be to use a q of 2.0, even though one could be wrongly attracted towards higher values for the sake of reducing the seismic forces, hence expecting smaller cross-sections and cheaper design solutions. This does not become an issue here, due to the fact that there abiding by the upper limitations of θ (say, 0.2) was not governing the design. This is due to the fact that the seismic action is rather high (a_{gR} of around 0.4g). For lower seismicity scenarios,

complying to θ can be a real issue, in which case the adopted behaviour factor, due the inaccurate approach of the code in estimating θ, is of the utmost importance. Under certain circumstances, one can even obtain the same design solution for utterly different seismicity regions [Silva *et al.*, 2017].

Given that the seismic design of scenario V3 was governed by deformation requirements, and knowing that intermediate gravity frames were assumed, it might not be competitive to assume such design solution. Thus, scenario V4 was introduced, in which the gravity frames are removed entirely, and every frame in the transverse direction contributes to the lateral resisting system as a whole. Given the way in which the division of seismic masses per frame is made, as well as how the θ factor is calculated, it is irrelevant if gravity frames exist or not. Hence, the only difference to V3 is the increase in the gravity loads of the beams. However, as observed, the same design solution was obtained. As demonstrated in Table 5, this solution is obviously cheaper than V3, because gravity frames are no longer needed. Regarding scenario V5, it was based on a fairly straightforward objective: since deformation requirements are governing the design, perhaps it could be a good approach to have a higher number of seismic frames in the structure, in this case, spaced at every 4m. In fact, as shown in Table 5, the same requirement ends up being very important for the design, but smaller sections for the structural members can be used, and the weight of a single seismic frame is reduced in comparison to the previous scenarios. However, globally speaking, the higher number of frames (10 SFs) in comparison to V3 (6 SFs and 4 GFs) and V4 (6 SFs) fails to ensure that a competitive solution is reached, as shown in Table 5. Finally, scenario V6 was thought of on the basis of trying to gauge the effect of having less, yet stronger, seismic frames, whilst unavoidably resorting to two intermediate gravity frames. As shown in Table 5, this ends up being the most competitive solution of the set. Still, the design is governed by the same deformation limit, but, even though member sizes are increased, the global quantity of steel in the structure (due to 4 SFs and 2 GFs) is the lowest. It is important to note that the same observations regarding the insensitivity of the solutions to q was observed in all scenarios, given that the same requirement governs all designs. Nevertheless, the full design was still carried out, making sure that force-related checks in the dissipative members were still guaranteed.

As one may infer from Table 5, solution V4 and V6 are the most (globally) competitive, the latter having the lowest amount of steel in the structure (M_{GLOB} of 139t), which accounts for both the seismic frames and gravity frames. Based on the fact that in V6 has frames (seismic and gravity) in the same transverse alignments as the (seismic) frames in V4, the latter was selected as the final design solution. In this way, uniformity/repetition of the multiple transverse frames is guaranteed, possibly simplifying the whole design and construction process.

On the influence of the elastic analysis method (MRSM vs ELFM)

One simple approach the code allows for the consideration of seismic effects is the use of equivalent lateral forces in the frame. To gauge how accurate this method is in comparison to the reference (MRSM) method, the V4 design scenario, with a q of 4, was considered. Table 6 shows a summarized comparison between the design solutions with the different analysis methods, and Table 7 summarizes the equivalent seismic lateral forces obtained with the ELF method.

Table 6. Comparison of seismic design solutions for MRF V4 q=4 between different analysis methods.

Method	BG ↑	BG ↓	CG ↑	CG ↓	T_I [s]	V_{el} [kN]	V_d [kN]	$\{d_rv/h\}_{MAX}$	θ_{MAX}	Ω
MRSM						2197	549	0.72%	0.114	1.75
ELFM	IPE450	IPE500	HE400B	HE450B	1.00	2294	573	0.74%	0.114	1.28

Table 7. Equivalent lateral forces for MRF V4 q=4.

Level	Mass [t]	z_k [m]	$z_k m_k$	S_d [m/s²]	λ	V_b [kN]	F_k [kN]
6	44	21.0	924.8				116
5		17.5	1218.0				153
4		14.0	974.4	1.72	0.85	573	122
3	70	10.5	730.8				92
2		7.0	487.2				61
1		3.5	243.6				31

As highlighted in Table 6, the same design solution is obtained with both analysis methods. A slight variation between the seismic base shears was obtained, with the simplified method overestimating in only 4% the more accurate approach. This is clearly indicative of, under certain conditions, how appropriate resorting to a more simplified methodology can be. It is important to note, however, that since ELFM overestimates the demand on the structure, the deformation check is closer to the limit (0.74%), and the Ω factor is reduced (1.28, a decrease of 30% in comparison to MRSM). This effect on Ω can be particularly relevant for the design of non-dissipative elements. Even though the seismic forces are increased, the decrease of the overstrength is significantly greater. Hence, one could expect the internal forces obtained in the seismic combination for non-dissipative members to be lower for ELFM than for MRSM.

On the influence of second-order effects

One important assumption of EC8-1 relates to the inclusion of second-order effects in the elastic analysis. Whether or not the current formulation of θ is accurate, the code suggests an approximate approach for the consideration of P-Δ effects, namely by increasing the seismic forces by $1/(1-\theta)$ if $0.1 < \theta \leq 0.2$. An alternative procedure would be to include non-linear geometrical effects (NLGA) within the analysis, which is basically mandated by the code if $0.2 < \theta \leq 0.3$. However, nothing prevents the designer to consider the more accurate approach for any value θ might take. Given this, it was found relevant to evaluate how the two approaches (simplified or NLGA) compare, at least for a simple case study, namely MRF V4 q=4 ELFM. Ultimately, one can compare the floor displacements amplified by $1/(1-\theta)$, with the ones obtained with non-linear geometrical effects accounted for in the analysis, as shown in Table 8. According to the results of the table, a maximum value of θ of 0.114 was obtained, entailing an increase of 13% of the seismic lateral forces according to the simplified method of the code. Since linear elasticity is assumed, the lateral displacements of structure are increased by the same amount, as are the internal forces in the members. However, when analysing the same frame with NLGA, one finds that the increase in lateral deformations is, in fact, negligible. In this way, using a simplified approach can be quite conservative, possibly leading to larger cross-sections in the members.

Table 8. Influence of second-order effects for MRF V4 q=4 ELFM.

Level	F_k [kN]	d_e [cm]	d_r [cm]	θ	θ_{MAX}	$(1-\theta_{MAX})^{-1}$	F_k x $(1-\theta_{MAX})^{-1}$			NLGA	
							$F_{k,\theta}$ [kN]	$d_{e,\theta}$ [cm]	$d_{r,\theta}$ [cm]	$d_{e,P-\Delta}$ [cm]	$d_{r,P-\Delta}$ [cm]
6	116	0.65	2.61	0.037			131	0.74	2.94	0.65	2.61
5	153	1.04	4.18	0.066			172	1.18	4.71	1.04	4.18
4	122	1.28	5.14	0.090	0.114	1.13	138	1.45	5.80	1.29	5.14
3	92	1.29	5.17	0.101			103	1.46	5.83	1.29	5.16
2	61	1.28	5.12	0.114			69	1.44	5.77	1.28	5.12
1	31	0.76	3.04	0.078			34	0.86	3.43	0.76	3.03

Table 9. Comparison of seismic design solutions for MRF V4 q=4 ELFM between steel and CFST columns.

	Steel	CFST
BG ↑	IPE450	
BG ↓	IPE500	
CG ↑	HE400B	◎ 457x10
CG ↓	HE450B	◎ 508x16
T_1 [s]	1.00	0.94
V_{el} [kN]	2294	2449
V_d [kN]	573	612
$\{d_r v/h\}_{MAX}$	0.74%	0.72%
θ_{MAX}	0.114	0.098
Ω	1.28	1.66
M_{STEEL} [t]	23.8	23.0
$V_{CONCRETE}$ [m^3]	-	13.8

It is important to note that the level of conservativism discussed before can be attributed to a number of reasons, the main one being that the code suggests an increase of the seismic forces by $1/(1-\theta_{MAX})$. However, as shown in the table, θ is far from being constant along the height of the frame, with values as low as 0.037. Hence, it might be overly conservative to assume that every storey will be equally susceptible to P-Δ effects, whilst on top of that assuming the worst case scenario of θ.

Steel (HEB) versus composite (CFST) columns

One alternative to the use of steel open sections are concrete-filled steel tube (CFST) members, which, due to a number of advantages, can prove to be a competitive structural solution. In order to gauge this effect in the MRFs considered herein, archetype MRF V4 q=4 ELFM was adopted. The seismic design was carried out by using circular CFSTs for the columns and IPE sections for the beams. Since the design of the steel frames was being governed by deformation requirements, ensuring that CFST columns of equivalent lateral stiffness in comparison to the original HEB sections is mandatory. However, as later discovered, the design of the composite system was also governed by the limit in the axial load in all columns imposed by EC8-1 ($N_{ED}/N_{pl,Rd}$ < 30%). Table 3.6 shows a summarized comparison between the design solutions with the different column types. For the CFST members, their designation expresses the relationship between the external diameter and thickness of the tube, in mm.

As shown in the following table, the use of CFST members instead of steel HEB columns can lead to a slight reduction in the total amount of steel (0.8t or a 3% decrease for a single frame). This, however, is attained by having to resort to around 13.8m^3 of concrete, and likely more expensive, possibly proprietary, beam-to-column connection details. However, and as demonstrated by Silva *et al.* [2017], the use of CFST columns in detriment of HEB steel members can significantly improve the seismic performance of the system.

Design of concentrically braced systems

The other lateral resisting system considered in this assignment was concentrically braced frames (CBFs), designed according to EC8-1 and EC3-1-1. Initial structural designs based on gravity loads for Ultimate Limit State (ULS) were also conducted, European S355 steel I-shaped IPE and H-shaped HEB sections were adopted for the beams and columns, respectively, and square hollow tubular

sections for the bracing members. Frames were designed with an elastic analysis using Autodesk Robot Structural Analysis Professional 2018 [Autodesk, Inc., 2018]. For both gravity and seismic design, beams and columns were assumed to be laterally restrained, hence no design checks of member stability were carried out.

Gravity design

For the design of the CBFs for gravity loads at ULS, a factoring of 1.35 and 1.50 of the permanent and imposed loads, respectively, was employed, with the same requirements as for MRFs. EC8-1 mandates the gravity design to be carried out without accounting for the braces. Given that for the design of CBFs beams were assumed to be pinned at the ends, as was the case of the base, new gravity designs were carried out, as summarized in Table 10.
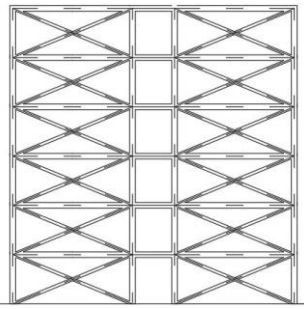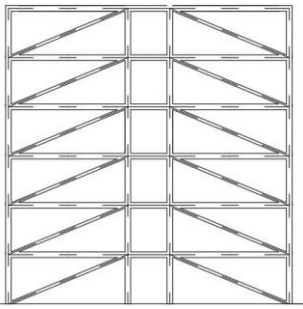
Table 10. Gravity ULS design solutions for pin-ended beams.

Longitudinal influence width [m]			4.0		6.0	
Member			Beam	Column	Beam	Column
	6		IPE400	HE180B	IPE 450	HE240B
	5		IPE450	HE180B	IPE 500	HE240B
	4		IPE450	HE180B	IPE 500	HE240B
Level	3		IPE450	HE200B	IPE 500	HE240B
	2		IPE450	HE200B	IPE 500	HE240B
	1		IPE450	HE220B	IPE 500	HE240B
Weight [t]			14.0		17.6	

Seismic design

Regarding the seismic design of the CBFs, only V3 (for X-shaped and single-diagonal) and V6 (for X-shaped, single-diagonal CFBs) were considered. Whilst for X-shaped and single-diagonal CBFs, two levels of behaviour factor were considered (q of 2 and 4). Table 11 summarizes the design scenarios considered for CBFs. The damage limitation performance requirement was considered by limiting the interstorey drift to 0.75% of the interstorey height, and second-order effects were considered by limiting θ to 0.2, applying the seismic force increase suggested by the code if between 0.1 and 0.2.

Table 11. Design scenarios for CBFs.

	X-shaped	Single-diagonal
Bracing type		
q	2 and 4	
Scenario	V3 and V6	

According to the European code, some uniformity in the dissipative behaviour is ensured along the height of the structure, hence preventing concentration of damage (e.g. soft storey collapse mechanism). However, the combination of this with other requirements may result in significant overdesign of the bracings, especially of the uppermost storey is considered. However, the code does not explicitly state whether this should or not be the case. Hence, and following the requirements for MRFs, the requirement for uniformity in Ω was evaluated by disregarding the uppermost storey. As before, all frames were designed based on the modal response spectrum analysis method (MRSM), with a selected few designed with the equivalent lateral force method (ELFM).

Steel X-braced CBFs

Regarding the design of X-CBFs, regardless of V3 or V6 scenarios, for q of 4, it was found that the design of the beams and columns was being governed by the maximum service deflection and axial ULS gravity load, respectively. After this, minimum braces were adopted (abiding by the maximum allowed value of non-dimensional slenderness of 2.0). In order to comply with the code's requirement regarding the uniformity in Ω ($\Omega_{MAX}/\Omega_{MIN} \leq 1.25$), the braces in the lower stories would need to be increased, thus increasing Ω_{MIN}. This makes the majority of the braces overdesigned, just to comply with the previous requirements. This means that even if q is reduced to 2, therefore increasing the seismic demand of the dissipative members, the reserve in capacity is sufficient in guaranteeing force-related checks. Hence, the same structure was obtained for X-CBFs for both behaviour factor levels. One important aspect to highlight is that, unlike MRFs, complying with the adopted limit in d_rv/h, as well as controlling θ, was not an issue. This is due to the inherently lower flexibility of these braced systems.

Table 12. Comparison of seismic design solutions for V3 and V6 steel X-CBFs.

		V3			V6		
q		2	4		2	4	
Member		Beam	Column	Brace	Beam	Column	Brace
Level	6	IPE400	HE280B	SHS160x5	IPE450	HE300B	SHS160x5
	5	IPE450	HE280B	SHS160x5	IPE500	HE300B	SHS160x5
	4	IPE450	HE280B	SHS160x6.3	IPE500	HE300B	SHS160x6.3
	3	IPE450	HE300B	SHS160x8	IPE500	HE300B	SHS160x8
	2	IPE450	HE300B	SHS180x8	IPE500	HE340B	SHS160x8
	1	IPE450	HE400B	SHS180x10	IPE500	HE400B	SHS180x8
T_1 [s]		0.60			0.30		
M [t]		22.2			26.7		
%M_{GRAV}		159%			152%		
W [kN]		3846			5768		
V_{el} [kN]		3560			4650		
V_{el}/W		93%			81%		
V_d [kN]		1780	890		2325	1163	
$\{d_rv/h\}_{MAX}$		0.45%			0.49%		
θ_{MAX}		0.02	0.04		0.02	0.05	
Ω		1.9	3.8		1.3	2.7	
M_{GLOB} [t]		178			138		
$\{M_{GLOB}\}_{NORM}$		1.3			1.0		

Given the aforementioned observations, the design solutions can be summarized as shown in Table 12. In the table, a number of parameters are provided, namely the: i) members adopted for beams, columns and braces; ii) fundamental period, T_1; iii) total steel weight of the design solution, M; iv) percentage of M in relation to the respective design solution for gravity design (Table 4), $\%M_{GRAV}$; v) total seismic mass, W, of the frame (Table 2), vi) elastic seismic base shear, V_{el}; vii) ratio of seismic base shear to seismic mass, V_{el}/W; viii) design seismic base shear, V_d, obtained by the quotient of V_{el} and q; ix) maximum value of d_rv/h obtained for the design solution; x) maximum value of θ obtained for the design solution; xi) value of overstrength, Ω, obtained for the design solution; xi) global amount of steel of the design solution (SFs and GFs); xii) normalized global amount of steel. As one may infer from the table above, the most competitive scenario is V6, with the lowest M_{GLOB}.

Steel single-diagonal CBFs

As an alternative to X-CBFs, single diagonal concentric bracings can be used. Hence, and in order to have a solid basis of comparison, the same design scenarios were adopted. In similar fashion to X-CBFs, the design of the beams and columns was governed by the maximum service deflection and axial load at ULS gravity, respectively. It is important to mention that even though higher drift ratios are obtained, the low flexibility of these braced systems still allows for the limit to be easily verified. Given the aforementioned observations, the design solutions can be summarized as shown in Table 13. Once again, the most competitive scenario is V6, with the lowest M_{GLOB}.

As mentioned above, the seismic design of the X-CBFs, in case of released beam elements, was being governed by the criterion of maximum service vertical deflection. This, of course, is a more complicated requirement to comply with due to the end releases of the member: for pin-ended beams, the deflection is going to be significantly higher in contrast to rigid beam-to-column connections, as is the case in the considered MRFs. In order to quickly gauge how the designs would change if this serviceability criterion was less critical, one archetype V6 single-diagonal CBF was considered.

Table 12. Comparison of seismic design solutions for V3 and V6 single-diagonal CBFs.

		V3			V6		
q		2	4		2	4	
Member		Beam	Column	Brace	Beam	Column	Brace
Level	6	IPE400	HE280B	SHS160x5	IPE450	HE300B	SHS160x5
	5	IPE450	HE280B	SHS160x5	IPE500	HE300B	SHS160x5
	4	IPE450	HE280B	SHS160x6.3	IPE500	HE300B	SHS160x6.3
	3	IPE450	HE300B	SHS160x8	IPE500	HE300B	SHS160x8
	2	IPE450	HE300B	SHS180x8	IPE500	HE340B	SHS160x8
	1	IPE450	HE400B	SHS180x8	IPE500	HE400B	SHS180x10
T_1 [s]		0.83			0.99		
M [t]		20.7			23.1		
$\%M_{GRAV}$		148%			131%		
W [kN]		3846			5768		
V_{el} [kN]		2666			3354		
V_{el}/W		69%			58%		
V_d [kN]		1333	667		1677	839	
$\{d_rv/h\}_{MAX}$		0.58%			0.70%		
$θ_{MAX}$		0.04	0.07		0.04	0.09	
Ω		1.3	2.6		1.1	2.2	
M_{GLOB} [t]		169			124		
$\{M_{GLOB}\}_{NORM}$		1.4			1.0		

Beams and columns were fixed in order to assess whether we can improve the design and have a governing design requirement related to the seismic design rather than a gravity design. As one might expect, it was shown that gravity design requirements, for fix-ended beams, are not as critical. Also, given the possible collapse mechanisms, compliance with the requirement of uniformity in Ω was not followed (this approach may be adopted for CBFs with rigid beam-to-column connections). One of the main changes related with the different end conditions of the beams is related with higher axial loads and bending moments for fix-ended members. This aspect hinders the design of single-diagonal CBFs, making it very complicated to reach a design solution for the beams. The only way to overcome this use X-CBFs, distributing the axial loads in the beams by diagonals in two bays. Still, significant axial loads and bending moments account for the critical design requirement. Shear demand for the short beams of 3m will also increase, not governing, however, the overall design provisions. It is important to mention that the fundamental period of the frame in this case was 0.57 sec, with an M_{GLOB} of 135t, which is higher compared to the scenario of pinned beams.

Comparison of concentrically bracing types

Given the fairly comprehensive database of designs described in this section, with multiple design solutions for various CBF configurations, it is possible to attain some comparisons between the systems, as shown in Table 14. As one may infer, both X-shaped and single-diagonal CBF solutions lead to fairly similar overall structural weights (M_{GLOB}). The most competitive, however, is the single-diagonal scenario, even though the other option is only 10% heavier. However, the fact that one would have overlapping braces in the X configuration, will also add some contribution to how less competitive it should be. Hence, provided with this pair of available options, one would likely choose the single-diagonal option. Perhaps, if other options were available (e.g. inverted and regular V-bracing across two consecutive stories, with alignment continuity at the midspan of the intermediate beam), they might prove to be more competitive as a whole.

Table 14. Comparison of seismic design solutions for V6 CBFs.

Bracing type	Scenario	M_{GLOB} [t]	$\{M_{GLOB}\}$ NORM
X-shaped	V6	138	1.1
Single-diagonal		124	1.0

Table 15. Seismic design solutions for single-diagonal CBF V6 q=4 with different analysis methods.

Method	Level	Beam	Column	Brace	T_1 [s]	M [t]	V_{el} [kN]	V_d [kN]	$\{d_r v/h\}_{MAX}$	θ_{MAX}	Ω
MRSM	6	IPE450	HE300B	SHS160x5	0.99	23.1	3354	839	0.70%	0.09	2.2
	5	IPE500	HE300B	SHS160x5							
	4	IPE500	HE300B	SHS160x6.3							
	3	IPE500	HE300B	SHS160x8							
	2	IPE500	HE340B	SHS160x8							
	1	IPE500	HE400B	SHS180x10							
ELFM	6	IPE450	HE300B	SHS160x5	0.79	23.2	4364	1091	0.43%	0.03	1.7
	5	IPE500	HE300B	SHS160x5							
	4	IPE500	HE300B	SHS160x6.3							
	3	IPE500	HE300B	SHS180x8							
	2	IPE500	HE340B	SHS180x8							
	1	IPE500	HE400B	SHS180x10							

Table 16. Equivalent lateral forces for single-diagonal CBF V6 q=4.

Level	Mass [t]	z_k [m]	$z_k m_k$	S_d [m/s^2]	λ	V_b [kN]	F_k [kN]
6	44	21.0	1387				220
5		17.5	1827				290
4		14.0	1462	2.18	0.85	1091	232
3	70	10.5	1096				174
2		7.0	731				116
1		3.5	365				58

On the influence of the elastic analysis method (MRSM vs ELFM)

In similar fashion to what was carried out for MRFs, the effect of the method of elastic analysis was also studied for a single CBF archetype, namely the single-diagonal CBF V6 with a q of 4. The comparisons obtained are summarized in Table 16. As one may infer, very slight variations were obtained in the final design solution, namely the diagonals in levels 2 and 3, which were defined as SHS160x8 for MRSM, were increased to SHS180x8 for ELFM. This can be mainly attributed to an overestimate of the seismic demand when accounting only for the contribution of the fundamental mode (ELFM). Hence, the overall elastic base shear (even if the period was the same) is higher. Unlike for MRFs, the results seem to indicate a higher level of dependency of the accuracy of the analysis method on higher then fundamental modes of vibration. Even though the difference is not substantial, if the seismic demand is overestimated, overdesigned solutions might be obtained.

Non-linear static and dynamic analyses

Nonlinear analyses were performed for one MRF archetype (V4) and one single-diagonal CBF (V6) system. Pushover analyses were carried out for both systems, and nonlinear time history analyses (NLTHA) are only performed only for the MRF system.
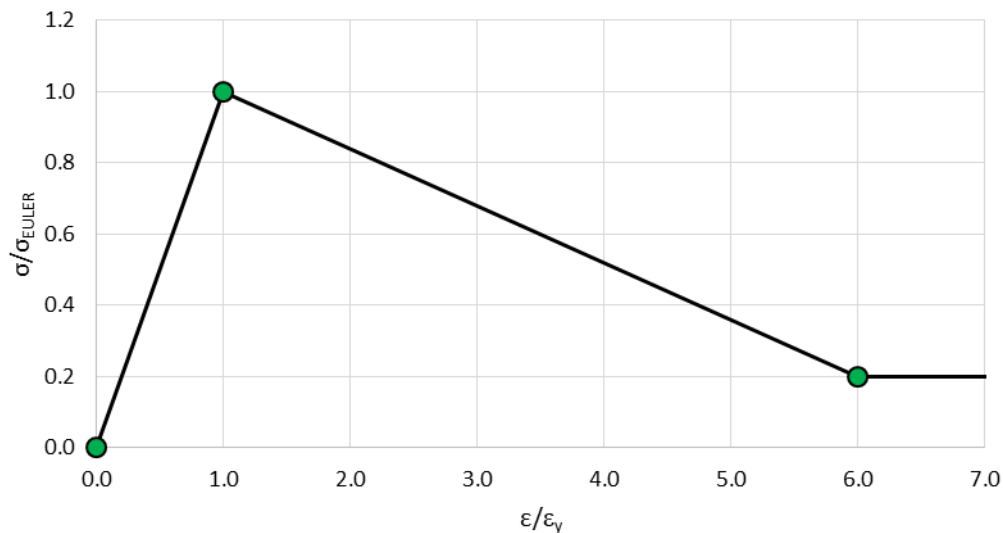
Figure 4. Load-deformation relationship of the brace element under compression.

Modelling Assumptions

The numerical model of the MRF system was generated using OpenSees [Mazzonni *et al.*, 2006], whilst the CBF model was attained using SAP2000. The masses were assumed as lumped at each floor and the floor nodes were constrained in the horizontal direction to mimic the rigid diaphragm behaviour. In the MRF model, nonlinear behaviour in all structural members was considered through a distributed plasticity approach. However, in the CBF model, material nonlinearity was defined with concentrated plasticity by using nonlinear hinges. In the case of columns, hinges were placed at member ends and for the braces, and axial tension-compression hinges were placed at the mid-sections. To simulate the buckling behaviour, a simplified method was utilized. The backbone curve of the brace hinge was defined as trilinear, where the compression capacity was set to the stress that corresponds to Euler buckling force. Post-buckling stiffness of these hinges was defined as negative until the stress dropped to 20% of the compression capacity (Figure 4).

Pushover Analyses

Nonlinear static analyses were performed to assess the performance/behaviour of the two systems under design level earthquake demands. These considered a first mode proportional loading pattern. The results obtained were evaluated by comparing the pushover response with the design levels of base shear and overstrength. Moreover, the determination of the displacement demands under the assumed level of earthquake, which is characterized by the elastic response spectrum (N2 method in EC8-1), as explained in the following lines:

   I.   The load pattern for the pushover analysis is assumed as the first mode shape of the frame;
   II. The structure is pushed up to an arbitrary roof displacement;
   III. Pushover curve is converted into modal capacity curve using the following dynamic conversion formula:

$$S_{d,1} = \frac{u_{xN1}}{\phi_{xN1}\, \Gamma_{x1}}$$

where, $S_{d,1}$ is the SDOF spectral displacement, u_{xN1} is the roof displacement of the actual system, ϕ_{xN1} is the first mode shape amplitude at the roof and Γ_{x1} is the participation factor for the first mode of vibration.

   IV. The modal displacement demand is determined using equal displacement rule;
   V.   Finally, the target displacement demand is computed through back-conversion by the following expression:

$$u_{xN1} = \phi_{xN1}\, \Gamma_{x1}\, S_{d,1}$$

   VI. Member deformations are checked under the above-mentioned target displacement.

Comparison with design base shear and overstrength for MRFs

The pushover response obtained for the MRF archetype is shown in Figure 6. As one may infer from the results shown in figure, the model exhibited a stable behaviour up to the maximum level of deformation adopted.

A number of interesting aspects can be observed in the figure above. Firstly, one can clearly see that the elastic base shear exceeds the capacity of the structure. Hence, a certain level of reduction of the seismic forces is required. However, assuming high levels of behaviour factor, for this particular case, leads to fairly overdesigned structures, as observed by comparing the design levels of base shear with the base shear associated with the formation of the first plastic hinge. In reality, this can be inferred

even at a design stage by the values of overstrength. With the use of IFBD though, the optimum value of q can be estimated, which, in this case, leads to a fairly accurate estimate of the real behaviour of the structure. As demonstrated, the difference between the design base shear for q of 2.1 (obtained with IFBD) and the base shear at the first plastic hinge is negligible, and probably exists at all due to rounding of q. More importantly, it is important to highlight the comparisons between the design-estimated overstrength and the real values of this parameter from the pushover curve. As one may conclude, a direct comparison of Ω from pushover and Ω from the design consistently leads an underestimate of the latter in comparison to the former. This means that the seismic demand during the design level was overestimated and, hence, the reserve of capacity in the structure (Ω) is lower than in reality. This however, can be attributed to the fact that, as mentioned in previous sections, the approach followed by the code of increasing the seismic demand by $(1-\theta_{MAX})^{-1}$ is not only overly conservative, but inaccurate. If the overestimate level of the seismic demand is accounted for when comparing the pushover and design values of Ω, a fairly good agreement between the two is found.
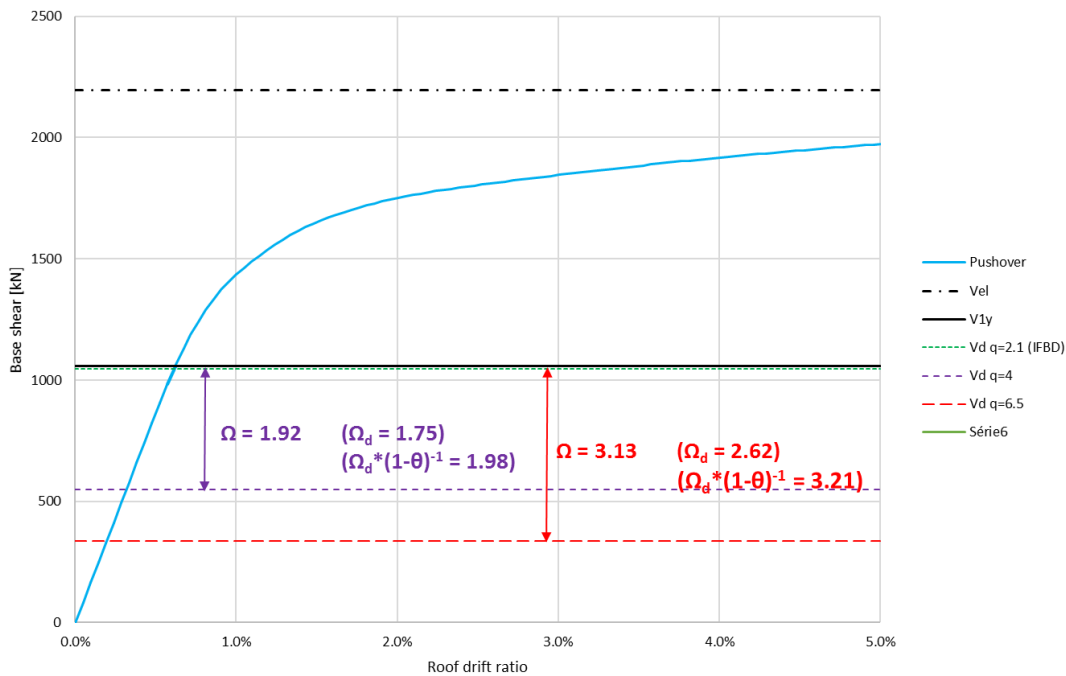
Figure 5. Pushover response for the MRF archetype.

Pushover-based assessment for MRFs

Modal capacity curve of the MRF is plotted together with EC8 elastic spectrum in Figure 6. The roof displacement demand is calculated as 20 cm which corresponds to a ductility demand *q* of 1.6 meaning that under design level demands, the structure is expected to remain essentially elastic. Moreover, member rotations are checked at the first story level to verify whether the capacity design principles are assured or not. Figure 7 and Figure 8 present nonlinear behaviour of the beam and column elements under increasing roof displacements. Results indicate that yielding starts at the base of inner columns and both ends of the middle beam nearly at the same time.
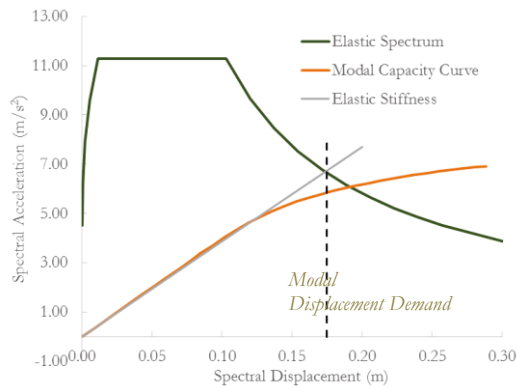
Figure 6. Modal capacity curve of the MRF. Design-level roof displacement demand, u_{xN1} = 20 cm.
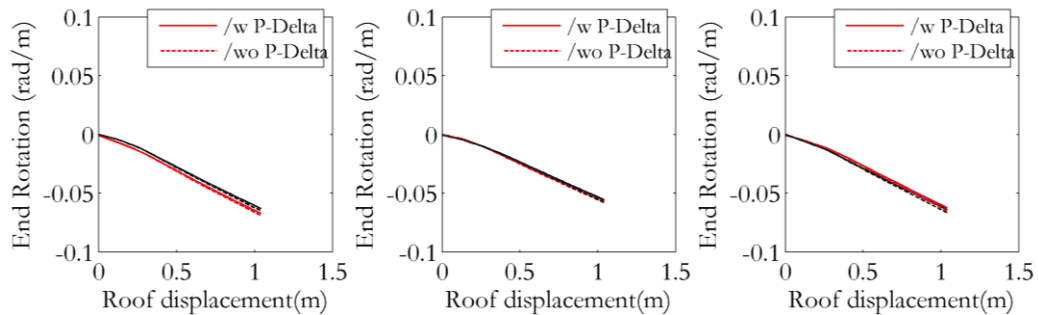
Figure 7. First story beam rotations versus roof displacement. Black lines represent the ith end rotations and red lines represent the jth end rotations.
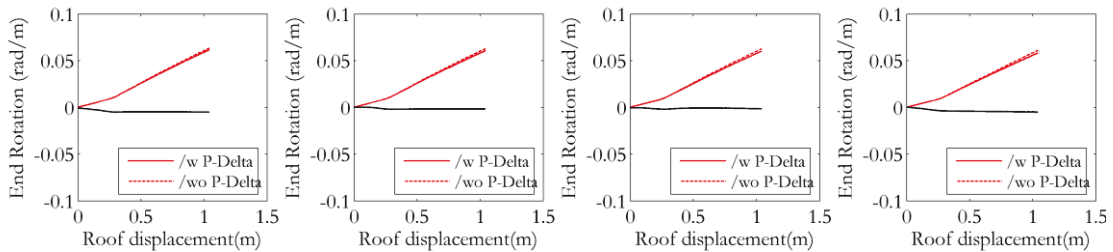
Figure 8. First story column rotations versus roof displacement. Black lines represent the top side end rotations and red lines represent the base rotations.

Comparison with design base shear and overstrength for single-diagonal

In similar fashion to what was performed for MRFs, the pushover response obtained for the CBF archetype is shown in Figure 9. Once again, the model exhibited a stable behaviour up to the maximum level of deformation adopted. Furthermore, the level of elastic base shear is, once again, higher than the lateral capacity of the structure. Unlike for MRFs, the application of IFBD was not tested. However, as before, assuming code-prescribed values of q leads to not optimum overstrength levels. Since compliance with the maximum allowed level of θ was not an issue in these systems, the simplified (seismic demand increase) approach of the code was not applied. Hence, a fairly good match between the Ω obtained pushover and Ω from the design exists. This, once again, underlines how both inaccurate and conservative the simplified approach may be, as it may convey a wrong perception of what the actual response of the structure is and, hence, lead to overdesigned solutions.
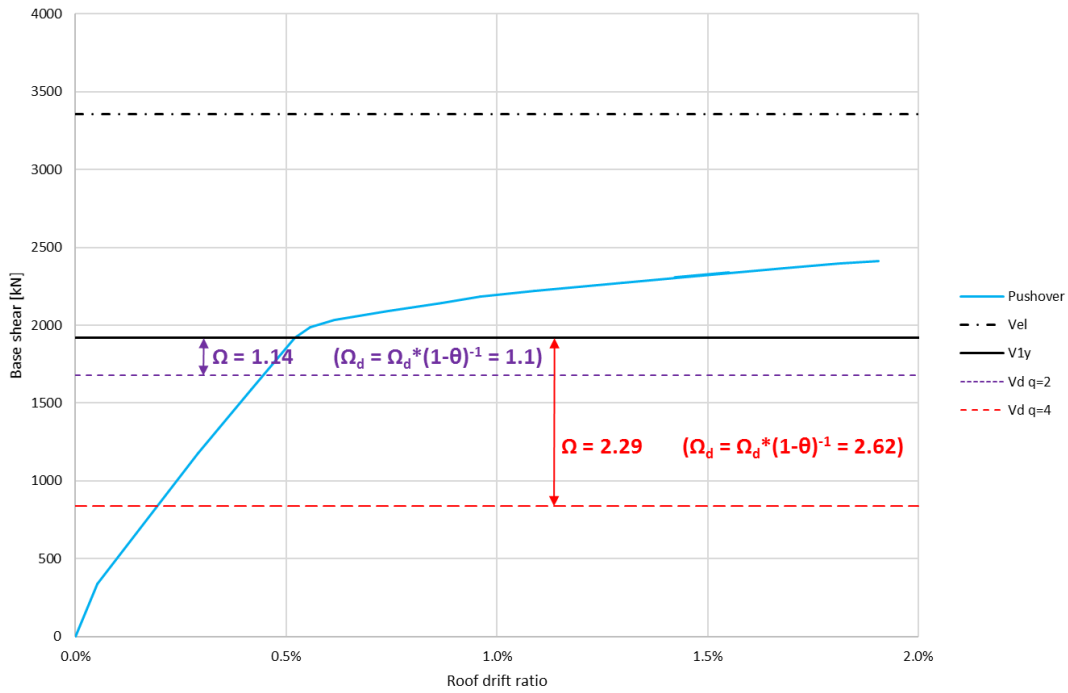
Figure 9. Pushover response for the CBF archetype.

Pushover-based assessment for CBFs

Modal capacity curve of the CBF is shown in Figure 6. The roof displacement demand, u_{xN1}, was calculated as 14cm, which corresponds to a ductility demand q of 1.2. Note that the target roof displacement is determined by assuming a secant stiffness of the CBF structure since buckling of the braces under compression occur quite early during the pushover analysis. Under the design level demands, braces buckle under compression forces and yielding occurs across the members under tension. It is noted that neither columns nor beams experience yielding. This shows that the intended control of damage is assured.
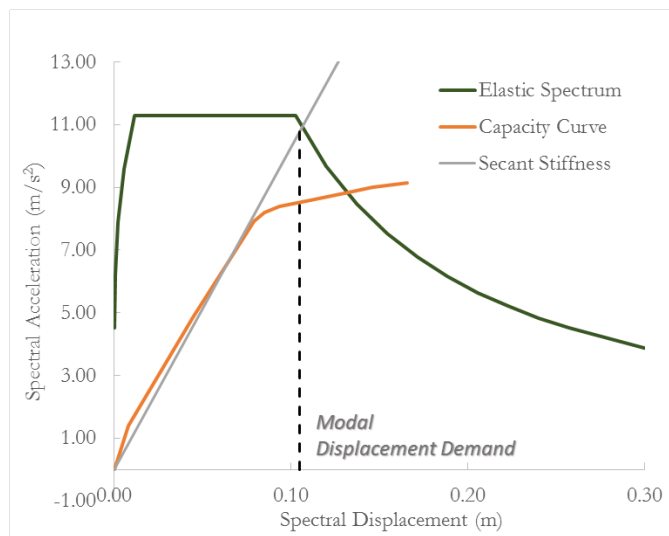
Figure 10. Modal capacity curve of the MRF. Design-level roof displacement demand, u_{xN1}= 14 cm.

NLTHA analyses

Nonlinear time history analyses (NLTHA) were performed for MRF model to assess the behaviour of the system under seven different earthquake ground motion accelerograms. The response spectra of the horizontal accelerograms, together with their mean spectrum are compared with the design spectrum (Type-I) of EC8-1, as shown in Figure 11. It is noted that the mean spectrum is consistently below the design spectrum for periods less 1.5 seconds.
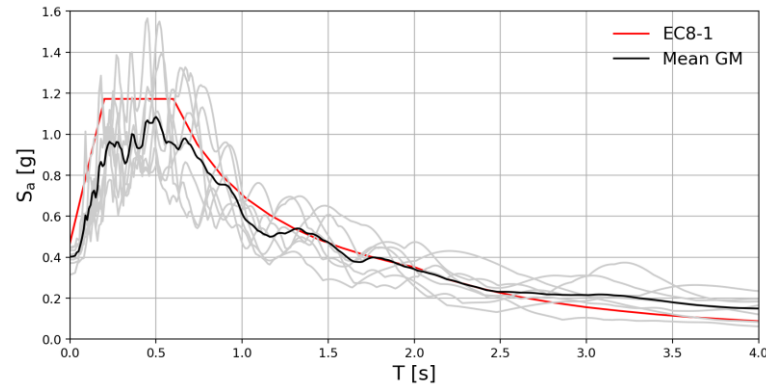
Figure 11. Response spectra of the provided ground motion records together with EC8 design spectrum.

The first story beam and column hysteresis loops under all seven dynamic loadings are shown in Figure 12. It was observed that all members remain, essentially, elastic. Regarding the interstory drift ratios, they remain under the damage limitation criteria defined in the European code for six out of seven earthquake records. The mean maximum interstory drift ratio is approximately 0.35%, well below the 0.75% IDR limit. To this end, the structure shows satisfactory performance for the provided suite of earthquakes with very limited damage. However, it is debateable whether the economic cost of the structure justifies the ensured level of reliability that is imposed by Eurocode provisions.
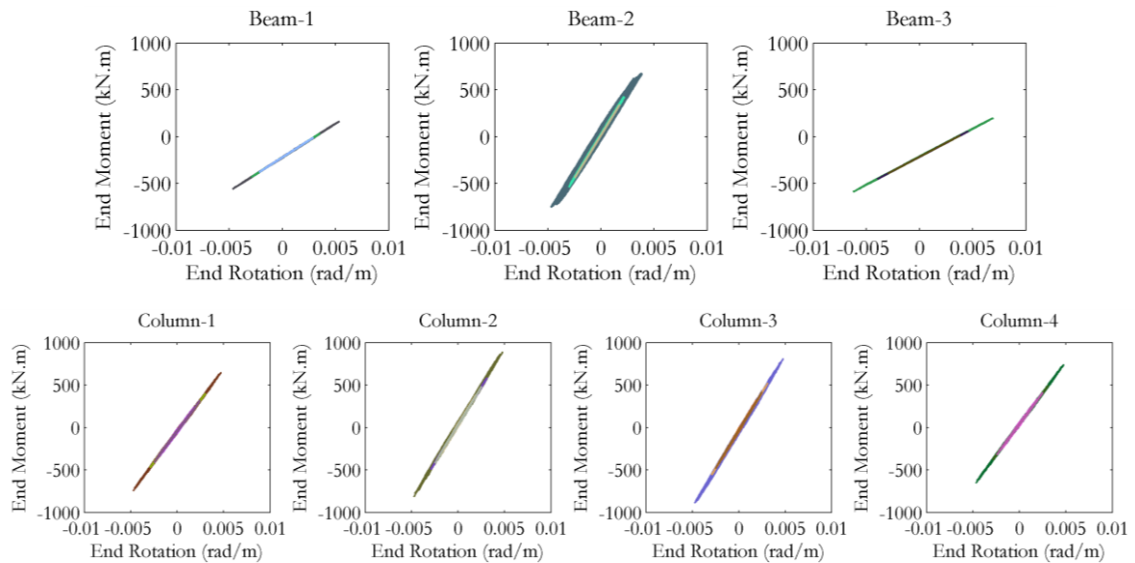
Figure 12. Moment-rotation hysteresis curves of the first story beams and columns under seven ground motion records.
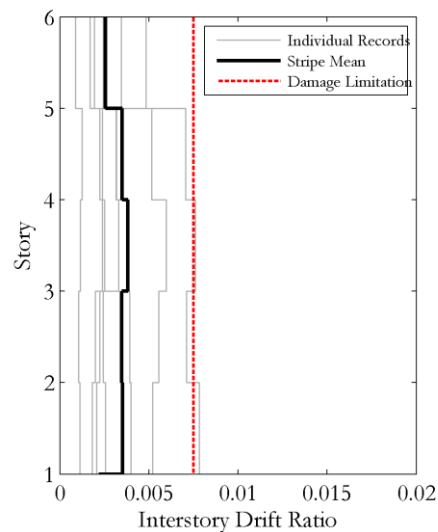
Figure 13 Response spectra of the provided ground motion records together with EC8-1 design spectrum.

Conclusion

Througout 14 desing scenarios considered, it is obvious that designs of MRFs in those cases are governed by deformation checks, hence rendering q ineffective. θ-q correlation is problematic. Simplified approach for P-Delta effects of EC8-1 may be innacurate. Effect of elastic analysis method is not substantial. CFST solutions for columns might be competitive, if seismic performance improvements are seen as important.

Designs of CBFs result in overdesign of braces due to interaction of λ, $\Omega_{MAX}/\Omega_{MIN}$. Consequently the reserve in capacity will render q ineffective. Serviceability drift checks are not critical as in MRFs, while service deflections of the beams are governing the design. Effect of elastic analysis method is more evident.

Pushover analysis indicates that capacity is lower than elastic seismic demand, hence, behaviour factor is required. Overestimate of seismic demand entails inaccuracy in Ω for MRFs (related to P-Delta effects in the code). Capacity design is ensured in both archetypes under consideration. NLTH analysis entails ground motion group of 7 records, with a mean demand lower than the design for T<1.5s. Satisfactory performance in terms of ISDR is obtained.

References

ANSI/AICS (2016): *ANSI/AISC 358-16: Prequalified Connections for Special and Intermediate Steel Moment Frames for Seismic Applications*, American Institute of Steel Construction (AISC), Chicago, USA.

Autodesk Inc. (2014): *Autodesk Robot Structural Analysis Professional 2018*, Autodesk, Inc., California, USA.

CEN (2004): *EN 1998–1 Eurocode 8: design of structures for earthquake resistance, Part 1, General Rules, Seismic Actions and Rules for Buildings*, European Commitee for Standardization (CEN), Brussels, Belgium.

CEN (2005): *EN 1993-1-1 Eurocode 3: Design of steel structures. Part 1-1, General rules and rules for buildings*, European Committee for Standardization (CEN), Brussels, Belgium.

Computers & Structures, Inc. (2014): *SAP2000 2014*, Computers & Structures, Inc., California, USA.

Elghazouli A.Y. (2009): *Seismic Design of Buildings to Eurocode 8*, CRC Press, Florida, USA.

Mazzoni S., McKenna F., Scott M.H., Fenves G.L. (2006): OpenSees command language manual, *Pacific Earthquake Engineering Research (PEER) Center*.

Silva A., Jiang Y., Macedo L., Castro J.M., Monteiro R., Silvestre N. (2017): Seismic design of composite moment-resisting frames with CFST members, *16ᵗʰ World Conference on Earthquake Engineering*, 16ᵗʰ WCEE 2017, Santiago, Chile.

Villani A., Castro J.M., Elghazouli A.Y. (2009): Improved seismic design procedure for steel moment frames, *Proceedings of the 6ᵗʰ International Conference on Behaviour of Steel in Seismic Areas: STESSA 2009,* Philadelphia, PA, USA.

Annexes:

Please look at: https://www.uni-weimar.de/summerschool/de/kurse/kursarchiv/fachkurse-2017/forecast-engineering/ → Papers & Presentation by the Participants

Digital Processing of Satellite Imagery in Civil Engineering Issues

KARAGIANNI Aikaterini
Aristotle University of Thessaloniki, Faculty of Engineering, School of Civil Engineering

Abstract

The rapid technological advances in the scientific area of Remote Sensing have attracted the interest of several sciences, including civil engineering, offering a rich source of information valuable to a wide range of issues and applications. Scientific and professional interests of civil engineering mainly include structures, hydraulics, geotechnical engineering, environmental, and transportation issues. Topics included in the context of the above may concern urban environment issues and urban planning, water resources and hydrological modelling, study of hazards, change detection and monitoring issues, road construction and road alignment studies.

Land cover information may contribute significantly in the study of the above subjects. Land cover information can be acquired effectively by visual image interpretation of satellite imagery or after applying enhancement routines and also by imagery classification. Visual image interpretation can be useful for the study of a wide range of relevant issues as the physiognomy and the structure of the built-up area, the road network, green areas, open areas and other land covers. Landsat 8 medium spatial resolution multispectral imagery presents particular interest in extracting land cover, because of the fine spectral resolution, the radiometric quantization of 12bits, the capability of merging the high resolution panchromatic band of 15 meters with multispectral imagery of 30 meters as well as the policy of free data.

In this study, a research on various methods of digital processing of satellite images is being done (enhancement, fusion, classification) and the results are evaluated statistically, as well as in combination with visual image interpretation. Landsat 8 multispectral and panchromatic imageries are being used, concerning the surroundings of a lake in north-western Greece. Land cover information is extracted, using suitable digital image processing software. The rich spectral context of the multispectral image is combined with the high spatial resolution of the panchromatic image, applying image fusion–pansharpening, facilitating in this way visual image interpretation. Further processing concerns supervised classification of the original and the fused image (pansharpened image) to delineate land cover. The classification of pansharpened image preceded the multispectral image classification. Corresponding comparative considerations are also presented.

References

Ehlers M., Klonus S., Åstrand P.J., Rosso P. (2010): Multi-sensor image fusion for pansharpening in remote sensing. *International Journal of Image and Data Fusion*, **1(1)**: 25-45.

Lazaridou M., Karagianni A. (2014): Visual satellite imagery interpretation for the city of Kastoria. In: Perakis, K. (ed), *Proceedings of the 1st International 'GEOMAPPLICA' Conference*; 08-10 September, 2014, Skiathos, Greece, 279-284.

Lazaridou M., Karagianni A. (2016): Landsat 8 multispectral and pansharpened imagery processing on the study of civil engineering issues. *23rd International Archives of the Photogrammetry, Remote Sensing and Spatial Information Sciences - ISPRS Archives*, **41**: 941-945, 23rd ISPRS Congress, 12-19 July, 2016, Prague, Chez Republic.

Lillesand T.M., Kiefer R.W. (1987): *Remote Sensing and Image Interpretation*. John Wiley & Sons, Inc.

Weng Q. (2011): Remote sensing of impervious surfaces in the urban areas: Requirements, methods and trends. *Remote Sensing of Environment*, **117**: 34-49.

Zhang Y. (2004): Understanding Image Fusion. *Photogrammetric Engineering and Remote Sensing*, **70(6)**: 657-661.

Turbomachinery Analysis in Frequency Domain

KARSHENASS Arash
Middle East Technical University

BARAN Ozgur Ugras
TED University

Abstract

These days, design process of aerospace and aeronautic industries depends heavily on Computational Fluid Dynamics (CFD) analysis techniques, while it becomes more dominant each year. From CFD point of view, current status of computers is acceptable for solution of most of steady problems. However, when it comes to unsteady calculations, it is not sufficient most of the times for industrial purposes. This issue is more prominent for turbomachinery and aeroelasticity studies where required calculation effort is extremely high due to simultaneous contribution of several physical events that are entirely in 3D pattern.

One way to overcome this problem is to use more suitable mathematical methods that fits the problem and requires less calculation. One of the recent methods for unsteady turbomachinery analysis is to use frequency domain instead of the time domain to improve equation by eliminating time-dependent parameters. In such methods, equations in frequency domain can be solved similar to steady/ average counterpart to be utilized to obtain unsteady solutions, which are periodic in time. In this study, unsteady inviscid flows inside turbomachines are investigated using three different methods in frequency domain; linearized harmonic, non-linear harmonic and harmonic balance. Harmonic methods are more suitable for considering blade flutter and forced response impacts on of unsteady flow behaviour between passages. In addition, multi-row analyses are conducted to encounter the interaction of stator and rotor on each other due to relative motion of rotor. The methods are applied for test cases evolving flutter and forced response disturbances and then extended to multi-row configuration in which both distortions coexist. Finally, results are compared to available experimental or computational results in literature.

Introduction

In order to obtain high load in turbomachines, multiple identical blades at a row is devised (with identical passages between them) that behave in the same manner. While instantaneous flow distribution at these passages is not identical in reality but there is not a sudden change in flow pattern between neighbouring passages at a row, thus it is possible to assume them all identical from mathematical point of view which means that it is periodic in space (both in steady and unsteady). This property had a huge influence on turbomachinery analysis in the last 50 years by which whole the blade passages of a row ($360°$) circumferentially can be truncated into a single passage and the approach is called single passage. However, to do this, specific periodic boundary condition must be applied on boundaries of a single passage domain.

Steady State Solution

For applying single passage approach into steady state problem, specific boundary condition needs to be utilized which is called blade to blade (B2B). In a work (Denton 1975), B2B method was applied for

the first time into a steady 2D and 3D inviscid flow between two blades in a finite volume scheme and adopted pseudo-time and relative frame of reference. In fact, it was the first 3D model solution in turbomachinery. Following that, several studies (Denton 1982,Denton 1990, Dawes 1988, Dawes 1992, Hah 1987, Arnone 1994, Gerolymos 2001) were done by the same approach but for viscous and turbulent flow. All these studies were done for only one row of a turbomachine, so that in another work (Denton 1979), the author introduced mixing-plane approach in which steady state solutions of multi-row machines can be obtained with only modelling of one passage from each row.

Lack of steady state solution

The two main aerodynamic problems in turbomachinery and aeroelasticity are Flutter and Forced response which cannot be obtained in steady state solution. However, all currently-running turbomachineries are designed based on steady state analysis. Flutter is defined as an unstable and self-excited vibration of body in an airstream, resulted from a continuous interaction between the fluid and the structure. Forced response is the vibration of blades due to large aerodynamic forces, raised from the interaction of rotor and stator due to rotation of rotors. Consequently, unsteady solution is vital for vibration analysis of blades and how they impact on the flow.

Unsteady Solution

As mentioned above, flow inside a turbomachine is periodic in space, so can be truncated into a single passage but a different boundary condition than B2B is required for this purpose. This type of boundary conditions will be discussed later. Additionally, unsteady solution inside a passage is periodic in time, so governing equations for a single passage domain can be treated using periodic equation specification, the frequency. Generally, there exists three type of solutions for CFD analysis in turbomachinery; Time-accurate, time-linearized and harmonic methods. Time-accurate method solves the unsteady equation entirely in time domain without any periodic solution assumption while time-linearized solves some part of it in time domain and some part in frequency domain by assuming periodic. Finally, harmonic method solves equations entirely in frequency domain by assuming periodic solution. Here it should also to note that no truncation of passages is possible in time-accurate method while it is possible in the two others. These methods are categorized in Figure 1 with their specifications in Table 1.
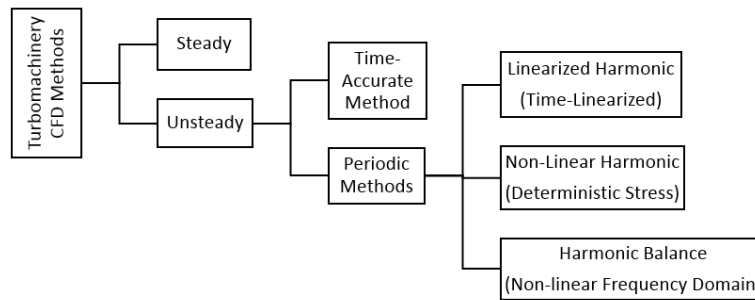
Figure 1. CFD methods in Turbomachinery.

Table 1. specifications of unsteady methods.

Unsteady Methods	Assumption of Single Passage	Assumption of Periodicity in Time	Domain to be Used
Time-Accurate	✗	✗	Only time
Time-Linearized	✓	✓	Both time and frequency
Deterministic-Stress	✓	✓	Both time and frequency
Harmonic Balance	✓	✓	Only frequency

Time-Accurate method

Time-accurate includes discretizing space and leaving time to be continuous to produce systems of ODE. This is called semi-discrete form of equation and advancing in time is known as method of lines. In general, unsteady solutions in CFD problems are obtained by time-marching method, making the unsteady solution advance in time-accurate way which can capture all linearity and non-linearity in fluid flow, but highly expensive in computation and when it comes to complex geometry of turbomachines with moving frames and interaction between multiple rows, required calculations soars and make it infeasible for industrial applications with current computational power and that is why no such modelling is seen in 20 century, however results of this model can be used as reference to check the validity of the two others. Finally, what will be obtained as solution, is a periodic solution in time for whole passages which are different only by a phase shift. As an example, a study (McMullen 2001) was done in U.S. Department of Energy Defence Programs with contribution of Stanford University on time-accurate unsteady analyses over whole rows of a turbine and a compressor in a massively-parallel computer with 750 CPUs. Running details are provided in Table 2 and shows that it is not applicable to industrial applications.

Table 2. Details of the time-accurate study.

	Blade Rows	Grid points	Execution Duration
Turbine	9	94 million	500 days
Compressor	23	NA	1300 days

Since flow pattern in turbomachinery is periodic both temporally and spatially, a single passage is periodic temporally. Typically, in time-accurate solution of periodic problems, the unsteady solution varies disordered (known as initial transient or initial solution decay) until it reaches repeating pattern in time (periodic state) which is the solution of problem and of our interest, Figure 2. Thus, results from initial transient solution are irrelevant which increase amount of calculations by several times and conditions become worse when time scale of initial solution is much larger than period of periodic solution. For instance, in a work (Mitchell 1995), about 95% of required time was related to generating irrelevant results of initial solution. Additionally, it is difficult to define mathematical criteria to determine whether the solution has reached periodic state or not and in fact the rate at which solution reaches the periodic state depends on physics of the problem. It is important to say that initial conditions determine the initial solution but periodic solution depends on periodic boundary conditions, thus determining a proper initial solution could decrease required calculation which is not available explicitly.
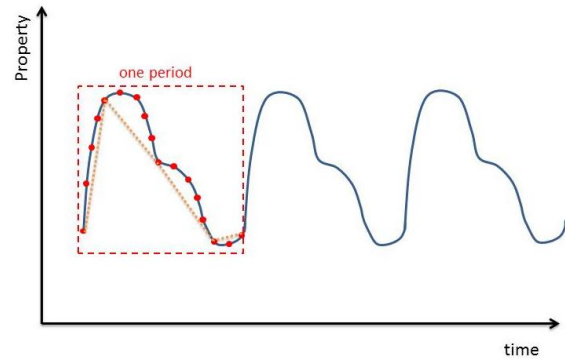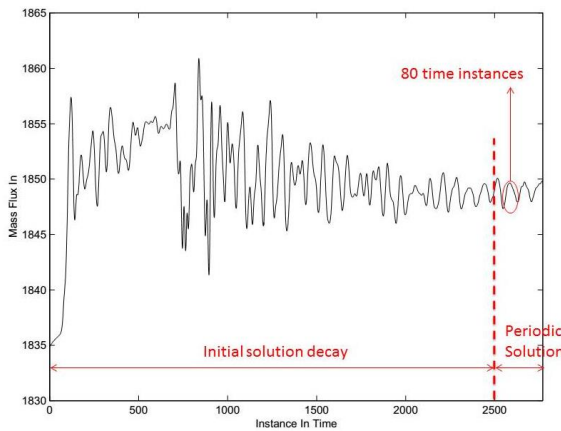
Figure 2. Time-accurate solution of periodic problem. **Figure 3.** Required time steps to get harmonic solution.

While we can increase time step magnitude (particularly in implicit method by using dual-time stepping) to pass quickly through initial decay solution, in periodic solution we cannot do it because the time-step is limited by number of points required to solve an oscillation, Figure 3. So we have to adaptively change the time step during evolution of solution, but there are two problems with it. Firstly, and as mentioned above, there is no clear mathematical criteria for determining whether the solution has reached the periodic form or not. Secondary, implementing variable time steps into a solver is not an easy job and adds an extra calculation cost.

Time-Linearized method

In this method, the first term of the Fourier series (as trigonometric interpolant) is used to represent the solution with the aim of eliminating the time-dependent parameters in governing equations and obtaining perturbed solution from time-independent perturbed equations that only rely on frequency. However, number of governing equations increase two or three times which have to be solved simultaneously. The method benefits from lower computation cost but there is a limit to utilize it; Source of harmonic (that force the equation to have harmonic solution) can be either harmonically varying boundary conditions or harmonic nature of governing equations but here in fluid mechanics only the first type is of our interest because neither Euler nor Navier-Stokes equations have harmonic nature inside them. At this method, unsteady solution (conservative or primitive variables) is decomposed into two parts, a mean solution and a perturbed solution. One of the most important advantages of this method over previous one is that there is no transient decay in solution and periodic solution can be obtained directly but steady solution still needs to be solved in time-domain. There are two different methods to use time-linearized category; time-linearized and Deterministic-Stress.

In a work (Ni and Sisto 1976), authors introduced the decomposition of unsteady equation into a steady equation (as the mean) plus a perturbed equation, $w = \bar{w} + \tilde{w}$ while perturbed variables must be small compared to those of steady ones with only one frequency of distortion. Then, unsteady equations are linearized about steady solution using only first term of Taylor series and considering only first order perturbations. Following that each equation of perturbed flow become a linear variable coefficient PDE which are hyperbolic in time, so can be solved using ordinary CFD methods. Since it is periodic in time, we can represent the solutions by the Fourier series in time with coefficients that vary in space. For 2D Euler equation, we will have:

$$\frac{\partial \tilde{w}}{\partial t} + \boxed{\frac{\partial F(\bar{w})}{\partial x}} + \boxed{\frac{\partial F(\bar{w}, \tilde{w})}{\partial x}} + \boxed{\frac{\partial F(\bar{w}, \tilde{w}^{2+})}{\partial x}} = 0 \qquad (1)$$

Depends only on mean variable $\bar{W}$

≈ 0 by assuming that $\tilde{W} << \bar{W}$

Depends on $\bar{W}$ and first order perturbation $\tilde{W}$

To solve this equation:

a.   First solve time averaged solution
b.   Calculate $\bar{A}$ and $\bar{B}$ from mean solution variable $\bar{w}$.
c.   Solve perturbed equation for specified temporal frequency.
d.   Sum up steady and perturbed solutions

Note that due linearization, flow must be free from shocks due to nonlinear nature of shocks in order to have exact results. If there exists a shock in problem (steady), perturbed solution cannot predict high details in shock however integrated force is nearly correct. Early unsteady studies of turbomachinery (Casper and Verdon 1981, Verdon and Casper 1984, Verdon and Casper 1980, Giles 1988a, Giles 1988b,

Ron-Ho 2012) till mid 80s used this method, mostly for potential and isentropic flows. Later authors of the work (Hall and Crawley 1987) used this method for Euler equation with shock-fitting and anothert work (Lindquist 1992) extends it for navier-stock equation with shock capturing. Note that all these studies were done on flat-palate cascades because the method can only include one perturbed distortion with one frequency. However, being linear make it possible to use superposition to sum multiple distortions with different frequencies which are solved separately.

Deterministic-Stress method

Deterministic-stress terms were proposed by the authors (Adamczyk and Goldstain 1978) but other works (Chen and Vasanthakumar 2000, He and Ning 2001) provide a method to adopt it for improvement of time-linearized method. In this approach, mean solution is not the steady solution and is updated by perturbed solution. Since the location of a shock in steady solution is not the mean location, time-linearized method faces problems in shock regions while this developed method makes it possible to handle shocks without problem. However, still a single perturbation with specific frequency and time period T can be adopted. Splitting equation 1 into two parts, time averaged solution and perturbed solution:

$$\frac{\partial F(\overline{w})}{\partial x} + \frac{1}{T}\int_0^T \frac{\partial F(\overline{w}, \widetilde{w}^{2+})}{\partial x} dt = 0 \qquad (2)$$

| Periodic in time interval T | Effect of unsteadiness on time averaged solution |

$$\frac{\partial \widetilde{w}}{\partial t} + \frac{\partial(\bar{A}\widetilde{w})}{\partial x} + \frac{\partial(\bar{B}\widetilde{w})}{\partial y} = 0 \qquad (3)$$

According to the two last equations, higher order perturbed terms are still neglected at unsteady part and only nonlinearities are added to time averaged solution. In spite of this, this method is widely used in turbomachinery. It can be solved in the same manner as mentioned above but time averaged and unsteadiness is coupled and must be solved instantaneously.

Harmonic balance method

There are three problems in time-linearized methods. Firstly, the steady state solution is still solved in time-domain which is expensive. Secondly, only one perturbed equation with a single frequency can be handled. Thirdly, due to linearization by Taylor series, perturbed variables must be small compared to mean solution. In the case of not satisfying any of above condition, the methods fail. (Giles 1992) proposed the feasibility of using harmonic balance method in turbomachinery and thus there will be no need to calculate mean solution in time domain. Following that, (Ning and He 1998, He and Ning 1998) formulated and developed the first order harmonic balance method. In continue, (Hall and Thomas and Clrak 2002) developed the method to full harmonic balance.

Boundary Conditions

In steady state analysis of turbomachinery (as discussed in the beginning), single passage approach is possible by adopting B2B boundary condition. But for unsteady turbomachinery analysis and also for aeroelasticity (both flutter & force response which are unsteady phenomena), we cannot reduce geometry to a single passage by using B2B, because blade structural dynamic modes is different than number of blade passages in unsteady flow; In other word, circumferential wavelength of unsteady disturbance is not the same as Pitch length of passages. However, if they are the same, we can use B2B in unsteady flows also; i.e. when rotor and stator have the same number of blades but such condition is

almost unrealistic. Consequently, entire of a turbomachine (with whole blades and all rows) need to be modelled.

Indore to be able to use single passage method in unsteady analysis, (Lane 2012) introduced B2B phase-shift periodicity phenomena and the boundary condition associated to that is phase-shifted periodic boundary condition, Figure 4. This is formed on the basis that adjacent passages in a row, should see the disturbances of the same amplitude but with a constant phase angel in time.
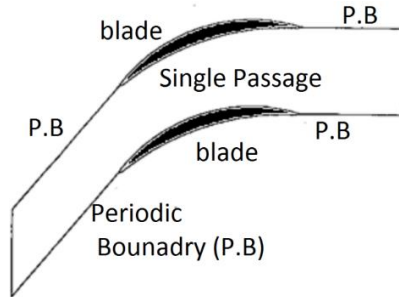
Figure 4. B2B boundary condition.

To see what B2B phase-shift periodicity is for flutter and force response, we can start as below.

For typical turbomachinery aeromechanic problems (flutter and forced response), structural dynamic vibratory patterns of blade and disk assemblies are typically of a cyclic symmetry mode, rotating circumferentially at a constant speed. For this kind of travelling wave modes, the radial lines with zero displacements are called nodal diameters. So the circumferential wavelength is defined by the number of nodal diameters.

For flutter, if N is the number of blades of row and n is the number of nodal diameters, then this constant time difference, inter blade phase angel (IBPA), is:

$$\sigma = \pm \frac{2\pi n}{N} \quad \left(n = 1,2,\dots,\frac{N}{2} \right) \tag{4}$$

σ also defines the circumferential wavelength in terms of blade pitch. Flutter instability corresponds to inter IBPA with small number of nodal diameters.

For forced response, let's consider the rotor row in a rotor–stator interactions, as shown in the Figure 5. For a rotor passage between Blade A and Blade B. at instant t_1, the trailing edge of the upper blade B of the rotor row sees the leading edge of a blade of the stator row. At t_2, the trailing edge of the lower blade A see' the leading edge of another blade of the stator row. It then follows that the instantaneous flow field around the upper blade B at t_1 must be the same as that around the lower blade A at t_2. The time difference between t_1 and t_2 is determined by the blade number of the adjacent blade row and the relative rotational speed between the two rows.
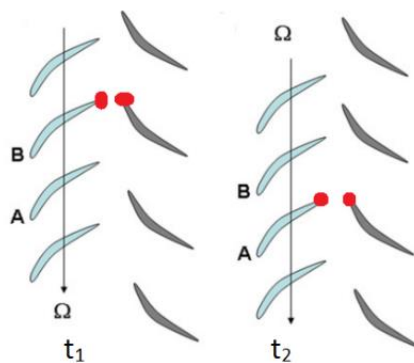
Figure 5. Forced response.

If a row with N blades is subjected to disturbances which are generated by adjacent row with M blades, IBPA would be:

$$\sigma = \pm \frac{2\pi M}{N} \qquad (5)$$

In IBPA, sign of + is for forward traveling wave, rotating disturbance is circumferentially traveling in the same direction of rotor itself and – is for backward disturbance where rotating disturbance is circumferentially traveling in the opposite direction of rotor.

Quasi 1D Nozzle

As the first step to get familiar how periodic methods works without the geometry and mesh complexity of turbomachines, a subsonic quasi-one dimensional converging-diverging nozzle, Figure 6, with harmonically changing back pressure as variable boundary condition is solved using time-linearized method while inlet stagnation pressure is fixed.
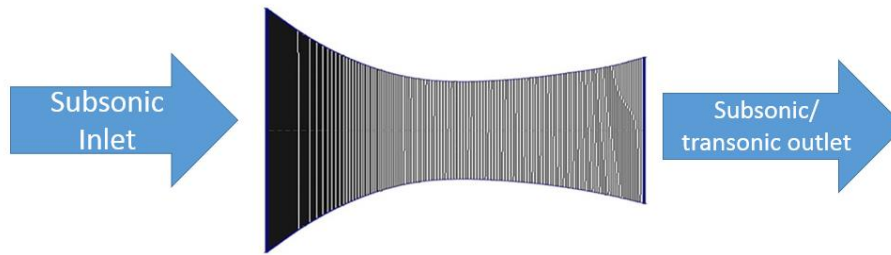
Figure 6. Converging-diverging quasi 1D nozzle.

Starting from integral form Euler equation for quasi 1D case, we have:

$$\frac{\partial}{\partial t} \int_{\Omega} WA dx = -\sum_{j=1}^{2} (FAn)_j + \int_{1}^{2} S dA \qquad (9)$$

Where:

$$W = \begin{bmatrix} \rho \\ \rho u \\ \rho E \end{bmatrix} \qquad F = \begin{bmatrix} \rho u \\ \rho u^2 \\ \rho u H \end{bmatrix} \qquad S = \begin{bmatrix} 0 \\ P \\ 0 \end{bmatrix}$$

Here, ρ,u,E,H and P are density, velocity, total energy, total enthalpy and pressure respectively.

In this method some assumptions are made. Firstly, it is assumed that unsteady solution is the combination of mean solution plus perturbation solution $W_{(x,t)} = \overline{W}_{(x)} + \widetilde{W}_{(x,t)}$. Secondary, it is assumed that the mean solution is the steady solution, thus $\frac{\partial \overline{W}_{(x)}}{\partial t} = 0$. As the third assumption, it is considered that the perturbation part has a linear effect on problem (F and S are changed linearly from $\overline{F}$ and $\overline{S}$ when W changes from $\overline{W}$), thus we can obtain F and S at unsteady point from steady point by using Taylor series.

For steady state solution we solve equation 10 directly.

$$-\sum_{j=1}^{2} (FAn)_j + \int_{1}^{2} S dA = 0 \qquad (10)$$

For perturbed part, adding aforementioned assumption into main Euler equation 9, we get:

$$\frac{d}{dt}\int_{1}^{2}\widetilde{W}_{(x,t)}Adx = -\sum_{j=1}^{2}\left(\bar{M}_F\widetilde{W}An\right)_j + \int_{1}^{2}\bar{M}_s\widetilde{W}\,dA \qquad (11)$$

Where:

$$\bar{M}_F = \frac{d\bar{F}}{d\bar{W}} = \begin{bmatrix} \dfrac{d\bar{F}_1}{d\bar{W}_1} & \dfrac{d\bar{F}_2}{d\bar{W}_1} & \dfrac{d\bar{F}_3}{d\bar{W}_1} \\[2mm] \dfrac{d\bar{F}_1}{d\bar{W}_2} & \dfrac{d\bar{F}_2}{d\bar{W}_2} & \dfrac{d\bar{F}_3}{d\bar{W}_2} \\[2mm] \dfrac{d\bar{F}_1}{d\bar{W}_3} & \dfrac{d\bar{F}_2}{d\bar{W}_3} & \dfrac{d\bar{F}_3}{d\bar{W}_3} \end{bmatrix} \qquad \bar{M}_s = \frac{d\bar{S}}{d\bar{W}} = \begin{bmatrix} \dfrac{d\bar{S}_1}{d\bar{W}_1} & \dfrac{d\bar{S}_2}{d\bar{W}_1} & \dfrac{d\bar{S}_3}{d\bar{W}_1} \\[2mm] \dfrac{d\bar{S}_1}{d\bar{W}_2} & \dfrac{d\bar{S}_2}{d\bar{W}_2} & \dfrac{d\bar{S}_3}{d\bar{W}_2} \\[2mm] \dfrac{d\bar{S}_1}{d\bar{W}_3} & \dfrac{d\bar{S}_2}{d\bar{W}_3} & \dfrac{d\bar{S}_3}{d\bar{W}_3} \end{bmatrix} \qquad (12)$$

Since boundary condition is harmonic, as the final assumption, we can say that our solution must follow that harmonic pattern. We can represent any harmonic function (with limited domain) with Fourier series $\widetilde{W}_{(x,t)} = \widehat{W}_{(x)}e^{i\omega tn}$. At here only the first term (first harmonic) of the Fourier series need to be considered and neglect the others, equation 13. The reason for this simplification can be explained by fundamental frequency; since our boundary condition varies with frequency ω, thus the dominant change in solution appears with frequency ω (fundamental frequency). While the change in solution with other frequencies $\frac{\omega}{2}, \frac{\omega}{3}, \frac{\omega}{4}$ and etc. are negligible compared to fundamental one. For simplicity at the rest, $\widehat{W}_{(x)}$ and $\widetilde{W}_{(x,t)}$ are replaced by $\widehat{W}$ and $\widetilde{W}$ respectively.

$$\widetilde{W} = \widehat{W}e^{i\omega t}$$
$$\widehat{W} = \widehat{W}_r + i\widehat{W}_i = |\widehat{W}|e^{i\varphi} \qquad (13)$$

Where $|\widehat{W}|$ is the amplitude of variation of solution, ωt is harmonic change of solution with time and φ is the phase shift which depends on location, demonstrating that how much it takes for a location to be affected by variation of boundary condition. Thus closer points to harmonically-changing BC have less ϕ and far points have larger ϕ.

Substitute equation 13 into equation 11, separating real and imaginary part and simplifying we get:

$$d\widehat{W}_r = \omega\widehat{W}_i + \frac{\left[\left(\bar{M}_F\widehat{W}_rA\right)_L - \left(\bar{M}_F\widehat{W}_rA\right)_R\right] + \bar{M}_s\widehat{W}_r(A_R - A_L)}{\Omega}d\tau$$
$$d\widehat{W}_i = -\omega\widehat{W}_r + \frac{\left[\left(\bar{M}_F\widehat{W}_iA\right)_L - \left(\bar{M}_F\widehat{W}_iA\right)_R\right] + \bar{M}_s\widehat{W}_i(A_R - A_L)}{\Omega}d\tau \qquad (14)$$

Decomposing each of these equations, we get 6 ODE equations that need to be solved simultaneously; real and imaginary parts of continuity equation, real and imaginary parts of momentum equation and finally real and imaginary parts of energy equation.

$$\widehat{W}_{r1}$$
$$= \left\{\omega\widehat{W}_{i1} + \frac{\left[\left(\bar{M}_{F_{11}}W_{r1} + \bar{M}_{F_{12}}W_{r2} + \bar{M}_{F_{13}}W_{r3}\right)_L A_L - \left(\bar{M}_{F_{11}}W_{r1} + \bar{M}_{F_{12}}W_{r2} + \bar{M}_{F_{13}}W_{r3}\right)_R A_R\right]}{\Omega}\right.$$
$$\left. + \frac{\left(\bar{M}_{S_{11}}W_{r1} + \bar{M}_{S_{12}}W_{r2} + \bar{M}_{S_{13}}W_{r3}\right)(A_R - A_L)}{\Omega}\right\}d\tau$$

$$d\widehat{W}_{r2}$$
$$= \left\{ \omega\widehat{W}_{i2} + \frac{\left[\left(\overline{M}_{F_{21}}W_{r1} + \overline{M}_{F_{22}}W_{r2} + \overline{M}_{F_{23}}W_{r3}\right)_L A_L - \left(\overline{M}_{F_{21}}W_{r1} + \overline{M}_{F_{22}}W_{r2} + \overline{M}_{F_{23}}W_{r3}\right)_R A_R\right]}{\Omega}\right.$$
$$\left. + \frac{\left(\overline{M}_{S_{21}}W_{r1} + \overline{M}_{S_{22}}W_{r2} + \overline{M}_{S_{23}}W_{r3}\right)(A_R - A_L)}{\Omega}\right\} d\tau$$

$$d\widehat{W}_{r3}$$
$$= \left\{ \omega\widehat{W}_{i3} + \frac{\left[\left(\overline{M}_{F_{31}}W_{r1} + \overline{M}_{F_{32}}W_{r2} + \overline{M}_{F_{33}}W_{r3}\right)_L A_L - \left(\overline{M}_{F_{31}}W_{r1} + \overline{M}_{F_{32}}W_{r2} + \overline{M}_{F_{33}}W_{r3}\right)_R A_R\right]}{\Omega}\right.$$
$$\left. + \frac{\left(\overline{M}_{S_{31}}W_{r1} + \overline{M}_{S_{32}}W_{r2} + \overline{M}_{S_{33}}W_{r3}\right)(A_R - A_L)}{\Omega}\right\} d\tau$$

$$d\widehat{W}_{i1}$$
$$= \left\{ -\omega\widehat{W}_{r1} + \frac{\left[\left(\overline{M}_{F_{11}}W_{i1} + \overline{M}_{F_{12}}W_{i2} + \overline{M}_{F_{13}}W_{i3}\right)_L A_L - \left(\overline{M}_{F_{11}}W_{i1} + \overline{M}_{F_{12}}W_{i2} + \overline{M}_{F_{13}}W_{i3}\right)_R A_R\right]}{\Omega}\right.$$
$$\left. + \frac{\left(\overline{M}_{S_{11}}W_{i1} + \overline{M}_{S_{12}}W_{i2} + \overline{M}_{S_{13}}W_{i3}\right)(A_R - A_L)}{\Omega}\right\} d\tau$$

$$d\widehat{W}_{i2}$$
$$= \left\{ -\omega\widehat{W}_{r2} + \frac{\left[\left(\overline{M}_{F_{21}}W_{i1} + \overline{M}_{F_{22}}W_{i2} + \overline{M}_{F_{23}}W_{i3}\right)_L A_L - \left(\overline{M}_{F_{21}}W_{i1} + \overline{M}_{F_{22}}W_{i2} + \overline{M}_{F_{23}}W_{i3}\right)_R A_R\right]}{\Omega}\right.$$
$$\left. + \frac{\left(\overline{M}_{S_{21}}W_{i1} + \overline{M}_{S_{22}}W_{i2} + \overline{M}_{S_{23}}W_{i3}\right)(A_R - A_L)}{\Omega}\right\} d\tau$$

$$d\widehat{W}_{i3}$$
$$= \left\{ -\omega\widehat{W}_{r3} + \frac{\left[\left(\overline{M}_{F_{31}}W_{i1} + \overline{M}_{F_{32}}W_{i2} + \overline{M}_{F_{33}}W_{i3}\right)_L A_L - \left(\overline{M}_{F_{31}}W_{i1} + \overline{M}_{F_{32}}W_{i2} + \overline{M}_{F_{33}}W_{i3}\right)_R A_R\right]}{\Omega}\right.$$
$$\left. + \frac{\left(\overline{M}_{S_{31}}W_{i1} + \overline{M}_{S_{32}}W_{i2} + \overline{M}_{S_{33}}W_{i3}\right)(A_R - A_L)}{\Omega}\right\} d\tau \tag{15}$$

All these equations are hyperbolic in time, so it can be solved by conventional CFD methods, such as direct solution method, flux vector splitting method or Godunov method. However, at here flux vector splitting method is adopted. Since all equations are derived by linearization of Euler equation, thus their eigenvalues are the same as those of Euler's. These values are used in splitting of fluxes both in solution of steady equations and solution of linearized perturbed equations.

Results

To obtain solution in a nozzle with 200 cells, equations 10 and equations 15 are solved to obtain $\overline{W}$ and $\widehat{W}$ respectively and finally equations 13 are adopted with the aim of obtaining $\widetilde{W}$. Solutions are obtained for two cases, subsonic flow and transonic flow in which a shock wave appears. For subsonic flow, static outlet pressure ratio to that of inlet is set to 0.92 in steady part while for transonic flow, this value is set to 0.75. In perturbed part of both cases, amplitude and radial frequency of sinusoidally varying outlet static pressure are set to 0.5% of steady outlet pressure and 1 respectively.

Subsonic flow
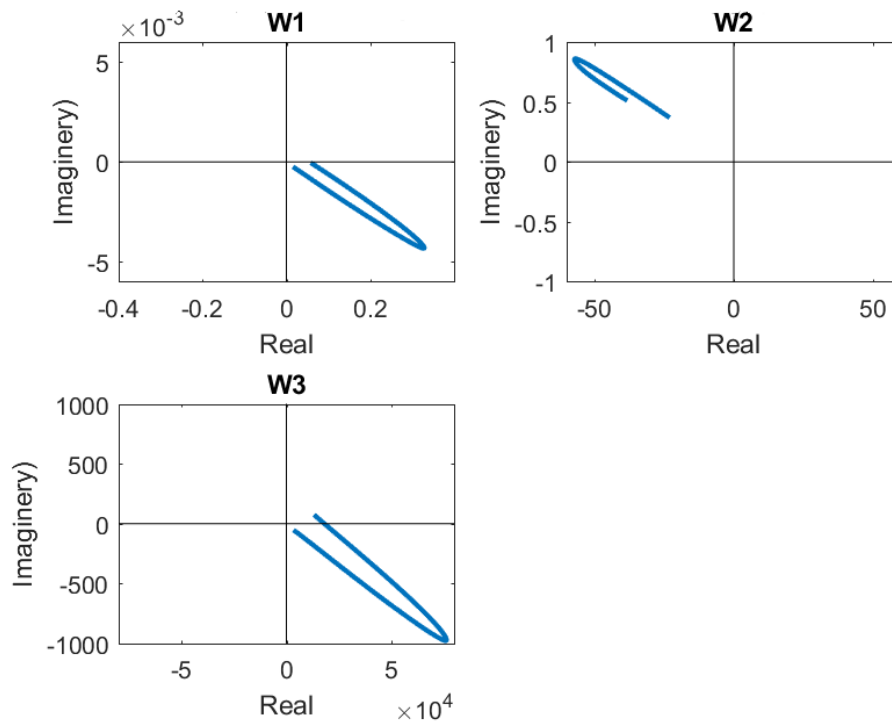
Figure 7. $\widehat{W}$ in real-imaginary coordinate.
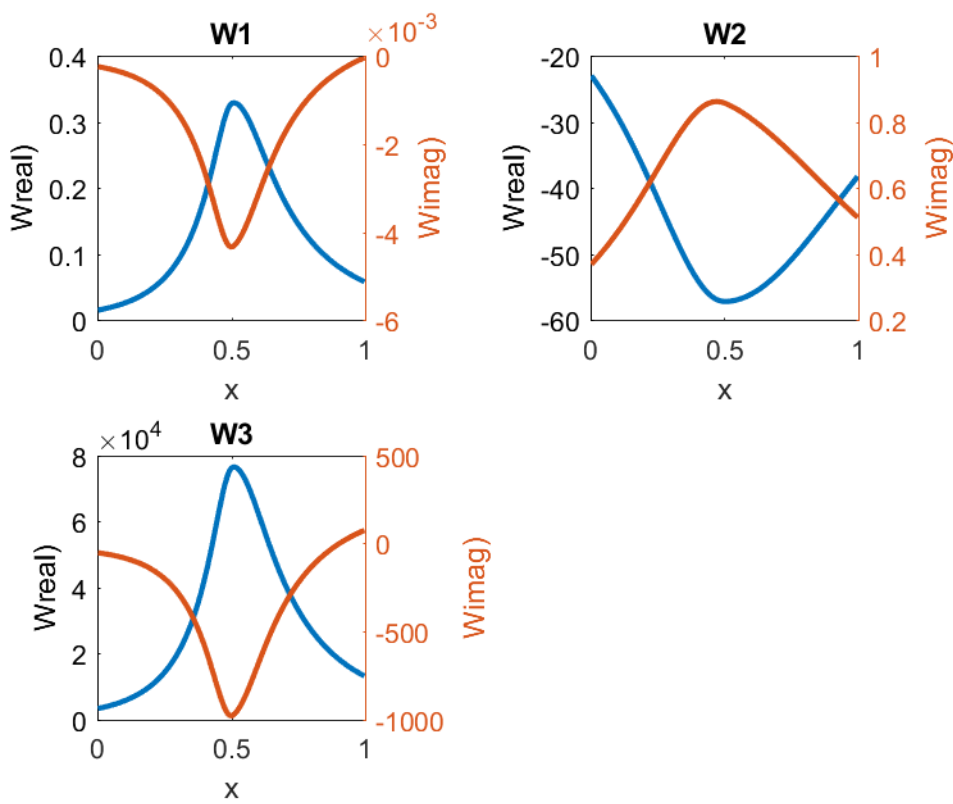
Figure 8. $\widehat{W}$ real and imaginary along nozzle.
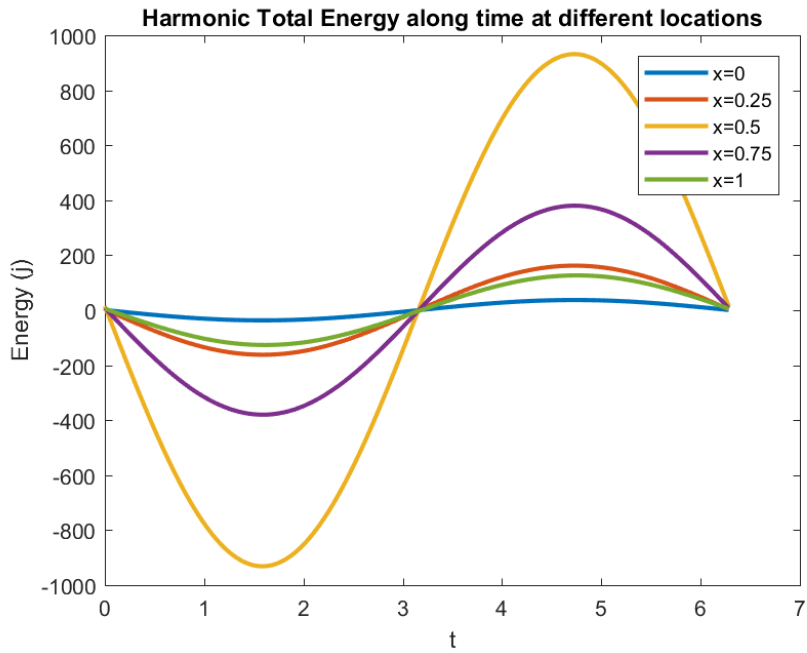
Figure 9. $\tilde{P}$ along time at different nozzle locations.
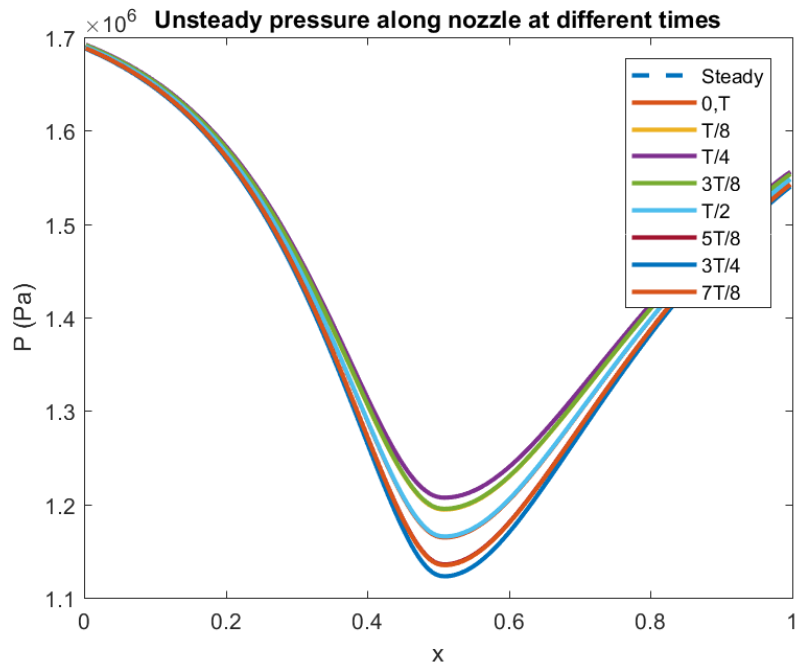
Figure 10. Pressure along nozzle at different time steps.

For validation, results of linearized harmon method are compared to those of unsteady method which are in good agreement.

Transonic flow
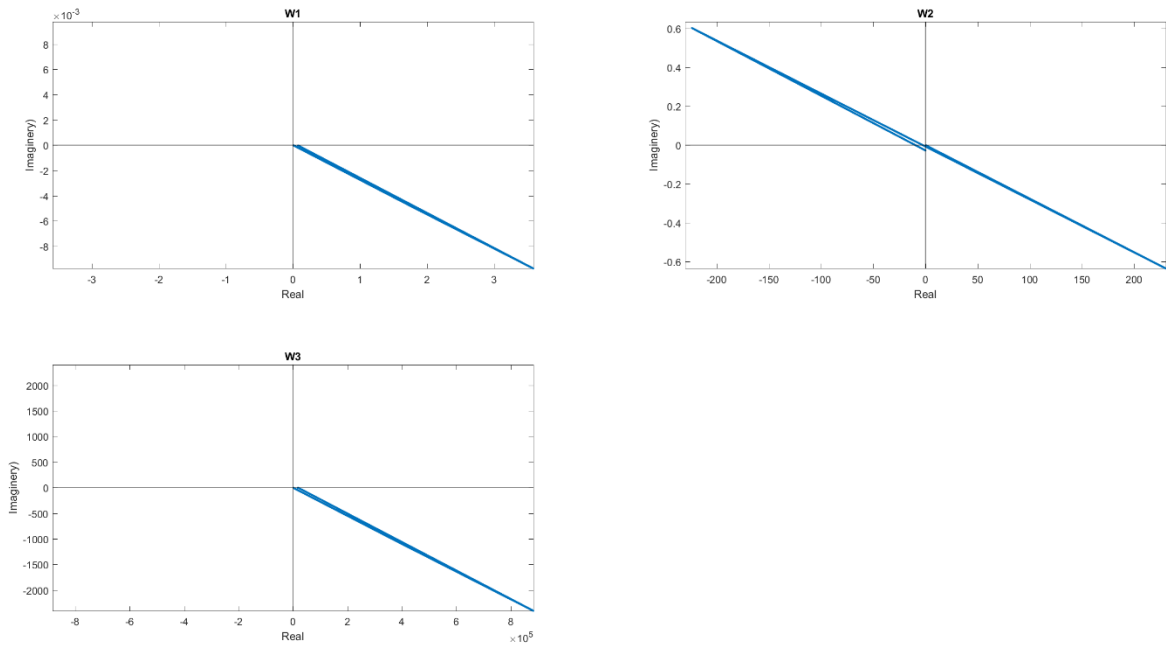
Figure 11. $\widehat{W}$ in real-imaginary coordinate.
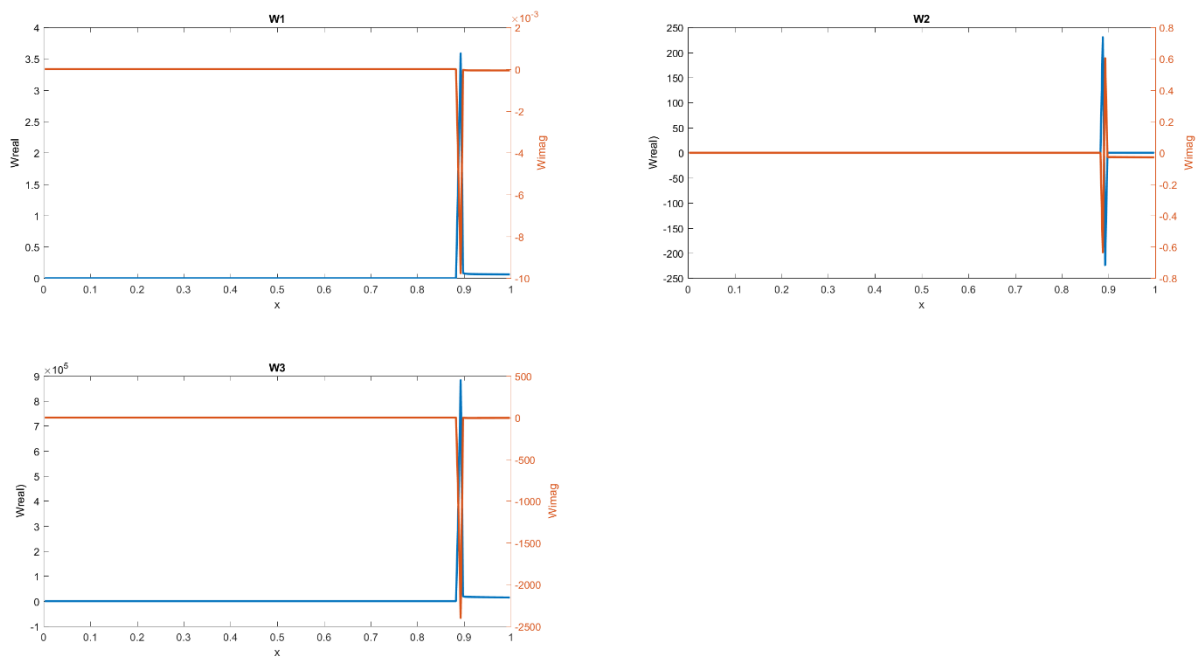
Figure 12. $\widehat{W}$ real and imaginary along nozzle.
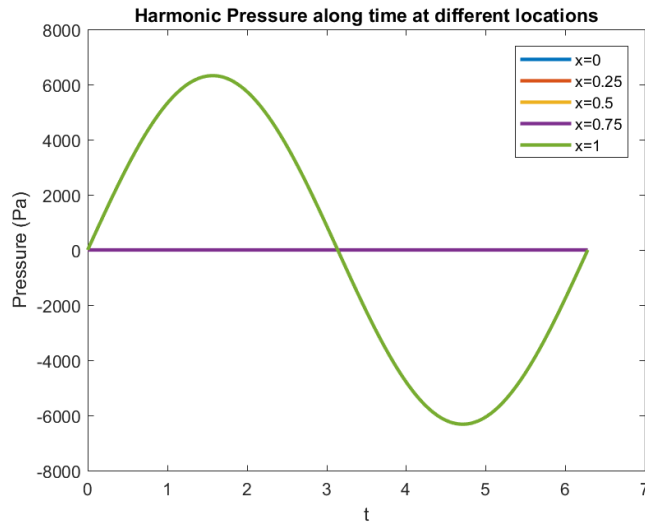
Figure 13. $\tilde{P}$ along time at different nozzle locations.
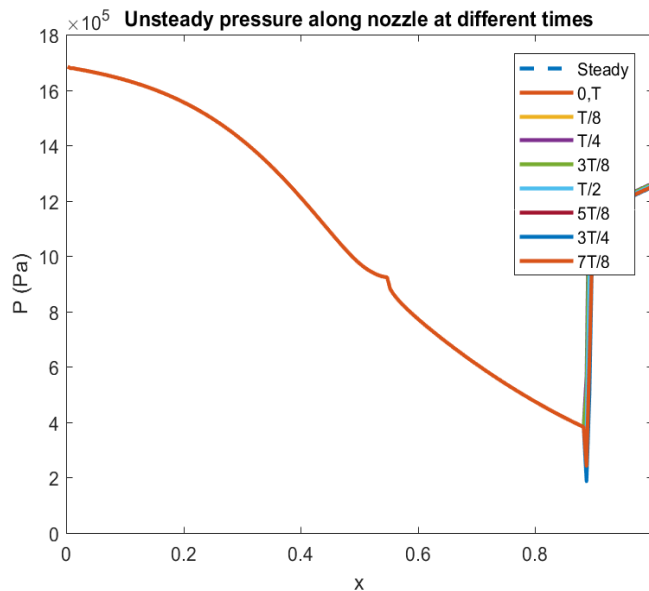
Figure 10. Pressure along nozzle at different time steps.

As seen in figures, the method cannot capture the correct solution due to existence of shock wave where an oscillation appears in solution. This is due to the fact that shock is entirely a non-linear phenomenon and consequently a linear method cannot handle it.

Future works

Extending the current methodology to include deterministic-stress, so transonic and supersonic flows in which shock wave appears can be solved. Following that harmonic balance is used to solve problems with multiple perturbed frequencies rather than just only a single frequency. After that, these method will be extended into 2D for solving blade flutter and forces response problems with suitable boundary condition which appears frequently in turbomachines. Finally, aeroelasticity will be included, so that the interaction between fluid and solid domains are possible to solve with the aim of obtaining amplitude and frequency of vibration of solid domain and its effect on fluid flow.

References

Adamczyk J.J., & Goldstein M.E. (1978): Unsteady flow in a supersonic cascade with subsonic leading-edge locus. AIAA Journal, 16(12), 1248-1254.

Arnone A. (1993): Viscous Analysis of Three-Dimensional Rotor Flows Using a Multigrid Method (Vol. 106266). National Aeronautics and Space Administration.

Caspar J.R., & Verdon J.M. (1981): Numerical treatment of unsteady subsonic flow past an oscillating cascade. AIAA Journal, Vol.19(12), 1531-1539.

Chen T., Vasanthakumar P., & He L. (2001): Analysis of unsteady blade row interaction using nonlinear harmonic approach. Journal of Propulsion and Power, 17(3), 651-658.

Dawes W.N. (1988): Development of a 3D Navier-Stokes solver for application to all types of turbomachinery. ASME paper, 88.

Dawes W.N. (1992): Toward improved throughflow capability: the use of three-dimensional viscous flow solvers in a multistage environment. ASME J. Turbomach, 114(1), 8-17.

Denton J.D. (1975): A time marching method for two-and three-dimensional blade to blade flows. HM Stationery Office.

Denton J.D. (1983): An improved time marching method for turbomachinery flow calculation. ASME Journal of Engineering for Power, 105(3), 514.

Denton J.D. (1992): The calculation of three-dimensional viscous flow through multistage turbo-machines. ASME J. Turbomach, 114(1), 18-26.

Denton J.D., & Singh U.K. (1979): Time marching methods for turbomachinery flow calculation. In In Von Karman Inst. for Fluid Dyn. Appl. of Numerical Methods to Flow Calculations in Turbomachines 47 p (SEE N80-12365 03-34).

Gerolymos G.A., Neubauer J., Sharma V.C., & Vallet I. (2002): Improved prediction of turbomachinery flows using near-wall Reynolds-stress model. Journal of turbomachinery, 124(1), 86-99.

Giles M.B. (1988): UNSFLO: A numerical method for unsteady inviscid flow in turbomachinery. Cambridge, Mass.: Gas Turbine Laboratory, Massachusetts Institute of Technology, 1988.

Giles M.B. (1988): Calculation of unsteady wake/rotor interaction. Journal of Propulsion and Power, Vol.4(4), 356-362.

Giles M.B. (1992): An approach for multi-stage calculations incorporating unsteadiness. ASME paper, (92-GT), 282.

Hah C. (1987): Calculation of three-dimensional viscous flows in turbomachinery with an implicit relaxation method. Journal of Propulsion and Power, 3(5), 415-422.

Hall K.C. (1987): A linearized Euler analysis of unsteady flows in turbomachinery (Doctoral dissertation, Massachusetts Institute of Technology).

Hall K.C., Thomas J.P., & Clark W.S. (2002): Computation of unsteady nonlinear flows in cascades using a harmonic balance technique. AIAA journal, 40(5), 879-886.

He L. (1990): An Euler solution for unsteady flows around oscillating blades. ASME J. Turbomach, 112(4), 714-722.

He L. (1992): Method of simulating unsteady turbomachinery flows with multiple perturbations. AIAA journal, 30(11).

He L., & Ning W. (1998): Efficient approach for analysis of unsteady viscous flows in turbo-machines. AIAA journal, 36(11), 2005-2012.

He L., & Ning W. (1998): Nonlinear Harmonic Analysis of Unsteady Transonic Inviscid and Viscous Flows. In Unsteady Aerodynamics and Aeroelasticity of Turbomachines (pp. 183-193). Springer Netherlands.

Lane F. (1956): System mode shapes in the flutter of compressor blade rows. Journal of the Aeronautical Sciences, 23(1), 54-66.

Lindquist D.R. (1992): Computation of unsteady transonic flowfields using shock capturing and the linear perturbation Euler equations (Doctoral dissertation, Massachusetts Institute of Technology).

McMullen M.S. (2003): The application of non-linear frequency domain methods to the Euler and Navier-Stokes equations. Stanford, CA: Stanford University.

McNally J.W. (1977): Numerical solution of periodic transonic flow through a fan stage.

Mitchell B.E. (1995): Direct Computation of the Sound Generated by Subsonic and Supersonic Axisymmetric Jets.

Ni R.H., & Sisto F. (1976): Numerical computation of nonstationary aerodynamics of flat plate cascades in compressible flow. Journal of Engineering for power, 98(2), 165-170.

Ning W., & He L. (1998): Computation of unsteady flows around oscillating blades using linear and nonlinear harmonic Euler methods. TRANSACTIONS-AMERICAN SOCIETY OF MECHANICAL ENGINEERS JOURNAL OF TURBOMACHINERY, 120, 508-514.

Ron-Ho N. (2012): A multiple-grid scheme for solving the Euler equations. AIAA journal.

Verdon J.M., & Caspar J.R. (1980): Subsonic flow past an oscillating cascade with finite mean flow deflection. AIAA Journal, 18(5), 540-548.

Verdon J.M., & Caspar J.R. (1984): A linearized unsteady aerodynamic analysis for transonic cascades. Journal of Fluid Mechanics, 149, 403-429.

Validation of adaptive versus conventional nonlinear static pushover analyses

MANOJLOVSKI Filip
Institute of Earthquake Engineering and Engineering Seismology, Skopje, Macedonia

Abstract

Detecting structure weak points or the overall deformation capacity is inevitable part of every single performed seismic evaluation. In order to obtain accurate results, it is clear that the nonlinear characteristics of the elements that constitute the whole structure have to be taken into account. After many years of developing different methods and their software implementation still the nonlinear dynamic and nonlinear static pushover methods are the most widely used and accepted by the engineers and researchers.

This study focuses on the comparison between single invariant load pattern and multi-mode adaptive pushover methods since this approach requires a lot less computing time, nonlinear modeling and load applying time compared to nonlinear dynamic analysis, but it is still accurate enough to be used in everyday practice.

A number of pushover analyses were performed using FEM software SeismoStruct and then compared to get the final conclusion.

This study implies that the multimode adaptive pushover procedure accurate enough as the conventional pushover methods and in some cases it may be in advantage because of the background theory.

Introduction

The earthquake occurrence and its impact on the existing structures have always been subject of research and topic of discussion among the scientists and engineers. But not only in the modern history, there are evidences that even hundreds of years ago, builders considered earthquake as a phenomenon that is inevitable and they have tried to improve the concept of building and the materials they use in constructing new structures.

Nowadays, in the modern computer era almost all properties of the materials that constitute the elements of the structure can be numerically reproduced. Hence the numerous calculations allow design of optimized constructions that could withstand all predicted loads, such as dead load, live load, wind load, earthquake load etc.

As it is well known the properties of the materials are not linear, hence the analysis, especially in seismic assessment procedure, has to incorporate the nonlinear characteristics in order to use the full potential of the elements consisting of one or more materials. The two most widespread and recognized types of nonlinear analysis are dynamic nonlinear analysis and static nonlinear pushover analysis. Generally, the dynamic nonlinear procedure is considered as the most accurate and type of analysis that describes realistically the behavior of any structure during strong motions that produce forces that deform the elements in deep nonlinearity. The drawbacks of this advanced analysis are the hardware requirements and the computing time as well as detailed definition of the hysteresis behavior and proper selection of

input ground motion data, steps that require deep knowledge of the nonlinearity of materials. On the other hand, the nonlinear static pushover analysis is considered accurate enough to be incorporated in almost all seismic code provisions. This type requires far less computing time and power, but also the theory and the modeling is simpler than the nonlinear dynamic analysis.

Nowadays there are types of pushover analysis that are even better from the well-known collapse (pushover) analysis, starting form defining adaptive load pattern, involving the higher tones of oscillation etc.

Within this study a comparison between pushover with single invariant load pattern and multimode adaptive pushover analysis has been done. The building was assumed to be reinforced concrete structure with flexible storey.

Nonlinear static pushover methods

What started back in the 1970's with the introduction of the pushover analysis, seemed like a promising substitute for the advanced nonlinear time history analysis. That was the main reason why several researchers dedicated their work to make the basis of pushover analysis method. Among the others, Freeman et al. (1975), Fajfar and Fischinger (1988), Saiidi and Sozen (1981), Lawson (1994), Kent K. Sasaki (1998) were some of the first and most well-known researchers. In the last decade, Chopra and Goel (2001), Rui Pinho and Stelios Antoniou (2005), Elnashai (2002), Gupta and Kunnath (2000) tried and succeeded to develop an improved pushover analysis that takes into account the higher modes of oscillation and the changeable stiffness characteristics of the analyzed system.

Conventional pushover analysis formulation

Conventional pushover analysis is the nonlinear incremental-iterative solution of the equilibrium equation in a finite element formulation

$$P = KU \qquad (1)$$

where, K is the nonlinear stiffness matrix, U is the displacement vector and P is a predefined load vector applied laterally over the height of the structure in relatively small load increments. This lateral load can be a set of forces or displacements that have a necessarily constant ratio throughout the analysis (fixed pattern). At the end of each iteration, the reaction vector P^e of the structure is calculated from the assemblage of all finite element contributions. The out-of-balance forces iteratively re-applied until convergence to a specified tolerance is reached.

$$\Delta U = [K_T]^{-1} \cdot (\lambda \cdot P_0 - P^e) \qquad (2)$$

where, ΔU is the calculated displacement increment within iteration, K_T is the current nonlinear (tangent) stiffness matrix, λ is the load factor within the corresponding load increment, P_0 is the initial load and P^e is the equilibrated load (reaction) of the previous iteration.

$$P^e = \sum \int_V B^T \cdot \sigma_{NL} \cdot dV \qquad (3)$$

where, B is the strain-displacement matrix of each element and σ_{NL} is the element nonlinear stress vector as determined by its material constitutive law.

Structure
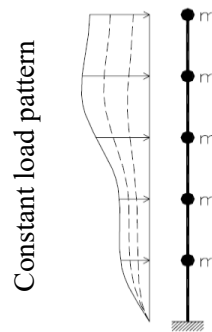
Figure 1. General constant load pattern for
pushover analysis.

The procedure continues either a predefined limit state is reached or until structural collapse is detected. The target limit state may be the deformation expected for the design earthquake in case of designing a new structure, or the drift corresponding to structural collapse for assessment purposes. Generally, this procedure allows tracing the sequence of yielding and failure on the member and structure level, as well as the progress of the overall capacity curve of the structure *fig. 3.2.*
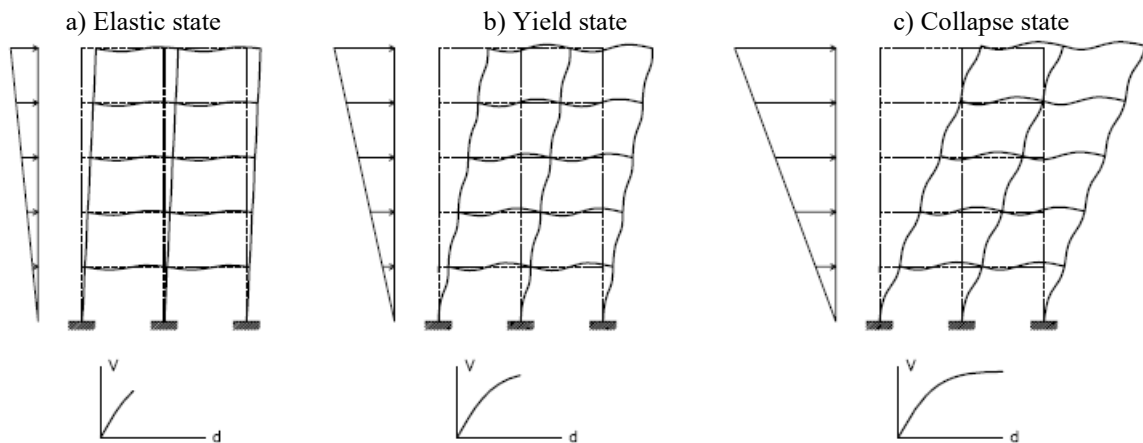
Figure 2. Deformation progress and corresponding capacity curves of conventional pushover analysis.

Single run adaptive force-based pushover analysis

Following Elnashai (2001) proposal for adaptive pushover single analysis algorithm, S. Antoniou and R.Pinho (2003) further developed, tested and implemented this state-of-the art method in SeismoStruct [SeismoSoft, 2004], a fiber-modelling FE program for seismic analysis of framed structures. This single run procedure is fully adaptive and multi modal and accounts for system degradation and period elongation by updating the force distribution at every step of the analysis. The dynamic properties of the structure are determined at each step by performing an eigenvalue analysis that considers the instantaneous structural stiffness.

The main steps that form the adaptive algorithm are:

  (i)   Definition of nominal load vector and inertia mass
  (ii)   Computation of load factor
  (iii)   Calculation of normalized scaling vector and
  (iv)   Update of loading force vector.

In adaptive pushover the loading vector shape is automatically defined and updated by the solution algorithm at each step, but the nominal vector P_0 is defined at the start of the analysis and must always feature a uniform rectangular distribution shape. Also in defining the start-up conditions for the analysis the inertia mass M of the structure has to be modeled, both lumped or distributed, depending on the algorithm.

The load factor is automatically increased by means of load control or response control incrementation strategy until the attainment of the target prescribed response displacement or rotation at the controlled node. Hence the loading vector P at any given analysis step is obtained as a product between its nominal vector P^0 and the load factor λ at that step.

The calculation of normalized scaling vector, F, used to determine the shape of the load vector (not the magnitude) at each step is computed at the start of each load increment. In order to take into account the actual stiffness state of the structure, an eigenvalue analysis is carried out at the beginning of each step. Hence the modal storey forces F_{ij} can be determined as:

$$F_{ij} = \Gamma_j \Phi_{ij} M_i \qquad (4)$$

Where *(i)* is the storey number and *(j)* is the mode number, Γ_j is the modal participation factor for the *(j)*'th mode, Φ_{ij} is the mass normalized mode shape value for the *(i)*'th storey and *(j)*'th mode, and M_i is the mass of the *(i)*'th storey.

Alternatively, the modal storey forces can be computed as:

$$F_{ij} = \Gamma_j \Phi_{ij} M_i S_{a,j} \qquad (5)$$

Where, $S_{a,j}$ represents the acceleration response spectrum ordinate corresponding to the period of vibration of the *(j)*'th mode. Ideally, in order to assure full consistency between demand and supply ductilities, multiple response spectra, derived for varying values of equivalent viscous damping, should be employed so as to reflect the actual energy dissipation characteristics of the structure at each step.

The lateral profiles are then combined using square root of sum of squares (SRSS) or complete quadratic combination (CQC) rules.

The loading vector can then be updated using total of incremental updating. With total updating, the load vector P_t at a given analysis step is obtained through full substitution of the existing balanced load by a newly derived load vector. This new loading vector is computed as a product between the current total load factor λ_t, the current normalized modal scaling vector F_t and the nominal load vector P_0.

$$P_t = \lambda_t F_t P_0 \qquad (6)$$

With incremental updating, the load vector P_t at given analysis step is obtained by adding a newly derived load vector increment to the load vector of the previous step P_{t-1}. The new load vector is computed as a product between the current load factor increment $\Delta\lambda$, the current modal scaling vector F_t and the nominal load vector P_0.

$$P_t = P_{t-1} + \Delta\lambda_t F_t P_0 \qquad (7)$$

normalized shape at step t   nominal load vector   new forces applied at step t

$P_t = \lambda_t X$
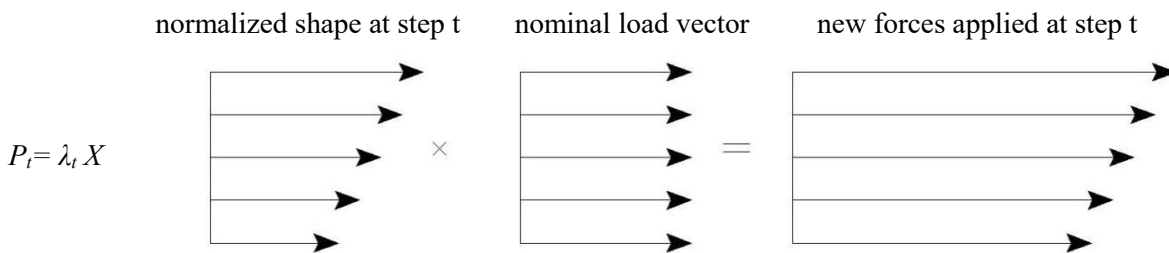
Figure 3. Graphical representation of loading force vector (calculated with total updating).

normalized shape at step t   nominal load vector   new increment of forces

$\Delta P_t = \Delta\lambda_t X$

existing forces   new increment of forces   new forces applied at step t

$P_t = P_{t-1} + \Delta Pt =$
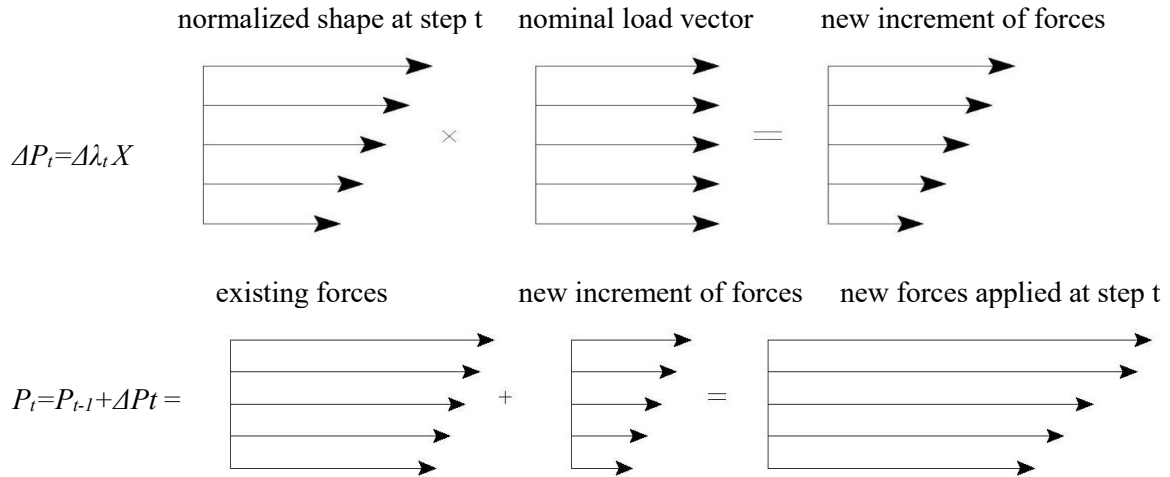
Figure 4. Graphical representation of loading force vector (calculated with incremental updating).

It is worth recalling that in adaptive pushover the response of the structure is computed in incremental fashion, through piecewise linearization, as shown in Figure 5. Therefore, it is possible to use the tangent stiffness at the start of each increment, together with the mass of the system, to compute modal response characteristics of each incremental pseudo-system through elastic eigenvalue analysis, and use such modal quantities to properly update i.e. increment the pushover loading vector.
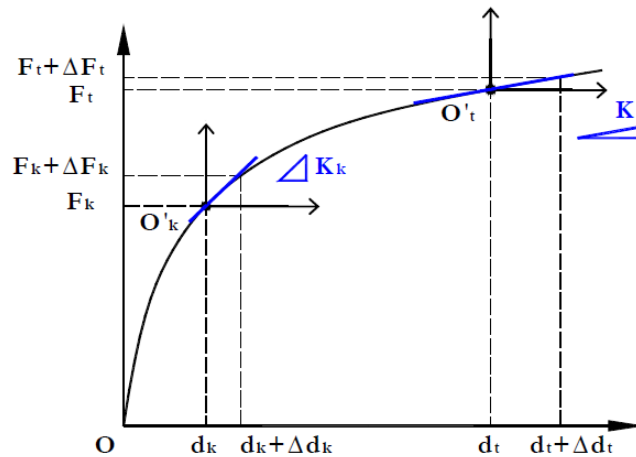
The use of tangent stiffness in updating (i.e. incrementing) the loading vector.

Figure 5. Piecewise linear incrementing the loading vector

Case study

Within the framework of this case study a newly designed structure according to the current Macedonian building codes was analyzed. It is eight storey residential building completely built of reinforced concrete using concrete grade MB30 and steel rebar type RA400/500, representing typical spatial frame structure. Columns cross-sectional dimensions range from 40/40cm; 50/40cm; 60/40cm; 70/40cm and beams 40/50cm. Regarding the main modules, in X-direction there are four parallel frames with spans 5.45m, 1.85m and 5.75m, in Y-direction there are six parallel frames with spans 3.70m, 4.20m, 6.00m, 1.90m and 3.00m. The building is divided in eight floors where the third floor represents flexible storey and is expected to be the weak part during the analysis. As dead load and live load, values of 7,5 kN/m^2

and 1,5 kN/m² respectively were added to the beam elements according to the belonged area and the self-weight of the constitutive elements was calculated by the software itself. The main point of interest was considered the comparison of the results obtained by pushover analysis with invariant load pattern and pushover analysis with adaptive multi-mode load.

Employed numerical tool and modeling

All calculations were performed using the FEM software SeismoStruct V.7.0.0., whose algorithm was primarily presented by S. Antoniou and R. Pinho, then developed and verified by SeismoSoft (earthquake engineering software solutions). The structure was interpreted as a three dimensional model with included material nonlinearity.

The material inelasticity is taken into account by the so called fiber approach that represents the cross-section behavior, where each fiber is associated with a uniaxial stress-strain relationship. The sectional stress-strain state of beam-column elements is then obtained through the integration of the nonlinear uniaxial stress-strain response of the individual fibers in which the section has been subdivided.

Such models feature additional advantages, which can be summarized as: (i) no requirement of a prior moment-curvature analysis of members, (ii) no need to introduce any element hysteretic response (it is implicitly defined by material constitutive models), (iii) direct modeling of axial load bearing moment interaction, (iv) straightforward representation of biaxial loading.

Distributed inelasticity frame elements can be implemented with two different finite elements formulation, the classical displacement based DB and the force based FB formulations. In a DB approach the displacements field is imposed, whilst in a FB element equilibrium is strictly satisfied and no restrains are placed to the development of the inelastic deformations throughout the member.

The distributed inelasticity modelling requires no modelling experience since all that is required from the user is to introduce the geometrical and material characteristics of structural members (i.e. engineering parameters). Its use is therefore highly recommended and will grant an accurate prediction of the nonlinear response of structures.
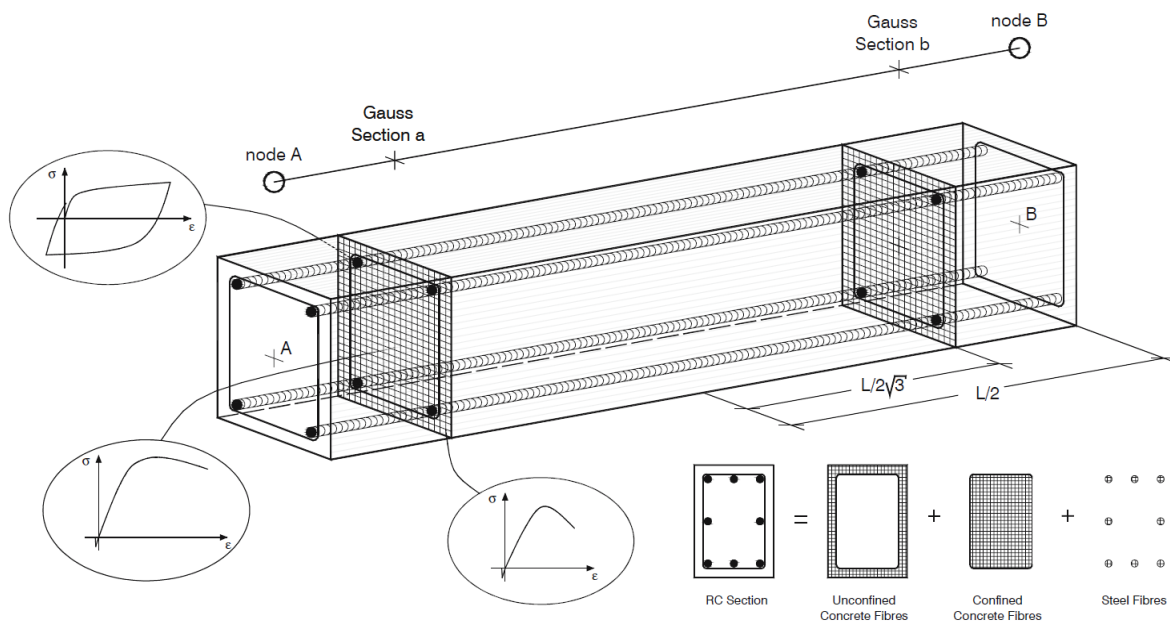
Figure 6. Fiber approach discretization of a typical reinforced concrete cross-section.
(Photo courtesy of SeismoStruct V.7.0.0. User manual)

For the purpose of these analyses an inelastic force-based plastic hinge element type (infrm FBPH) was used. This is plastic hinge element featuring a distributed inelasticity force-based formulation, but concentrating such inelasticity with a fixed length of element. The advantages of this type of element are not only a reduced calculation time, but also a full control of the plastic hinge length.

SeismoStruct software enables the user to select between eleven incorporated material types and by making use of these material types, unlimited number of different materials is possible. For the purpose of this research Mander et al. nonlinear concrete model (con_ma) was used. That is uniaxial nonlinear constant confinement model that follows the constitutive relationship proposed by Mander et al (1988). The concrete section may contain any general type of confining steel, either spiral or circular hoops, or rectangular hoops with or without supplementary cross ties. These cross ties can have either equal or unequal confining stresses along each of the transverse axes. A single equation is used for the stress-strain equation. The influence of various types of confinement is taken into account by defining an effective lateral confining stress, which is dependent on the configuration of the transverse and longitudinal reinforcement. An energy balance approach is used to predict the longitudinal compressive strain in the concrete corresponding to first fracture of the transverse reinforcement by equating the strain energy capacity of the transverse reinforcement to the strain energy stored in the concrete as a result of the confinement.

The user friendly material definition menu in SeismoStruct lets the user easily define the calibrating five parameters in order to fully describe the mechanical characteristics of the material, (i) compressive strength-f_c, (ii) tensile strength-f_t, (iii) modulus of elasticity-E_c, (iv) strain peak stress-ζ_c and (v) specific weight-γ. On Figure 7, the adopted stress strain diagram for the analysis is shown.

For the reinforcing steel material, a uniaxial bilinear stress-strain model with kinematic strain hardening, where the elastic range remains constant throughout the various loading stages, and the kinematic hardening rule for the yield surface is assumed as a linear function of the increment of plastic strain is adopted. This simple model is also characterized by easily calibrating parameters and by computational efficiency. Also five parameters have to be defined, (i) modulus of elasticity-E, (ii) yield strength-f_y, (iii) strain hardening parameter-μ, (iv) fracture/buckling strain ξ_{ult} and (v) specific weight-γ.
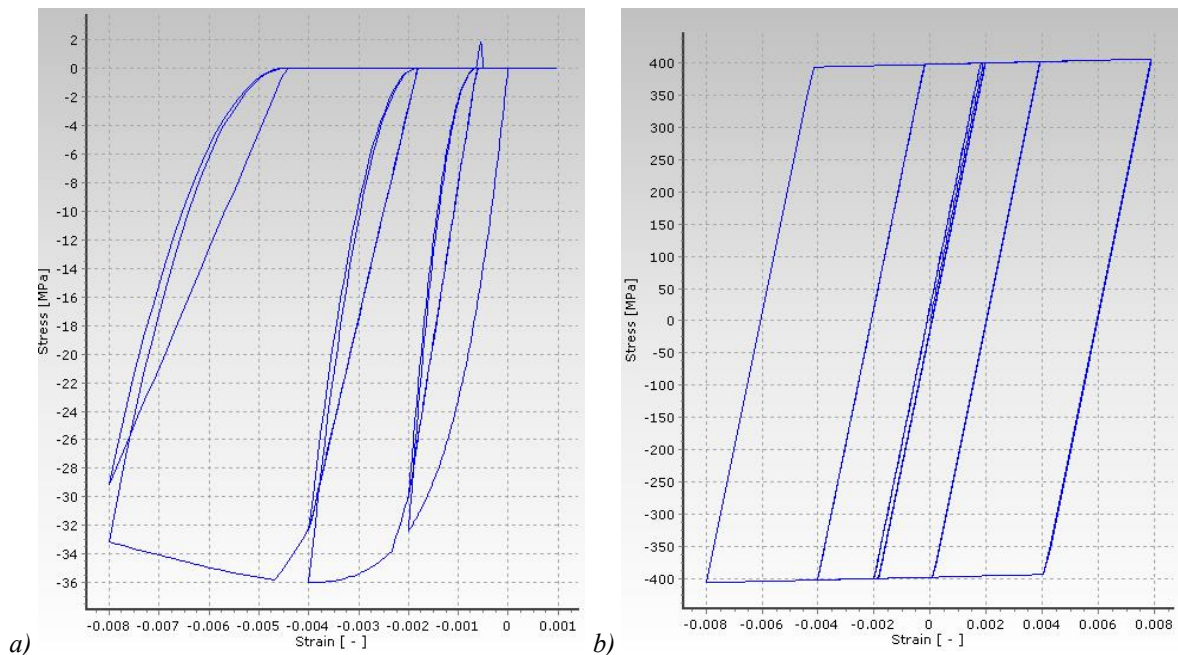
Figure 7. Stress strain relationship for the confined concrete (a), Stress strain relationship for the reinforcing steel (b).

Within the context of performance based engineering it is well known that engineers are capable of identifying the exact moments of time when different performance limit states are reached. This can be sufficiently carried out in the software by definition of performance criteria where the attainment of the certain value, like material strain, section curvature, element chord-rotation etc. is automatically monitored. For the purpose of these analyses the material strain was adopted as criteria to determine the performance of the structure. The advised values are +0.0001 for cracking of structural element, -0.002 for spalling of concrete cover, -0.006 for crushing of core concrete, +0.002 for yielding of steel and +0.06 for fracture of steel.

Description and discussion of the results

For the purpose of this research a multi-mode adaptive and single mode with mass proportional and mode shape proportional invariant load pattern pushover analyses were performed. The parameters that were compared are:

- Pushover capacity curves
- Shear profiles
- Interstorey displacements
- Storey displacements

These are essential parameters in the performance based engineering where the displacements, drifts and strains are the decisive when the structure behavior is assessed. Due to the type of analysis there is option to select the results from a desired point of time, when a change in the global or local system has happened. The points of interest are yielding of steel, spalling off the concrete cover, and crushing of concrete core has been reached for the first time during the performed pushover analyses.
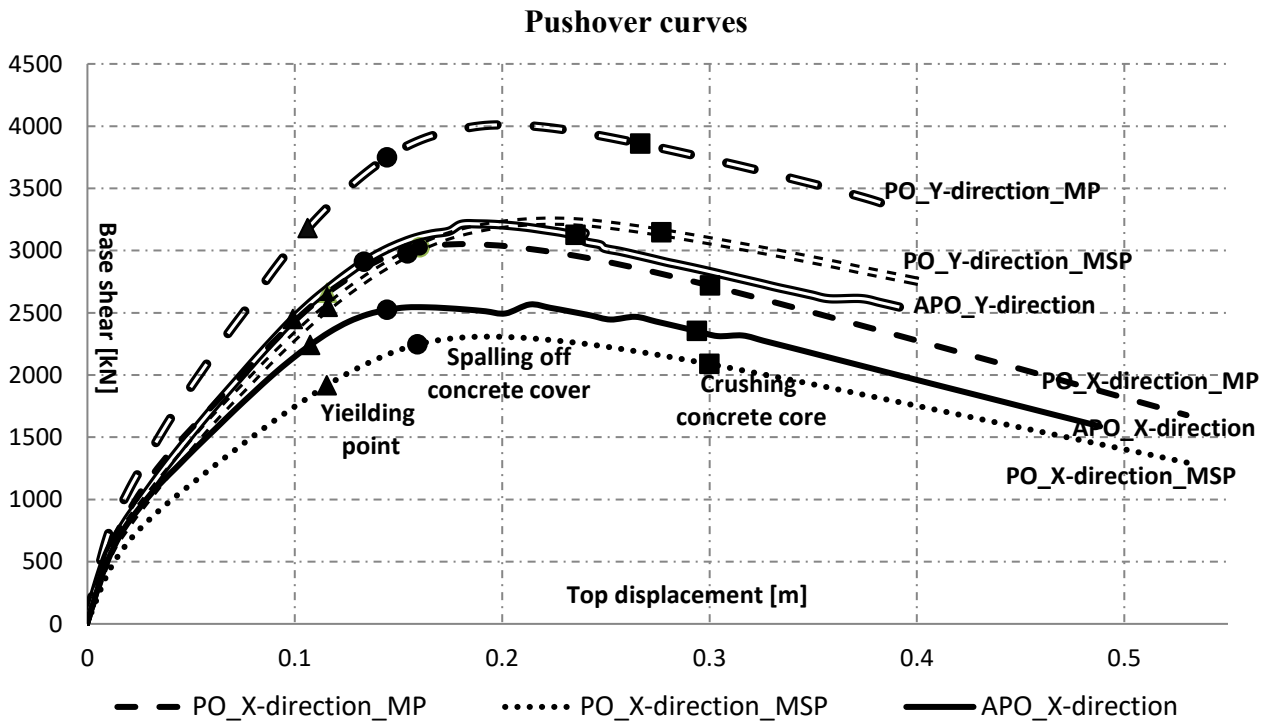
Figure 8. Pushover curves comparison.

The capacity curves for all horizontal loading distribution as expected follow the same shape but still differ from one another. The ones with adaptive and triangular (first mode shape) load pattern are closer where the difference in x-direction is at most 200 kN and in y-direction not more than 50 kN, but the curves from mass proportional load pattern give considerably bigger shear force, in x-direction difference from 700 kN and in y-direction 800 kN. The reason is that the triangular or mode shape pattern is connected to the attainment of maximum allowable plastic hinge rotation, which is defined in each code provision, and the mass proportional load pattern is connected to attainment of storey mechanism which requires bigger force to be reached, with exception of structures with flexible storey located usually in the ground base. On Figure 9 the upper stated view is graphically presented.
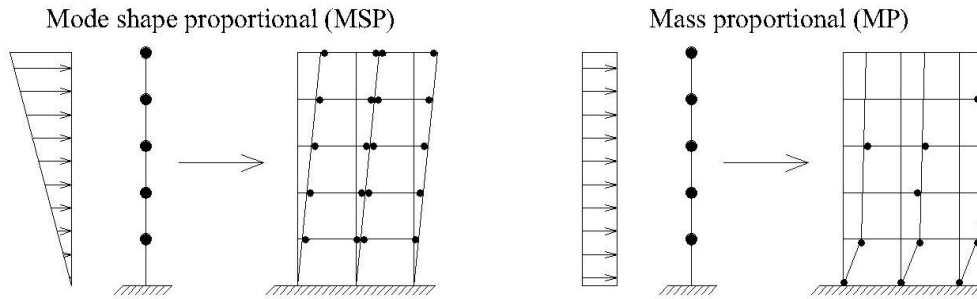
Figure 9. Mode shape and mass proportional loading distribution.
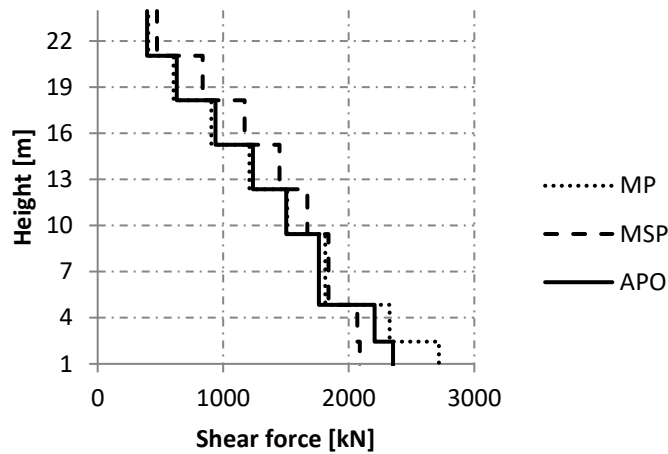
Figure 10. Shear profiles_crushing of core concrete_X-direction.
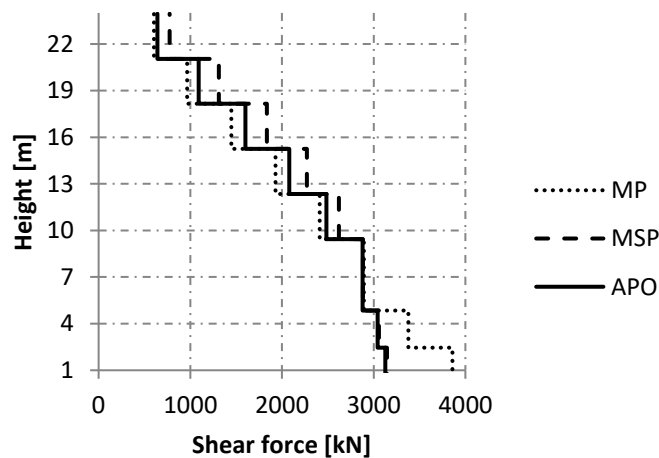
Figure 11. Shear profiles_crushing of core concrete_Y-direction.
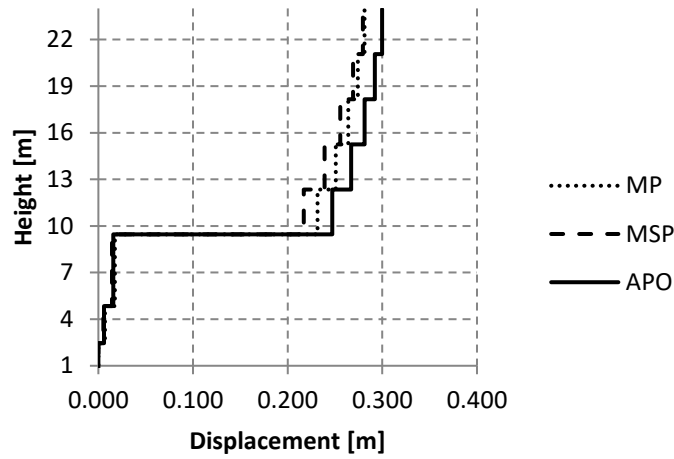
Figure 12. Interstorey displacements_crushing of core concrete_X-direction.
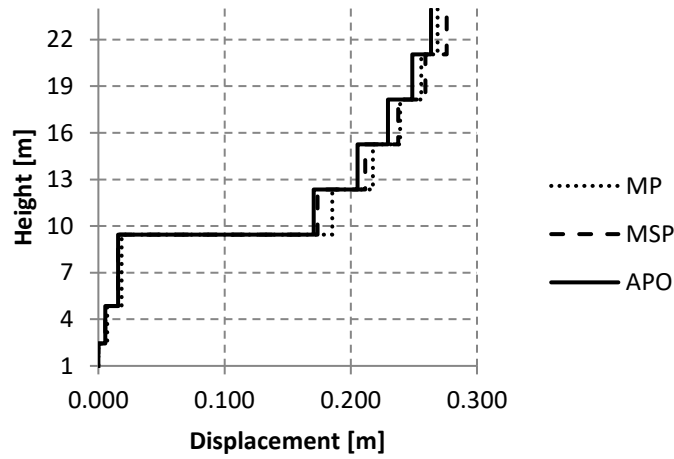
Figure 13. Interstorey displacements_crushing of core concrete_Y-direction.
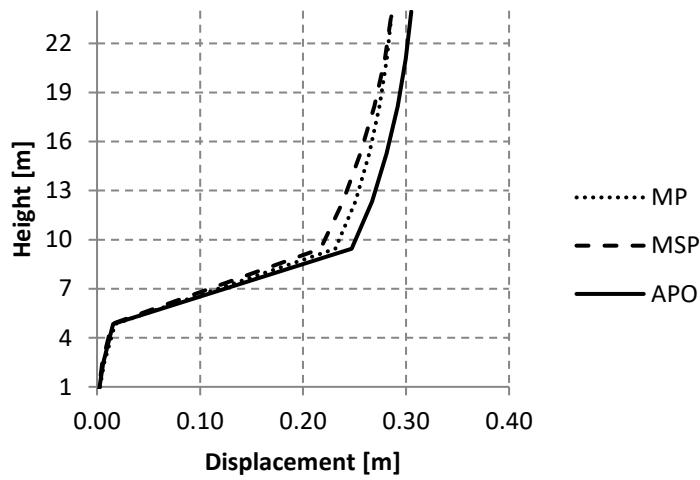
Figure 14. Storey displacements_crushing of core concrete_X-direction.
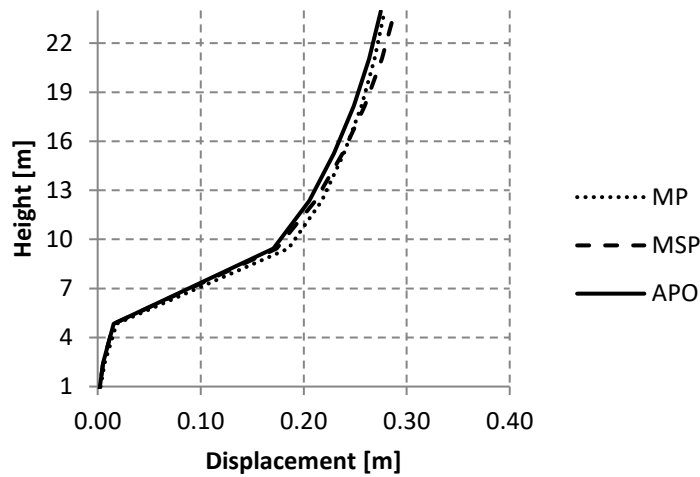
Figure 15. Storey displacements_crushing of core concrete_Y-direction.

From the capacity curves the behavior in terms of deformation capacity can be concluded, meaning that in x-direction the structure deforms under smaller value of base shear, 2250, 2500 and 3000 considering mode shape proportional, adaptive and mass proportional loading vector respectively and in y-direction, 3200, 3200 and 4000 considering mode shape proportional, adaptive and mass proportional loading vector respectively where the value of the base share is considerably bigger. This also leads to the conclusion that in x-direction the structure is more flexible and ductile than in y-direction.

In Table 1 values of displacements and corresponding base shear are shown where it is noticeable that the values for the latter load distribution show base shear considerably bigger for displacements that are close to one another.

From the shear and interstorey drift profiles it is obvious that the third storey experiences biggest deformations and is known as flexible storey. Hence is the most vulnerable and experiences the biggest interstorey drifts, from 1,15% in the point of yielding of steel to 5% in the point of crushing of core concrete in x-direction and 0,83% in the point of yielding of steel to 3,5% in the point of crushing of core concrete in y-direction. This can be also confirmed by storey displacements where the slope of the curve is noticeable to be biggest in the region of the flexible storey.

Having in mind the latter statements it is logical to be concluded that the first plastic hinge appears on the flexible storey and then the nonlinear behavior of the elements/hinges either spreads on the same storey or in its vicinity.

From the capacity curves it is clear that the difference between pushover analysis with mode shape proportional load and adaptive pushover is small, starting from 0% up to 15% and the main reason is assumed to be that the fundamental mode of vibration is clear and activates most of the mass of the structure.

Table 2. Values of the points of interest.

Point of interest		APO_X-direction	APO_Y-direction	PO_X-direction_MP	PO_X-direction_MSP	PO_Y-direction_MP	PO_Y-direction_MSP
Yielding point	Displacement	0.108	0.099	0.116	0.115	0.106	0.116
	Base shear	2241.452	2447.657	2658.889	1917.097	3178.460	2546.336
Spalling off concrete cover	Displacement	0.144	0.133	0.160	0.159	0.145	0.154
	Base shear	2523.710	2908.760	3025.265	2246.475	3748.873	2977.266
Crushing concrete core	Displacement	0.294	0.235	0.300	0.300	0.267	0.277
	Base shear	2352.461	3126.814	2718.140	2088.033	3858.992	3145.005

As commented in the previous conclusion and confirmed by the step-by-step output from the software, the behavior in x-direction is led by forming a storey mechanism while in y-direction the rotation of the plastic hinges and the inclination of the structure above the flexible storey is obvious. On Figure 16 the deformations and the storey mechanism is shown, where a) is in y-direction and b) is in x-direction.
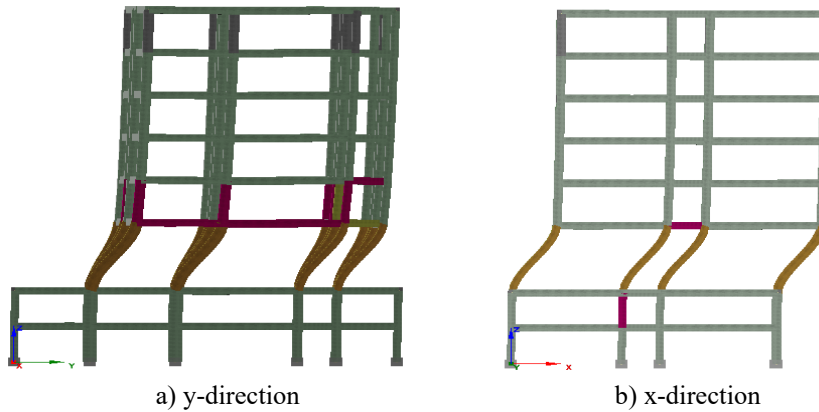
a) y-direction   b) x-direction
Figure 16. Last step of analysis deformation.

Conclusions

Nonlinear static procedures also known as pushover methods represent an easier and simpler alternative to nonlinear dynamic analysis procedures. They overcome the major disadvantages like, (i) requirement for site specific ground motions compatible with the seismic hazard spectrum for the site, (ii) computational demand to model and analyze 3D models, constituted by thousands of elements, (iii) numerous runs required to get the average response of the structure, (iv) computational time.

The loading pattern in pushover analysis has always been applied in invariant fashion with the assumption that the structure's response is controlled by a single fundamental mode shape and that remains unchanged during the analysis. According to the most building codes two lateral load patterns are recommended to be applied, first mode proportional (triangular) and mass proportional (uniform). On the other hand according to FEMA 440 report the effectiveness of conventional nonlinear static methods is questionable because of (i) inaccurate prediction of deformation when the higher modes are important, (ii) neglecting sources of energy dissipation such as kinetic energy and viscous damping, inability of reproducing peculiar dynamic effects, (iii) inability to account for redistribution of inertia forces due to progressive yielding resulting changes in dynamic properties of the structure, (iv) inaccurate prediction of local damage concentrations, (v) difficulty in incorporating three dimensional and cyclic earthquake loading effects. Thus, due to the limitations that arise from the mentioned features, the dynamic response obtained by static procedure and its reliability have to be carefully evaluated.

The research confirms that the adaptive pushover analysis could be a recognized procedure in terms of seismic behavior analysis of structures and an improved substitution of conventional pushover procedure in code provisions. Results proved that the mind appealing theory of the adaptive load yields good results and parameters that could assess the seismic capacity.

References

Chopra A.K. (2011): *Dynamics of structures, theory and applications to earthquake engineering*, fourth edition, Prentice Hall, USA.

Seismosoft (2014): *SeismoStruct v7.0 – A computer program for static and dynamic nonlinear analysis of framed structures.* available from http://www.seismosoft.com.

Vassilis K. Papanikolaou and Amr S. Elnashai. (2005) *Evaluation of conventional and adaptive pushover analysis I: Metogology,* Journal of earthquake engineering **Vol. 9, No. 6**, pp. 923-941.

Mander J.B., Priestley M.J.N. and Park R. (1988): *Theoretical stress-strain model for confined concrete,* Journal of structural engineering, **Vol. 114, No. 8**, pp. 1804-1825.

Papanikolaou V.K., Elnashai A.S., and Parea J.F. (2005): *Limits of applicability of conventional and adaptive pushover analysis for seismic response assessment,* Mid – America earthquake center, Civil and environmental engineering department, University of Illinois at Urbana – Campaign.

Federal Emergency Management Agency (FEMA) (1997): *NEHRP guidelines for the seismic rehabilitation of buildings*, BSSC Seismic rehabilitation project.

Federal Emergency Management Agency (FEMA) (2006): *NEHRP recommended provisions: design examples,* BSSC.

Mwafy A.M. and Elnashai A. S. (2000): *Static pushover versus dynamic collapse analysis of RC buildings,* Engineering structures, **Vol. 23, No. 5**, pp. 407-424.

Pinho R. and Antoniou St. (2005): *A displacement based adaptive pushover algorithm for assessment of vertically irregular frames,* 4th European workshop on the seismic behavior of irregular and complex structures, Thessaloniki, Greece, 26-27 August 2005.

Paret T.F., Sasaki K.K., Eilbeck D.H., and Freeman S.A. (1996): *Approximate inelastic procedures to identify failure mechanisms from higher mode effects,* Eleventh world conference on earthquake engineering, Paper No. 966.

Antoniou St. and Pinho R. (2003): *Development and verification of a displacement based adaptive pushover procedure,* Journal of earthquake engineering, **Vol. 8, No. 5**, pp. 643-661.

Kunnath S.K. (2004): *Identification of modal combination for nonlinear static analysis of building structures.* Computer-Aided Civil and Infrastructure Engineering. , 19, pp. 246-259.

Dynamic analysis and comparison of pedestrian load models for footbridges

NÉMETH Gábor
Budapest University of Technology and Economics

CSILLAG Fruzsina
Delft University of Technology

Abstract

In the history since now, the dynamic effects on footbridges have rarely caused the failure of the structure, however they have led to serviceability problems several times. As a result, they have created discomfort, or even inhibited the pedestrians from crossing. For that reason, it is indispensable to determine the dynamic behaviour of footbridges, and to take the vibrations into account during the design stage. Besides, the theme's importance is emphasized by the fact that the modern structures tend to be more and more slender, and lighter, hence more and more susceptible to dynamic effects.

Although, the imposed loads on footbridges have low intensity, but they act as dynamic load, thus they play a great role in triggering the vibration of the footbridge particularly in the lateral direction. Resonance occurs if the natural frequencies for slim, lightweight bridges coincide with the walking frequencies of the pedestrians, creating accelerations of such a level that they are often regarded as annoying. Thus, the need for an accurate a priori dynamic analysis of pedestrian bridges became vital.

The official Hungarian code – the Eurocode – only defines the requirement for the comfort levels, nonetheless fails to give detailed guidelines. Thus, the aim of our research is the comparison of different codes, used by the Hungarian structural engineers. We analysed the SÉTRA, the non-official Proposal Annex C, and the British National Annex in our paper. First, we built finite element models of two footbridges, namely the Bagers Bro footbridge in Malmo, and the Horton footbridge by using the program Sofistik, then we applied the loads prescribed in the above mentioned guidelines to the two models.

Moving on, we created a load model, which reflected better the real behaviour of pedestrians in order to determine the punctuality of the guidelines. Our load model included the randomness of both the number of pedestrians and the frequencies of the walking. We applied the individual pedestrian load according to Bachmann. From each load cases, we gained data of acceleration and displacement, which enabled us to perform the comparison.

Introduction

The imposed loads of pedestrian bridges are low in intensity but act as periodic dynamic loads, thus playing a significant role in the (vertical, horizontal or torsional) vibrating of the bridge. For these impacts, when designing a pedestrian bridge, it is necessary to analyze whether the structure meets the serviceability requirements and does not exceed the limits for acceleration and deformation during vibration.

Dynamic examination of the footbridges is quite complicated and is a very complex task. For this reason, the designer must make simplifications (structural damping, density of pedestrian traffic, etc.), choosing a suitable guide to design. Different standards give the typical frequencies of different types of movement, prescribe the mass of the people and make other simplifications. The question arises, how much by the standards pedestrian load models reflect reality, contain sufficient, perhaps excessive security? This article is based on this idea.

Review of current codes

Eurocode Proposal Annex C and the requirements of EC

In 2001, an annex was made to Eurocode. This proposal has never been officially accepted, but many design engineers use it as a guide to design footbridges.

Eurocode is a collection of building standards in force in the European Union, developed and issued by the European Committee for Standardization. The most important limitation is the comfort criteria in EC 0 (Table 1). Pedestrians are more sensitive to horizontal vibrations than vertical ones. Eurocode limits these vibrations accordingly, and also determines when dynamic tests are required.

Table 1. Recommended maximum accelerations by EC 0.

Condition	Maximum acceleration [m/s^2]
Vertical vibrations	0.7
Horizontal vibrations due to normal use	0.2
Exceptional crowd conditions	0.4

A verification of the comfort criteria is required if the fundamental frequency on the deck is less than

- 5 Hz for vertical vibrations,
- 2,5 Hz for horizontal (lateral) and torsional vibrations.

The EC does not provide clear, usable instructions besides the limit values and the limitation of the frequency of the deck. It sets requirements, but it does not write anything about the calculation of its fundamental frequencies, the load models or the methods of verification. Therefore, in engineering practice, when calculating the dynamic behavior of pedestrian bridges, other standards and guides are used by engineers instead of Eurocode.

SÉTRA

SÉTRA (Service d'Études Techniques des Routes et Autoroutes) published in 2006, is a proposal by the Technical Department for Transport, Roads and Bridges Engineering and Road Safety – which is a technical department within the Ministry of Transport and Infrastructure in France – for the evaluation of the dynamical behavior of pedestrian bridges.

The guide's suggestions are based on experiments, for the examination of lock-in these are based on Pont de Solférino, for modeling the pedestrian load these based are on laboratory conditions.

EN 1991-2 British National Annex

The British National Annex for Eurocode 1991-2 is based on the researches of Barker and MacKenzie (Barker and MacKenzie 2005). The British National Annex surpasses many aspects of the previous two guides, as it takes into account the different modes of walking – running, and it uses a moving

force model instead of locally pulsating load. Both aspects show that this load model can be the closest to reality, but it does not provide any recommendation for evaluating the structural response.

Modeling of footbridges

In order to compare the pedestrian load models, we have modeled two highly different geometry. The first bridge is a simple bridge with a steel-concrete composite structure, while the second is a truss bridge curved along both planar and altitude way. Different construction design obviously results different dynamic behaviors, so it is also possible to study various types of loads recorded in the standards.

Horton footbridge

The Horton footbridge (Figure 1), built in Hillingdon in 2013 is a relatively common, generally designed bridge, which can be sensitive to pedestrian-induced vibrations.
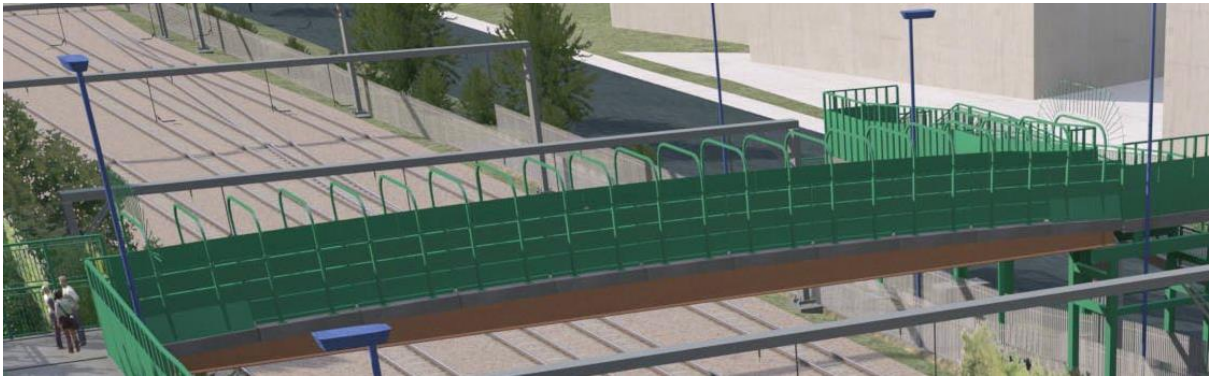
Figure 1. Visualization of Horton footbridge (http://www.railengineer.uk/2013/02/19/running-free/).

The Horton footbridge has a straight axis with a 33-meter long span, and it's perpendicular to the obstacle. The cross section of the bridge (Figure 2) is made of two steel main girders of I-section, 1.5 meters apart, and a reinforced concrete slab with a width of 3 m and a thickness of 15 cm. The two main girders are connected by 7 welded C-section cross girders.
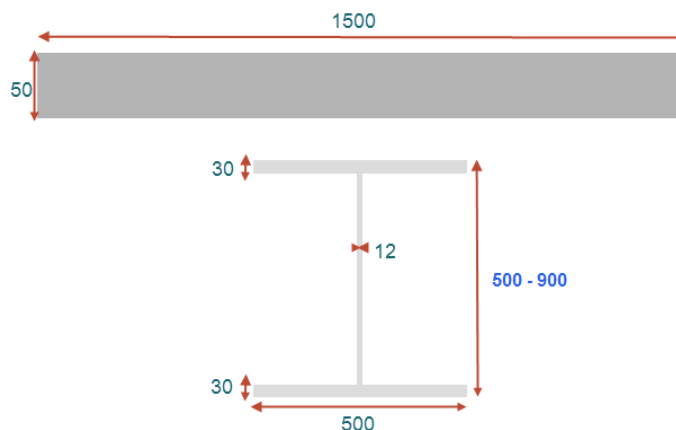
Figure 2. Cross section of Horton footbridge.

(http://myengineeringprojects.blogspot.hu/2013/08/vibration-analysis-of-pedestrian-bridge.html)
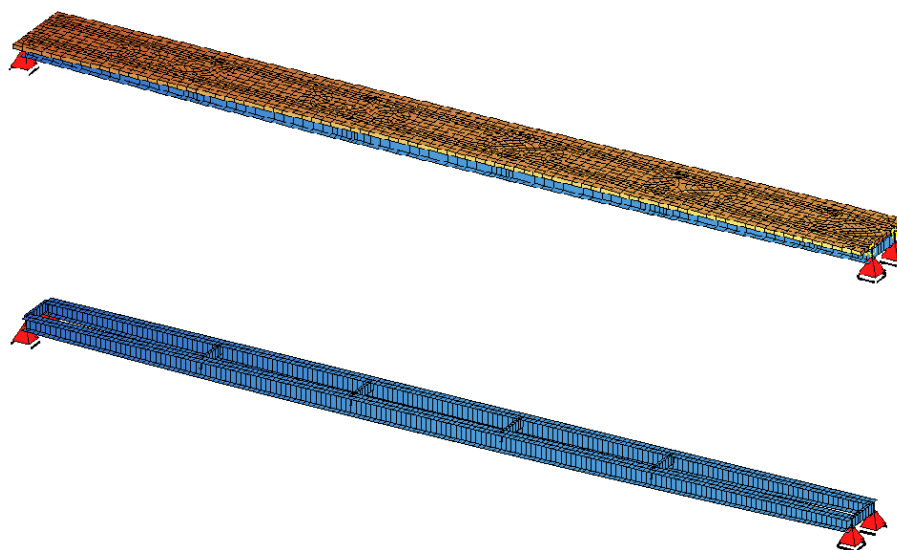
Figure 3. FE model of Horton footbridge with and without deck.

Based on the above we built the finite element model of the structure (Figure 3). The main and cross girders were composed of beam elements, the slab was modeled with shell element, the connection of the steel and concrete parts of the composite structure was solved with kinematic boundary conditions.

The role of the deck is key in the models as pedestrians will move on this surface. From the standards we have examined, only the British National Annex of Eurocode 1 requires a moving pedestrian load. For these examinations and for our own model, we created lanes on the deck.

Structural damping has been added to the finite element models according to the suggestion of fib. The calculation of the eigenfrequencies (Table 2) was carried out using the dynamic module of the applied finite element program. The number of eigenmodes was determined based on activated masses and dangerous frequency ranges.

Table 2. Eigenfrequencies and eigenmodes of Horton footbridge.

Number of mode	f [Hz]	Type	Modal mass [%]			Should be analyzed according to these standards
			x	y	z	
1	1.780	Pure bending (Figure 4)	0.02	0.00	81.83	SÉTRA, Annex C, British Annex
2	4.936	Pure twisting	0.00	23.80	0.00	-
3	6.640	Pure bending (Figure 5)	0.10	0.00	0.00	British Annex
4	7.358	Pure twisting	0.00	56.99	0.00	-
5	11.994	Local twisting of the deck	0.00	0.00	0.00	-
6	14.203	Pure bending	0.44	0.00	8.83	-
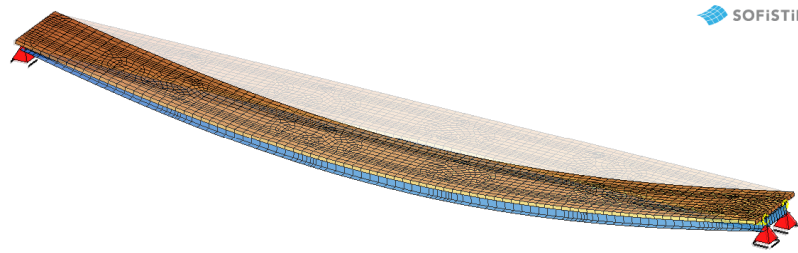
Figure 4. Horton footbridge, 1st eigenmode (vertical bending).
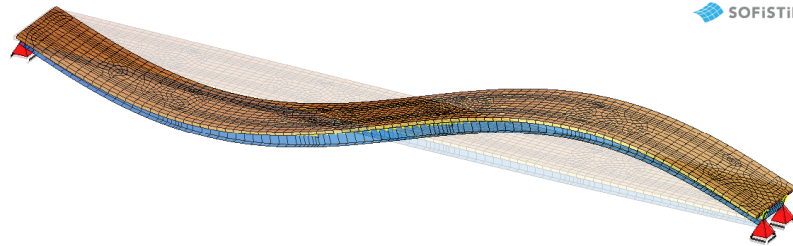
Figure 5. Horton footbridge, 3rd eigenmode (vertical bending).

The frequency range of the walk is 1.3 to 2.5 Hz, running is 2 to 3.5 Hz, so according to the literature only the first eigenfrequency falls in the critical range. However, of the 3 standard, the British Annex sets more stringent requirements that vertical shapes below 8 Hz should also be examined, so the third mode is also to be studied.

Bagers Bro

Bagers Bro (Figure 6) is a built pedestrian and cycling bridge in Malmö, Sweden. The bridge is a curved steel truss with a 37 m span and 2.4 m width. The bridge is curved both in plan and elevation, reaching its highest 1.5 meter height in the middle (Sjöström 2014).

The grid of the bridge consists of three longitudinal beams, struts forming triangulars and cross girders (Figures 7 to 8). The deck made of a material called 'G9 Rustik' made from recycled plastic.
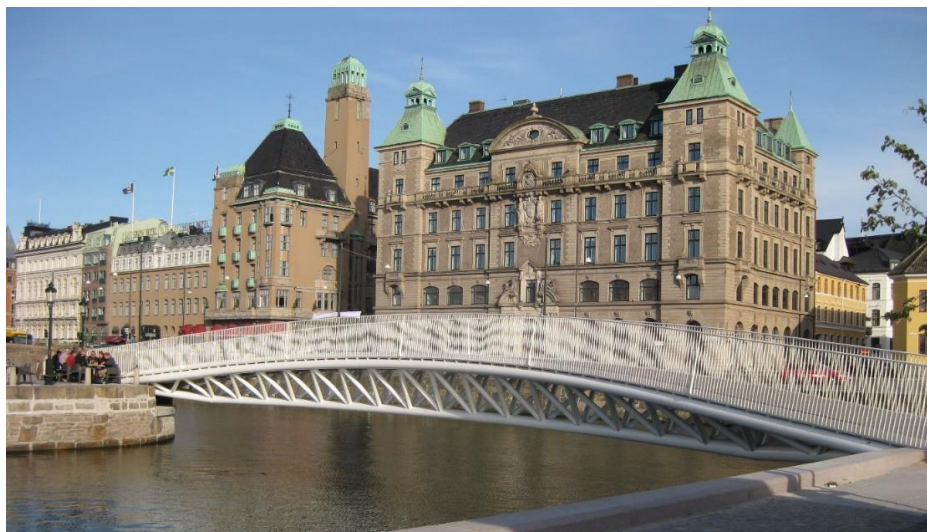
Figure 6. Bagers Bro footbridge in Malmö.
(https://commons.wikimedia.org/wiki/File:Bagers_bro,_Malm%C3%B6.jpg)
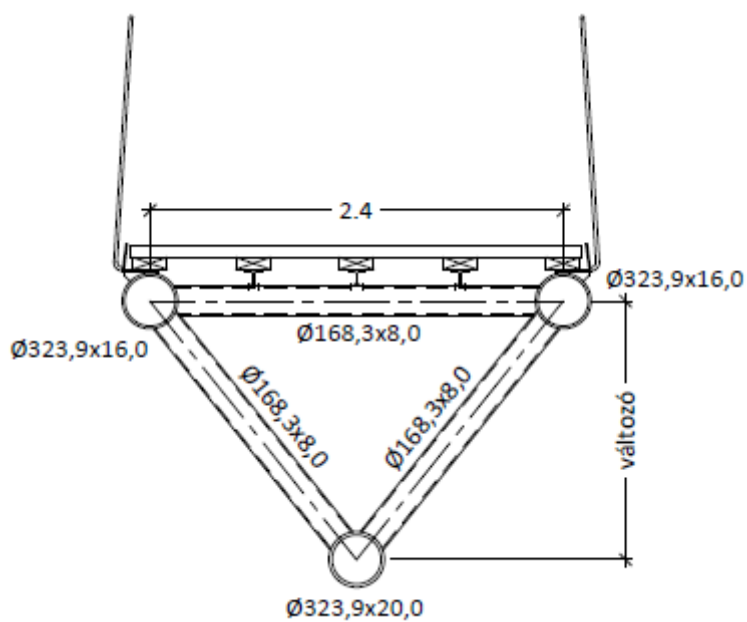
Figure 7. Cross section of Bagers Bro.
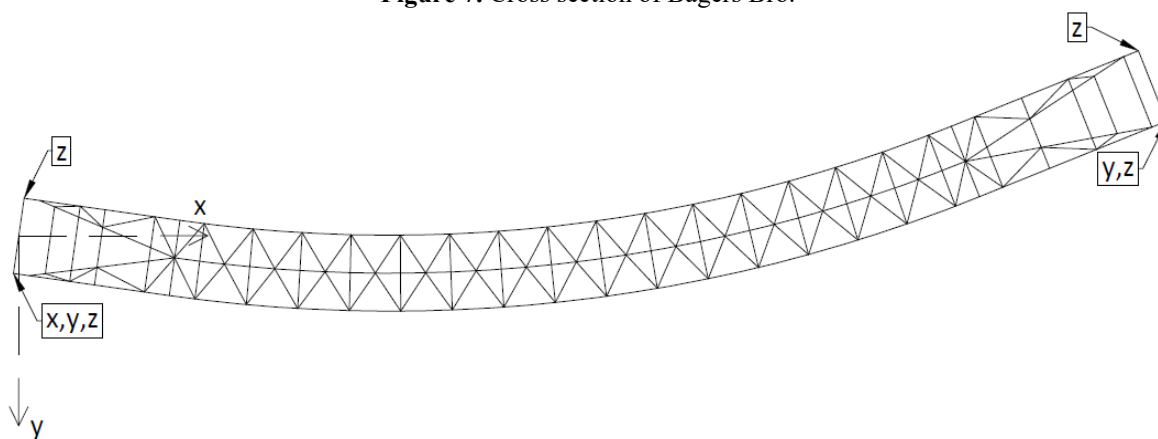
Figure 8. Plan view of Bagers Bro.

The main girders and the struts were modeled as beam elements (Figure 9). Longitudinal hot rolled HEB beams have not been introduced into the model because their weight and stiffness are insignificantly small compared to the closed tubular sections. Eigenfrequencies are shown in Table 3.
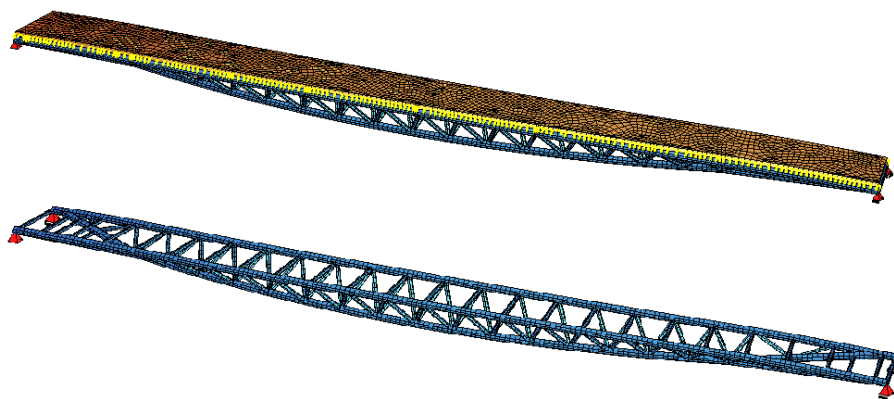
Figure 9. FE model of Bagers Bro with and without deck

Table 3. Eigenfrequencies and eigenmodes of Bagers Bro.

Number of mode	f [Hz]	Type	Modal mass [%]			Should be analyzed according to these standards
			x	y	z	
1	1.60	Vertical bending (Figure 10)	0.74	7.53	72.88	SÉTRA , Annex C, British Annex
2	2.98	Horizontal bending	0.60	73.30	7.85	-
3	6.26	Vertical bending (Figure 11)	0.66	0.00	0.03	British Annex
4	9.70	Twisting	2.02	0.09	0.00	-
5	9.94	Twisting and horizontal bending	0.67	0.28	7.00	-
6	12.97	Vertical bending and twisting	1.06	0.14	4.53	-
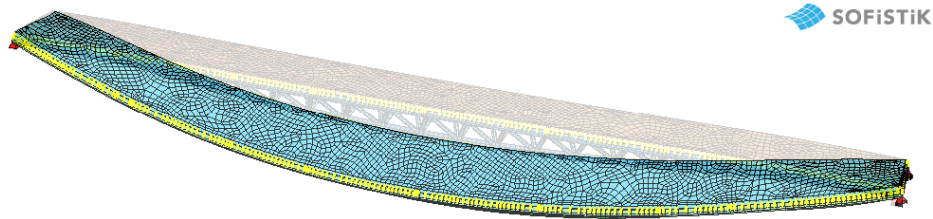
Figure 10. Bagers Bro, 1st eigenmode (vertical bending).
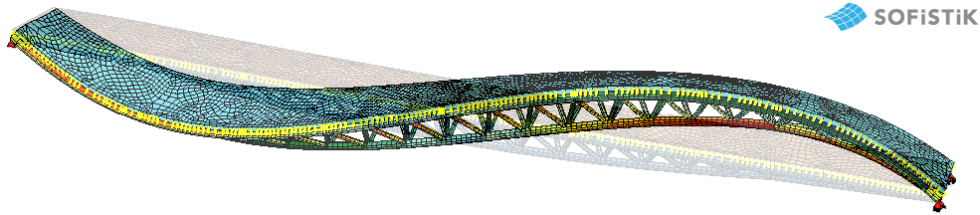
Figure 11. Bagers Bro, 3rd eigenmode (vertical bending).

Compared to the (Sjöström 2014) literature where writers had the exact geometry of the bridge, we get almost the same eigenfrequencies, and the shapes are almost perfectly matched.

Taking into account the pedestrian loads

In the first part of the analysis, loads corresponding to the standards were applied to the models. Then we examined the bridges with our own pedestrian model. Our goal with our own pedestrian model was to create a load model closer to reality. For this we used Bachmann's formula (Bachmann 1987), but the variables were randomly replaced by the appropriate distributions.

Many people have studied the Fourier coefficients of pedestrian loads, of which Bachmann's results spread best (Bachmann 1987). In our model we apply the following relation to vertical loading:

$$F_v = F_0 + F_{1,v} \cdot \sin(2\pi \cdot f_s \cdot t) + F_{2,v} \cdot \sin(4\pi \cdot f_s \cdot t - \varphi_2) + F_{3,v} \cdot \sin(6\pi \cdot f_s \cdot t - \varphi_3) \tag{1}$$

Where: F_0 – weight of pedestrians

$F_{i,v}$ – part of the i-th harmonic of the load

f_s – frequency of step

φ_i – phase angle of the i-th harmonic

Harmonics were evaluated according to Bachmann's recommendations (Bachmann 1987). Load depends to a great extent on the frequency and mass of pedestrians, so we treated them as a probability variable.

The experiments show that the values of the step frequencies follow the normal distribution, the expected value of the density function being 2 Hz, and the deviation is 0.175 (Bachmann 1995). Depending on the density function, the distribution function is also given. In our pedestrian model, the probability is defined by randomly generated numbers 0 to 1. These probability values are assigned frequencies by the inverse of the distribution function.

The mass of pedestrians follows a normal distribution like the frequency. The expected value is 73.9 kg and 14.9 for standard deviation according to EFSA Scientific Committee. The masses of pedestrians were produced by the inverse distribution functions assigned to random probabilities similar to the frequency.

The number of people crossing the bridge has been calculated so that we can compare with the load models of standards. So we got three load cases: 1 person, 8 people and 15 people.

People on the bridge arrive randomly to the bridge. This was taken into account by shifting the excitation of pedestrians. This was accomplished by the phase angles in the Bachmann formula. The variable is a random number value between 0 and $\pi/2$, which changes per pedestrian.

Results and evaluation

Of the standards, only Annex C deals with single pedestrians, thus the maximum acceleration values are compared in Table 4 with the values obtained from our own load model.

It can be seen from the table that the results from single pedestrian load are negligible low acceleration values, so taking such loads into consideration in planning is useless.

The single pedestrian load model proposed by Annex C differs in many respects from our model, resulting the difference between maximum acceleration values. Our own moving load model operate only for the time of crossing the bridge – unlike the load model DLM1, which is to be operated until the maximum is reached in term of acceleration values – so it excite the structure for a shorter time. The frequency of the pulsating load is also different, as in the case of our load model, pedestrians passes the random rate of normal distribution, in contrast to the first eigenfrequency prescribed in DLM1. The static load, i.e. the self-weight of pedestrian, is ignored by the standards for dynamic loads, since it is only relevant to the deflection of the structure and does not affect the acceleration value. However, our load model was prepared according to Bachmann, which is why the static F_0 component is also included.

Table 4. Comparison of single pedestrian load models

Single pedestrian	Horton		Bagers Bro	
	Annex C	Own	Annex C	Own
Load case	DLM 1	1 person	DLM 1	1 person
Static load [N]	0	739	0	739
Amplitude of dynamic load [N]	280	296	280	296
Max. acceleration [m/s^2]	0.020	0.0047	0.034	0.002
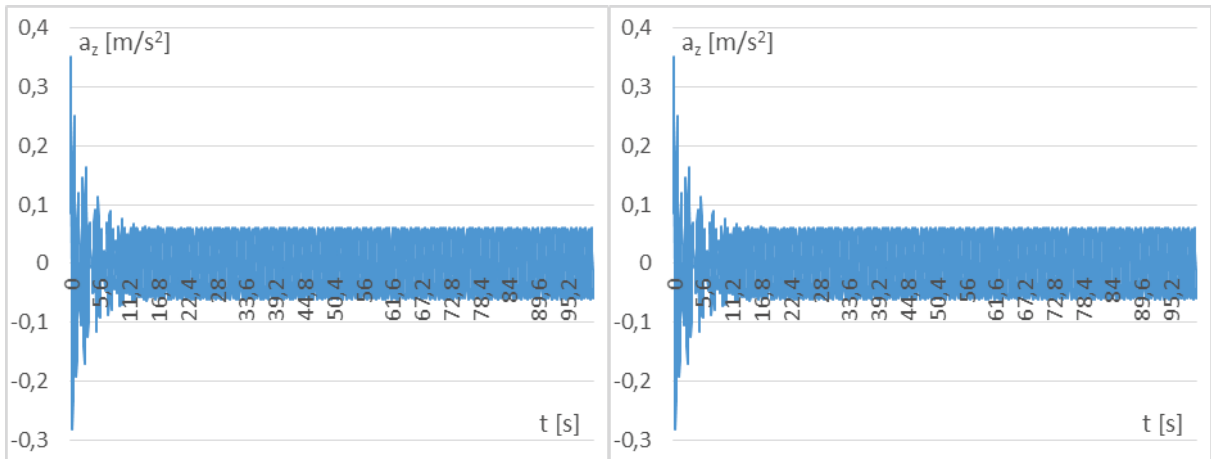
Figure 12. Vertical accelerations of the significant points on Horton (left) and Bagers Bro (right) (DLM 2).

For examining the pedestrian group, for example, the results for DLM2 (Figure 12) are presented.

The diagrams show the combined effect of two processes. On the one hand, the structural response to pedestrian excitation: the acceleration values increase from 0s to 10s and then stabilize. On the other hand, peak values can be observed in the first 8 seconds. The reason for this is that the mass was suddenly applied to the structure, which resulted in a peak acceleration, which was attenuated according to structural damping. As shown, the two phenomena are superimposed, but only the first phenomenon is relevant for the maximum acceleration/displacement values, since the second phenomenon cannot actually happen, as the pedestrians keep coming up to the bridge and not suddenly jump over the entire length of the deck. Stable vibration occurs with a constant amplitude periodic vibration, which results in a standing wave nature diagram associated with the eigenfrequency of the structure.

For a more accurate evaluation of the data, a fast Fourier transform was performed (Figure 13). Fourier analysis can be used to read the frequencies that are associated with the eigenmodes, so the structural response can be clarified.

It can be seen from the figures that only the first vibration pattern is activated.

By examining the British Annex, we can see that the accelerations are moving on gradually (Figure 14), and there are no visible bursts due to the suddenly dropped load mentioned above.
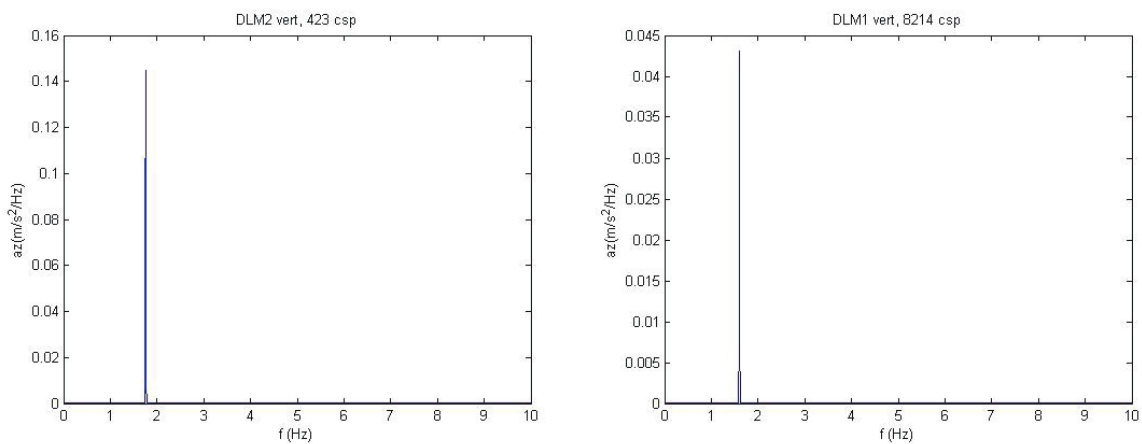
Figure 13. Vertical accelerations of the significant points on Horton (left) and Bagers Bro (right) (DLM 2) in frequency domain.
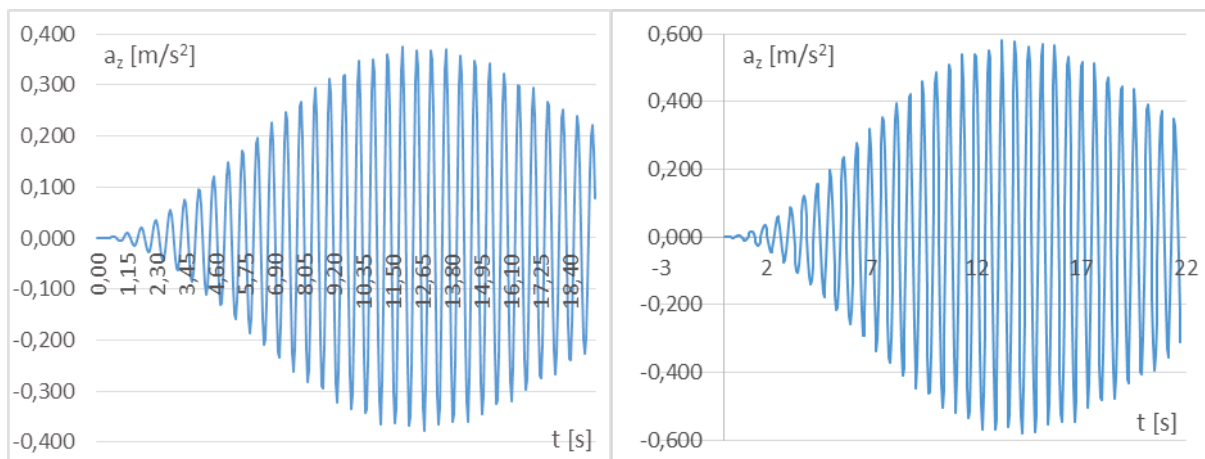
Figure 14. Vertical accelerations of the significant points on Horton (left) and Bagers Bro (right) (BS NA pedestrian group).

As can be seen from Table 5-6, the acceleration values from our own load model are roughly one order of magnitude lower than the values from standard load models. The most important reason for this is the interplay of moving loads with random properties. Randomly generated weight, frequency of steps, and phase difference can create synchronization between concentrated loads, but never as much as the standards assume.

Table 5. Comparison of pedestrian groups of 8 people.

8 people	Horton			
	SÉTRA	**Annex C**	**BS NA**	**Own**
Load case	8 people	DLM 2	Pedestrian group	8 people
Static load [kN]	0	8	0	5.9
Amplitude of dynamic load [kN]	0.0065 kN/m² (~0.6435)	0.84	0.493	~2.36 (random)
Max. acceleration [m/s²]	0.03	0.062	0.377	0.0054
Limit [m/s²]	Max comf.	0.7	1.32	-
	Bagers Bro			
Load case	8 people	DLM 2	Pedestrian group	8 people
Static load [kN]	0	8	0	5.9
Amplitude of dynamic load [kN]	0.014 kN/m² (~ 1.24)	0.84	0.422	~2.36 (random)
Max. acceleration [m/s²]	0.184	0.116	0.582	0.010
Limit [m/s²]	Max comf.	0.7	1.32	-

Table 6. Comparison of pedestrian groups of 15 people.

15 people	Horton			Bagers Bro		
	SÉTRA	Annex C	Own	SÉTRA	Annex C	Own
Load case	15 people	DLM 2	15 people	15 people	DLM 2	15 people
Static load [kN]	0	8	5.9	0	8	5.9
Amplitude of dynamic load [kN]	0.0089 kN/m^2 (~0.88)	0.84	~4.43 (random)	0.0192 kN/m^2 (~1.71)	0.84	~4.43 (random)
Max. acceleration [m/s^2]	0.042	0.062	0.0057	0.256	0.116	0.010
Limit [m/s^2]	Max comf.	0.7	-	Max comf.	0.7	-

The second most important difference is due to different application in space of the point load. In our own model, pedestrians are scattered across the deck, but in the British National Annex, which is still the closest to reality, there is a concentrated force that embraces the effect of the total of eight people. Annex C also "compresses" the load of 8-15 pedestrians in a concentrated force, and the SÉTRA guide simulated the effect of the pedestrian group as a surface load along the deck. It can be seen that even the amplitude of the dynamic load and the time of loading have less effect on the magnitude of the maximum acceleration values than the load arrangement.

Our own, moving force model has, in both bridges, caused less accelerations than the load models of standards. The model of the British National Annex stands closest to the reality of the movement of the load. However, as noted in the evaluation of the pedestrian group, the amplitude of the dynamic load exceeds the other two standards, and hence the pedestrian group resulted in higher acceleration values than others.

Az Annex C szerint felvett tehermodellek vezettek az általunk generált tehermodellhez legközelebbi eredményre. Az effektív gyalogosszámot és a szinkronizáció hatásának mértékét, a SÉTRA és az Annex C hasonló nagyságú konstansokkal veszi figyelembe, ez a végeredményben is megmutatkozik.

The load models of Annex C have led to the closest results to the load model generated by us.

Summary

We have examined three guidelines for the dynamic design of footbridges, and we have prepared our own pedestrian load model which is close to reality. The analysis was carried out on two pedestrian bridges, and we draw the conclusions from their results.

Our numerical studies show that it is not worth to analyze the case of a single pedestrian because its impact is far below the influence of the pedestrian group. Crossing of a pedestrian group and crowd is completely different, so they have to be treated differently. Assuming the freely chosen travel speed of the pedestrian groups can be well modeled even numerically, but for crowd conditions, the inclusion of results (synchronization factors) based on experimental tests are indispensable.

Based on the results of our own realistic load model, the results of the SÉTRA and Annex C are more closely aligned with the results of the simulated numerical Monte Carlo simulations, despite the fact that the British National Annex uses a moving load model.

Based on the results we can conclude that pedestrian groups and crowds are also worth examining, because these can be governing (depending on the standard) and we have found that the Eurocode limit is valid for the two investigated bridges.

Our goal was not to add a new method to dynamic design, as designing practice requires a faster, simpler model. We wanted to draw attention to the fact that standards' models have a great reserve factor and it could be much more accurate on the basis of experiments or simulations.

References

Bachmann H. (1995): *Vibration Problems in Structures: Practical Guidelines*. Birkhäuser Basel.

Bachmann H., Ammann W. (1987): *Vibrations in structures: Induced by man and machines*. IABSE.

Barker C., MacKenzie D., DeNeumann S., Ko R. (2005) : Footbridge Pedestrian Vibration Limits – Part 1: Pedestrian Input. Footbridge 2005 – Second International Conference

Sjöström A., Clausén C., Ingemansson V., Austrel P.E., Persson K., Sandberg G., Bard D., Novak C., Ule H. (2014): Vibration insulation of footbridges so as to reduce human discomfort. Internoise 2014 – 3rd International Congress on Noise Control Engineering

Seismic Analysis of Steel Storage Tanks: Overview of Design Codes Used in Practice

PANTUSHEVA Mariya
Department of Steel, Timber and Plastic Structures, University of Architecture, Civil Engineering and Geodesy (UACEG), Sofia, Bulgaria

Abstract

Seismic provision of all types of structures is of paramount importance in regions defined by medium and high seismic hazard. This is all the more true in the case of steel storage tanks, as these often contain toxic, flammable and explosive substances or the fuels needed for post-state recovery after a catastrophic event. Additionally, steel storage tanks could be an integral part of special facilities related to national security and defence.

The current paper presents an overview of the European design codes used in practice regarding the analysis, behaviour and design of steel tanks under earthquake loading, namely EN 1998-4 (BDS EN 1998-4:2006, along with the national annex BDS EN 1998-4:2006/NA:2012) and EN 14015 (BDS EN 14015:2005). Other legislative documents - API Standard 650 and API Standard 620 are also considered. The aim of the paper is to compare the provisions provided by the aforementioned documents focusing on the aspects that require further investigation and regulation, as well as those not dealt with in the regulatory framework. Special attention is paid to the effects that a seismic event would have on the stationary roofs of vertical cylindrical steel storage tanks.

Introduction

Seismic Hazard

Every day hundreds of earthquakes shape the landscape of our Earth. According to data provided by IRIS (Incorporated Research Institutions for Seismology), more than 1 500 per year is the frequency of the seismic events that could cause possible damage to structures in the regions they occur. The number of earthquakes happening per year worldwide, their magnitude, energy release and energy equivalents, as well as some examples for major earthquakes, are presented in Figure 1.

Structures should keep their integrity during an earthquake, in order to preserve human life, avoid environmental pollution and material loss. This is why in regions with non-negligible seismic activity all structures should be designed taking into consideration such events.

Steel Storage Tanks

Special attention should be paid to the seismic design of steel storage tanks as these structures are very specific and have certain features that make their behaviour particularly different from that of a building. The storage facilities are presented by a diversity of members varying in size, shape, operational pressure and temperature, functional requirements and characteristics. Each type has its own specifications regarding analysis, design and detailing.

This article focuses on vertical cylindrical steel storage tanks. The latter are easy for fabrication, erection and maintenance and most suitable for containing large amounts of liquids. Those liquids vary from water and other substances used in the brewing, wine and food industry to the raw materials or waste products in manufacturing. Vertical cylindrical steel storage tanks present the largest share of the containers used in the petroleum and oil refining industry. Steel tanks may also be essential for the life and health of the public and for post-earthquake recovery. Eventual destruction or damage in these facilities could lead not only to material loss but also to the loss of human life and long-lasting consequences for the environment.
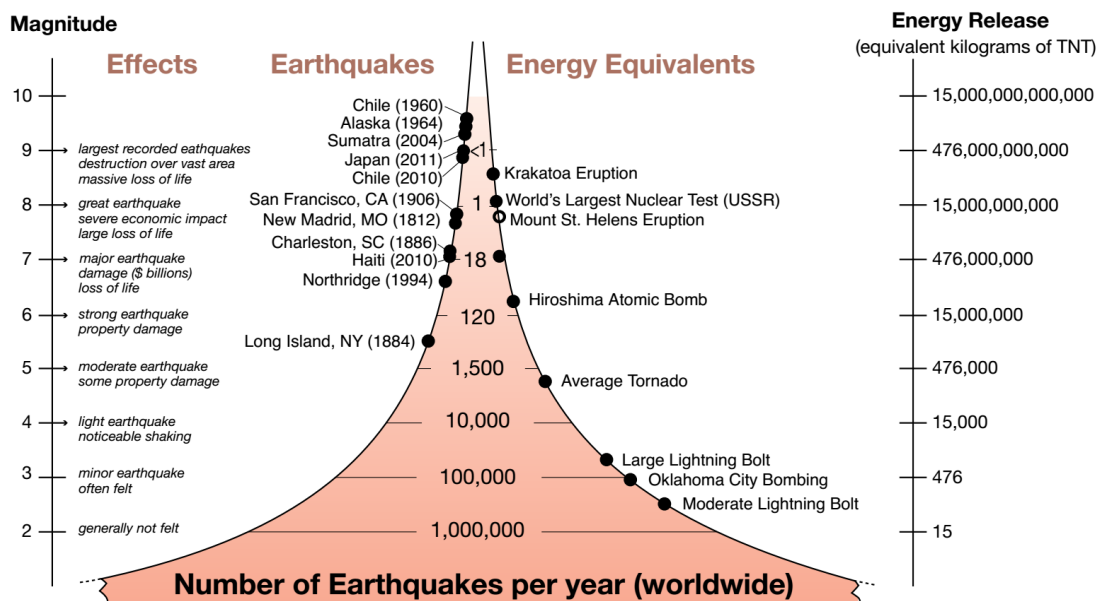
Figure 1. Number of earthquakes per year (worldwide), source: IRIS.

History of Incidents

Incidents with storage facilities around the world as a result of seismic activity are not uncommon. Some of the most severe cases happened in Chile in 1960, USA: Alaska 1964; Japan: Niigata 1964 and Tokachi in 2003. The consequences were accounted in numerous casualties, air and water pollution, infernos that could not be put down for days, financial and infrastructural losses. Lighter incidents are more common, but do not make the statistics. Even though they cause considerably less damage than major ones, their frequency is what makes them relevant.

Predicting the behavior of the soil-tank-liquid system and their interaction during an earthquake is a problem of a considerable analytical complexity. For that reason, it would be highly beneficial if the structural engineer is guided through the design process by regulatory procedures and provisions.

Theme

The aim of this paper is to review some of the most commonly used legislative documents for seismic design of steel storage tanks and to compare the methodology, recommendations and design procedures they provide in an attempt to point out some unregulated issues and draw a path for future development.

Legislative Documents

European Design Codes

In the 1970s the Commission of the European Community (presently the European Commission), initiates the development of the Eurocode standards, that later turn into a single unified system governing structural design within the European Union (EU). The unification and compliance of the design codes, along with the technical specification of materials is crucial for ensuring the accuracy of predesign assumptions and a lifetime guarantee of adequate safety of the actual built structure.

This paper reviews only documents related to the seismic design of steel tanks, namely:

- EN 1998-4 Eurocode 8: *Design of structures for earthquake resistance - Part 4: Silos, tanks and pipelines* (BDS EN 1998-4:2006, along with the national annex BDS EN 1998-4:2006/NA:2012). This document supplements EN 1991-4, EN 1993-4 и 1998-1 upon matters regarding the seismic design of facilities used for containment, transmission and processing of gas, granular, or liquid materials.

- EN 14015: *Specification for the design and manufacture of site built, vertical, cylindrical, flat-bottomed, above ground, welded, steel tanks for the storage of liquids at ambient temperature and above* (BDS EN 14015:2005). Interest presents Annex G: *Recommendations for seismic provisions for storage tanks* (informative). Whereas EN 1998-4 is an integral part of the system of Eurocodes, EN 14015, Annex G is based on the provisions given in API 650, Annex E. This is possible since the API design code provides prescriptions for application outside of the USA. Most of the signature used in EN 14015 is different from the one used in Eurocode.

US Design Codes

The American Petroleum Institute (API) is the biggest national trade association representing the oil and natural gas industry in the United States of America. The organization has developed and maintains more than 680 standards and recommended practices, some of which having regulatory status. Due to the robust development of the USA's industry, especially the oil industry, tank studies and therefore standards are well presented by a variety of documents (e.g. AWWA D100 by the American Water Works Association, API 12F, API 12D, API 620, API 650).

This paper reviews:

- API Standard 650: *Welded Tanks for Oil Storage*, Twelfth Edition, March 2013 and specifically its Annex E: *Seismic Design of Storage Tanks* (normative) and Annex EC: *Commentary on Annex E* (informative).

- API Standard 620: *Design and Construction of Large, Welded, Low-pressure Storage Tanks,* Twelfth Edition, October 2013 presented by Appendix L: *Seismic Design of API 620 Storage Tanks*.

API 650 and API 620 follow the rules and are compliant with ASCE 7: *Minimum Design Loads and Associated Criteria for Buildings and Other Structures*.

Scope

Scope of Provisions

EN 1998-4 provides principles, application rules and additional criteria required for the seismic design of storage tanks. This standard does not give stringent limitations in regard of design pressure or operational temperature and thus covers a large group of structures, considerably different in their nature, behaviour and main characteristics. This is one of the reasons the code has only two annexes, in

which specific verification rules and detailed methods of assessment are given only for certain types of tanks. In addition to the scarce application, those recommendations are not regulatory in nature, but only informative.

EN 14015, API 650 and API 620 cover limited range of tanks in regard to shape, location, fabrication, erection methods, temperature and design pressures of the stored liquids, but are considerably more thorough in their provisions. They provide recommendations and regulations for the whole process of designing a steel tank – from the technical sheet data and necessary documentation, through the requirements for the materials, design, fabrication, erection, testing and inspection of the built facility. These legislative documents are amended by a number of annexes, most of which regulatory.

The cases of floating roofs are not entirely covered neither by EN 1998-4, annex A, nor by API 650, Annex E.

Scope of Allowable Design Pressures and Temperatures

It is interesting to point out that although based on API 650 provisions, EN 14015 covers a larger group of structures. The maximum design pressure for tanks in the scope of in EN 14015 is 500 mbar, and in API 650 it is around 180 mbar (2.5 lbf/in^2), which is nearly 3 times less. In this regard API 620 covers the largest range – up to around 1035 mbar (15 lbf/in^2) design pressure. The scope of admissible design temperatures also vary.

Scope of Materials

EN 1998-4 provides rules and recommendations for carbon steel structures. EN 14015, API 650 and API 620 could be applied to tanks made from materials other than carbon steel – austenitic stainless steel, duplex stainless steel, aluminum and nickel alloys. The standards also give exact specifications and requirements to the materials that could be used for fabrication of the different part of the tanks.

Required Documentation

EN 14015, API 650 and API 620 establish the necessary documentation of a construction project – technical characteristics, design calculations, drawings as built, supplier inspection documents, material certificates, documents regarding welding, examination and testing, documentation on the supplementary systems – heating or cooling systems, safety systems, etc. EN 1998-4 do not provide such regulations.

The rights and responsibilities of all parties participating in the construction process – purchaser, steel manufacturer, tank manufacturer, cover supplier, etc. are regulated in EN 14015 and API 650. EN 1998-4 leaves some decisions in the design process to the Owner (Purchaser). In API 650 this practice is brought to a further extent. The code marks every paragraph where a decision or an action is required by the Purchaser. Furthermore, anyone who wants to make an inquiry or a proposition is welcomed to do so. The procedure and the contact information are available in API 650, Annex D : *Inquiries and Suggestions for Change* (informative).

Analysis

The special circumstance that predetermines differences in the behaviour of a storage tank compared to that of a building is the presence of liquid contained in the tank.

Analysis Methods

EN 1998-4 refers to the four methods specified in 4.3.3, EN 1998-1-1:2004. The standard prescribes seismic design based on linear behaviour of the structure and the ground under the foundation unless otherwise required. It also states that in order to obtain the maximum hydrodynamic pressure induced by seismic action, the use of nonlinear dynamic (time-history) analysis is necessary. However, under certain circumstances, simplified methods with direct application of the response spectrum analysis are allowed.

EN 14015, API 650 and API 620 are based on methods using "an equivalent lateral force analysis that applies equivalent static lateral forces to a linear mathematical model of the tank based on a rigid wall, fixed based model" (API 650). Dynamic analysis methods are not included within the scope of Annex E of API 650 but are permitted in lieu of the given provisions for investigation of the fluid-structure and soil-structure interaction. API 620 adopts the prescriptions given in API 650.

Model

The essential factor in modelling is the correlation between the adopted geometrical characteristics, stiffness, ductility, strength, mass and damping and the real structure.

The analysis model could be a detailed three-dimensional or a simplified one.

Simplified Models

It is generally accepted that the behaviour of a storage tank and its content under earthquake loading is described by two components – impulsive and convective. Further information on the methodology is given in EN 1998-4, Annex A: *Seismic Analysis Procedures for Tanks* (informative). The "rigid impulsive" and the "sloshing" pressure components with enough accuracy represent the behaviour of a rigid tank. Alas, this is almost never the case with steel tanks. Annex A, EN 1998-4 suggests the presence of a third component, taking into account the flexibility of the tank's wall.

The other three standards use simplified provisions, considering a rigid tank fixed to the foundation.

Spatial Models

It is true that given the complexity of the problem, a 3D rigorous analysis requires high efforts and computational resources, but to this day simplified provisions cannot ensure ubiquitous coverage. As an omission of all the aforementioned legislative documents could be noted the lack of regulations regarding analysis through a 3D model. The obtained results from such a model should be with higher accuracy than those from the simplified models.

Although governing for silos, rule 3.2 (4)P of EN 1998-4 addressing spatial analysis is not listed as applicable for steel tanks.

Damping

EN 1998-4 proposes the use of a global average damping of the whole system, taking into account the contributions of the different damping values of the components of the soil-structure-fluid system. The US design codes have adopted the same differentiation between the damped response spectra for the impulsive and for the convective mode.

Seismic Action Parameters

Site Ground Motion

EN 1998-4 adopts the seismic action parameters and the elastic response spectrum as regulated in EN 1998-1. The no-collapse requirement should be fulfilled in the case of a reference seismic action associated with a reference probability of exceedance, P_{NCR}=10% in 50 years, or a reference return period, T_{NCR}= 475 years. For comparison – in EN 14015, API 650 and API 620 the maximum earthquake ground motion is considered to be caused by an event with a 2% probability of exceedance within a 50-year period (a recurrence interval of approximately 2500 years). It is interesting to note that historically Annex E of API 650 was based on the same probability of exceedance and reference return period as defined in the present Eurocodes, but this approach was considered economically impractical in regions where earthquakes are less frequent (excluding the west coast of the US) and later was changed.

Site Ground Types

EN 1998-4 differentiates between seven ground types - from A to E, S_1 and S_2. API 650 specifies six groups: A to F and EN 14015 adopts a different approach regulating only three soil profiles – types A, B and C.

Reliability Differentiation Classes

EN 1998-4 distinguishes between four importance classes (I-IV), depending on the potential economic, environmental and social consequences of failure. The risk increases in an uprising manner from Class I to Class IV, IV referring to situations posing an exceptional risk.

EN 14015, Annex G does not attend such matters. API 650 differentiates between three seismic use groups, SUG III being the most stringent. The comparison between the values of the importance factors provided by the different design codes is presented in Table 1.

Table 1. Comparison between tank importance factors according to BDS EN 1998-4/NA and API 650.

BDS EN 1998-4:2006/NA:2012			API 650		
Importance class	Structures	Importance factor - γ_I	SUG	Structures	Importance factor - I
I	Structures of minor importance for public safety	0.80			
II	Ordinary structures, not belonging to the other categories	1.00	I	Low risk the risk for public safety; negligible economic and social consequences of failure	1.00
III	Structures whose seismic resistance is of importance in view of the consequences associated with a collapse	1.20	II	Medium risk for public safety and local economic or social consequences of failure	1.25
IV	Structures whose integrity during earthquakes is of vital importance for civil protection	1.60	III	Very high risk for public safety and large economic and social consequences of failure	1.50

Both regulations let the Purchaser specify the importance category of the facility.

Behaviour Factor

When determining the behaviour factor (q) for the tank, as for other structures, consideration is paid to the ability of its components to dissipate the energy accumulated by the earthquake. In the damage limitation state, elastic response is assumed (q =1), while for ultimate limit states behaviour factors greater than 1,5 for silos and tanks raised above ground are allowed, only under certain conditions. However, there is still an upper bound dictated by the type of the supporting structure (2.4, EN 1998-4).

API 650 has adopted a similar approach. Instead of using a different behaviour factor, the standard defines a response modification factor (Table E.4 API 650) that is applicable to the values of the response spectrum. Table 2 presents a parallel and a comparison between the behaviour factor used in the Eurocode system and the response modification factor regulated by API 650.

Table 2. Comparison between Behaviour Factor (EN 1998-4) and Response Modification Factors (API 650).

Design Code:	EN 1998-4		API 650	
Anchorage system	$q_{maximum}$ (impulsive)	q (convective)	R_{wi}, (impulsive)	R_{wc}, (convective)
Self-anchored	2	1	3.5	2
Mechanically -anchored	2.5	1	4	2

The response modification values adopted in API 650 are considerably higher than those prescribed in EN 1998-4.

Seismic Design

Design Combinations

EN 1998-4 gives the following provisions for combining the effects of seismic and other actions:

- Dynamic earth and groundwater pressures or the effects of connecting systems should be accounted for during the analysis, where necessary;

- The content's effects should be considered as variable loads. As a minimum requirement two levels of filling should be considered – empty and full tank. In batteries consistent of a number of tank cells, analysis of different combinations of full and empty cells is required. (2.5.2, EN 1998-4).

In API 650 and API 620 every possible load combination is explicitly defined (5.2.2, API 650).

In cases of axial symmetry of the tank, only one horizontal and one vertical component of the seismic action could be analysed. In all other cases, it is necessary to take into account all three main directions. Combining the maximum effects of those components can be done by the 100% - 30% - 30% rule (EN 1998-4).

Combining the maximum effects of the impulsive and convective seismic response could be done by using the "square root of the sum of squares". In some cases, it is considered non-conservative and as an alternative rule, a sum of the absolute values of the maximums could be applied. API 650, Annex E prescribes using SRSS method unless a direct sum combination is required by the applicable regulations. Additionally for determining the base shear, "an alternate method using the direct sum of the effects in one direction combined with 40 % of the effect in the orthogonal direction is deemed to be equivalent to the SRSS summation" (API 650) is proposed.

Structural periods of vibration

The simplified procedure for fixed base cylindrical tanks given in Annex A, EN 1998-4 defines the natural periods of the impulsive responses, in seconds, with the expression:

$$T_{imp} = C_i \frac{\sqrt{\rho} H}{\sqrt{s/R} \sqrt{E}} \qquad (1)$$

where:

C_i is a coefficient for determining the impulsive natural period of the tank system;

H is the height to the free surface of the liquid;

R is the tank radius;

s is the equivalent uniform thickness of the tank wall;

ρ is the mass density of liquid;

E is the Modulus of elasticity of tank material.

All in corresponding units (A.3.2.2, EN 1998-4)

The formula for the same component provided by API 650, annex E is the following:

$$T_i = \left(\frac{1}{\sqrt{2000}} \right) \left(\frac{C_i H}{\sqrt{\frac{t_u}{D}}} \right) \left(\frac{\sqrt{\rho}}{\sqrt{E}} \right) \qquad (2)$$

Where:

D is the nominal tank diameter, [m], t_u corresponds to s from Formula (1), but measured in [mm] and C_i, H [m], ρ [kg/m^3] and E [MPa] have the same meaning in both formulas. After substitution of D with 2R, it becomes clear that the formulas provided by EN 1998-4 and API 650 are the same.

In EN 1998-4 the natural period of the convective response, in seconds, is defined as:

$$T_{con} = C_c \sqrt{R} \qquad (3)$$

C_c being a coefficient for determining the convective natural period of the tank system and R - the tank radius [m];

The equation governed by API 650 for the convective period is:

$$T_c = 1.8 K_s \sqrt{D} \qquad (4)$$

The sloshing period coefficient K_s is defined as:

$$K_s = \frac{0.578}{\sqrt{\tanh\left(\frac{3.68H}{D} \right)}} \qquad (5)$$

If (5) is substituted in (4) the formula presented in API 650 could be expressed by:

$$T_c = C_c^* \sqrt{R} \qquad (6)$$

$$C_c^* = \frac{1.471}{\sqrt{\tanh\left(\dfrac{3.68H}{D}\right)}} \qquad (7)$$

In this case the prescriptions of EN 1998-4 and API 650 could be compared. The results presented in Table 3 show that the differences are negligible.

Table 3. Comparison between C_c coefficient values according to EN 1998-4 and API 650.

EN 1998-4		API 650	
H/R	Cc	Cc*	D/H_T
3,0	1,48	1,47	0,67
2,0	1,48	1,47	1,00
1,0	1,52	1,51	2,00
0,5	1,74	1,73	4,00
0,3	2,09	2,08	6,67

Effective masses and heights

Table A.2 of EN 1998-4 presents the impulsive (m_i) and convective (m_c) masses as fractions of the total liquid mass. Respectively "h_i" and "h_c" represent the heights at which the impulsive and convective wall pressure resultants are acting, measured from the base of the tank. API and EN 14015 provide formulas and graphics for direct determination of the latter.

Table 4 presents a comparison between the values for these parameters obtained by the referred design codes. The signature follows the standards' regulations. The differences between the calculated masses vary between 3% and 8% and the deviation in the calculated heights is between 2% and 14%, depending on the height to radius ratio of the tank.

Table 4. Comparison between the effective masses and heights according to EN 1998-4, EN 14015 and API 650.

	effective impulsive mass			effective convective mass			impulsive height		convective height	
Code:	EN 1998-4	EN 14015	API 650	EN 1998-4	EN 14015	API 650	EN 1998-4	EN 14015	EN 1998-4	EN 14015
H/R	m_i/m	T_1/T_T	W_i/W_p	m_c/m	T_2/T_T	W_c/W_p	h_i/H	H_1/H_T	h_c/H	H_2/H_T
3,00	0,842	0,746	0,855	0,158	0,160	0,153	0,453	0,430	0,825	0,820
2,00	0,763	0,790	0,782	0,237	0,230	0,230	0,448	0,400	0,751	0,840
1,00	0,548	0,555	0,577	0,452	0,430	0,437	0,419	0,370	0,616	0,610
0,50	0,300	0,280	0,289	0,700	0,660	0,667	0,400	0,370	0,543	0,560
0,30	0,176	0,180	0,175	0,824	0,760	0,767	0,400	0,370	0,521	0,510

Design Methods

The system of Eurocodes prefers the limit states design approach, while EN 14015, API 650 and API 620 use allowable stress design methods (ASD).

EN 1998-4 distinguishes ultimate limit state (ULS) concerning structural failure and damage limitation state (DLS) ensuring the preservation of the "integrity" and "minimum operating level" of the facility.

EN 14015 makes a differentiation between operating basis earthquake (OBE) condition and a safe shutdown earthquake (SSE) condition that could be compared respectively to the ULS and DLS states defined in EN 1998-4.

In Section L.4 *Special Provisions for Tanks Requiring Performance Level Designs*, API 620 addresses even further differentiation - an operating level earthquake (OLE), a contingency level earthquake (CLE) and an aftershock level earthquake (ALE) when required by regulations or the Purchaser.

Annex E of API 650 states that the fundamental purpose of the standard is protection of life through prevention of catastrophic collapse of the tank. It does not exclude, however, damage to the tank or related components during an earthquake.

Design Impulsive and Convective Pressure and Pressure Resultants

EN 1998-4 Annex A gives a proposal for simplified method of obtaining the design pressures and pressure resultants caused by seismic action in vertical cylindrical or prismatic steel tanks, fully or partially fixed with anchors on a rigid or flexible foundation.

Formulas for the impulsive and convective pressure components are presented along with their respective horizontal resultant forces Q_i, Q_c and base moments immediately above and immediately bellow the base of the tank - respectively M_i, M_i', M_c, M_c'. All aforementioned standards provide formulas for calculation of the overturning moments and lateral (sliding) forces acting on the tank during a seismic event. API 620 gives additional provisions for calculation of the seismic pressure resultants for insulated tanks.

The idea behind the formulas provided by EN 1998-4 and API is basically the same. Nevertheless, due to differences in the design philosophy and the nature of the standards, the results obtained are different.

A comparison between the different design approaches is presented in the article "*Analytical Research of the Behaviour of Steel Tanks with Volume V=500 m³ and V=2000 m³ during the Seismic Influence*" (Zdravkov 2010). The author studies two tanks with different parameters situated in Sliven, Bulgaria through the design methodologies prescribed by EN 1998-4, EN 14015 and API 650. He concludes that the values for T_{conv}, m_i, m_c, h_i and h_c are similar, but there are considerable differences in the values obtained for the overturning moment, sliding force and the maximum height of the wave for the first sloshing mode of the liquid contained in the tank. The most explicit differences are observed between the calculations carried out according to API 650 and EN 1998-4.

Design Checks

The design checks prescribed in EN 1998-4, EN 14015, API 620 and API 650 concern: general stability, design of tank's shell, bottom and the joint between them, anchorage and foundations.

According to EN 1998-4 in seismic design situation overturning or bearing capacity failure of the soil are not allowed. Under certain circumstances limited sliding or uplift are acceptable.

Possible tank failures are described in 3.5.2, EN 1998-4. Steel tanks are prone to certain types of failure specific only this type of structures, such as "elephant foot" failure mode - buckling by vertical compression with simultaneous transverse tension. The resistance of the shell must be determined as for persistent or transient design situations.

While Eurocode gives only general recommendations for the main parts of the tank, EN 14015, API 650 and API 620 have a considerably larger scope of regulation. They provide requirements regarding the piping, connections, internal components, venting, floating covers, heating and/or cooling systems, stairways and walkways, ladders, earthing connections, temporary attachments and insulation.

They also provide structural requirements for thicknesses and dimensions of the different parts of the tank. API 650 even has an Annex A: *Optional Design Basis for Small Tanks* (normative) that provides the designer with the opportunity for certain types of tanks to avoid further calculations and choose typical sizes of tanks and obtain their capacities from a table. Also, API 650 commentary to Annex E provides Example Problems. In Eurocode such practices are not incorporated.

Complementary Measures

EN 1998-4 prescribes complementary safety measures such as bunding (the tank or tank group shall be surrounded by a ditch or an embankment). The design checks subjected to the bunding shall be more stringent than the ones for the tank itself. This is because the purpose of the enclosure is to retain its full integrity (without leakage) under the design seismic action relevant to the ULS of the tank.

Detailing

In comparison to EN 14015, API 650 and API 620, EN 1998-4 lacks provisions for detailing. In the US practice drawings and typical details with dimensions and clearances abound along with tables for direct choice of sections and sizes. Eurocode has a rather theoretical approach, while US design codes are a lot more oriented for use in practice, facilitate the designer and save time.

Sloshing Effect

The ground motion during an earthquake induces waves on the free surface of the liquid contained in the tank. Both European and US regulations provide formulas for calculation the height of those waves. The results obtained by following the rules in these documents, however, considerably differ from one another (Zdravkov, 2010). For such vastly used legislative documents, discrepancies like these are inadmissible.

All the regulatory documents reviewed in this paper have one thing in common – none of them provides any recommendations for seismic analysis of the roof structure. API 650 EC.7.2 considers designing the roof and shell to resist sloshing wave to be impractical and does not provide such procedure. In EN 14015 the matter is discussed by a single sentence „The purchaser may specify if a freeboard is to be provided to minimize or prevent overflow and damage to the roof and upper shell."

Both EN 1998-4 and API 650 prescribe that unless otherwise specified, a sufficient freeboard above the maximum operating level in regard of the sloshing wave height shall be provided. Less freeboard should be sufficient if the roof is designed for the pressures caused by the wave, but no further prescriptions for that design are presented.

Conclusions

On the base of the review and comparison between the main legislative documents acting in the European Union and in the USA regarding the seismic design of steel tanks, the following conclusions can be made:

- The design of every single structure in the territory of Bulgaria or any country with medium or high seismic hazard is essential for prevention of the loss of human life and environmental pollution;

- In the territory of the European Union both EN 1998-4 and EN 14015 are in force. The signature used in them is different and furthermore - the nature of the design approach (limit states vs. ASD). This additionally hampers the design process, especially when carried out by an engineer used to working according to the Eurocode system.

  Approaching the same problems the two design codes provide different results.

All of this said an unification between the legislative documents acting in the same country is advisable. If by following the provisions of the two design codes, a proper similarity in the results is achieved, this would make them much more plausible;

- The system of Eurocodes does not give stringent requirements and procedures for seismic design of steel storage tanks. Annex A of BDS EN 1998-4 concerning seismic design of such facilities has only an informative, not a regulatory character. Also the provided procedures apply to very narrow scope of the large variety of tanks and are valid only under certain prerequisites.

  Further development of the design code is advisable. Some good practices from API could be adopted. For example detailed regulations, provision of typical details and measures and a more practical, rather than theoretical approach;

- The methodology proposed in EN 1998-4, EN 14015, API 650 and API 620 is suitable for approximate manual calculations of steel tanks by obtaining pressures and generalized forces and moments immediately below and above the joint cylindrical shell wall - foundation. Analysis through computational software is not considered. With the advanced technology nowadays a rigorous analysis through a proper spatial model should not present significant difficulties and at the same time give more realistic results;

- Apart from calculating the height of the wave excited by the seismic action, the design codes do not refer to any possible effects this wave might have on the structure of roof of the tank. They do not provide any way to obtain the pressures caused by this wave (if the freeboard is insufficient), nor prescribe relevant design checks for the roof structure.

  The main considerations are the circumferential shell, the bottom of the tank and the joint to the foundation.

Given the difference in the values for the sloshing wave height obtained by the different design codes, the opinion of the author is that the matter about roof design under a seismic situation should not be taken so lightly. Especially if the contained fluid is toxic and a possible leak could have serious consequences. Studies of the seismic behaviour of stationary roofs of steel storage tanks will be the focus of the future research work of the author.

References

API Standard 620: Design and Construction of Large, Welded, Low-pressure Storage Tanks, Twelfth Edition, 2013.

API Standard 650: Welded Tanks for Oil Storage, Twelfth Edition, 2013.

EN 14015:2005 Specification for the Design and manufacture of site built, vertical, cylindrical, flat-bottomed, above ground, welded, steel tanks for the storage of liquids at ambient temperature and above (BDS EN 14015:2005).

EN 1991-4:2006 Eurocode 1 - Actions on structures - Part 4: Silos and tanks.

EN 1993-4-1:2007 Eurocode 3 - Design of steel structures - Part 4-1: Silos.

EN 1993-4-2:2007 Eurocode 3 - Design of steel structures - Part 4-2: Tanks.

EN 1998-1:2005 Eurocode 8: Design of structures for earthquake resistance - Part 1: General rules, seismic actions and rules for buildings.

EN 1998-4 Eurocode 8: Design of structures for earthquake Rresistance - Part 4: Silos, tanks and pipelines (BDS EN 1998-4: 2006 and the national annex BDS EN 1998-4:2006/NA: 2012).

Zdravkov L. (2010): Analytical Research of the Behaviour of Steel Tanks with Volume V=500 m^3 and V=2000 m^3 during the Seismic Influence. In: Proceedings *of the Third national symposium in steel, wooden and combined constructions 2010,* Sofia, Bulgaria, Paper No. 7, 9 pp.

Accumulation of damage in split-X concentrically braced frames under fully reversed cyclic constant amplitude loading

RAYCHEVA Lora
Department of Steel and Timber Structures, University of Architecture, Civil Engineering and Geodesy (UACEG), Sofia, Bulgaria

Abstract

This current paper presents a characteristic aspect of cyclic non-linear behaviour of steel concentrically braced frames with braces, intersecting into a floor beam (Split-X CBFs). During an experimental programme three test specimens of one-bay one-storey Split-X CBF with braces of welded H-cross section were tested under fully reversed cyclic constant amplitude loading. The experimental observations prove the development of a distinctive mechanism of damage accumulation in braces which is presented by sequence of characteristic stages.

The typical stages of the damage accumulation process are defined and energy-based criteria for low-cycle fatigue endurance is formulated. Progressive drop of the energy dissipation capacity of the structure is observed when the accumulated damage in braces reaches a specific stage, corresponding to brace fracture due to significant accumulation of plastic strains, fatigue and/or exhaustion of material ductility. Based on the experimental study, a numerical equation defining the relation between brace elongation and low-cycle fatigue endurance is formulated. A non-linear analysis case study and low-cycle fatigue checks are presented.

Introduction

Concentrically braced frames (CBFs) are traditional and popular system for seismic resistant design. Nowadays CBFs are widely implemented in single storey industrial frames, multistorey buildings and industrial engineering facilities. This system has proved its efficiency for lateral loads by providing sufficient stiffness and strength due to its complete truss action which is the main reason for its popularity. The dissipative behaviour of conventional CBFs is provided primarily by yielding of braces in tension and to a smaller extent by plastic rotation in buckled braces.

Provision of the structural ductility demand is related to ensuring formation of the predefined plastic mechanism that excludes concentration of plastic deformations in a single storey. In this regard Eurocode 8 requires limitation of the brace overstrength among all storeys and capacity design for all non-dissipative elements so assuring formation of global plastic mechanism.

Scientific research in the sphere of inelastic cyclic behaviour of CBFs with different configuration of braces prove that the system energy dissipation capacity and the resultant plastic mechanism is highly sensitive to the specific configuration of braces within the braced frame as well.

Detailed research on the CBFs cyclic behaviour performed by *Khatib et al. 1988* reveals that the intended plastic mechanism and expected ductility of the system may be obstructed due to ocurrance of intersecting beam bending as a result from the formation of unbalanced vertical forces after buckling of compression brace in inverted V-CBFs. This type of structural behaviour reflects in induction of supplementary and non-uniform deformations in braces along the building height and eventually – in reduction of structural ductility and endurance. An inherent tendency for ununiform distribution of deformations is attributed to the Split-X configuration of CBFs. It is related with the induction of horizontal inertia force in the intermediate level where braces intersect which suggests overloding of

lower level and respectively greater lateral stiffness and strength demand of the lower level of a two-story X-CBF. *Lacerte and Tremblay 2006* also prove the propensity of Split-X CBF to concentrate inelastic deformations in a single story and the subsequent reduction of system ductility and endurance. Authors propose criteria for homogenious plastic deformations distribution achieved by limitation of the ratio of lateral force resistance of two adjacent stories. Further investigations on Split-X CBFs are performed by *Jay Shen et al. 2014* in numerical study of six- and twelve-storey CBFs with braces that split into a floor beam. Authors confirm the tendency for concentration of inelasting deformations in a single story. Authors prove the effect of splitting beam stiffness on the type of resultant plastic mechanism and the uniformity of plastic deformations along the building height due to presence of unbalance forces in elastic and post-buckling stage. Most of the authors are unanimous about the major influence of brace slenderness on Split-X CBFs behaviour.

Deep research regarding the influence of splitting beam stiffness on the seismic response of chevron CBFs is performed by *Mario D'Aniello et al. 2015*. Authors highlight the relation between the beam-to-bracing stiffness ratio and global and local performance parameters influencing the seismic response of inverted V-CBFs. As a result of the extensive numerical parametric study they propose analytical expressions for controlling the local brace ductility demand and the plastic mechanism at different performance levels.

Experimental programme, conducted in UACEG, Bulgaria in 2011 (*Georgiev, 2013*) have shown that non-homogeneous plastic deformations may be observed in single storey X-CBFs with diagonals that intersect into a horizontal splitting beam due to the non-concurrent buckling of the two compressed braces from a couple. *Georgiev and Raycheva, 2017* prove the significance of the mutual splitting beam and column bending stiffness, acting as supplementary horizontal stiffness system for the regularity of plastic deformations distribution in Split-X CBFs. An analytical model is proposed for defining the sufficient splitting beam and column stiffness.

The review of the experimental and numerical investigation on the inelastic behaviour of Split-X CBFs proves the tendency of this system for ununiformity of deformations distribution along the building height and concentration of deformation demand in a single story.

Even if the formation of the anticipated plastic mechanism is ensured, an unfavourable effect related with the nature of CBFs cyclic behaviour is representative for this type of system. CBFs cyclic behaviour is characterized with typical pinching of the hysteresis loops, resulting from the accumulation of plastic elongations in tensioned braces and the following cyclic reduction in brace buckling resistance. Bracing members have a tendency to perform severe concentration of plastic deformation in their mid-length section when exposed to reverse cyclic loading which leads to premature fracture of the element. Being the main dissipative elements in the CBF system, the mentioned premature brace fracture results in reduced ductility of the system and thus raise the issue for proper evaluation of the low-cycle fatigue endurance of braces in CBFs. Deep research on the types of failure mechanism due to reversed plastic strains in steel material is performed by *Nip et al. 2010*. The author defines a variation of typical LCF named extremely low-cycle fatigue. The mechanism of cyclic failure of the tested standard steel specimen is related with the type of observed fracture surfaces. ELCF failure mechanics is explained with interaction of material ductility exhaustion and fatigue crack development and is attributed to failure at number of cycles lower than 100. LCF and ELCF failure mechanism may be found characteristic for Split-X CBFs due to specificities of brace cyclic behaviour which is described with interaction of global (accumulation of cyclic residual elongations in tensioned braces and the growth of bending strains in reversed compression) and local (cumulative bending strains of high intensities in the warped zones of the bent buckled brace) plastic strains accumulation in the mid-zone of braces and due to the ununiformity of deformations distribution, typical for this type system. This specific mechanism of failure of braces in Split-X CBF, was observed during the experimental programme, performed in UACEG, Sofia, Bulgaria, 2016 and described in detail in the current paper.

Together with material cyclic tests, researchers point the importance of performing cyclic tests of assemblage of structural elements where the specificities of the assemblage behaviour and the connection used affect the mechanism of strain distribution and the process of damage accumulation.

Krawinkler et al. 1983 proposes recommendations for experimental studies on the damage accumulation and life prediction of steel components that lay down in the basics of *ATC-24 1992* (Applied Technology Council), Guidelines for Cyclic Seismic Testing of Structural Components of Steel Structure.

A main issue of author's research is the assessment of the mechanism for damage accumulation in braces with built-up "H-shape" cross section during full reversal cyclic constant amplitude tests, their tendency of premature fracture due to significant damage accumulation (LCF or ELCF) and its influence on the overall ductility of the Split-X CBF. Basic test observations, analyses of results and proposal for criteria for assessment of accumulated damage in braces of Split-X CBF is presented in the current paper.

Experimental programme

In the scope of the conducted experimental programme three test specimens of one-bay one-story concentrically braced frame with braces, intersecting into an intermediate beam were designed, manufactured and tested. The test specimens are with dimensions 4000 height and 3000 spacing between columns. Braces are designed of built-up H-shape cross section from steel S235JR with slenderness of $\overline{\lambda} = 1,28$. Table 1 summarizes the cross-sections and steel-grade used for elements of each specimen. The cross section of braces are presented by the signature that should be read as follows: F80/5 (flange width 80mm and thickness 5mm) и W120/5 (web height 120mm and thickness 5mm). Columns were oriented with their minor axes in the frame plane while the beams were traditionally oriented with its major axis. Intermediate beams are designed, following a proposed procedure (*Georgiev and Raycheva, 2017*) for determination of necessary resultant stiffness of splitting beam and columns. All the connections between elements are realized as pinned with the exception of the connection between the intermediate beam and columns, which can be classified as partially – rigid.

Table 1. Specimen elements sections and steel grade.

	Specimen 1	Specimen 2	Specimen 3
Columns	HEA320/S275	HEA320/S275	HEA320/S275
Top Beam	HEA200/S275	HEA200/S275	HEA200/S275
Intermediate Beam	IPE200/S275	HEA240/S275	IPE200/S275
Braces	H(F80/5,W120/5)* /fy,act=303MPa	H(F80/5,W120/5)* /fy,act=303MPa	H(F80/5,W120/5)* /fy,act=303MPa

The tests were conducted by applying controlled displacement at the top of the frame by a hydraulic actuator. The test setup is illustrated in Figure 1.

Each of the test specimen was exposed to two type of tests: monotonically increasing applied lateral displacement of 100mm (Test 1) and statically applied cyclic displacement at the top of the frame in fully reversal symmetrical cycles with constant amplitudes of 90, 120 and 150 mm (Test 2) for Specimen 1, 3 and 2, respectively. For each of the tests during each cycle, the significant visible damage is captured. Distinctive displacements and strains were registered by strain gauges (SGs) and inductive displacement transducers (ITs), installed at characteristic places. The adopted loading protocol is in accordance with the test purpose and meets the recommendations for experimental studies on the damage accumulation and life prediction of steel components by *Krawinkler et al. 1983* and *ATC -24*.

Figure 1. Experimental setup.
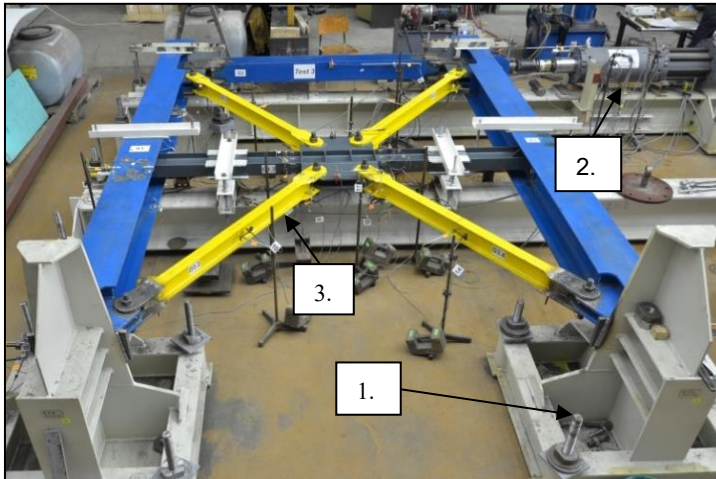
1. Supporting stand
2. Hydraulic actuator
3. Test specimen

Mechanism of damage accumulation

Observations from the cyclic constant-amplitude Test 2 revealed the existence of distinctive process of damage accumulation in the brace mid-section. The observed mechanism is represented by sequence of seven characteristic stages that are defined and illustrated by photos in Figure 2.

Each of the defined stages is described by the following:

1. Occurrence of local buckling of one of the flanges at the concave side of the bent buckled brace. The warped zones are realized as local cumulative strain concentrators. Together with local strains, bending strains from global brace buckling are accumulated in the same mid-section. The interaction of global and local effect of strain accumulation presents extremely harmful conditions for the brace endurance.

2. Occurrence of local buckling of both flanges at the concave side of the bent buckled brace.

3. Occurrence of local buckling of one of the flanges at the convex side of the bent buckled brace. This can be explained by buckling of the fibres from the convex side during brace elongation. These fibres have been plastified and elongated in previous cycle of compression and in load reversal they turn to be compressed and elongated which provokes their buckling.

4. Initiation of surface crack at the flange at the local buckling wave with maximum curvature.

The subsequent stages develop rapidly in the range of up to two cycles.

5. Concentration of inelastic deformations and formation of sharp bend in the brace web. As illustrated in Figure 3, the brace deformed shape can be approximated with two straight elements and a curvature of constant radius between them. Occurrence of crack in the brace flanges may be associated with fracture that leads to rapid concentration of bending deformation in the brace web and modification of the deformed brace shape to one with two straight elements and absence of smooth curvature.

6. Tearing of the flange along its width and propagation of the crack towards the web.

7. Occurrence of flange tearing of other brace flange.

A variation of the type of local buckling, described in Stage 1 was observed for the brace that buckles second from the compressed pair of braces. The observed deformed shape is characterized with warping of the flange at its full length, forming sort of "macro-wave". The descried brace deformation is presented in Figure 3.
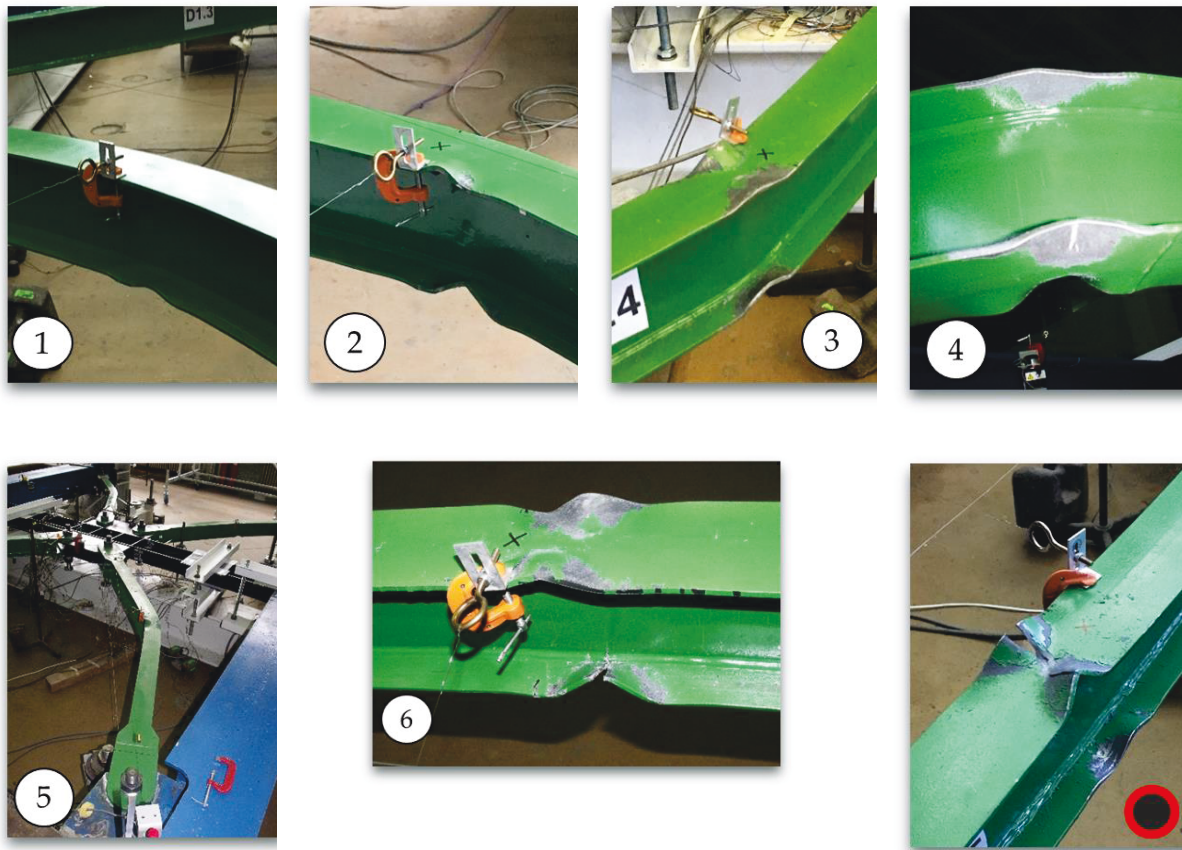
Figure 2. Stages of damage accumulation in braces after reversal cyclic test of constant amplitude of the applied top displacement.

During the performed constant amplitude cyclic test, total brace fracture was not observed. The brace web preserved its integrity. The web tearing was achieved by applying larger displacement than the adopted constant amplitude.

The observed stages develop in the exposed sequence for single brace but among the four braces in a specimen, their occurrence is asynchronous. This may be attributed to the non-concurrent buckling of both braces from a couple, caused by insufficient bending stiffness of the intermediate beam and/or different initial imperfections of braces. This matter is studied in detail by *Georgiev, 2017*.
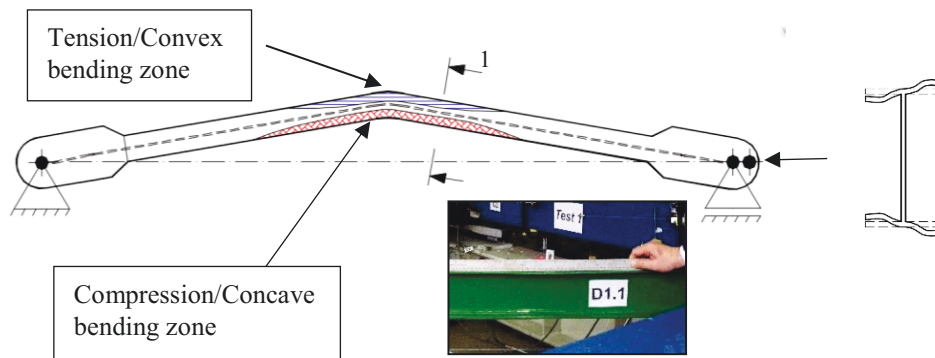
Figure 3. Variation of brace local buckling, formation of "macro-wave".

Assessment of accumulated damage in braces

Energy-based approach

The effects of damage accumulation are assessed through energy-based approach adopted in the research of *Castiglioni et al. 1996 & Bernuzi et al. 2000*. It is related with definition of "cyclic energy dissipation reduction factor" (αi), represented by the ratio of the amount of dissipated energy during the current cycle (E_i) and the amount of dissipated energy during a reference cycle (E_b):

$$\alpha_i = \frac{E_i}{E_b} \tag{1}$$

Considering the characteristic hysteresis response of CBFs, the first cycle in which the distinctive pinching effect occurs is regarded as a reference cycle. The value of the defined criteria at each cycle of the applied load history for the test of Specimen 1 is illustrated in Figure 4.

Three distinctive ranges can be distinguished. First, characterized with rapid drop of dissipated energy, a plateau of constant energy dissipation capacity and subsequent rapid drop, after the first initiation of surface crack at a brace flange. The last branch may be related with drop of system energy dissipation capacity due to significant amount of accumulated damage.

Criteria for significant loss of dissipated energy due to cyclic damage accumulation in braces and low-cycle fatigue fracture is proposed by defining a lower bound of the "cyclic energy dissipation reduction factor" $\alpha_{fr}=0,6$. Similar approach is used by *Castiglioni and Calado 1996*. This value of α_{fr} is derived by a reduction coefficient $\beta=0,8$ by which the value of α_i at the plateau is multiplied. The adoption of $\beta<1,0$ is associated with the observed ductile mechanism of brace fracture and the fracture surface.

The observed fracture surface is indicative for fracture at extremely low-cycle fatigue (ELCF). Referring to the deep research on the cyclic steel fracture mechanics and fracture surfaces, performed by *Nip et al. 2010*, ELCF is related with fracture due to interaction of steel ductility exhaustion and fatigue crack development. The observed surface associated with this type of failure is described as "mixed" of ductile and fatigue damage surface. According to cyclic test observations of steel material, ductile fracture leads to relatively uneven surface that is dull in appearance, often exhibiting cup-and-cone profile. While fatigue failure is by a series of 'beach' marks that indicate the progressive advancement of a fatigue crack. The observed fracture surface of tested specimens is described with fatigue surface at the crack initiation areas and ductile surface while developing of the crack.
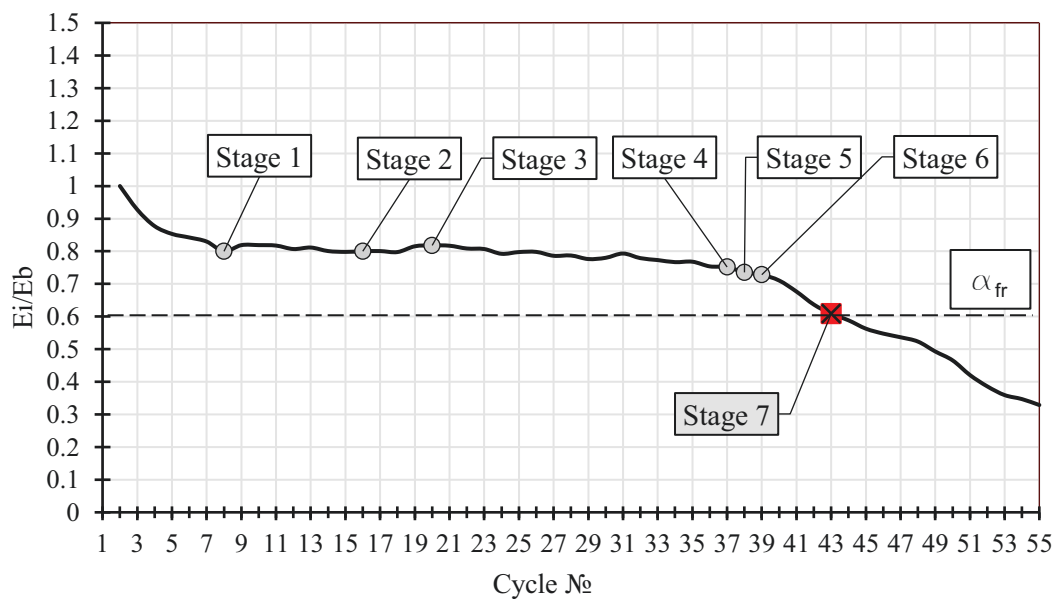
Figure 4. Relation between the cyclic energy dissipation reduction factor
and the number of cycles for Specimen 1.

Juxtaposition of the cyclic energy dissipation reduction factor histories for the performed three cyclic constant amplitude tests reveals the similarities between them that is indicative for the development of universal mechanism for damage accumulation in braces of built-up H-cross section. Moreover, it can be noticed that the slope of the falling range after fracture initiation is almost constant.

It is evident from Figure 5 and Figure 6 that the number of cycles to a specific stage of accumulated damage and the value of the applied load amplitude are in reverse relation. This relation is in correspondence with the Palmgren-Miner rule (*Ballio et al. 1995*).

Analytical assessment of brace endurance

In order to assess the degree of accumulated damage in H-braces of Split-X CBF due to real ground motion records, an analytical equation is defined:

$$\delta(N) = 60 - 30log(N) \qquad (2)$$

The proposed equation (2) relates the axial deformation amplitude of a single brace, δ corresponding to the number of cycles to failure, N. It is derived using the experimental results from the performed three cyclic constant amplitude tests of a single-story Split-X specimens. They relate the number of cycles to fracture, defined by the limit value α_{fr} and the amplitude of the applied lateral displacement. The proposed formula (2) was defined by shifting of the experimentally observed relation to the safe side with deviation of 0,834. The following assumptions are made when deriving equation (2):

- linear relation between global (elongations/shortenings) and local (strains) brace deformations (*Ballio and Castiglioni 1995*);

- validity of equation (2) for brace axial deformation amplitudes not less than the axial deformation at firt yield: $\delta > \delta y$;
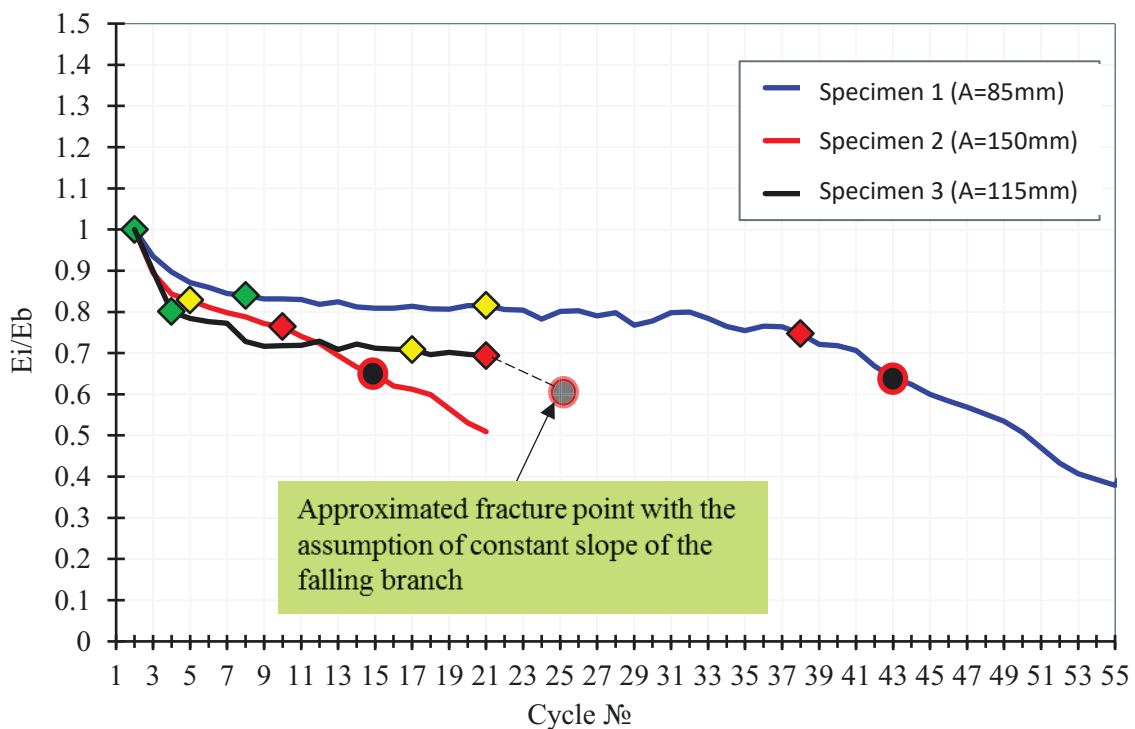
Figure 5. Cyclic energy dissipation reduction factors for the three cyclic constant - amplitude tests.
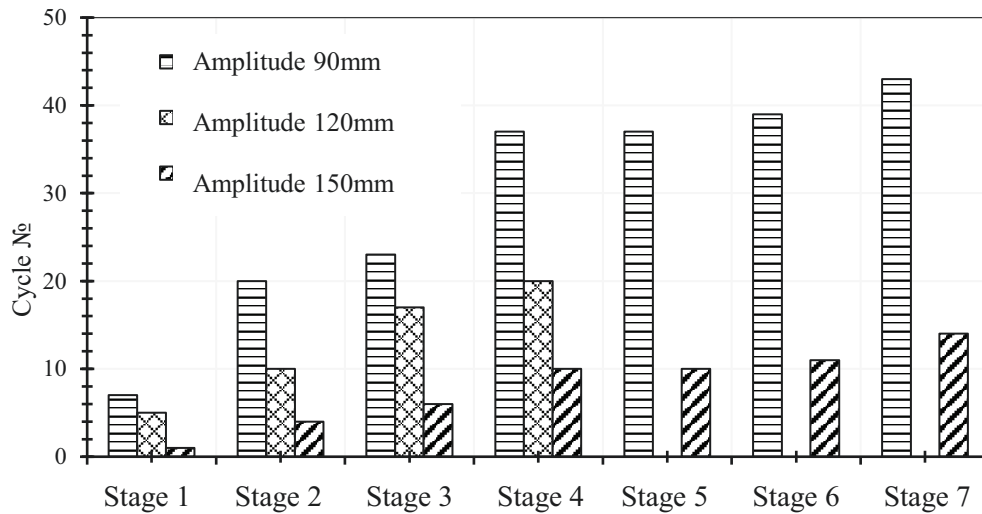
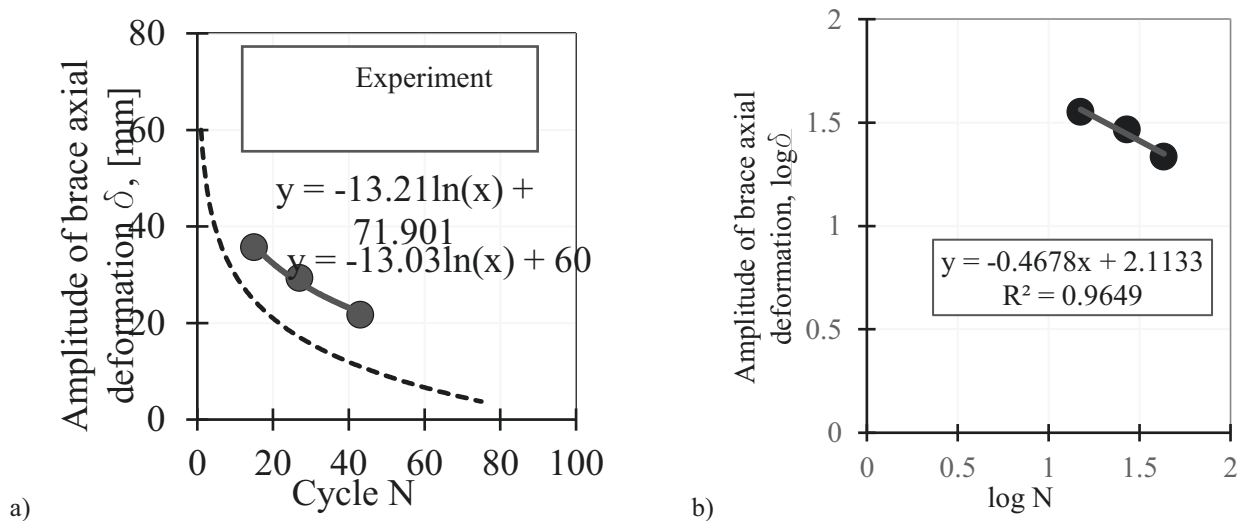**Figure 6.** Relation between the number of cycles at first occurrence of significant stage of accumulated cyclic damage for the three tests.

The experimental and numerical relations are illustrated in Figure 7. If the experimentally formulated relation from Figure 7a is presented in log-log format, the Coffin-Manson, 1950s linear relation for the low-cycle fatigue life is obtained (Figure 7b). The fatigue ductility exponent may be assessed to has value of 0,47. Previous test research by *Castiglioni and Calado 1996*, have demonstrated values in the range of 0,5-0,7. The similarity between these values and the values, derived by the current tests proves the adequacy of the experimentally obtained relation.

After processing of the test results, the relation between a single brace axial deformation and the horizontal roof displacement of the test specimen is derived with the assumption for equality of the axial deformation and degree of cyclic damage accumulation of both braces in a pair (equation (3)). During the performed tests this assumption was not fully met – braces observed different stages of accumulated damage. In this point of view, the proposed equation (2) may be treated as conservative, regarding effects from ununiformity of the plastic strains and the stages of accumulated damage between the two braces from a couple.

a)

b)

Figure 7. Experimental and numerical relation between brace axial deformation amplitude at fracture and number of cycles to fracture: a) absolute values; b) log-log format.

$$\delta = 0,85.\Delta.cos\alpha / 2 \qquad (3)$$

Similar equation is proposed by *Georgiev, 2013*.

The proposed equation (2) may be treated as conservative and well-capturing the brace low-cycle fatigue life. The application of the proposed equation (2) for assessment of accumulated damage in braces of two-story Split-X CBF is illustrated through a series of dynamic time-history analysis.

Case study

Geometry and general assumptions

The case study presented hereafter is based on a plane Split-X CBF-MB frame extracted from a two-storey building, Figure.8. The frame consists of three 8m bays with nominally pinned beam-to-column joints and pinned column bases. The Split-X CBF systems are located as shown in the figure. Hot rolled HEA profiles and IPE profiles for columns and floor beams are used. Composite action with the concrete slab is not considered (*Georgiev et al., 2017*).

The design of the presented building is conducted for vertical loads and for seismic design situation. The structural linear elastic model was formed using beam finite elements. Split-X CBF members are designed and modelled as follows. Split-X CBF columns are continuous. All joints between splitting beams and columns and the joints between beams and columns are assumed nominally pinned. The elements simulating the braces are defined through constant H-shape section and joined to the frame by simple pin connections. Split-X CBF column bases were designed and detailed as pinned which is considered the most practical approach for this type of system. Diaphragm action of floor and roof concrete decks is simulated by diaphragm constraint.
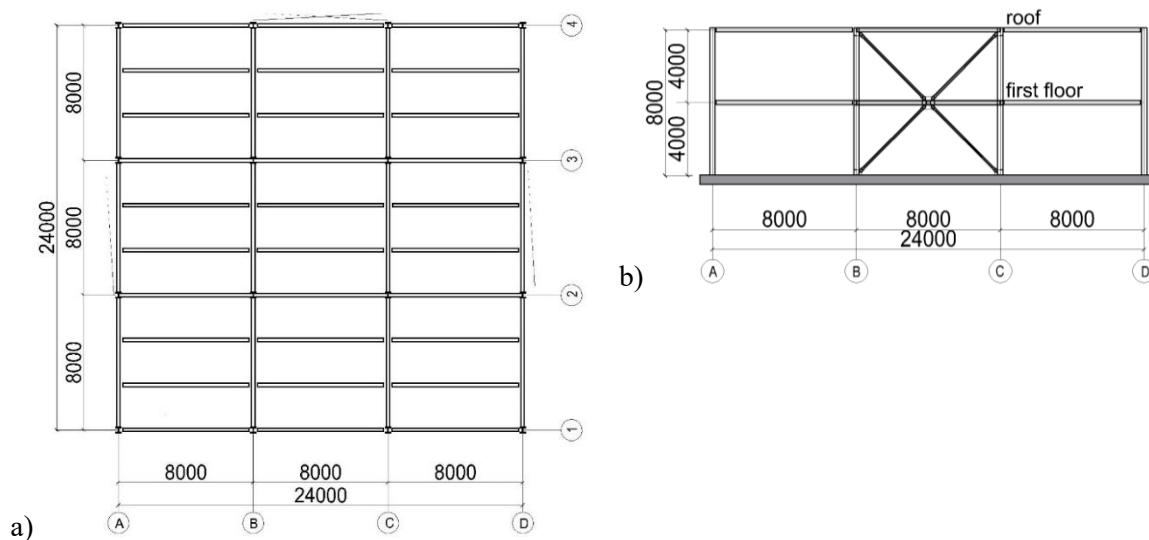
Figure 8. 2D building frame and building plan.

Table 2. Cross sections and steel grade used for the Split-X CBF elements.

| Model | Storey | Split-X CBF | | | Building frame | | |
		Braces	Columns	Splitting beams	External columns	Internal columns	Beams
AISC	1	F180.12W160.8/ S235	HEB 300 / S275	HEB 300/ S275	HEA 200/ S275	HEA 240/ S275	IPE360 HEA400/ S275
	2	F150.10W160.8/ S235	HEB 300 / S275	HEB300 /S275	HEA 200/ S275	HEA 240/ S275	IPE300

	HEA340/ S275

Table 3. Characteristics of the design response spectrum for elastic analysis

Design response spectrum for elastic analysis	Type 1
Reference peak ground acceleration	$a_{g,R} = 0.30g$
Importance class II (Ordinary building)	$\gamma_I = 1.0$
Ground type	B ($T_B = 0.15$ s, $T_C = 0.50$ s)
Behaviour factor q	4.0
Damping ratio	5%

The elastic analysis performed in the case study follow the requirements of AISC-2010 for design of SCBFs, a both-diagonals model is created (AISC Model). The characteristics of the design response spectrum used in the multi-modal response spectrum analysis are presented in Table.3.

Nonlinear dynamic analysis

Structural model

In order to demonstrate the application of equation (2) and to assess the state of accumulated damage in braces of two-story Split-X CBFs, exposed to real strong ground motion, a series of seven nonlinear dynamic analysis were performed. The finite element modal for dynamic analysis is created using the software SeismoStruct v.7. Nonlinear hysteresis steel material model of Menegotto-Pinto is adopted and the specific parameters used are calibrated to experimental results. Inelastic force-based fibre elements are used for modelling Split-X CBF elements. Brace buckling is provoked by imposing an initial geometric imperfection in the middle of a single brace (*D'Aniello et al. 2013*). P-Delta effects are taken into account by modelling a leaning column. Overview of the structural model and the adopted material model are presented in Figure 9.

Ground motion records

Non-linear dynamic analyses (time history with direct integration) were performed. The examined braced frame was subjected to a family of ground motion records obtained from Far-Field-Record set with PGA not much larger than 0.3g. This set was considered appropriate for collapse evaluation of the investigated frame. The set includes seven real records of the strongest horizontal ground motions from the PEER NGA database and refers to sites located greater than or equal to 10 km from fault rupture, all having magnitude more or equal to 6.5. Adjustment of the selected strong ground motion records was achieved through the software SeismoMatch which is able to process ground-motion records so that their spectral acceleration response matches target response spectrum (TRS). Matching of the records was based on Eurocode 8 rules for recorded accelerograms. The adjusting process was performed for all seven signals. The criterion of Eurocode 8, stating that in the range of periods between 0.2T1 and 2T1 no value of the mean spectrum should be less than 90% of the corresponding value of the elastic response spectrum, was fulfilled. List of selected strong ground motion records and their basic characteristics is shown in Table 4.

Table 4. List of selected strong ground motion records

Earthquake				Recording Station	Recorded Motions		Matched Motions	
ID №	M	Year	Name	Name	PGA max (g)	PGV max (cm/s)	PGA max (g)	PGV max (cm/s)
1	7.1	1999	Hector Mine, USA	Hector (90)	0.34	42	0.52	32
2	6.9	1995	Kobe, Japan	Kakogawa (CUE90)	0.34	23	0.33	31
3	7.5	1999	Kocaeli, Turkey	Duzce (270)	0.35	11	0.67	31
4	6.9	1989	Loma Prieta, USA	090 CDMG	0.39	45	0.34	45
5	6.5	1987	Superst. Hills, USA	Poe Road (temp)	0.35	10	0.52	40

| 6 | 7.6 | 1999 | Chi-Chi, Taiwan | TCU 045 | 0.36 | 22 | 0.52 | 49 |
| 7 | 6.5 | 1976 | Friuli, Italy | Tolmezzo (000) | 0.35 | 22 | 0.52 | 69 |

a)   b)
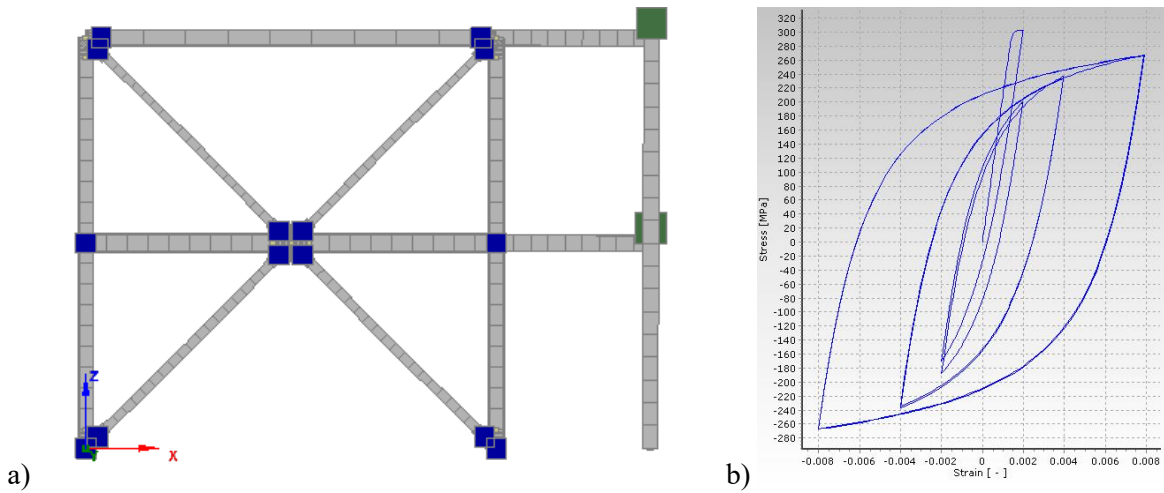
Figure 9. Split-X CBF FE model for dynamic analysis a) steel hysteresis Menegotto-Pinto model b)

a)   b)
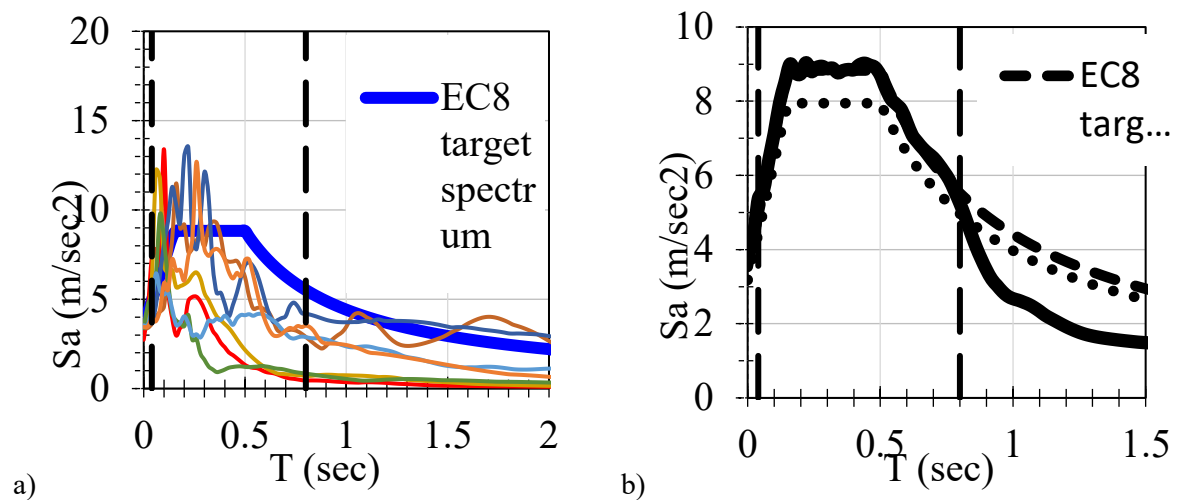
Figure 10. Response spectrums of the recorded accelerograms and Target RS a) Target Response Spectrum, 90% Target RS and Mean Matched RS b).

Table 5. Damage index.

Seismic Record	Damage Index
	AISC Split-X
1. Hector Mine	0,138
2. Kobe	0,133
3. Kocaeli	0,150
4. Loma Prieta	0,148
5. Superstition Hills	0,130
6.Chi-Chi	0,075
7.Friuli	

As TRS the Eurocode type 1 Response Spectrum (RS), based on PGA 0.3g and Soil Type B was used. Figure 10a illustrates the RSs of the recorded accelerograms and the TRS. The Mean Matched RS of the matched accelerograms, the TRS and the 90% TRS are shown in Figure 10b.

Accumulated damage in braces

In order to make assessment of the stage of accumulated damage in braces, equation 2 is used. It gives a conservative relation between the single brace axial deformation amplitude δ corresponding to the number of cycles to failure N. The time history of brace axial elongations and shortenings are taken from the SeismoStruct nonlinear model output for the inelastic force-based fibre elements. Number of cycles was counted by rainflow method, ignoring all cycles with amplitudes less than 5mm. The former was adopted since the proposed formula is very conservative for amplitudes less than 5mm (brace yielding axial deformation). Based on equation 2 and the Miner's rule, damage index was calculated and reported in Table 5. In all cases the damage index appears well below one, demonstrating very low degree of accumulated damage in braces.

Conclusion

The performed cyclic constant amplitude tests on Split-X CBFs reveals a distinctive mechanism of damage accumulation in braces. The observed system behaviour proves the good endurance of braces with built-up H-cross sections, described by lack of sudden brace fractures, development of stable gradual cumulative damage mechanism and lack of total brace fracture. This satisfactory cyclic behaviour may be attributed to the shape of braces cross-section – welded H-shape that in comparison with tube cross sections, exhibited superior endurance.

The defined criteria for assessment of the number of cycles related with significant drop of Split-X energy dissipation capacity and the proposed numerical equation for assessment of the degree of accumulated damage at variable amplitude cyclic load of a single brace is applicable in assessment of Split-X premature fracture of braces when performing dynamic analysis with real strong ground motions.

Acknowledgements

References

ANSI/AISC 341 (2010): Seismic Provisions for Structural Steel Buildings.

ATC-24 (Applied Technology Council) (1992): Guidelines for Cyclic Seismic Testing of Structural Components of Steel Structure.

Eurocode 8: Design of structures for earthquake resistance - Part 1: General rules, seismic actions and rules for buildings; EN 1998-1:2004.

Ballio G., Castiglioni C. (1995): A unified Approach for the Design of Steel Structures under Low and/or High Cycle Fatigue, *Journal of construction steel research*, Vol. 34, №1, 1995.

Bernuzzi C., Calado L., Castiglioni C. (2000): Low-cycle fatigue of structural steel components: a method for re-analysis of test data and a design approach based on ductility, *ISET Journal of Earthquake Technology*, Paper No. 401, Vol. 37, No.4.

Castiglioni C., Calado L. (1996): Low-cycle fatigue behaviour and damage assessment of semi-rigid beam-to-column connections in steel, Article, *IABSE reports*, doi.org/10.5169/seals-56915.

D'Aniello M., Costanzo S., Landolfo R. (2015): The influence of beam stiffness on seismic response of chevron concentric bracings, *Journal of Constructional Steel Research* 112 (2015) 305-324.

D'Aniello M., Ambrosino G., Portioli F., Landolfo R. (2013): Modelling aspects of the seismic response of steel concentric braced frames, *Steel and Composite Structures*, Vol. 15, No. 5, pp. 539-566.

Georgiev Tzv. (2013): Study on seismic behaviour of "X" CBFs with reduced diagonal sections, *PhD Thesis (in Bulgarian)*, UACEG, Sofia.

Georgiev Tzv., Zhelev D., Raycheva L., Rangelov N. (2017): INNOSEIS - Valorization of innovative anti-seismic devices, work package 6 – deliverable 6.2 specifications for device manual, *European Commission Research Programme of the Research Fund for Coal and Steel*.

Georgiev Tzv., Zhelev D., Raycheva L., Rangelov N. (2017): NNOSEIS - Valorization of innovative anti-seismic devices, work package 4 – deliverable 4.1. Volume on case studies for low-rise buildings, European Commission Research Programme of the Research Fund for Coal and Steel, *(Articles in Press)*

Georgiev Tzv., Raycheva L. (2017): Influence of splitting beam and column stiffness on CBFs ductile behaviour, *EUROSTEEL 2017*, September 13–15, Copenhagen, Denmark *(Articles in Press)*

Khatib I., Mahin S. and Pister K. (1988): Seismic behavior of concentrically braced steel frames, Report No. UCB/EERC – 88801, *University of California, Berkeley*.

Krawinkler H., Zohrei M., Lashkari-Irvani B., Cofie N., Hadidi-Tamjed H. (1983): Recommendations for Experimental Studies on the Seismic Behavior of Steel Components and Materials, *The John A. Blume Earthquake Engineering Center*, Department of Civil Environmental Engineering, Report No. 61.

Lacerte M., Tremblay R. (2006): Making use of brace overstrength to improve the seismic response of multistorey split – X concentrically braced steel frames, *Canadian Journal Civil Engineering* 33: 1005-1021 (2006), NRC Canada.

Nip K., Gardner L., Davies C., Elghazouli A. (2010): Extremely low cycle fatigue tests on structural carbon steel and stainless steel, *Journal of Constructional Steel Research* 66 (2010) 96-110.

Seismosoft (2014): SeismoStruct v7.0 – A computer program for static and dynamic nonlinear analysis of framed structures, available from http://www.seismosoft.com.

Shen J., Wen R., Akbas B. (2014): Mechanisms in two – story X – braced frames, *Journal of Constructional Steel Research* 106 (2015) 258-277.

Shen J., Wen R., Akbas B., Doran B., Uckan E. (2014): Seismic demand on brace – intersected beams in two – story X – braced frames, *Engineering Structures* 76 (2014) 295-312.

T-stub macro components of beam to column connections following the loss of a column

TADIC Ivana
Attending Erasmus university: Department of Steel Structure and Structural Mechanics, PUT, Timisoara, Romania
Home university: University of Belgrade, Faculty of civil engineering, Belgrade, Serbia

Supervisor professors: DINU Florea and CIUTINA Adrian
Department of Steel Structure and Structural Mechanics, PUT, Timisoara, Romania, Erasmus+ mobility programme

Abstract

Nowadays, more and more attention is dedicated to designing the structures that will be able to resist accidental loading conditions such as fire, explosions, impacts or consequence of human error. These actions may easily cause failure of the elements located in the vicinity of the hazard, effecting other elements of the structure to fail as well. Therefore, the need is to prevent disproportionate or progressive collapse by creating more robust structure. In order to achieve endurance of the structures primary importance is in structural elements, continuity between elements as well as ductility of elements and their connections. Beam to column connections represent one of the essential parts required to be investigated and evaluated in order to provide enough strength, stiffness and ductility in connection. This master thesis work focuses on examination and evaluation of macro components of T-Stub elements in bolted beam to column connections, their ultimate capacity and ductility under large deformation demands. Existing experimental studies were used to identify ultimate strength and deformation capacity and the data was used to validate numerical models and employed in a parametric numerical study on two main parameters, distance between the bolts and end-plate thickness (Marginean, 2017). The main objectives were the studying of the post yielding behavior for different failure modes, as well as investigation of capacity, ductility and stiffness of T-stub macro components.

Introduction

In order to ensure sustainability and usability of Steel Frame Structures during its service life time and resistance to extreme loading conditions (gas explosions, impacts, terrorist attack etc.) special considerations have to be taken into account regarding the design of structure. Therefore, it is important to provide certain requirements in design that will assure an adequate structural resistance and durability. These requirements consider a combination of strength, ductility, continuity and energy absorption of system. One of the main failure mechanism is referred to as progressive or disproportionate collapse where one or several structural bearing members suddenly fail causing other elements of construction one after another to the failure (*Menchel, 2009*). The basic characteristic of progressive collapse is that the final state of failure is much greater than the initial failure state. First studies and research works dedicated to mentioned structural problems started after the collapse of Ronan Point apartment in 1968 (Figure 1) leading to the development of concept of robust design of structures. Robustness is described as an ability of a structure to withstand disproportionate collapse because of accidental loadings. Many design guidelines like Eurocode, General Servise Administration (GSA), US Departement of Defense (DoD) mitigate the potential of progressive collapse to happen and ensure existing of tranfer load paths as well as robustness by implementing new set of regulations and rules using different methods. These methods consider alternative load paths, tying member hardening of elements and specific local resistance method. In all of these methods linear and nonlinear analysis were developed and linear method has found to be more conservative one. Even though, the great amount of guidelines are

provided, no specific provisions for achieving more robust structures are defined, only some guidance to prevent progressive collapse by increasing strength and ductility. Considering all mentioned facts and importance of transferring the load into foundations through alternative paths in steel frames, the biggest concern would be dedicated to connections that usually represent most vulnerable part of structure. Therefore, the need for ensuring rotation and deformation capacity is of significant importance. In bolted beam to column connections that are known as commonly used, the main indicator of its resistance is issued through T-stub macro-components. Hence, improving the characteristics of this joint components influence on improving overall connection behavior.
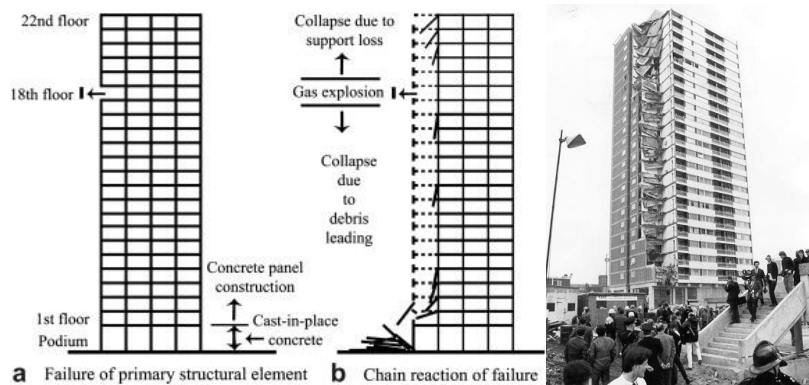

Figure 1. Ronan Point collapse, London, 1968.

Literature review

In alternative load path method the purpose of the structural analysis is to ensure that the steel frame structure can bridge over a damaged column. In this "missing" column scenario extreme tensile forces develop. The mechanism that occurs in these specific conditions is known as catenary action and it is capable to provide adequate load resistance after flexural capacity of the beam is reached, hence, the load-carrying capacity is increased after the plastic hinge formation occurs. Catenary forces produce strong tying forces in the joints and form a mechanism that provide transportation of loads into foundations through surrounding columns and avoid the collapse. Many researches and experiment tests were introduced on the subject of catenary behaviour. In *Lee et al (2009)* it is shown that the tensile force in the beam increases drastically while internal beam moments decrease due to appearance of catenary behaviour in beam after the plastic moment has been reached. The catenary effects can be initiated only with sufficient ductility so that enough plastic hinges can form in order of failure mechanism to be created. Regarding joints classifications by stiffness and strength, partial strength and semi rigid joints are considered as more economic and simple solutions. However, as noted in document by (*Ribeiro et al, 2014*), even though it is very popular to use in structural systems, it can lead to prying action on the beam-column contact and can influence the stiffness of connection and early joint failure. Rules for prediction of strength and stiffness of the joint configuration have been included in modern design codes as Eurocode 3, but no specific guidelines for characterization of ductility is available (*Ribeiro et al, 2014*).
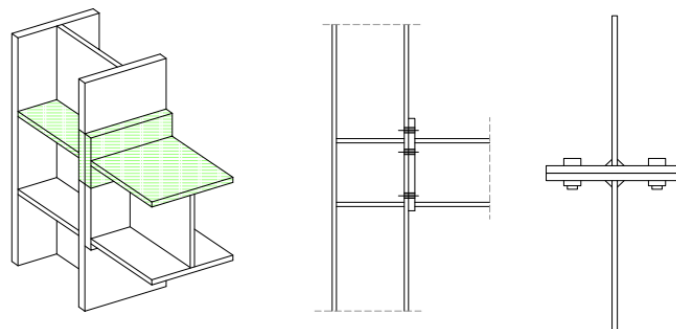

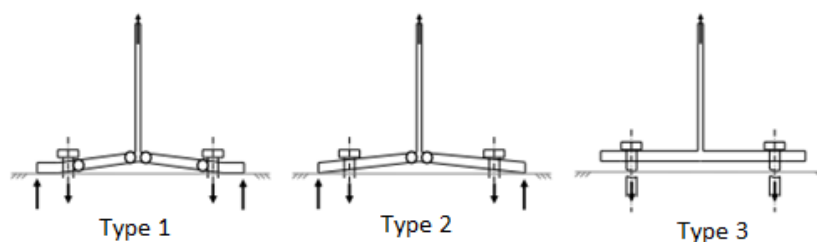**Figure 2.** T-stub component in beam to column connection.

Figure 3. T-stub failure modes (*Ribeiro, 2014*).

T-stubs are basic components of the component method used in EN 1993-1-8 for evaluation of strength and stiffness of bolted end-plate beam to column joints (Figure 2). According to Eurocode 3, T-stub macro-component fails down by 3 types of failure mode, named 1, 2 and 3.

For mode type 1 two plastic hinges per flange leg are developed with the complete yielding of the flange: one at the bolt axis due to bending moment induced by the prying forces, and another next to the weld toe. For mode type, one plastic hinge per flange leg is developed before the failure of the bolts, while for plastic mode type 3, no plastic hinges are developed, being the plastic resistance limited by bolt's strength (Figure 3). A t-stub's plastic resistance is minimum value obtained from described three (*Ribeiro, 2014*).

Large number of different researches gave a valuable contribution to explanation of T-stub overall behaviour. (*Geramia et al, 2010*) showed the influence of connection configuration and different vertical and horizontal arrangement of the bolts observing end plate joint and connection with stems under cyclic loading. They concluded that with changing the horizontal distance between the bolts in both types of connection failure occurred by plastic hinge formation in beam, while as for the vertical distance variation the moment capacity has shown to be higher in stem connection than in end plate. However, their suggestion for better connection is end plate connection because of higher probability of failure mode changing in stem T-stub joint. Large research on different types of bolted connections was conducted in research by (*Tan and Yang, 2012*). The authors showed how catenary action develops due to large deflections in the beams and influence on increasing the resistance of the beam depending, also, on type of connection. In extended end plate connection the greatest flexural stiffness of all seven specimens were observed due to ability of this connection to achieve its load capacity without influence of catenary action. Regarding the influence of number of bolt rows it is concluded that increasing connection depth from 2 to 4 bolt rows the load-carrying capacity of connection but slightly decreases the rotation capacity and because of this catenary action becomes less. Numerical assessment evaluate the performance of two solvers, Explicit dynamics and Static solver where it is shown the advantage of explicit solver in simulating complete failure while static solver could only simulate the fracture initiation. In general, it is concluded from numerous studies and researches that the weld zone in weld plated bolted connection is one of the critical places for fracture to occur, and in almost every experiment specimens reach the failure of the bolt before failure of the flange, which is in accordance with this thesis results. The need to define post yielding behavior of T-stub and ensure enough ductility and rotation capacity is highlighted in order to provide better joint performance under extreme loading conditions.

Experimental program and results

Test set up

Main objectives of experimental program were to investigate capacity of bolted T-stub connections under large deformation demands according to Eurocode propositions and to predict response of T-stub components. These tests are already evaluated and explained in (*Anwar, 2017*) for end plate thicknesses of 10 mm and 12 mm and in (*Marginean, 2017*) for end plate thicknesses 15 mm and 18 mm, with increasing the bolt distance for each thickness, using 100, 120 and 140mm. General configuration and dimensions of T-stub are shown in the Figure 4.
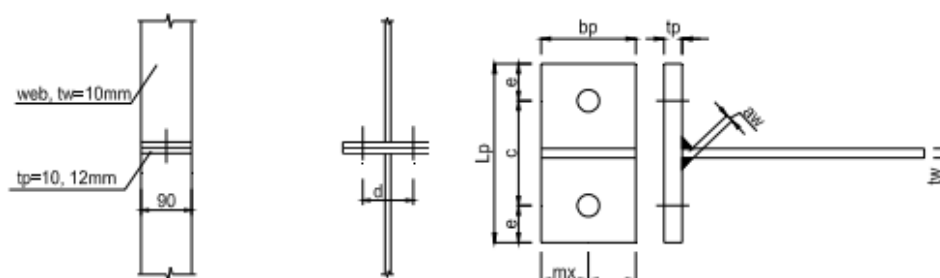
Figure 4. Bolted T-stub geometry.

The experimental program is Phase 3 out of 7 in CODEC research project 2012-2016. Specimens were subjected to room temperature 20˚ and evaluated temperature 540˚ and exposed to normal and high strain rate. Bolts are class 10.9, i.e. ultimate strength is 1000 MPa and yield strength of the bolt is 900MPa, and diameter 16 mm. Web of T-stub is welded for the flange using 7 mm weld throat thickness. All end plates and web were fabricated from the different steel grade and material properties for every thickness plate needed to be tested. The material calibration was executed and the results were evaluated from tensile tests of the coupon taken from the same end plates as T-stub macro-components. Coupons were tested under quasi-static 0.005 mm/sec and dynamic loading conditions of 10 mm/seconds. Tested material coupons used for different end plate thicknesses are shown in Table 1.

Table 1. Material properties for T-stub components.

Part	Thickness	Coupon	Material	Yield strength
	mm			N/mm^2
T-stub web	10	P19	S355	390
T-stub flange	10	P20	S235	310
T-stub flange	12	P21	S235	305
T-stub flange	15	P22	S235	275
T-stub flange	18	P23	S235	420
Bolt	16		10.9	965

Models name are defined like T-10-16-100, where T represents T-stub, 10 is thickness, 16 is bolt diameter and 100 for bolt distance. In total, there are 12 models.

T-stubs are design to achieve ductile failure modes based on static loading conditions according to Eurocode 1993-1-8. The testing was done in Politehnica University Timisoara laboratory. For strain rate loading, an initial loading at 0.05mm/s is applied for two seconds, afterward the imposed displacement is done at a rate of 10mm/second (*Anwar, 2017*). The force was applied directly from the testing machine, using a displacement control. Rod type position sensors measure the displacements directly from the movement of the end plate as they are connected at the center of the end plate for both of the flanges of the T-stub specimen (*Anwar, 2017*).Visual image correlation machine is used for measuring strains and displacements.

Results

Figure 5 show one result for experimental force displacement relationship of tested specimens, thickness 10 mm for static and dynamic load conditions. It is observed that the stiffness and the resistant values are directly dependent on the geometrical characteristics and material properties of the flange and bolts. It can be observed that with increasing the distance between the bolts the deformation capacity increases but there is a reduce in the resistance, while with increasing the thickness of the end plate the resistance is bigger but deformation capacity decreases. Increasing distance from 100 mm to 120 mm deformation capacity increases but with reduction of resistance and from 120 mm to 140 mm only the increase in deformation capacity appears without reduction in total resistance. However, the failure is ultimately attained due to the fracture of the bolts in all cases (*Marginean, 2017*).
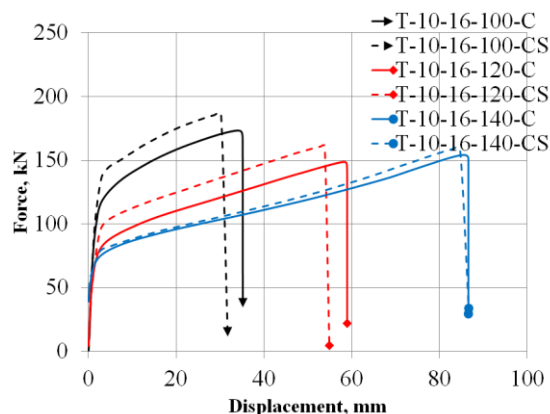
Figure 5. Force displacement curve for T-10-16-100C/CS.

In the figure suffix C is for cold (room) temperature conditions with strain rate 0.5 mm/seconds replicating quasi-static conditions; while suffix Cs is for cold (room) temperature with high strain rate of 10 mm/seconds.

Numerical assessment

### Calibration of material specimens in FE model

For numerical assessment of both, material coupons and T-stub models, Abaqus software is used with Dynamic Explicit solver. Material specimens were used to determine material properties of flanges and web in T-stub model. For the calibration of the steel material to be used in T-stub component, a tension coupon tests were extracted from the T-stub macro-components. For the same class of the coupon three different tests were performed and the results were found to be almost the same. Five different coupons were tested, thickness 10 mm for flange and web of T-stub, and thicknesses 12, 15, 18 mm for other flanges. In material property section elastic, plastic behaviour and damage criteria are defined. To define a linear-elastic behaviour in Abaqus, two parameters were used, Young's modulus of elasticity of 210 GPa and Poissons's ratio of 0.3. Value for density is 7.85x10-9. For the plastic material property modified stress-strain curves were used, different one for every coupon. Nominal stress-strain curves from experimental tests were modified to true stress - strain curves according to equations given in Eurocodes EN-1993-1-5 (*Anwar, 2017*).

$$\sigma_{true} = \sigma \cdot (1+\varepsilon_{eng}) \qquad (1)$$
$$\varepsilon_{true} = \ln(1+\varepsilon_{eng}) \qquad (2)$$

These formulas are valid up to the necking point, after which material seems to soften but it actually hardens. Namely, after initially linear behaviour of material response, the plastic deformation of material occurs. After yield strength point an incremental increase in stress will produce a progressively larger increase in strain and this is the effect of strain hardening in material making it tougher as the strain increases (*Levanger, 2012*). During plastic deformation under a tensile load, a section exhibits high localized extension and thinning called the necking zone. The material increases its load bearing capacity per unit cross-section area, as a result of the strain hardening effect (Figure 6).

In a finite element analysis, the input must be in the form of a true stress/true strain relationship, meaning the stress and strain that each element experience in order to produce the same global response as the tensile test. The plastic data define the true yield stress of the material as a function of true plastic strain and the first piece of data given defines the initial yield stress of the material and, therefore, should have a plastic strain value of zero (*Abaqus manual user, 2012*). Behaviour under failure mode is represented through several additional points and further changed through iterations to provide the best possible match in the resulting force/displacement curve. The final fracture was simulated using the Damage Initiation criterion and Damage Evolution for ductile materials through different coefficients. This material property defines the behaviour of material after the ultimate strength is reached. These coefficients depend on the mesh size and shape as well.
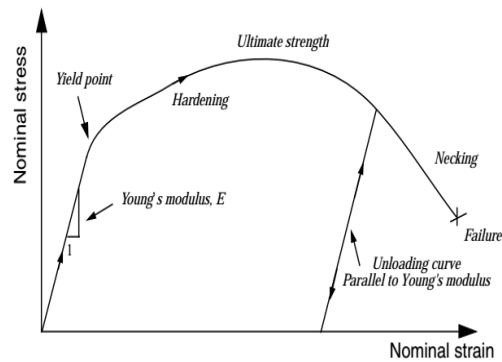
Figure 6. Nominal stress-strain curve.

The analysis in FE model is calculated using Abaqus Explicit Dynamic solver, as has been proven valuable in solving quasi-static problems as well as dynamic. Compared to Implicit method, Explicit procedure resolve better complex contact interaction while Abaqus Implicit may face some convergence problems. Loading was applied through boundary conditions and defining the longitudinal displacement and fixing movement in all other directions.

The plastic behaviour has shown the significant dependency on mesh size element, especially for higher strain values. The size of element is chosen to be 10 mm with increasing the number of elements per thickness. Experimental force/displacement behaviour was validated numerically and different material properties and mesh sizes are established to be used in T-Stub models. Following Figure 7 shows very good approximation of the real behaviour for coupon P20 and comparison with experimental response.
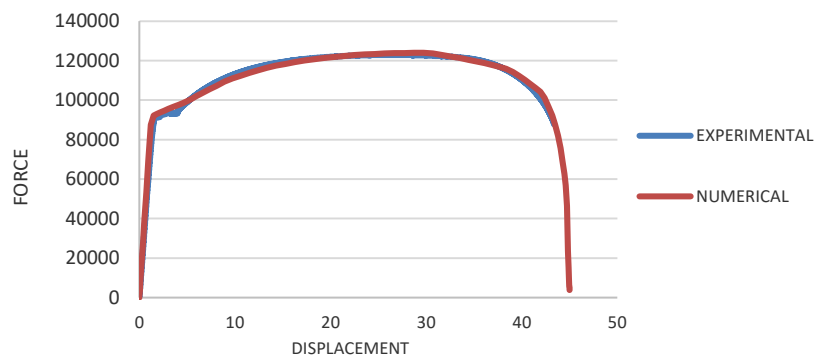

Figure 7. Force-displacement comparison

Description of T-stub numerical models

The T-stub models are created using precise measurements evaluated before testing from the specimens. Material properties are determined using experimental coupons tests previously described. In order to validate numerical models different material properties for each thickness of end plate are implemented. In order to create T-stub components as it is in realistic case, the connection between its parts is made. Instances of T-stub and bolt are chosen and position constraints are added for creating the connection between bolts and T-element. Dynamic explicit step with mass scaling was used to simulate quasi static response for testing T-stub at room temperature with low strain rate. Time target increment is set to 5x10-6 for mass scaling option in order to accelerate speed of calculations. Two references points are defined at the opposite sides of T-stub and were coupled using rigid body type with all degree of freedom constrained on the surface of T-stub. One reference point was fixed using displacement/rotation boundary conditions. Other reference point was allowed to have displacement along the longitudinal axis of the T-stub to replicate realistic experimental conditions. Approximate global size of the seed is 7 mm, and around the holes for the bolts size of the mesh is reduced.

202

Two and three elements per thickness were set up in seed edges option in order to make finer mesh geometry and to produce more accurate results, and size of elements is reduced around bolt holes.

Validation against experimental results

In order to carry out the parametric study numerical models were validated against experimental ones and then calibrate by increasing the distance between the bolts. Validation was done using F-δ response which explains overall behaviour of T-stubs. Models used for validation were specimens T-10-16-100, T-10-16-140, T-15-16-100 and T-15-16-140. Here are presented results for T-10-16-100/140 (Figure 8).
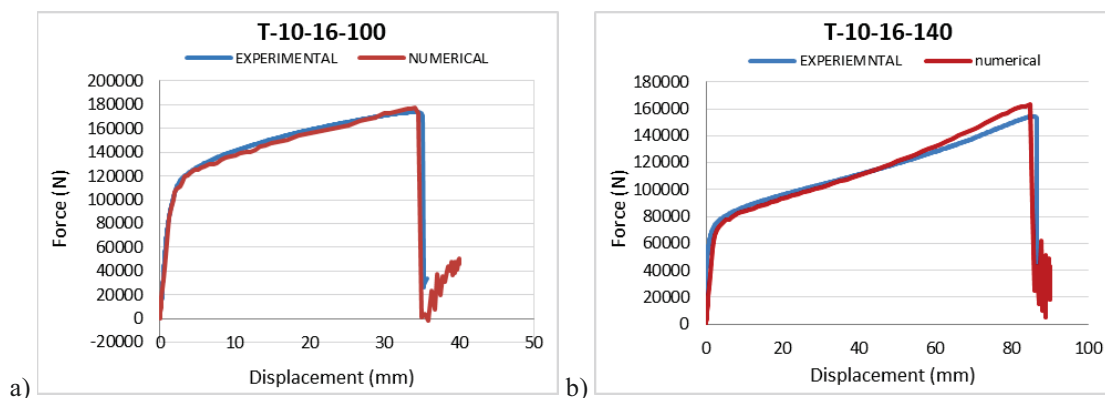
Figure 8. Numerical vs experimental results – validation of T-10-16-100.

It can be observed that the numerical models accurately predict the global behavior of the T-stub component, especially elastic stiffness and the plastic transitions are matching well. Increasing the bolts distance causes decrease in yield strength. Also, with increasing the distance between the bolts reduction in ultimate strength is observed which occurred due to bending of bolts. Both validated thicknesses models failed due to bolt rupture, as well as all other numerical models, which is another indicator of good matching with experimental testing.

Parametric study

Parametric study consists of changing geometrical properties of T-stub model - varying the distance between the bolts and thickness of end plates – flange of T-stubs. For different thicknesses of end plates, different steel material was used in experimental tests, thus different material properties are used for modeling. In order to get valid relationship between new thicknesses used in parametric study material properties of the calibrated numerical models material properties were made the same. Thickness of 22 mm and distance of 80 mm are added to already defined models from experimental tests. Steel grade for web and flange are S355 and S235 respectively, and bolts are class 10.9.

Failure modes models

Generally, behaviour of T-stubs components can be described through failure modes regarding ductility, stiffness and strength. Failure mode 1 is characteristic for ductile and partial-strength/partial-rigid type of connection where failure occurs due to yielding of the flange while for mode 2 and mode 3, failure occurs at brittle components of specimens, usually by bolt rupture. Using equations given in Eurocode 3, it is possible to calculate the force at which the fracture will occur as well as evaluate if there is a reserve of capacity (Table 2). Model T-10-16-100 is chosen for describing failure mode 1.

Table 2. Failure modes Eurocode 1993-1-8.

| Model	Mode 1	Mode 2	Mode 3
	kN	kN	kN
T-10-16-100	92	99	339
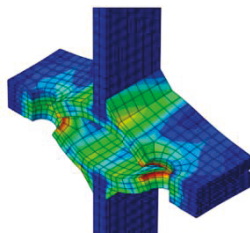
Figure 9. Plastic hinges development in numerical models.

For specimen T-10-16-100 predicted failure mode 1 is first reached at force value 92 kN. The analysis of equivalent plastic strain PEEQ also confirms these observations, namely in Figure 9 is shown the development of two plastic hinges, in T-stub flange near the weld toe and in bolt axis, which is in accordance with EN description of T-stubs behaviour in mode 1.

In numerical force-displacement response the yielding starts at approximately around 85 kN (Figure 10), which is the same as Eurocode predicts. But the failure occurs long after that. Plastic strains continue to develop after the yielding point because of the plasticity and strain hardening of the materials (*Anwar, 2017*). Therefore, T-stub is able to carry much more load after the yield point is reached when failing in mode 1 and mode 2, i.e. these modes show large reserve of capacities beyond failure criterion of Eurocodes. The ultimate failure of T-stub is at a load of 177 kN but failure occurs because of the fracture of the bolts. Displacement at yielding point is around 1.4 mm, while the ultimate displacement amounts 34 mm, which is indicator of high ductility. Even though the failure of the T-stub is occurred because of the failure of the bolts, the force at the failure is lower than full capacity of the bolts, at 304 kN. This is because of the interaction between bending in the bolts and axial force in T-stub. The increase in bending of the bolts is due to large deformations in flanges and increased prying forces.
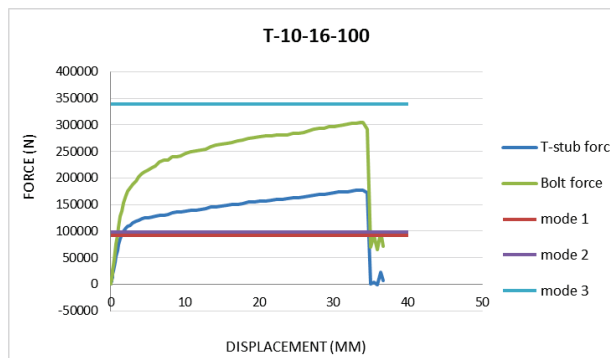
Figure 10. Force-displacement behavior of T-stub, Eurocode failure modes.
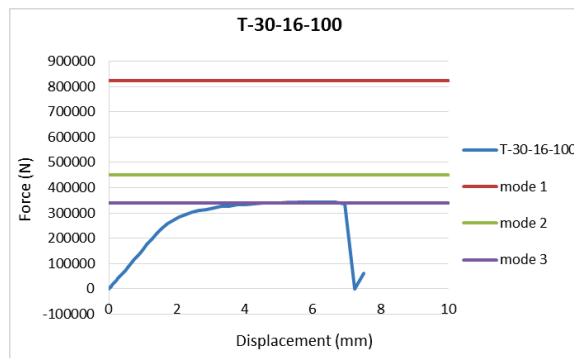
Figure 11. T-stub model response for failure mode 3.

To define a failure mode 3, T-stub model with flange thickness 30 mm is chosen with distance between the bolts 100 mm. T-stubs with thick flanges has a very small deformation of the flange and all the damage take place through break of the bolts. Failure mode 3 indicates brittle failure of the T-stub, due to fracture of bolts and no yielding is observed in flange or development of plastic hinges. Numerical model shows the same result as Eurocode equations predict, the force in T-stub increasing until fracture of the bolts, where the T-stub fails, meaning the failure mode 3 is governing, and no reserve capacity is observed (Figure 11).

Influence of varying distance between the bolts

Figure 12 presents influence of varying distance between the bolts on failure modes of T-stubs. Model of T-stub with thickness of end plate 12 mm is chosen for explanation. General observations show that overall capacity of the T-stub is reduced with increasing the distance between the bolts. Also, this reduction is more accentuated for failure mode 1 compering to failure mode 2, while mode 3 has no influence on increasing the distance.
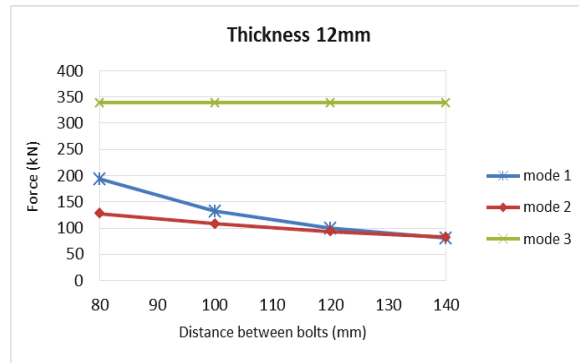
Figure 12. Influence of variation of bolt distance on failure mode.

With increasing the distance between the bolts, ductility of T-stub raises, but at the same time reduction in strength is observed. This is unusual because with increasing the distance more material is added to the element and yet, strength falls.

Overall capacity was calculated as highest force value in force-displacement response of T-stub. For fixed thickness of 10 mm T-stub force is decreasing with increasing the distance between the bolts while for the bolts force no significant changes are notable. This reduction in ultimate capacity of T-stub is caused by interaction between axial force and bending moments in the bolts. Due to deflections in the flanges the prying forces are developing and causes on bending moments in bolts to appear. The prying forces and, therefore the bending of the bolts are higher with increasing the distance between the bolts. Right graph is presented for thickness of 18 mm in order to show differences in magnitude of bolt moment. For thinner plate increase in bolt moment values is more noticeable with increasing the distance between bolts than for thicker plate which indicates bigger prying forces as a result of smaller thickness (Figure 13). The increase in the prying forces is because of the increased bending of the endplates due to enhanced ductility of T-stubs (*Anwar, 2017*).

Other observed properties with changing two geometrical parameters were: capacity of the T-stub, ductility, initial stiffness, yield strength and ratios F_u/F_y where F_u presents ultimate force at failure, and F_y presents yield strength, and d_u/d_y where d_u presents maximum displacement and d_y displacement at yield point. Ductility was presented through maximum displacement at failure. Initial stiffness was obtained by fitting a linear polynomial to force-displacement curve until around 25% of ultimate force, as was done in (Muntean et al, 2010). Yield force was determined using testing procedure recommended in (ECCS, 1986).

Increasing this distance results in improving the ductility of the T-stub which can be observed through increase in maximum displacement at failure. But, this increase is not the same for every thickness. For thinner plates, like 10 mm, increase in ductility is very large with growing the distance between the bolts, while for thicker plates, like 18 mm, difference in ductility is slightly increasing. The reason is less plastic deformation of thicker flange.
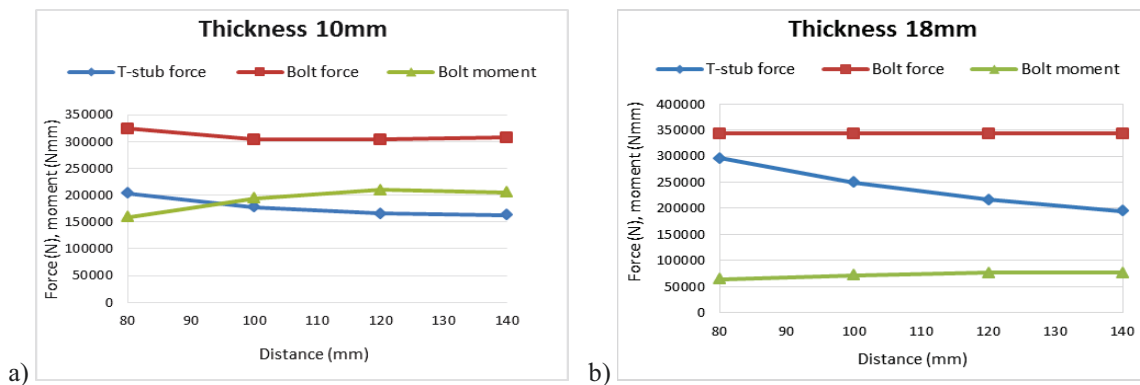

Figure 13. Variation of T-stub force and bolt forces on distance between the bolts.
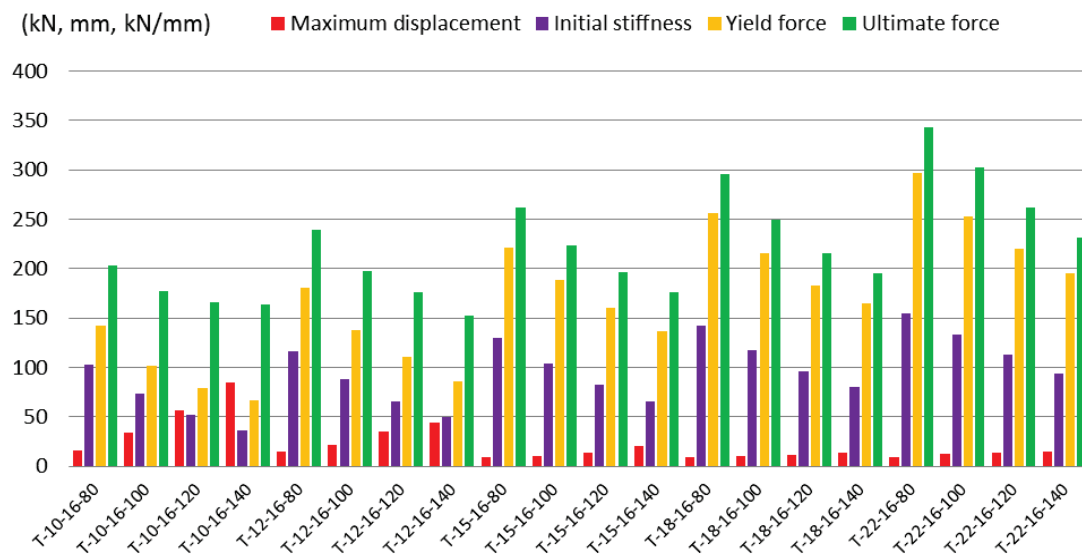
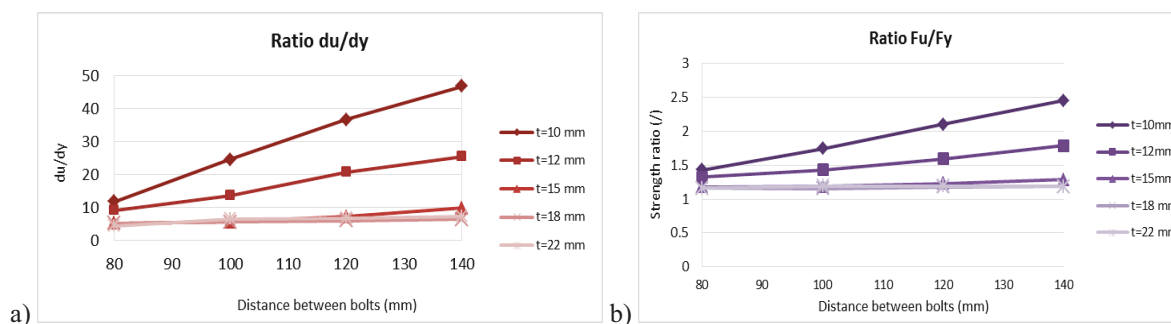**Figure 14.** Influence of changing the bolt distance.

Figure 15. Deformation capacity (a), strength capacity (b).

On the other side, by increasing the distance between the bolts the yield strength decreases. Hence, the beginning of plastic behavior starts earlier. Opposite of ductility, decrease in yield strength is observed to be in the same degradation magnitude for all thicknesses. Indicator of initial stiffness is elastic slope which experiences reduction with bigger displacement. These variation of bolt distance on overall behaviour is resented in Figure 14.

n order to evaluate how much reserve deformation capacity T-stub can obtain after the yield point is reached, ratio between ultimate displacement and yield displacement is calculated. Also, important parameter that shows additional reserve capacity of T-stub macro components beyond its yield point is over strength ratio and presented through Fu/Fy ratio and it is observed that with increasing the distance between the bolts this parameter increases too, increasing that way the plasticity (Figure 15).

Influence of varying thickness of end plate

In order to study the failure mode variation on thickness, model with fixed distance 140 mm is chosen (Figure 16). It can be observed that increasing the end plate thickness has no influence on failure mode 3, because for this mode resistant is dependent on bolts. On the other hand, for mode 1 and mode 2 yield capacities increases with thicker flanges, and is reaching ultimately mode 3. Adding more material in longitudinal direction improves capacity. Failure mode 1 is governing mode for thickness of 10 mm, and has a large increase till thickness of 22 mm, while failure mode 2's increase is less. Hence, transition from failure mode 1 to failure mode 2 can be located between 12 and 13 mm thickness.
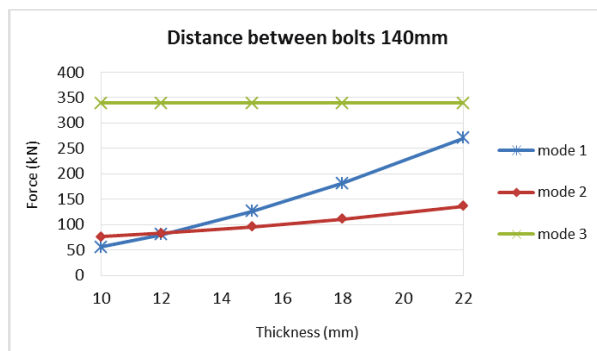
Figure 16. Influence of variation of thickness on failure mode.

Figure 17 shows how changing thickness influences on T-stub force, bolt force and bolt moment. Force in the bolts exhibits slight increase for smaller thicknesses but mostly remains the same, without changing for thicker plates. Whereas, the T-stub force experiences increase. This improvement in axial capacity is due to reduced bending of the bolts. Namely, for bigger thicknesses deformation of the flange is minimized and hence, the prying forces that cause bending of the bolts are decreased.

Figure 18 shows changing of ductility, yield strength, stiffness and ultimate strength. While the increase in capacity is obtained with thicker flange, opposite consequences are observed for ductility. Increasing the thickness of end plate results in decreasing in maximum displacement at failure. Ultimate displacement was smaller for models with thicker end plates that failed in mode 2 or 3 involving bolt failure. It can be seen that is different amount in decrease of ductility for each distance, where for the distance of 80 mm no drastic change in ductility is noted, while for distance 140 mm, the curve goes from 90 mm (T-10-16-140) to 10 mm (T-22-16-140), it changes more rapidly.

Enlargement of yield strength, i.e. beginning of non-linear behavior, and ultimate strength also occurs by increasing the flange thickness. For each distance the increase of yield strength with thicker plates is found to be in the same proportion, opposite of ductility. When observing the initial stiffness, thicker end plate thickness increase initial stiffness which is indicator of high elastic behavior.

Reserve deformation capacity after reaching the yield point presented through du/dy ratio is also decreasing with thicker plates, which can be seen at Figure 19. As already mentioned, this less deformation causes smaller prying force too, therefore the brittle failure of bolts is governing and thicker plates reach mode type failure 3. The over strength ratio as indicator of reserve strength capacity also exhibits a decrease with increasing the thickness, due to reduced ductility of T-stub changing in disproportionate manner for each distance. For example, observing distance of 80 mm, T-22's reserve in capacity is 80% of T-10's, but for 140 mm bolt distance it is 48 %.
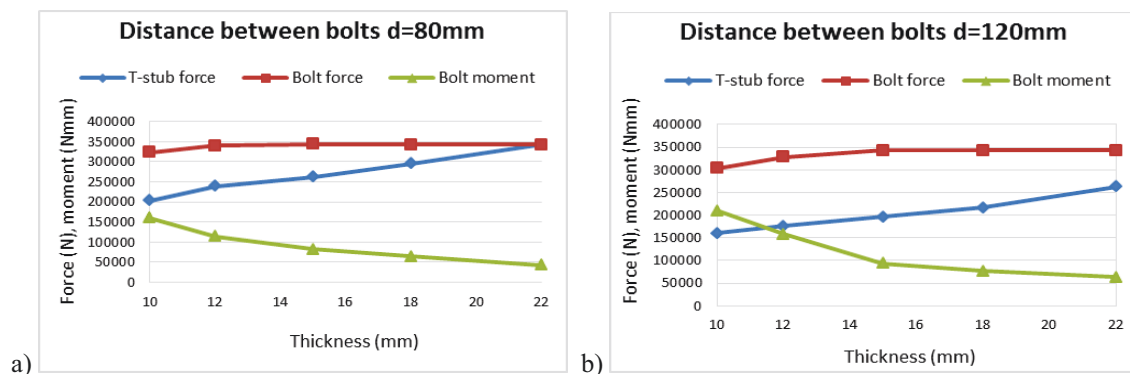

Figure 17. Variation of T-stub force and bolt forces with increasing thickness of end plate.
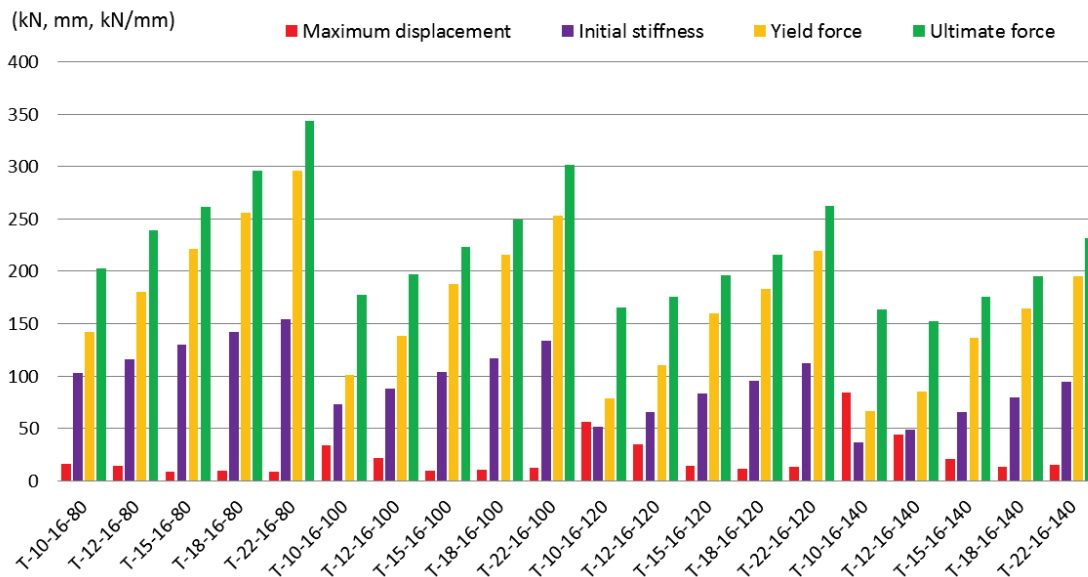
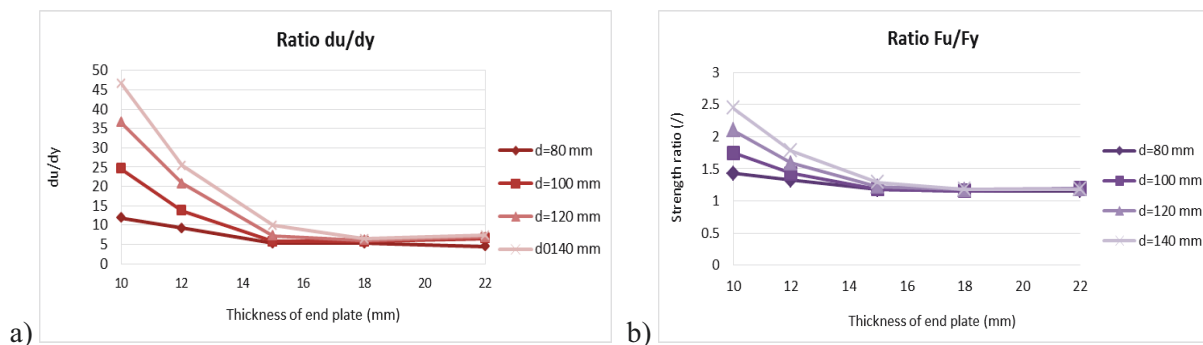**Figure 18.** Influence of changing the thickness of end plate.

Figure 19. Deformation capacity (a), strength capacity (b).

Conclusions

From research framework program of CODEC project (Structural connection and collapse control performance based design of multi storey structures under accidental actions) experimental results were gathered and observed in order to investigate results of tests and further, replicate behaviour in numerical model. Numerical modelling and parametric study followed. Based on results of tensile data of coupons specimen behaviour, calibration of material was done. Coupons models were validated with experimental results from extracted specimens. Calibration was done for each thickness using finite element analysis in software Abaqus. The models replicate exact behaviour of experiment. Stresses and equivalent plastic strains found to be the same as experimental data showing good match between finite element analysis and experiment tests. As experimental program was designed with different material properties for different end plate thicknesses, parametric study was carried out in order to investigate how variation of thickness influences on behaviour of T-stub. Therefore, calibrated T-stub models were used for parametric study, but with the same material properties for all thicknesses and distances between the bolts, so that the models can be compared regarding both, thickness of flange and bolts distance. Some of the main conclusions are presented:

- All of described models exhibit ductile failure mode 1 or mode 2, but it was due to fracture of the bolts, which are brittle components in T-stub model.

208

- Increasing the bolt distance influence on increasing the prying forces due to large deformations of the flange and, hence, more bending in the bolts. Axial-bending moment interaction also causes the failure of the bolts before they reach their ultimate capacity. On the other hand, increasing the flange thickness decrease the prying forces and, hence, reduces the bending of the bolts.

- Increasing distance between the bolts yield strength decreases, same as yield capacity. But, maximum displacement increase, indicating larger ductility. Due to bigger distance, deformation of the flanges is bigger, hence the prying forces raises, resulting in higher bending moment in bolts and, in the end, reduced ultimate capacity, as mentioned. Opposite, increasing the thickness of end plate, influences on decreasing the ductility but improving the yield strength and ultimate axial strength.

- Over strength ratio as indicator of reserve capacity, exhibits reduction with thicker end plates, but increased bolt distance gives enhancement in reserve capacity and ductility.

- Regarding stiffness, parametric study showed that with increasing the bolts distance, decrease in initial stiffness occurs. Similarly, increasing the flange thickness results in increasing the initial stiffness.

As the main purpose is designing connection that will resist progressive collapse, and provide enough reserve capacity, it would be important to ensure enough ductility in order to develop catenary action but at the same time attain not to cause significant reduction in moment and ultimate capacity of connection. The goal would be to investigate and increase ductility with thinner plates, because the changes are significant, while for thicker plates playing with distance between the bolts gives no high differences.

Some of the recommendations from [6] would be to increase distance between the bolts in seismic areas where ductility is required, but avoid it in non-seismic regions. Also, since the failure of all models occurs due to fracture of the bolts, improving capacity of the bolts would improve overall behaviour of T-stub.

References

Anwar G.A. (2016/2017): *Ultimate deformation and resistance capacity of bolted T-stub connections under different loading conditions*. M.Sc. thesis, publisher: Czech Technical University in Prague.

ECCS – Technical Committee 1 – Structural Safety and Loadings Technical Working Group 1.3 – Seismic design. "Recommended Testing Procedure for Assessing the behavior of Structural Steel Elements under Cyclic loads"

Geramia M., Saberi H., Saberi V., Daryanb A.S. (2010): Cyclic behavior of bolted connections with different arrangement of bolts. *Journal of Constructional Steel Research 67 (2011) 690–705*

Levanger H. (2012): *Simulating Ductile Fracture in Steel using the Finite Element Method: Comparison of Two Models for Describing Local Instability due to Ductile Fracture*. Master thesis

Marginean I.M. (2017): *Robustness of moment steel frames under column loss scenario*. PhD thesis.

Menchel K. (2009): *Progressive Collapse: Comparison of Main Standards, Formulation and Validation of New Computational Procedures*. Universite libre de bruxelles, Faculte des sciences appliquees

Muntean N., Grecea D., Dogariu A. and Dubina D. (2010): Strength and ductility of bolted t-stub macrocomponents under monotonic and cyclic loading. SDSS'Rio, Brasil 2010 Stability and ductility of steel structures.

Ribeiro J.N.B., Rigueiro M.C., Santiago A., Rodrigues J.P.C. (2014): Assessment of the T-stub joint component at ambient and elevated temperatures. *Fire Safety Journal 70, 1–13*

Ribeiro J.N.B. (2014): Assessment of the behaviour of T-stub joint under impact loading. M.Sc. thesis

Simulia (2012): Getting Started with Abaqus: Interactive Edition, *Get. Started with Abaqus Interact. Ed.*, p. 4.50-4.54.

Tan K.H., and Yang B. (2012): Numerical analyses of steel beam-column joints subjected to catenary action. *Journal of Constructional Steel Research, 70(1), 1-11*

Experimental in-situ testing of the structures of Cevahir sky city residential complex in Skopje by forced and ambient vibration methods

GAREVSKI Mihail
Institute of Earthquake Engineering and Engineering Seismology, IZIIS- Skopje

GJORGJIEV Igor
Institute of Earthquake Engineering and Engineering Seismology, IZIIS- Skopje

JEKIKJ Goran
Institute of Earthquake Engineering and Engineering Seismology, IZIIS- Skopje

ZHUROVSKI Aleksandar
Institute of Earthquake Engineering and Engineering Seismology, IZIIS- Skopje

Abstract

Structural vibration testing and analysis contributes to progress in many industries, including aerospace, auto-making, manufacturing, wood and paper production, power generation, defense, consumer electronics, telecommunications and transportation. The most common application is identification and suppression of unwanted vibration to improve product quality. The term vibration describes repetitive motion that can be measured and observed in a structure. Unwanted vibration can cause fatigue or degrade the performance of the structure. Therefore, it is desirable to eliminate or reduce the effects of vibration. In other cases, vibration is unavoidable or even desirable. In this case, the goal may be to understand the effect on the structure, to control or modify the vibration, or to isolate it from the structure and minimize structural response. Vibration analysis is divided into sub-categories such as free vs. forced vibration, sinusoidal vs. random vibration, and linear vs. rotation-induced vibration.

Free vibration is the natural response of a structure to some impact or displacement. The response is completely determined by the properties of the structure, and its vibration can be understood by examining the structure's mechanical properties. The forced vibration testing methodology is based on the resonant concept. Forced vibration is the response of a structure to a repetitive forcing function that causes the structure to vibrate at the frequency of the excitation.

The need for testing the behavior of full scale structures under dynamic loads stems from the fact that the analytical calculations cannot account for all complexities involved. This paper presents the results obtained by application of forced vibration testing and ambien vibration testing of four 42 storey residential skyscraper buildings constructed as reinforced concrete shear wall structural systems consisted of 40 cm, 30 cm and 25 cm thick reinforced concrete shear walls to define their dynamic characteristics. Experiments have been carried out using shakers and sensors within the IZIIS' Dynamic Laboratory.

Introduction

Structural system and structural components of the Cevahir sky city residential complex

The subject of the following analyses are the four 42 storey residential skyscraper buildings, constructed by "Cevahir Holding" in Aerodrom Municipality in Skopje (figure 1). The buildings are constructed as a reinforced concrete shear wall structural systems, consisted of 40 cm, 30 cm and 25 cm thick reinforced concrete shear walls, 20 cm thick reinforced concrete storey slabs and reinforced concrete foundation piles with a diameter of 100 cm and a length of 24 m, interconnected with 175 cm thick reinforced concrete foundation slab.

The storey scheme consists of two basement levels, ground floor and 40 storeys. The full structural height is 134 m.


Figure 1. Blocks of the "Cevahir Sky City" residential complex.

Testing methodology and equipment

The forced vibration testing methodology is based on the resonant concept. By application of a dynamic harmonic force on the top of the building, the resonant frequencies are excited, if the frequency of the force is equal to one of the natural frequencies of the building in the corresponding direction. The frequency of the force can be gradually changed in small steps. The resonant state is reached when the acceleration response at the measurement point becomes maximum and then decreases while the frequency of the force still increases. In this manner, frequency response curves can be obtained for each orthogonal direction and torsion. On the other hand, the ambient vibration testing methodology is based on ambiental excitation such as wind, traffic, influences from the regular usage of the building, etc. Sensitive seismometers are capable of catching the produced vibrations which are of a random type of signal, consisting of excitation frequencies in a broad frequency range, enough to excite several modes of structural vibration.

For a forced vibration generation in horizontal direction, two GSV-101 (Geotronix, USA) vibration generators were used for generating sinusoidal excitation force with frequencies in the range from 0.4 to 8.0 Hz. Each generator is capable of producing excitation force with an amplitude of up to 2.5 tons (Figure 2).

a)   b)
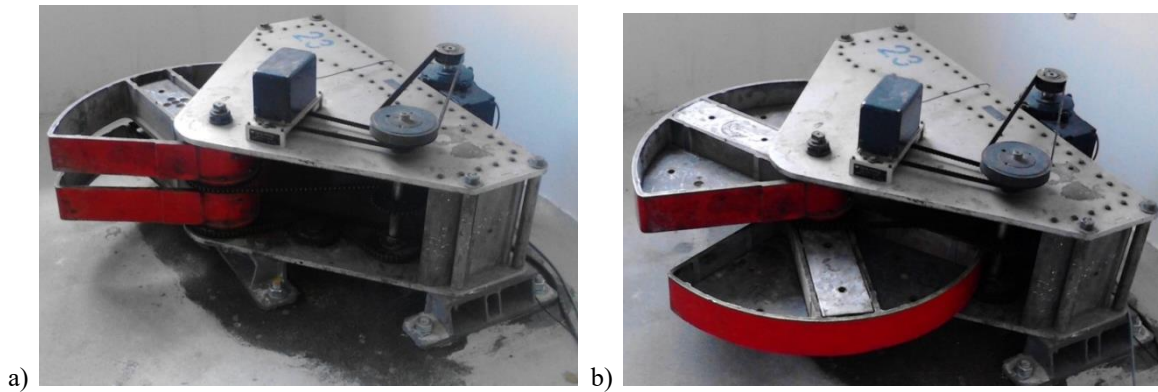
Figure 2. GSV-101 (Geotronix, USA) – position of the shaker baskets for maximal excitation force (a) and zero excitation force (b).

The inertial excitation force, produced by the vibrators, is directly dependent on the lumped mass on the vibrators' rotating baskets and their rotating velocity. The calculation of the inertial excitation force is demonstrated in Equation 1.

$$p(t) = \left(me\omega^2\right)\sin(\omega t) \qquad (1)$$

Where $p(t)$ represents the inertial excitation force, e represents the radius of the rotating mass centroid around the rotation center, m represents the lumped mass on vibrators' rotating baskets and ω represents the angular frequency of the rotating mass. The dependency of the excitation force on the frequency of the rotating mass is graphically demonstrated in Figure 3.
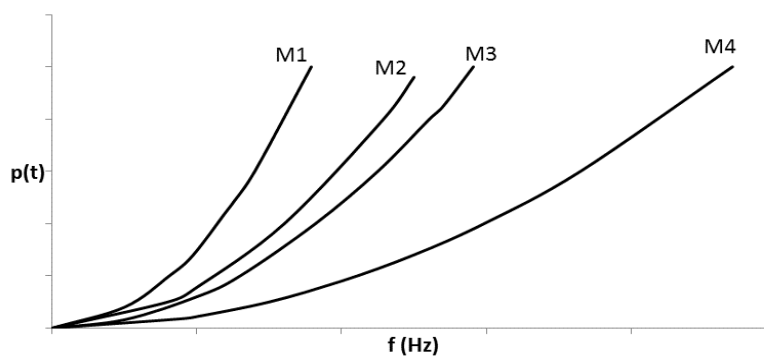
Figure 3. Relations between excitation frequency, rotational lumped mass and generated excitation force (M1>M2>M3>M4).

Figure 3 clearly shows that the excitation force is weak for low frequency excitation due to its centrifugal nature, regardless the lumped mass on the shaker baskets. Therefore, difficulties occur often in the attempts for producing excitation force with high intensities and excitation frequency lower than 1.5 Hz. Besides the mentioned disadvantages, the main advantage of the forced vibration tests over the ambient vibration tests is the high signal-to-noise ratio (S/N) which means that the recorded signal consists of mainly usable and noise-free components, which allows application of conventional structural dynamic analysis techniques, while in ambient vibration records, the noise is often a dominant component along the spectrum. The second advantage is the fact that the excitation force is a controlled and measurable quantity.

Twelve accelerometers PCB Piesotronics Model 393B12 with sensitivity of 10,000 mV/g, with a range of up to 4.9 m/sec2 (0.5g) are used for registration of the structures' response. The vibrations were registered with a sampling frequency of 2048 Hz. The data acquisition system consists of module NI cDAQ-9178 and 3 card module NI 9234.

Special software for structure's response analyses, developed in IZIIS (SHMART_2D MATLAB), was used in the process of collecting and analyzing data from the ambient and forced vibration tests. Together with this software, a commercial one (ARTeMIS) applying the Frequency Domain Decomposition (FDD) identification method was used for processing the collected ambient vibration data.

Testing program

The testing program consisted of the following:

- Ambient vibration testing on the 40th floor of the blocks A, B and C that already have their infill walls finished;

- Ambient and forced vibration testing of the whole structure of the block D before the infill walls construction finishes.

The measuring equipment for registering ambient vibration has been placed on the 40th floor of blocks A, B and C (Figure 4).
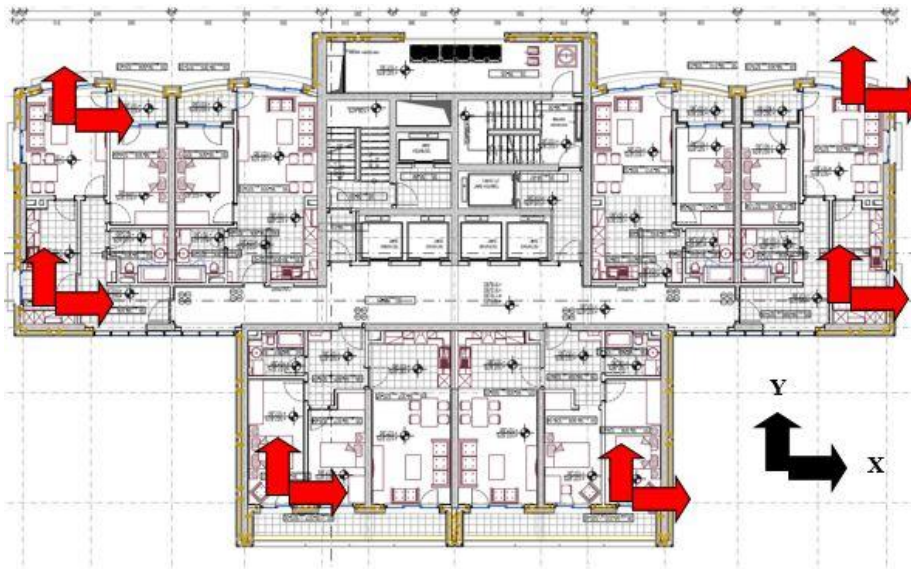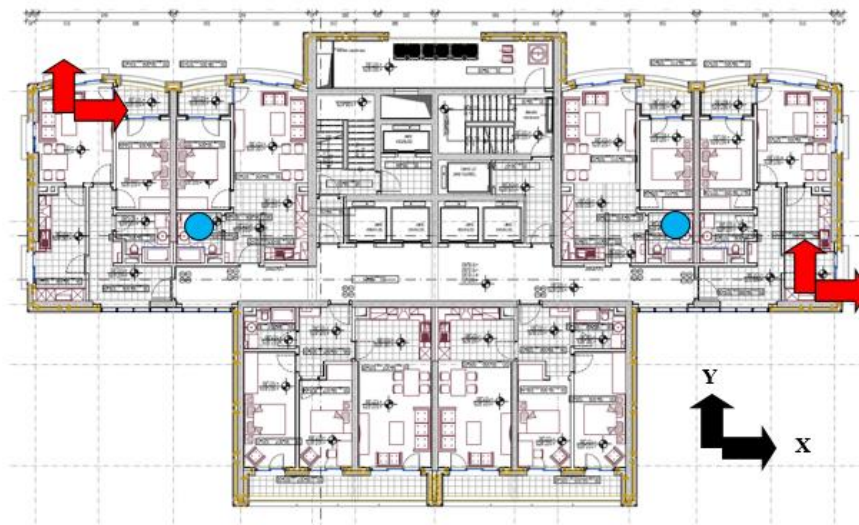

Figure 4. Plan of 40th floor - Instrumentation for ambient vibration registration of blocks A, B and C (red arrows).

The measuring equipment for registering forced vibration of the block D has been placed on every fourth floor of the building at the two diagonal edges. The measurement has been carried out for two orthogonal directions, at each measuring point and torsion.

Forced vibration testing was carried out for determination of the structure's dynamic characteristics in both horizontal orthogonal directions and torsion, in frequency range from 0.4 up to 8.0 Hz, by forced vibration generation (developing resonance conditions in the structure).

For the purpose of successful forced vibration testing, the force was applied on the 40th floor of the building (Figure 5) where the zero point of any mode shape never occurs and the values of the mode shape vectors are the highest for the first mode and among the highest for the higher modes.

The excitation forces were applied as sinusoidal in transversal, longitudinal and torsional direction, with an excitation frequency range estimated to include the natural frequency of the structure in the corresponding direction. In this particular case, the shakers were mounted on the 40th floor, in a mutual position from which the effects of torsional components of transversal excitation would be minimal. The measuring equipment was placed at the two diagonal edges of the building. The measurement was carried out in two orthogonal directions, at each measuring point.

Figure 5. Plan of 40th floor - Forced vibration generators' placement on the block B (blue dots) and plain instrumentation sheme (red arrows).

The vertical instrumentation configuration covered placing the referent instruments on the 40th floor and mobile instruments on the floors no. 36, 33, 29, 25, 21, 17, 13, 9, 5, 1, 0 and -2 on the same vertical as the referent instruments (Figure 6). The recorded data of the forced vibration measurements were processed in SHMART_2D, a system of MATLAB based software codes, programmed in IZIIS for real time data processing and post processing. Butterworth band pass zero-phase digital filter was used for clearing the recorded data from harmonic components and noise in the non-observed frequency ranges.

The structure was tested by applying 3 different levels of lumped masses on the shaker baskets. As demonstrated in Equation (1), the excitation force is a function of the rotating mass and the rotation frequency. The polynomial function of the excitation force has been obtained applying least squares method for every particular rotating mass applied for producing sinusoidal excitation force.
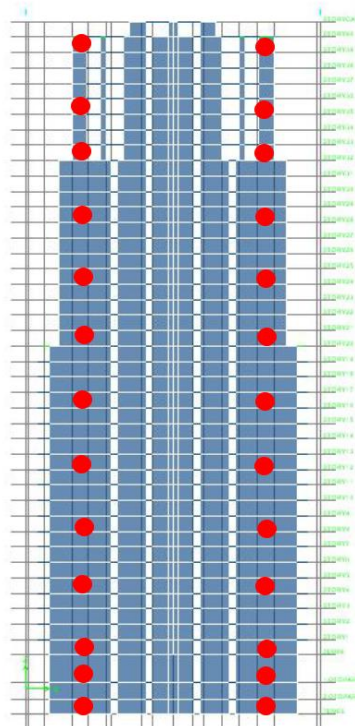
Figure 6. Vertical sensor configuration (red dots) for forced vibration registration of block D.

Results

Forced vibration test of block D

Modal frequency identification

The natural frequencies of the identified modes of the structure were obtained by gradually increasing the excitation frequency and locating the frequency of the most intense structural response, which is the natural frequency of the structure's corresponding mode. By generation of forced vibrations in both orthogonal directions, as well as torsional vibrations, the resonant of higher modal frequencies and the corresponding vibration mode shapes in these directions were defined. The first mode in both orthogonal direction and torsion were unable to be identified by forced vibration testing due to the low angular frequency of the vibrators' rotating mass and inability for generating critical intensity of excitation force.

The obtained frequency response curves for the second mode in the two horizontal orthogonal directions and torsion are presented in the following charts (from Figure 7 to Figure 9).
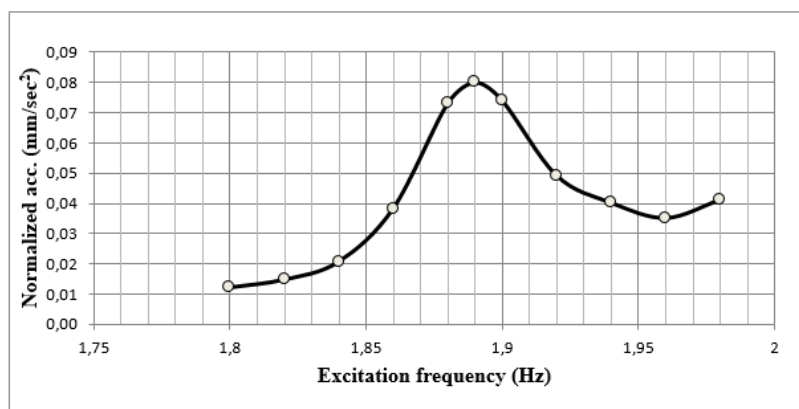

Figure 7. Excitation frequency response curve in Y direction – II mode.
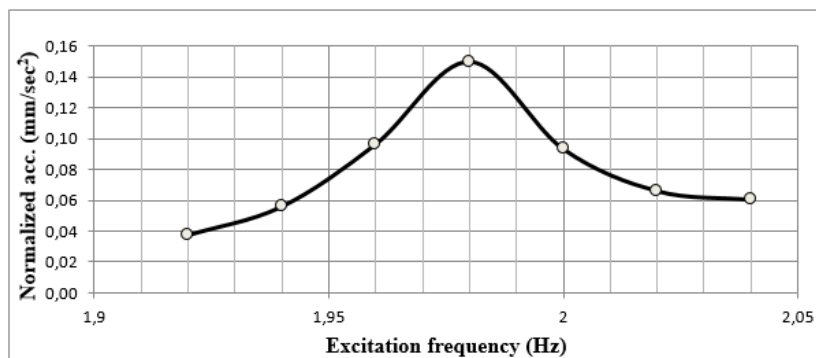

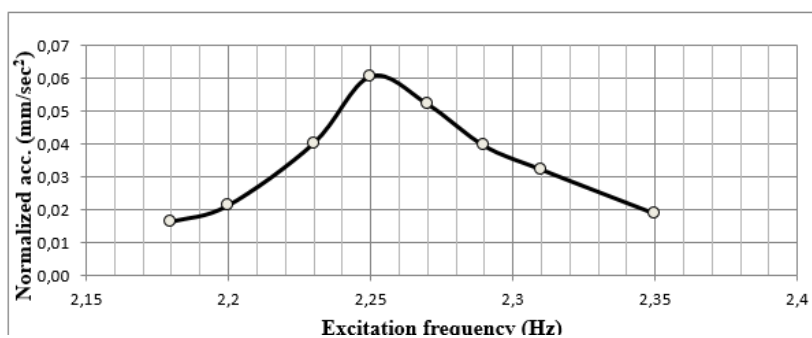**Figure 8.** Excitation frequency response curve in torsion – II mode.

Figure 9. Excitation frequency response curve in X direction – II mode.

Damping

Damping coefficient ξ of each identified mode in the state of resonance was obtained applying the half-power method and the logarithmic decrement method.

The half-power method consists of locating the resonant frequency f_r and two nearby frequencies f_1 and f_2, located in the frequency spectrum (Figure 10) by application of Equation (1).
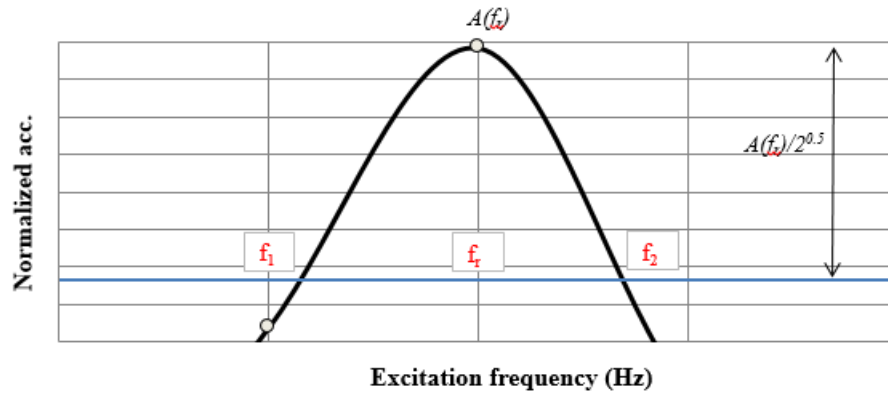
$$A(f_1, f_2) = \frac{A(f_r)}{\sqrt{2}} \tag{1}$$

Figure 10. Locating f_1 and f_2.

After locating required frequency values (f_r, f_1 and f_2), damping value for the particular mode is obtained in percent applying Equation (2).

$$\xi = \frac{f_2 - f_1}{2 f_r} \times 100\% \tag{2}$$

For the logarithmic decrement method, the decaying curve was obtained along the response amplitudes using the least square exponential curve fitting, observing the response after the sudden stop of the harmonic excitation by switching off the shakers during excitation in resonant state. (Figure 11)
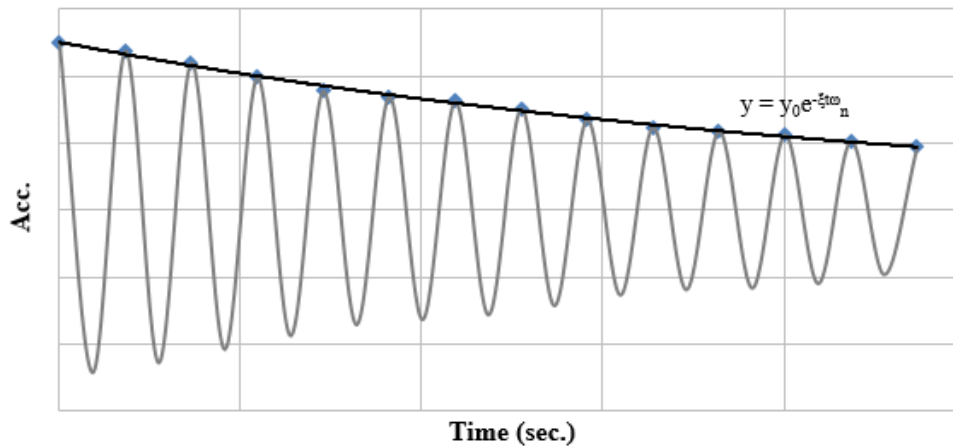

Figure 11. Logarithmic decrement curve fitting.

The exponential function of the decaying curve that fits the amplitudes of the damped oscillation is defined in Equation (3).

$$y = y_0 e^{-\xi \omega_n t} \tag{3}$$

where *ξ* represents the damping ratio, *ω_n* is the oscillation angular frequency measured in *rad/sec²* (*f=ω_n/2π*), *t* is the time of the observation in seconds. The optimal exponential curve fitting function has been obtained applying the least square method.

Natural frequencies of the structural modes and the calculated corresponding damping ratios are presented in Table 1.

Direction / Mode	Freq. (Hz)	Half-power (%)	Logarithmic decrement (%)
Y / II	1.89	1.5	0.5
T / II	1.98	0.8	0.4
X / II	2.25	1.3	0.6

**Table 1**. Natural frequencies and damping ratios from forced vibration testing

The mode shapes of the structure were obtained by instrumentation of every fourth storey from the 40th storey down to the foundation level (Figure 12- Figure 14). The 40th storey was constantly instrumented with 4 sensors and considered as referent, while the remaining 8 sensors were shifted to lower storeys after each test.
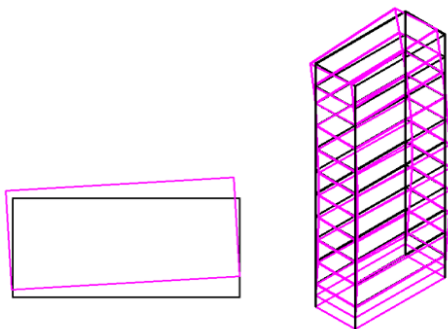
Figure 12. II Mode shape in Y direction (1.89 Hz) - the 40th floor (left), the whole structure (right).
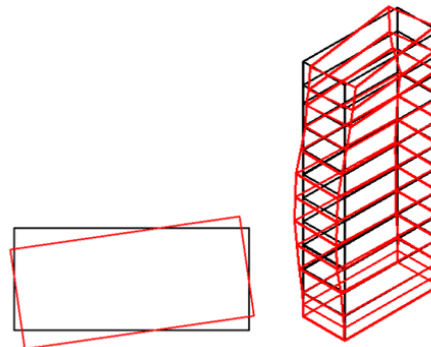
Figure 13. II Mode shape in torsion (1.98 Hz) - the 40th floor (left), the whole structure (right).
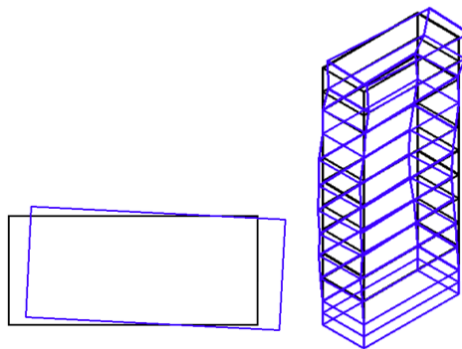
Figure 14. II Mode shape in X direction (2.25 Hz) - the 40th floor (left), the whole structure (right).

Ambient vibration measurements

The measurements were performed for all four blocks of the residential complex. Ambient vibration testing of the blocks A, B and C has been conducted by placing accelerometers on the 40th floor of the buildings for the purpose of identifying only the natural frequencies of each of the three blocks individual. Ambient vibration testing of the block D has been conducted along with the forced vibration testing of the whole structure of the building for the purpose of identifying the natural frequencies and the mode shapes of block D. The recorded ambient vibration data were processed in ARTeMIS Extractor software applying the Frequency Domain Decomposition (FDD) identification method and then compared with the results obtained by processing the vibration records in SHMART_2D MATLAB based software.

Direction / Mode	SHMART_2D Freq. (Hz)	ARTeMIS Freq. (Hz)	Direction / Mode	SHMART_2D Freq. (Hz)	ARTeMIS Freq. (Hz)
Y / I	0.53	0.5	Y / I	0.46	0.46
T / I	0.67	0.7	T / I	0.64	0.64
X / I	0.73	0.8	X / I	0.74	0.72
Y / II	1.87	1.9	Y / II	1.84	1.84
T / II	2.0	2.0	T / II	1.98	1.96
X / II	2.27	2.3	X / II	2.24	2.26
T / III	3.7	3.7	T / III	3.68	3.7
T / IV	5.5	5.6	T / IV	5.53	5.52

Table 2. Block A- Natural frequencies obtained by SHMART_2D and ARTeMIS.   **Table 3**. Block B- Natural frequencies obtained by SHMART_2D and ARTeMIS.

Direction / Mode	SHMART_2D Freq. (Hz)	ARTeMIS Freq. (Hz)	Direction / Mode	SHMART_2D Freq. (Hz)	ARTeMIS Freq. (Hz)
Y / I	0.45	0.5	Y / I	0.47	0.48
T / I	0.65	0.7	T / I	0.67	0.65
X / I	0.75	0.8	X / I	0.73	0.73
Y / II	1.93	1.8	Y / II	1.9	1.9
T / II	2.0	2.0	T / II	2.01	2.0
X / II	2.35	2.3	X / II	2.27	2.28
T / III	3.82	3.8	T / III	3.87	3.85
T / IV	5.7	5.7	T / IV	5.7	5.75

Table 4. Block C- Natural frequencies obtained by SHMART_2D and ARTeMIS.   **Table 5**. Block D- Natural frequencies obtained by SHMART_2D and ARTeMIS.

Conclusions

The results from experimental in-situ testing of the "Cevahir Sky City" residential complex, constructed in Aerodrom municipality in Skopje, is presented in this report. Two independent tests were performed. Firstly, an ambient vibration test on the 40th floor of blocks A, B and C were conducted for the purpose of identifying the structures' natural frequencies. Later, ambient and forced vibration testing of the whole structure of block D was carried out. The horizontal excitation was generated by two GSV-101 (Geotronix, USA) vibration generators which were placed on the 40th floor.

The natural frequencies of block A, B and C were identified. For block D natural frequencies, mode shapes and damping coefficients were obtained from both - ambient and forced vibration tests. From the data analysis during the testing period, it is concluded that:

- There is a good correlation between the results obtained from force and ambient vibration tests. The natural frequencies of all four blocks are similar, which brings a conclusion that there have been no temporary or local imperfections in the construction process;

- Identified structural mode shapes indicate that the structural interstorey stiffness distribution is favorable and it follows the structural design recommendations for high-rise building in seismic prone regions.

Information about the dynamic properties of the buildings, gathered by performing non-destructive tests of forced and ambient vibration tests combined, can be used for continuous structural health monitoring process of the residential complex. The importance of gathering information about the state of the structures right after they are constructed, is of crucial importance since provides important reference values which represent the healthy state of the structures.

Obtaining parameters of newly constructed, healthy structures is a benefit for the process of monitoring structure's state over time, after their exposure to extensive exploitation and also after future seismic events. Possessing required information for healthy structures will be used for tracing the structures' health history and, the most important, comparison of the healthy state parameters with the ones obtained at any time in the future, which makes the process of identifying eventually occurred damages much easier.

The present timing for the in-situ testing program of the "Cevahir Sky City" residential complex is favorable because it provided an information about the initial health state of the buildings, which provides the possibility of structural health monitoring process over their state during long time exploitation.

References

Garevski M., Gjorgjiev I., Jekikj G., Zhurovski A., Naumovski N. (2016): Experimental in-situ testing of the structures of Cevahir Sky City residential complex in Skopje by forced and ambient vibration methods, *IZIIS Report 2016-22,* Skopje, Republic of Macedonia, Institute of Earthquake Engineering and Engineering Seismology.

Garevski M., Cifliganec V., Jekikj G., Gjorgjiev I., Naumovski N., Zhurovski A. (2013): Analysis of dynamic properties of 9-Storey residential building by application of forced vibration testing and ambient vibration measurements, *IZIIS Report 2013-30,* Skopje, Republic of Macedonia, Institute of Earthquake Engineering and Engineering Seismology

Petkovski M., Tashkov Lj., Born, C.S., (1992): Full scale dynamic test of the 105- storey Ryugyong Hotel in Pyongyang, *Proceedings of the Tenth World Conference on Earthquake Engineering,* Madrid, Spain, 19-24 July, 2789- 2793.

Taleb R., Bouriche F., Remas A., Boukri M., Kehila F. (2012): Use of ambient and forced vibration tests to evaluate seismic properties of an unreinforced masonry building rehabilitated by dampers, *Proc. of the Fifteenth World Conference on Earthquake Engineering,* Lisbon, Portugal.

Tashkov Lj., Krstevska L. (2011): Experimental in-situ testing of residential buildings built in Dc-90 system located in Becici, Montenegro by ambient and forced vibration methods, *IZIIS Report 2011-39,* Skopje, Republic of Macedonia, Institute of Earthquake Engineering and Engineering Seismology.